Studying Polyoxometalates for Application in Redox Flow Batteries

Faye Cording

A thesis submitted for the degree of

Doctor of Philosophy

Chemistry - School of Natural and Environmental Sciences

Newcastle University

October 2020

Abstract

Energy storage is important to an energy sector in which renewable energy sources become more prevalent and the use of energy from fossil fuels is minimised. As energy from renewable sources is produced intermittently (e.g. from wind and solar photovoltaic systems), energy storage can be used to stabilise these energy sources by storing excess energy produced during times of low demand and releasing it later.

Redox Flow Batteries (RFBs), a type of secondary battery, are an energy storage technology that is of interest to both large-scale energy storage and smaller off-grid energy storage systems. RFBs have differences in operation compared to other secondary batteries. For instance, all of the active material of an RFB is dissolved in the electrolytes and no plating or intercalation reactions occur at the electrodes during charge and discharge. Further, the electrolytes are stored in external tanks and transported to the cells of an RFB by using pumps. This decouples the power and energy content of an RFB; power and energy can be adjusted independently by varying the size of the cell stack or the volume of electrolyte.

In RFB research, a common endeavour is the investigation of active materials that could target some of the limitations of the most mature RFB, the all-vanadium RFB, which uses vanadium ions as the active species. Polyoxometalates (POMs) are one type of compound that have been studied as RFB active materials. POMs are anionic metal-oxygen clusters containing early transition metals, termed the addenda atoms of the POM, which are often tungsten, molybdenum and vanadium. These elements can exhibit reversible redox reactions when incorporated into a POM. An additional element, such as silicon or phosphorus, is sometimes present in the core of a POM and is termed a heteroatom.

In this work, aspects of POMs for application in symmetric and asymmetric RFBs are investigated. Symmetric RFBs use the same active species in the positive and negative half-cell whereas asymmetric RFBs use a different species in each half-cell. $[SiV_3W_9O_{40}]^{7-}$, a mixed-addenda POM containing tungsten and vanadium, is studied as an active species for a symmetric RFB. Selected electrochemical properties of two POMs containing one type of addenda atom but a different heteroatom, $[SiW_{12}O_{40}]^{4-}$ and $[CoW_{12}O_{40}]^{6-}$, are also investigated in relation to their application as the active material in the negative electrolyte of an asymmetric RFB.

In symmetric flow cell testing of $[SiV_3W_9O_{40}]^{7-}$, coulombic efficiencies were >98% with 65% of the theoretical capacity of the battery accessed and a capacity fade of 2.7% over 50 cycles observed. Analysis of cycled $[SiV_3W_9O_{40}]^{7-}$ electrolytes did not indicate decomposition had occurred, indicating stability of $[SiV_3W_9O_{40}]^{7-}$ to the charge/discharge testing conditions in this study. In a study of the kinetics of the electron transfer of

$[SiW_{12}O_{40}]^{4-}$, an electron transfer constant (k^0) of ~10^{-2} cm s^{-1} was obtained by using Electrochemical Impedance Spectroscopy, which is four orders of magnitude higher than k^0 values reported for the redox reactions of the VRFB (the VO_2^+/VO^{2+} and V^{3+}/V^{2+} redox couples). In the testing of $[CoW_{12}O_{40}]^{6-}$ as an anolyte in an asymmetric flow cell, coulombic efficiencies of >97% were observed and up to 79% of the theoretical capacity was accessed. The results suggest that $[CoW_{12}O_{40}]^{6-}$ is worthy of further investigation as an anolyte species as it can accept more electrons per molecule than $[SiW_{12}O_{40}]^{4-}$, a species that has been tested in a flow cell in other studies. The direction of further work for the flow cell testing of $[SiV_3W_9O_{40}]^{7-}$ and $[CoW_{12}O_{40}]^{6-}$ and the study of the kinetics of $[SiW_{12}O_{40}]^{4-}$ is discussed.

Acknowledgements

I would like to thank my supervisor, Prof. Ulrich Stimming, for his help and input and the opportunity to carry out this project. I would also like to thank my second supervisor, Dr Elizabeth Gibson, for meeting with me during my time as a postgraduate student for discussions that I found very helpful. In addition, I am grateful to Dr Jochen Friedl for his guidance and expertise in the first half of my project.

Thank you to the members of the Stimming research group, past and present. I enjoyed getting to know all of you and working alongside you, and I have greatly valued your friendship. Specific acknowledgements must go to Felix Pfanschilling and Jochen Friedl whom I worked with when carrying out Electrochemical Impedance Spectroscopy in Section 4.4, Matthäa Holland-Cunz who provided the sample of $[PV_{14}O_{42}]^{9-}$ used in Section 5.5 and to Jochen Friedl and Thomas Beresford-Peirse whose work is featured in Section 5.6. I am also appreciative of the wider chemistry community in the Bedson Building who provided help in many ways, including those based in the office and in the electronic and mechanical workshops.

Finally, thank you to my family for being there for me and for offering support and encouragement during my studies, and always.

Publications

Redox flow batteries—Concepts and chemistries for cost-effective energy storage. M. V. Holland-Cunz*, F. Cording*, J. Friedl and U. Stimming, *Front. Energy*, 2018, **12**, 198–224.

Asymmetric polyoxometalate electrolytes for advanced redox flow batteries. J. Friedl*, M. V. Holland-Cunz*, F. Cording, F. L. Pfanschilling, C. Wills, W. McFarlane, B. Schricker, R. Fleck, H. Wolfschmidt and U. Stimming, *Energy Environ. Sci.*, 2018, **11**, 3010–3018.

(*equal contribution)

Contents

List of Figures

Chapter 1 - Introduction

1.1 The Need for Energy Storage

In 2017, the increase in the global mean surface temperature of the Earth that was attributable to human activities was assessed to be 1°C above pre-industrial levels (1850–1900).[1] The global atmospheric concentration of carbon dioxide reached 407.8±0.1 parts per million in 2018, a level that was 147% of pre-industrial levels.[2] The Paris Agreement entered into force on November 4th 2016 with a goal to keep the increase in the average global temperature this century to well below 2°C, and a more specific aim to limit this increase to 1.5°C.[3] A special report by the Intergovernmental Panel on Climate Change (IPCC) (a report invited as part of the Paris Agreement) stated that if the target of 1.5°C is to be adhered to, global net anthropogenic CO_2 emissions must reach net zero level by 2050.[4] By limiting global warming to 1.5°C instead of 2°C, it is expected that the risk to natural and human systems will be lower due to smaller rates and magnitudes of climate change.[5] This includes decreased frequencies and intensities of temperature-related extremes, and the ability of natural and human systems to adapt is enhanced when rates of change are lower.

The IPCC special report also notes that "the energy system transition that would be required to limit global warming to 1.5°C above pre-industrial conditions is underway in many sectors and regions around the world", continuing that "electrification, end-use energy efficiency and increased share of renewables amongst other options are lowering energy use and decarbonizing energy supply in the built environment".[6] In the United Kingdom, changes in the mix of fuels that are used for electricity generation, which included growth in the use of renewables, contributed to a 60% reduction in greenhouse gas emissions from the energy supply sector between 1990 and 2017.[7] For the July–September 2019 quarter, renewable energy sources accounted for a record share of total electricity generation in the United Kingdom, a value of 38.9% which exceeded the share of electricity that was generated from gas for the first time.[8] This was composed of electricity generation from bioenergy (12.0%), onshore wind (9.2%), offshore wind (9.8%) and solar photovoltaic technology (6.0%). In its New Energy Outlook 2019, Bloomberg New Energy Finance predicted a move globally from two-thirds of energy being supplied by fossil fuels in 2018 to two-thirds of the energy supply coming from zero-carbon sources by 2050, with 50% of the world's electricity supplied by wind and solar power.[9] Thus, renewable energy sources are a fixture of the energy supply at present, and will be a fixture of energy supplies in the future.

The intermittency of energy production from renewable sources (e.g. wind and solar photovoltaic) means that energy storage also has a role to play in an energy supply sector that contains a widening share of renewable energy. In a situation where electricity generation from a wind or solar photovoltaic installation exceeds or falls short of demand, energy storage can capture excess energy for later use or ensure supply is not interrupted. Energy storage is already deployed on the grid for matching energy supply with demand and to provide ancillary services,[10] and mechanical energy storage, specifically pumped hydro energy, is a mature technology. According to a report published in 2013, pumped hydro storage plants represented almost 99% of energy storage capacity worldwide.[10] However, installation of these systems requires considerations of topography and other technologies offer more flexibility in deployment location.

Electrochemical energy storage is another subset of energy storage technology. In the context of the transition of energy supplies towards renewable sources with a variable energy output, secondary batteries such as lead-acid, nickel-cadmium, sodium sulphur, sodium nickel chloride and lithium-ion varieties have all been included as technologies worthy of consideration.[11] Batteries, being of a modular design, offer flexibility in the location of their deployment, as well as scalability. These features mean that batteries can be considered for both grid-scale energy storage and decentralised energy systems that consist of a renewable energy source (e.g. solar photovoltaic cells installed on a rooftop) coupled with an energy storage technology. By 2050, ‘behind-the-meter’ electricity generation by homes and businesses, through the use of decentralised energy systems, is predicted to account for 5% of world electricity[9] and, more generally, energy storage installations are expected to proliferate rapidly across the world in the coming years. The total power and capacity of energy storage installed worldwide is forecast to rise from 9 gigawatts (GW) and 17 gigawatt-hours (GWh) in 2018 to 1095 GW/2850 GWh by 2040, an expansion that will be aided by a predicted decline of lithium-ion battery costs.[12]

A further electrochemical energy storage device, which sits alongside conventional secondary batteries as a technology of interest to the expansion of energy storage, is the redox flow battery (RFB). RFBs differ in operation compared to conventional secondary batteries and have some advantageous characteristics.

1.2 Redox Flow Batteries

RFBs utilise the redox reactions of species that remain in the liquid phase throughout the reaction in order to store and release energy. A typical single cell of an RFB consists of two half-cells containing a positive electrode (cathode) or a negative electrode (anode) that are divided by a separator, such as an ion exchange membrane. The separator prevents the crossover of active species between half-cells but allows the passage of ions in the supporting electrolyte to complete the electrical circuit. The positive electrolyte (catholyte) and negative electrolyte (anolyte) which contain the active materials are pumped continuously into each half-cell, where the redox reactions take place, and are then returned to the storage tanks. The electrodes have either a ‘flow-through’ configuration in which the electrolyte flows through a porous electrode or a ‘flow-by’ configuration in which the electrolyte flows past a planar electrode. Electrons move through the electrode towards an adjacent metallic or carbon-based current collector that conducts the electrons to the external circuit.

Flow-through electrodes are typical of RFBs that use the reactions of liquid-phase species whereas flow-by electrodes are used when the half-cell reaction involves a gaseous reactant, such as hydrogen at an anode that uses the H^+/H_2 redox couple. In a flow-by configuration, gaseous species that flow in a channel parallel to the electrode diffuse laterally to the electrode surface.[13]

Figure 1.1 shows a schematic of an RFB cell. In a large-scale RFB installation, individual cells are connected in series using bipolar plates to produce cell stacks with higher voltages.

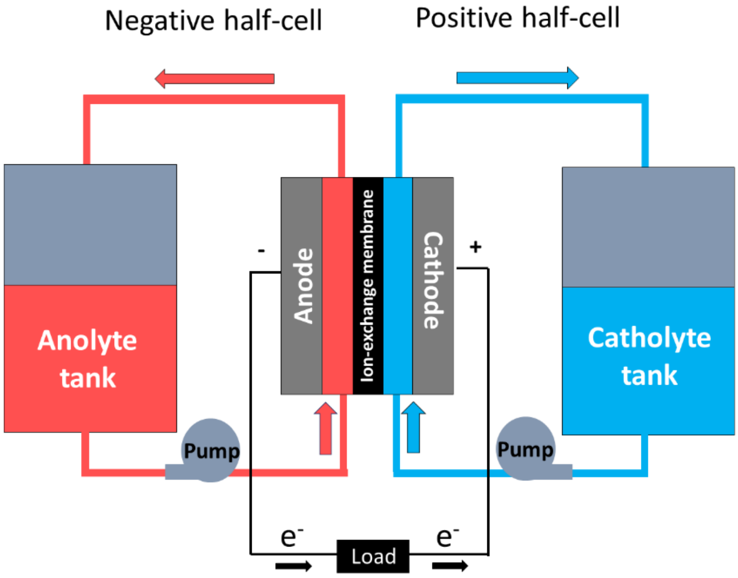

Figure 1.1 - Schematic diagram of a single RFB cell in discharge mode.

There are advantages to the design of an RFB when compared to other secondary batteries. As the electrolytes of an RFB are stored in tanks that are external to the cell stack, the energy storage capacity and power of an RFB are decoupled. This is a difference in design when compared to other secondary batteries where the electrolyte volume is fixed within the battery. The capacity and power of an RFB can be adjusted independently by varying the volume of electrolyte that is stored or the size of the cell stack, respectively. While the electrolytes can be toxic and/or corrosive (state-of-the-art RFBs use an acidic supporting electrolyte), they are typically aqueous solutions meaning that RFBs do not present the same risk of flammability as lithium-ion batteries.

A further benefit of RFBs is the inertness of the electrodes, which serve as the site for the reactions of the active species but do not store any active material. When a conventional secondary battery undergoes a charge/discharge cycle, the electrode materials expand and contract which leads to degradation over time.[14] As the active species of an RFB are dissolved in the electrolytes throughout charging and discharging, the electrodes are not subjected to continuous plating or intercalation reactions meaning that electrode deterioration is minimised and cycle lifetimes are longer. The predicted lifetime of the most mature RFB technology is >10000 cycles, compared to an indicative value of >2000 cycles for the lead-acid battery and 5000 cycles for the dominant type of lithium-ion battery with a graphite anode.[11] The component of an RFB that limits its lifetime is typically the cell stack. Wearing of the membrane is a source of performance fade and a lifetime of 10–15 years for the cell stack of an RFB undergoing 1000 charge/discharge cycles per year has been suggested.[15] The electrolyte storage tanks, plumbing, structural components, power electronics and controls of an RFB can be expected to have longer useful lifetimes,[16] but replacement of the pump may be required periodically. The membrane between half-cells is typically not completely efficient at preventing the crossover of active species. As this crossover is a source of capacity fade, continued electrolyte maintenance may be necessary. However, with stack and pump replacement, RFBs can have a calendar lifetime of more than 20 years.[15]

Important parameters to describe RFB performance are the coulombic efficiency and the voltaic efficiency. The coulombic efficiency is the ratio of the current transferred upon discharge, Q_{out}, to the current transferred upon charge, Q_{in} (Equation 1.1). A low value indicates that crossover of active species has occurred or that a side reaction has taken place.

$$Coulombic\ Efficiency = \frac{Q_{out}}{Q_{in}} \times 100\% \tag{1.1}$$

The voltaic efficiency is the ratio of the average discharging voltage, $V_{discharge}$, to the average charging voltage, V_{charge} (Equation 1.2).

$$Voltaic\ Efficiency = \frac{V_{discharge}}{V_{charge}} \times 100\% \tag{1.2}$$

The theoretical voltage of an RFB can be calculated from the difference between the standard electrode potentials (E^0) of the anodic and cathodic reactions, but the charging voltage and discharging voltage can be very different to the theoretical voltage in practice. The magnitude of the discrepancy between the charging and discharging voltage of a cell when current is flowing is indicated by the voltaic efficiency. The lower the value of the voltaic efficiency, the greater the deviation from the theoretical voltage that is required for a selected current to flow. The opposition to current flow is represented by the total resistance of a cell, R_{total}, which is shown in Equation 1.3. R_{ohm} includes the resistance to ionic transport in the electrolyte and the resistance of the membrane and depends on the design of the cell and the components used. R_{mass} is the mass transport resistance which is influenced by electrolyte flow rate and concentration. R_{CT} is the charge transfer resistance of the anodic and cathodic redox reactions and depends on the chemical species employed as the active materials in an RFB. R_{CT} is discussed in later chapters.

$$R_{total} = R_{ohm} + R_{CT} + R_{mass} \tag{1.3}$$

The product of the coulombic efficiency and the voltaic efficiency is the energy efficiency, which indicates how much of the energy supplied to charge a battery is extracted upon discharge (Equation 1.4). The energy efficiency can be indicated for a single cell or for a complete RFB system. For a single RFB cell, the energy efficiency is affected by the kinetic, ohmic and mass transport losses that reduce the voltaic efficiency, as well as crossover or side reactions that reduce the coulombic efficiency.[17] For a complete RFB system, other losses also impact the energy efficiency such as energy losses due to temperature control, pumps and other equipment, and acceptable energy efficiencies can be in the 70–80% range for commercial RFB systems when including these additional losses.[17]

$$Energy\ Efficiency = \ CE \times VE \times 100\% \tag{1.4}$$

Other commonly reported parameters are the energy density, either the volumetric energy density (unit of Wh L^{-1}) or gravimetric energy density (Wh kg^{-1}), and the power density (W cm^{-2}). The power density is calculated from the product of the current (I) and the cell voltage (V) divided by the active surface area of an RFB (generally the effective area of the separator[18]) and is shown in Equation 1.5. A typical power density for an RFB cell is 0.1 W cm^{-2}.[14]

$$Power\ density = \frac{I \times V}{active\ surface\ area} \tag{1.5}$$

The energy density (volumetric) of an RFB depends on the concentration of active species (c), the number of electrons transferred (n) and the cell voltage as shown in Equation 1.6, where F is the Faraday constant. This value is divided by two when used to calculate the energy density of a complete RFB due to the separate volumes of catholyte and anolyte. Dividing by 3600 converts the volumetric energy density to the unit of Wh L^{-1} (1 Wh = 3600 J). Volumetric energy densities are commonly reported using this unit.

$$Volumetric\ Energy\ Density = \left(\frac{nVcF}{2}\right) \div 3600 \tag{1.6}$$

For a typical RFB that uses active materials that transfer one electron per molecule, a concentration of 1.5 M in each electrolyte, and a theoretical cell voltage of 1.26 V, the volumetric energy density would be 25 Wh L^{-1}. Values reported for the volumetric energy density of state-of-the-art RFBs are 20–33 Wh L^{-1}.[19] This is lower than values for lithium-ion batteries which are in the region of 200–400 Wh L^{-1}.[20] A factor contributing to the lower energy density is that RFBs tend to use aqueous electrolytes which means that the cell voltage is limited by the electrochemical window of water (1.23 V) although a cell voltage in excess of this (e.g. 1.6 V[21]) can be tolerated when the electrode materials have a high overpotential for the water decomposition reactions (e.g. carbon-based electrodes). The electrolytes of lithium-ion batteries are non-aqueous and are stable over a greater voltage range.

The theoretical capacity of an RFB is also often reported (Equation 1.7) where v is the volume of electrolyte and the divisor of 3600 converts this value to the unit of ampere-hour (Ah) (1 Ah = 3600 C).

$$Theoretical\ capacity = \frac{ncvF}{3600} \tag{1.7}$$

The percentage of the theoretical capacity of an RFB that is accessed in practice (the electrochemical yield) can be calculated using the capacity observed and the theoretical capacity, as shown in Equation 1.8.

$$Electrochemical\ yield = \left(\frac{Observed\ capacity}{Theoretical\ capacity}\right) \times 100 \tag{1.8}$$

One of the first descriptions of an RFB was the iron-chromium RFB that was patented by NASA in the 1970s.[22] At its inception, the conceivable applications of this RFB were in the area of bulk power storage in large installations used for peak shaving and load levelling by the electric utility network, and as an energy storage device that could be coupled with an intermittent power source such as solar power in small installations.[23] During operation, ferric and ferrous ions (Fe^{2+} and Fe^{3+}) are oxidised or reduced at the cathode and chromic and chromous ions (Cr^{2+} and Cr^{3+}) are oxidised or reduced at the anode (Equations 1.9 and 1.10).

$$Fe^{3+} + e^{-} \rightleftharpoons Fe^{2+}\ (E^{0} = 0.77\ \text{V vs SHE}) \tag{1.9}$$

$$Cr^{2+} \rightleftharpoons Cr^{3+} + e^{-}\ (E^{0} = -0.41\ \text{V vs SHE}) \tag{1.10}$$

The work on the iron-chromium RFB by NASA ended in the mid-1980s without commercialisation of the system, reflecting a decreased appetite for the development of energy storage at the time due to a lowering of crude oil prices.[24] Difficulties encountered in its development included the formation of unreactive chromium species at 25°C, and a final report by NASA suggested an operating temperature of 65°C to shift the equilibrium towards formation of the reactive chromium species. This required the use of mixed reactant solutions to counter the inefficiency of the state-of-the-art membranes of the time at this elevated temperature.[25] Commercialisation of the iron-chromium RFB has been attempted more recently. A 250 kW/1 MWh demonstration of an iron-chromium battery was developed in California in 2014,[26] but the company responsible went into liquidation soon afterwards.[27]

It was also in the mid-1980s that another type of RFB was pioneered by researchers at the University of New South Wales in Australia: the all-vanadium RFB (VRFB).[28] Unlike the iron-chromium RFB, the VRFB has seen intensive development and has been commercialised by companies around the world such as redT (recently rebranded to Invinity Energy Systems after a merger with Avalon Battery) and Rongke Power.[29, 30] In January 2020, there were 65 VRFB projects worldwide that were listed as operational, under construction, contracted or announced in the Department of Energy Global Energy Storage Database.[31]

The VRFB uses the four oxidation states of vanadium for its charge/discharge reactions: vanadium(II), vanadium(III), vanadium(IV) and vanadium(V). The cathodic and anodic reactions are as follows:

$$VO_2{}^+ + 2H^+ + e^- \rightleftharpoons VO^{2+} + H_2O \ (E^0 = 1.00 \text{ V vs SHE}) \quad 1.11$$

$$V^{2+} \rightleftharpoons V^{3+} + e^- \ (E^0 = -0.25 \text{ V vs SHE}) \quad 1.12$$

In order to prepare the electrolytes, a mixture of vanadium(III) and vanadium(IV) species in a 50:50 mole ratio (termed a $V^{3.5+}$ electrolyte) is often used and is charged to form an anolyte containing V^{3+} and a catholyte containing VO^{2+} before battery operation.[32] The use of a single element greatly simplifies electrolyte regeneration if crossover has occurred and imbalanced the capacity of the electrolytes, as rebalancing is achieved in a relatively simple manner by remixing the electrolytes periodically. Avoiding contamination of the anolyte or catholyte with disparate chemical species from the other half-cell is the main asset of the VRFB but the fluctuating price of vanadium, which has climbed recently, is a disadvantage. A major use of vanadium is in the production of steel and so its consumption rises and falls in response to global steel production. The annual average price of vanadium (as V_2O_5) increased year-on-year from US\$7.45 kg^{-1} to US\$30.86 kg^{-1} in the 2016–2018 time period.[33] The cost of the VRFB electrolytes is one factor that is driving research into alternative RFB active materials that could be less costly.

The single-element chemistry of the VRFB invites a discussion of the differences between two types of RFB: symmetric and asymmetric. Schematic diagrams indicating the operation of a symmetric and an asymmetric RFB are shown in Figure 1.2.

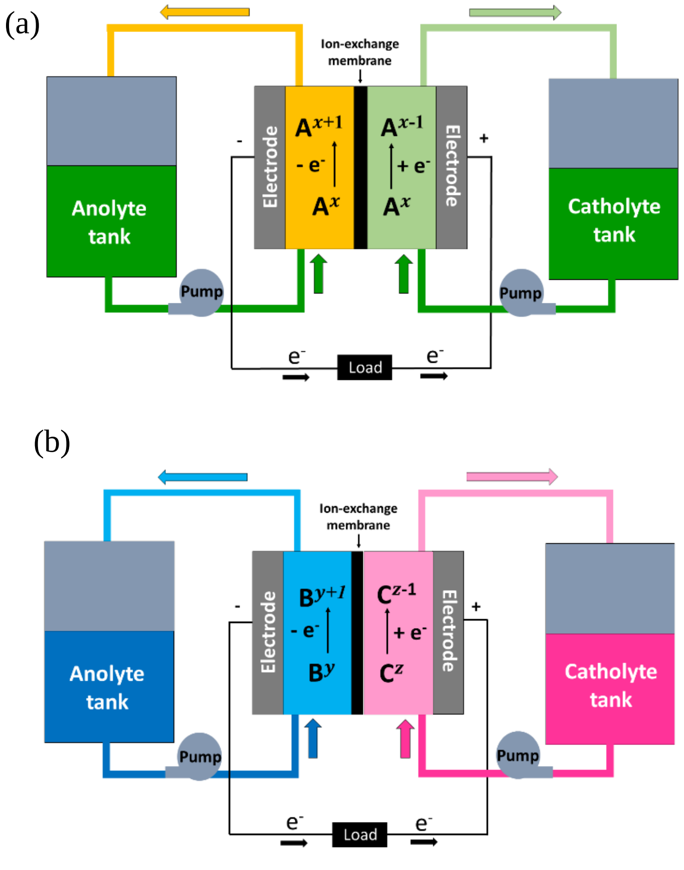

Figure 1.2 - Schematic diagram of a symmetric RFB, (a), and an asymmetric RFB, (b), where the active species can lose or gain one electron per molecule. The reactions shown are those that occur when charging the cell.

A symmetric RFB (Figure 1.2a) is based on a single parent species that can exist in three or more oxidation states, which may or may not all be charged species. In the symmetric RFB schematic in Figure 1.2a, A is the active species in the electrolyte in both half-cells and x is oxidation state of A before the cell is charged. Upon charge, A^x is oxidised to A^{x+1} in the anolyte and reduced from A^x to A^{x-1} in the catholyte. In the discharged state, the composition of the anolyte and the catholyte of a symmetric RFB is the same (in the schematic in Figure 1.2a, they both contain species A^x). As the VRFB is based on one element, it is often referred to as a symmetric RFB, although the composition of the anolyte and catholyte are not the same in a discharged VRFB. A wealth of species have been considered for the role of a symmetric RFB active material, some of which are discussed in Section 1.2.2.

An asymmetric RFB is based on the redox couples of different chemical species in the positive and negative half-cell. In Figure 1.2b, the anolyte and catholyte contain different active species, B^y and C^z where y and z are the oxidation states of B and C when the cell is in the discharged state. When the asymmetric cell is charged, B^y is oxidised to B^{y+1} and C^z is reduced to C^{z-1}. An example of an asymmetric RFB is the iron-chromium RFB. Asymmetric RFBs are discussed first in Section 1.2.1.

1.2.1 Asymmetric Redox Flow Batteries

In addition to the iron-chromium RFB, other asymmetric RFBs have reached commercialisation, or an advanced stage of development. One example is the bromine-polysulphide RFB, the half-cell reactions of which are shown in Equations 1.13 and 1.14. Upon charge, bromide ions are oxidised to bromine at the cathode, which complexes with an additional Br^- ion to form the tribromide ion (Br_3^-), while the S_4^{2-} anion is reduced to S_2^{2-} at the anode.

$$3\mathrm{Br}^- \rightleftharpoons \mathrm{Br}_3^- + 2\mathrm{e}^- \ (E^0 = 1.09 \text{ V vs SHE}) \qquad 1.13$$

$$S_4{}^{2-} + 2\mathrm{e}^- \rightleftharpoons 2S_2{}^{2-} \ (E^0 = -0.265 \text{ V vs SHE}) \qquad 1.14$$

The bromine-polysulphide RFB was patented in 1984[34] and later investigated by Regenesys Technologies, Ltd in the 1990s and early 2000s. The company produced three scales of bromine-polysulphide modules (S-, M- and XL-series) with 5 kW, 20 kW and 100 kW power output and a 1 MW pilot scale facility was built at Aberthaw Power Station in the United Kingdom.[35] A 15 MW/120 MWh demonstration plant that used up to 120 XL-series modules was under construction at Little Barford Power Station, also in the United Kingdom, but the plant was never fully commissioned and funding was later withdrawn.[36] Issues encountered with the bromine-polysulphide RFB include crossover, deposition of sulphur species in the membrane and concerns over the formation of H_2S and Br_2 gases.[37]

The zinc-bromine RFB is a further system that has reached commercialisation and is an example of a hybrid RFB, containing one half-cell with solely liquid-phase reactants and one half-cell in which a plating/dissolution reaction occurs at the electrode during charge and discharge. A patent for a static zinc-bromine battery was granted in 1885,[38] but initial development of zinc-bromine flow batteries was carried out by Gould, Inc. and Exxon in the late 1970s/early 1980s.[39, 40] The zinc-bromine RFB is currently marketed by companies such as Redflow and Primus Power.[41, 42] The Br_3^-/Br^- redox couple is the cathodic reaction (Equation 1.13) while plating and dissolution of zinc occurs at the anode upon charge and discharge (Equation 1.15).

$$Zn^{2+}(aq) + 2e^- \rightleftharpoons Zn(s) \ (E^0 = -0.76 \text{ V vs SHE}) \qquad 1.15$$

The low cost of the reactants is one benefit of this technology and the theoretical voltage (1.82 V) is higher than that of the VRFB (1.25 V). The energy density is 70–80 Wh L^{-1} compared to 20–33 Wh L^{-1} for the VRFB.[19, 24] Non-uniform deposition of zinc at the anode during charging can result in the growth of dendrites, a source of internal short circuits. A smooth electrode surface can be regained by performing maintenance procedures, such as regular full discharge to strip the anode of residual zinc.[21] Complexing agents such as quaternary ammonium salts are added to the electrolyte to ensure that elementary bromine formed at the cathode is complexed and contained within an organic phase that travels with the electrolyte, with bromine in both phases reduced during discharge.[37] This lowers self-discharge by limiting the diffusion of bromine through the membrane to the zinc anode.[43]

Other cathode reactions have been coupled with a zinc anode and investigated as hybrid RFBs including the Ce^{4+}/Ce^{3+} redox couple in a zinc-cerium RFB[44] and the I_3^-/I^- couple in a zinc-polyiodide RFB[45] but the commercialised zinc-bromine variant is the most mature at this time.

The iron-chromium, polysulphide-bromine and zinc-bromine RFBs are important examples of RFBs that have been scaled-up to a size commensurate with energy storage on a large scale, although the zinc-bromine RFB is the only one that is in commercial production at this time. All are relatively mature RFB concepts, having been developed in the latter half of the 20th century. More recently, research into RFBs has seen the emergence of organic active species as an alternative to metal-ion chemistries, and increased focus on the use of non-aqueous solvents in supporting electrolytes. Novel operating concepts have also been developed which stretch and challenge the definition of an RFB.

RFBs based on redox-active organic molecules instead of metal ions could address concerns about the high cost of the active material of mature RFBs (i.e. the VRFB) as these species could be synthesised from low-cost, abundant materials. Further, there is the potential to tailor organic active species to suit requirements and improve battery performance, by tuning the solubility and redox potential through modifying the structure.

The use of organic active species in one half-cell is an avenue that has been explored, such as in the first organic/inorganic RFB reported by Xu *et al*. in 2009, which used cadmium (the Cd^{2+}/Cd redox couple) at the anode and tetrachloro-*p*-benzoquinone at the cathode.[46] A variant of this RFB chemistry was reported by the same authors that used another benzoquinone species in the positive half-cell (4,5-dibenzoquinone-1,3-benzenedisulfonate) and the $PbSO_4/Pb$ redox couple in the negative half-cell.[47] A metal-free organic/halogen RFB was later reported that used an anthraquinone species, 9,10-anthraquinone-2,7-disulfonic acid (AQDS), as the anode-active material and the Br_2/HBr redox couple at the cathode.[48]

Benzoquinones and anthraquinones are members of the quinone family of compounds which are aromatic structures that contain a six-membered ring with two carboxyl groups as their core structural characteristic (Figure 1.3a). Quinones can undergo a two-proton two-electron reduction to hydroquinones, with a variable reduction potential that is dependent on the structure of the quinone. The composition of AQDS (which contains only the earth-abundant elements of carbon, sulphur, hydrogen and oxygen) and the ability to modify the reduction potential through the addition of hydroxyl groups to the two aromatic rings are advantageous aspects of this species that were highlighted in the study of its application in the anthraquinone/bromine RFB.[48] These two properties (i.e. preparation using affordable raw materials and tunability of redox properties) exemplify some of the arguments in favour of the development of organic active species for RFBs.

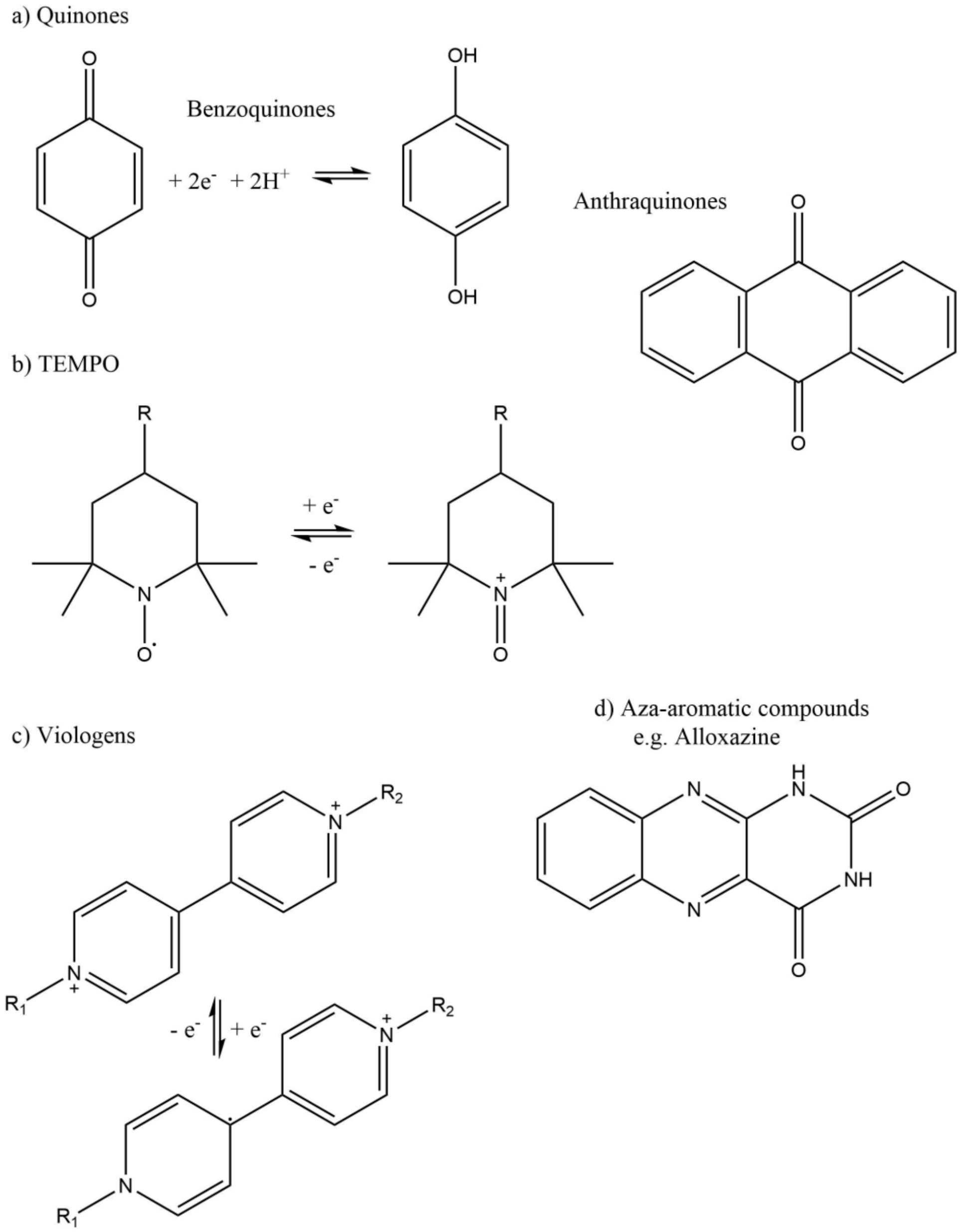

Figure 1.3 - Families of organic compounds that have been investigated as RFB active species. (a) quinones, (b) TEMPO radicals, (c) viologens and (d) aza-aromatics.

In later work, the anthraquinone/bromide chemistry demonstrated stability to extended charge/discharge testing in an RFB, with an average capacity retention of 99.84% and an average coulombic efficiency of 98.35% observed over 750 cycles.[49] RFBs that use a quinone species in the negative half-cell saw further development following this work, with the replacement of bromine by the less toxic ferrocyanide ion ($[Fe(CN)_6]^{4-}$) in the catholyte.[50-52]

The first RFB to utilise an organic molecule in both half-cells was presented by Li *et al*. in 2011.[53] The molecule used in the catholyte was TEMPO (2,2,6,6-tetramethylpiperidine-1-oxyl, see Figure 1.3b). TEMPO is a heterocyclic, stable nitroxide radical that can be oxidised to an oxammonium cation. N-methylphthalimide, which can be reversibly reduced to a radical anion, was used in the anolyte. The supporting electrolyte was non-aqueous (a 1 M $NaClO_4$ solution in acetonitrile) and the theoretical voltage of the system was 1.6 V. Coulombic efficiencies of around 90% were observed over 20 cycles, but the degree of capacity retention over these cycles was not stated.

Yang *et al*. reported the first aqueous organic RFB in 2014, which combined a benzoquinone species in the positive half-cell (1,2-benzoquinone-3,5-disulfonic acid, or BQDS) with an anthraquinone species in the negative half-cell (anthraquinone-2-sulfonic acid or anthraquinone-2,6-disulfonic acid) in a supporting electrolyte of 1 M H_2SO_4.[54] Flow cell testing did not show a noticeable change in capacity over 12 charge/discharge cycles and over 90% of the theoretical capacity of the battery was accessed. The concentration of active species in the electrolytes was modest at 0.2 M and was at the solubility limit of anthraquinone-2-sulfonic acid, indicating that further work could include efforts to increase the solubility of these active species. Later work described an increase in the performance of the same quinone-based aqueous RFB concept.[55] The sodium sulfonate salts of BQDS and anthraquinone-2,6-disulfonic acid were converted to the free acid form (sulfonic acids) by exchanging the sodium ions for protons, which increased solubility. Charge/discharge testing was carried out using electrolytes with an active species concentration of 1 M. Through modifying the flow field (switching from a flow-by configuration to a design with flow-through characteristics) and making changes to the electrode design (increasing the accessible surface area), a peak power density of 100 mW cm^{-2} was observed, compared to 0.025 W cm^{-2} in the previous system.[54]

It was realised that BQDS underwent a chemical transformation during charge/discharge testing, through the nucleophilic addition of water to the aromatic ring. Although a coulombic efficiency of 100% was observed over 100 cycles, the composition of the catholyte shifted from its initial composition to an alternative species which could still be cycled with anthraquinone-2,6-sulfonic acid. After 400 cycles, BQDS was fully converted to a species in which all of the carbon atoms in the six-membered ring that did not bear a sulfonic acid group were hydroxylated (1,2,4,6-tetrahydroxybenzene-3,5-disulfonic acid) through the reaction mechanism of Michael addition. A ‘Michael-reaction-resistant’ benzoquinone species was later reported for application in a catholyte, which had a minimum number of unsubstituted positions.[56]

Whereas all of the aforementioned RFBs using quinone species had acidic supporting electrolytes (0.5 M H_2SO_4–3 M H_2SO_4), Liu *et al*. reported an aqueous organic RFB that used neutral supporting electrolytes (1 M NaCl).[57] 4-hydroxy-2,2,6,6-tetramethylpiperidin-1-oxyl (4-HO-TEMPO) was used in the catholyte and a viologen compound, 4,4-dimethyl bipyridinium dichloride (methyl viologen, see Figure 1.3c), was used in the anolyte. Viologens are 4-4'-bipyridine derivatives in which the nitrogen atoms have been alkylated and possess a formal positive charge. Methyl viologen, a dication, underwent a one-electron redox reaction to a monocationic radical at the anode. Coupled with the one-electron reduction of 4-HO-TEMPO at the cathode, the theoretical cell voltage was 1.25 V. The capacity retention was 99% after 100 cycles. The solubility limit reported for methyl viologen, at 3.0 M in a 1.5 M NaCl supporting electrolyte, was higher than for quinone species that were reported in previous studies, but the solubility of 4-HO-TEMPO (0.5 M) limited the theoretical energy density of the system (8.4 W h L^{-1} for a 4-HO-TEMPO/methyl viologen concentration of 0.5 M).

Another aqueous organic RFB that used a TEMPO derivative in the catholyte and methyl viologen in the anolyte was reported by Janoschka *et al*.[58] The cell employing 'TEMPTMA' (*N*,*N*,*N*-2,2,6,6-heptamethylpiperidinyl oxy-4-ammonium chloride) and methyl viologen had an energy density of 38 Wh L^{-1} for a theoretical cell voltage of 1.4 V and active material concentrations of 2 M. The solubility of TEMPTMA, which contains a hydrophilic trimethylammonium chloride group, was 2.3 M in 1.5 M NaCl, showing how structural differences in TEMPO species can correspond with increased solubility. Capacity retention was demonstrated over 100 cycles.

In later work, Hu *et al*. reported a further variant of a TEMPO/viologen aqueous organic RFB that used the same TEMPO species as Janoschka *et al*. but a different viologen species as anolyte: 1,1'-bis[3-(trimethylammonio)-propyl]-4,4'bipyridinium tetrachloride ($(NPr)_2V$).[59] In $(NPr)_2V$, the nitrogen heteroatom in each aromatic ring is substituted with a (trimethylammonio)-propyl chain. After 500 charge/discharge cycles, the capacity retention was 97.48% and the peak power density was 134 mW cm^{-2}. The capacity retention for the flow cell with $(NPr)_2V$ exceeded the capacity retention of a further flow cell that was tested in the same investigation which used methyl viologen in the anolyte (91.21%). The higher capacity retention was attributed to the higher stability of the $[(NPr)_2V]^{+\bullet}$ radical that is generated during charging of the RFB. It was thought that the greater charge repulsion between $[(NPr)_2V]^{+\bullet}$ species due to the positively-charged ammonium groups in this structure made it less susceptible than methyl viologen to a radical-quenching dimerization process.

Methyl viologen has been used in further aqueous RFBs, coupled with ferrocene compounds as the catholyte species for instance.[60] The two ferrocene compounds in this study were functionalised with hydrophilic ammonium groups and had solubilities of around 3 M, which corresponded to theoretical energy densities of 45.5 Wh L^{-1} and 35.8 Wh L^{-1} for a theoretical cell voltage of 1.05 V. Using an active species concentration of 0.5 M, coulombic efficiencies in initial flow cell tests were greater than 99%. Long-term cycling of a flow cell that used (ferrocenylmethyl)trimethylammonium chloride and methyl viologen was undertaken later. The peak power density during this test was 100 mW cm^{-2} and an analysis of solutions after 700 charge/discharge cycles indicated no chemical degradation had occurred in the catholyte or anolyte. The capacity loss was 0.05% per cycle and the source of this was to be a focus of ongoing studies.

The redox reactions of methyl viologen were the subject of other studies. A further one-electron reduction of methyl viologen is possible but has been found to produce an insoluble species and this reaction is therefore unsuitable for RFB applications. N-functionalisation of methyl viologen with hydrophilic groups such as alkylammonium groups instead of a methyl groups in order to increase solubility, as well as extending the conjugation of the molecule to reduce the potential gap between the two one-electron reductions, have been studied as ways of accessing both one-electron reductions in an aqueous RFB.[61, 62] Methyl viologen was also investigated in a non-aqueous electrolyte (acetonitrile),[63] paired with a ferrocene species that was soluble in organic solvent in the catholyte (a variation of the catholyte species previously reported[60]). Methyl viologen bis(trifluoromethane)sulfonamide was found to exhibit two reversible one-electron reductions. In a flow cell test, the capacity retention was 91.8% after 100 cycles and 78.4% of the theoretical capacity was accessed, indicating that the second reduction of methyl viologen was accessible and that it was possible to overcome the solubility issues of this species.

TEMPO, viologen and quinone compounds were studied as organic active species for RFBs in the work discussed so far. A further family of compounds to highlight in this overview of asymmetric RFBs are aza-aromatic molecules (Figure 1.3d), which have been investigated as anolyte species. Noting that the isoalloxazine backbone of riboflavin 5' phosphate (a vitamin B2 derivative and a cofactor in biological reactions) could undergo a two-electron reduction, an alloxazine species was prepared for an RFB study. This species was 'alloxazine 7/8-carboxylic acid' (an isomeric mixture) which contained a carboxylic acid group on the phenyl ring for increased solubility (in pH 14 KOH solution, the solubility was 2 M).[64] Pairing this species with the $[Fe(CN)_6]^{4-}/[Fe(CN)_6]^{3-}$ redox couple in the catholyte gave a theoretical voltage of 1.2 V. A coulombic efficiency of 99.7% was observed and 91% of the initial capacity was retained over 400 cycles at an alloxazine concentration of 0.5 M. The peak power density was 0.35 W cm^{-2} at a current density of 0.58 A cm^{-2}, and the normal operating current density was 100 mA cm^{-2} over 400 charge/discharge cycles. A computational study of several alloxazine derivatives showed that the addition of electron donating groups or electron withdrawing groups could decrease or increase the reduction potential over a range that spanned 400 mV, highlighting the possible tunability of these structures and how computational studies could be used to select functional groups that modify a property in a desired way. An unmodified flavin structure (a sodium salt of riboflavin-5’-phosphate) has also been tested as an anolyte species.[65] Derivatives of phenazine have also been examined, which is a further example of a molecule that acts as cofactor in biological redox reactions and can undergo a two-electron redox reaction.[66]

In addition to small organic molecules, redox-active polymers have also been investigated as RFB active materials. One example is an all-polymer RFB that used a polymer containing TEMPO units at the cathode and a polymer that contained viologen units at the anode.[67] The polymers also contained quaternary ammonium units for increased solubility. The supporting electrolyte was 2 M NaCl and a low-cost cellulose-based dialysis membrane was used as a separator. Energy densities of around 10 Wh L^{-1} were reported for the polymer electrolytes. After 10000 cycles, 80% of the initial capacity was retained in a static, unpumped cell, while faster capacity fade occurred in a pumped cell which was thought to be attributable to oxidation of the active species by atmospheric oxygen. The compatibility of size exclusion membranes with polymeric active species means that the use of more expensive Nafion ion exchange membranes as separators can be avoided in polymer RFBs.

Winsberg *et al*. investigated a hybrid TEMPO polymer/zinc RFB.[68] Different TEMPO polymers were synthesised for use as catholyte species, which were intended for use in either water or organic solvent. These were combined with a zinc foil anode. As in the previous study, a size exclusion membrane was used as a separator. Two of the polymers were ‘poly(TEMPO-co-PEGMA)’ species, where PEGMA = poly(ethylene glycol methacrylate, and the proportion of PEGMA comonomer in the structures differed. One polymer had a 1:1 TEMPO:PEGMA ratio and could be dissolved in water. The other polymer had a greater TEMPO:PEGMA ratio and could be dissolved in alkyl carbonates. Theoretical energy densities of 8.1 Wh L^{-1} and 4.1 Wh L^{-1} were reported for non-aqueous and aqueous RFBs that used the poly(TEMPO-co-PEGMA) catholytes, respectively. In flow cell tests of 500 and 1000 cycles, both the non-aqueous and aqueous TEMPO polymer/zinc systems showed some capacity fade (e.g. 81% of the initial discharge capacity was retained in the non-aqueous flow cell after 500 cycles). Coulombic efficiencies were up to 99.7% for the non-aqueous cell and above 90% for an aqueous cell. Although the non-aqueous polymer electrolyte had a higher theoretical energy density, the flow cell had to be operated at lower current densities (up to 4 mA cm^{-2}, compared to up to 20 mA cm^{-2} for the cell that used aqueous electrolytes).

Also investigated was a non-aqueous polymer RFB that utilised two polymers containing the boron-dipyrromethene (BODIPY) unit.[69] It was shown that BODIPY exhibited two redox reactions that corresponded to reduction to a 'BODIPY$^{-\cdot}$' species and oxidation to a 'BODIPY$^{+\cdot}$' species. The BODIPY monomers were copolymerised with different groups to generate two different polymers that could be used as the anolyte and catholyte. A static cell test using two BODIPY polymers and propylene carbonate as the solvent had coulombic efficiencies of 89%, with an initial 30% reduction in capacity for the first 10 cycles followed by a stable capacity for the next 90 cycles. The energy densities of the polymer electrolytes were 0.5 Wh L^{-1}.

It has been highlighted that the RFBs with organic active species described here used either an aqueous or non-aqueous supporting electrolyte. The rationale for investigating RFBs that use non-aqueous electrolytes is that higher energy densities could be realised, as higher cell voltages are possible through the use of an organic solvent that is stable over a greater voltage range than water. For instance, acetonitrile has an electrochemical window of 6.1 V and propylene carbonate has an electrochemical window of 6.6 V.[70] However, while non-aqueous RFBs can have higher theoretical energy densities than aqueous RFBs, ionic conductivity is lower for organic solvents which can lead to high internal resistance and poor voltage efficiency.[70] Consequently, the current density for non-aqueous RFBs can be two to three orders of magnitude lower than state-of-the-art aqueous RFBs.[70] In the non-aqueous RFBs outlined here, current densities of 0.35 mA cm^{-2} and 1.4 mA cm^{-2} were reported[53, 68] whereas current densities for the aqueous RFBs included 50 mA cm^{-2}, 60 mA cm^{-2} and 100 mA cm^{-2}.[58, 60, 64] These examples illustrate that aqueous RFBs can operate with higher current densities. However, some non-aqueous RFBs buck the trend, operating at a current density of 10–40 mA cm^{-2} for example.[63] In a review of non-aqueous RFBs, it was concluded that achieving low internal resistance and better cell performance by improving the conductivity of the electrolyte and the membrane were urgent needs for non-aqueous RFBs.[70]

Increasing energy density by a means other than, or in conjunction with, switching to non-aqueous electrolytes is also a theme in RFB research. For instance, a semi-solid flow cell which used slurries of suspended electrode material was presented by Duduta *et al*.[71] The theoretical energy densities were an order of magnitude higher than values for conventional aqueous RFBs. The electrolytes were suspensions that contained a nanoscale conducting carbon network formed by Ketjen black in an alkyl carbonate/$LiPF_6$ solution with micrometre-scale particles of electrode material distributed throughout the network ($LiCoO_2$ for the cathode and $Li_4Ti_5O_{12}$ for the anode). An active material concentration of up to 12 M was possible for the semi-solid suspensions and a theoretical energy density for suspensions containing $LiCoO_2$ and $Li_4Ti_5O_{12}$ with 40 vol% solid at an average discharge voltage of 2.35 V was 397 Wh L^{-1}. Cell testing was carried out in intermittent flow mode in which a single volume of each semi-solid suspension was pumped into the cell to be discharged and later displaced by a new volume. This marked the first demonstration of a fully operational semi-solid flow cell. While high theoretical energy densities are possible for this concept, the higher viscosity of the electrolytes of semi-solid flow cells is associated with greater parasitic energy losses due to the additional energy that is required to pump the electrolytes.

A non-aqueous TEMPO/Li flow cell was also reported.[72] The catholyte was a solution of TEMPO in an alkyl carbonate mixture with a $LiPF_6$ supporting electrolyte. A 'lithium-graphite hybrid' anode was used, at which lithium-ion intercalation occurred. The anode compartment contained a static TEMPO electrolyte while a flowing TEMPO electrolyte was circulated through the graphite felt cathode. TEMPO was found to exhibit a high solubility of 5.2 M in the alkyl carbonate/$LiPF_6$ mixture and with a 2.0 M TEMPO concentration at a voltage of 3.5 V, the theoretical energy density was 188 Wh L^{-1}. In cell testing, a lower concentration of TEMPO was used (0.1 M), with the system operating at a current density of 10 mA cm^{-2}. Coulombic efficiencies were above 99% over 100 cycles and the average capacity retention was 99.8% per cycle. At higher concentrations of TEMPO (0.8 M, 1.5 M and 2.0 M), the viscosity of the electrolytes increased which necessitated operation at lower current densities (>2.5 mA cm^{-2}) and the coulombic efficiencies reported were above 84%, indicating lower performance when using higher TEMPO concentrations.

There are myriad combinations of half-cell reactions reported for asymmetric RFBs and this review is not exhaustive. It aimed to provide an indication of the direction of research into asymmetric RFBs at present, such as the investigation of RFBs that use redox-active organic molecules (examples being quinone, TEMPO, viologen, aza-aromatic and polymeric active species). A noticeable limitation of organic active species is the possibility of detrimental side reactions that are not observed with metal ions. For instance, addition of hydroxyl groups to quinone species through Michael addition or nucleophilic substitution involving hydroxyl ions or water in aqueous electrolytes was identified as a source of capacity loss in RFBs that used quinones as anolyte species.[73] In another study, it was shown that 4-HO-TEMPO can undergo a disproportionation reaction with protons or be chemically reduced by hydroxide ions, with capacity fade in flow cell testing attributed to the latter side reaction, even in near-neutral conditions.[74] Thus, the existence of side reactions of organic species should be considered during the development of RFB active species. However, the advantageous characteristics of organic active species are clear, and have already been outlined: tailorable properties and structures that are based on low-cost chemical elements. These compounds can also be used in neutral supporting electrolytes such as 1 M NaCl. This is an advantage in terms of promoting the safety profile of RFBs as the VRFB, the leading RFB technology that organic RFBs seek to challenge, uses acidic supporting electrolytes. Further, power densities and theoretical energy densities have been reported in laboratory-scale tests of aqueous organic RFBs that rival those of the VRFB. An additional advantage is seen with the use of organic, polymeric active species as size exclusion membranes can be used instead of more expensive ion exchange membranes. In an analysis of the capital costs of the VRFB, the ion exchange membrane represented one quarter of the total capital cost of the VRFB.[75] Avoiding the use of ion exchange membranes would be beneficial to the capital cost of any new RFB chemistry.

Also outlined in this section were possible routes to RFBs with high energy densities that involve changes to the classical operation of an RFB, such as the use of semi-solid electrolytes and lithium-intercalation electrodes. These asymmetric RFB concepts invoke aspects of lithium-ion battery operation and can increase theoretical energy densities above what is possible for RFBs based solely on solution-phase species, but they also complicate RFB operation. Electrolytes containing dispersed active material have higher viscosities than solutions of solvated species and when an electrode in one half-cell is involved in the charge/discharge reaction, the energy and power of an RFB system is no longer decoupled. This highlights that there are trade-offs to be made if these types of RFB chemistries were to be considered as competitors to state-of-the-art RFBs that were worth furthering beyond laboratory-scale testing.

1.2.2 Symmetric Redox Flow Batteries

Symmetric RFBs are “RFBs consisting of a single parent molecule that can be oxidised and reduced to facilitate the positive and negative electrode half-reactions, respectively”.[76] In the discharged state, the composition of the catholyte and anolyte of a symmetric RFB are the same. As noted, the identity of the anolyte and catholyte species in a discharged VRFB is different (V^{3+} and VO^{2+}) meaning that the VRFB is not truly symmetric by this definition but is still regarded as a symmetric RFB. By using electrolytes based on the same parent species, or the same element in the case of the VRFB, chemical contamination of the electrolytes that is caused by active material crossing the separator between half-cells can be avoided and charge rebalancing after extended cycling is simplified as chemical separations are not required.[76]

The active species of symmetric RFBs must have a possible three or more oxidation states, with a suitable separation in potential between the redox reactions to allow these processes to be used as the cathode and anode reactions in an RFB. As for asymmetric RFBs, several organic species have been tested for symmetric RFBs. In one example, polythiophene was tested as a symmetric RFB active material.[77] Polythiophene is a redox-active polymer that bears a delocalised π-electron system. It was found that polythiophene could gain an electron for each repeating unit when a negative potential was applied and lose an electron for each repeating unit when a positive potential was applied. The separation in potential between these processes was 2.5 V. The distinguishing feature of other redox-active organic species tested for application in symmetric RFBs is the presence of a free radical in the molecule. For instance, Duan *et al*. used a nitronyl nitroxide radical (2-phenyl-4,4,5,6,-tetramethylimidazoline-1-oxyl-3-oxide or PTIO) as the active species under test in their symmetric non-aqueous RFB.[78] PTIO underwent a disproportionation reaction and so could be reduced to an aminoxyl anion at the anode and oxidised to an oxoammonium cation at the cathode upon charge, through gain and loss of one electron which occurred at the same N-O bond reaction site in the molecule. The separation between these redox processes was 1.73 V. Similarly, Hagemann *et al*. prepared molecules containing two of the same nitronyl nitroxide radical moieties for testing in symmetric flow cells by incorporating an ethylene glycol chain as a linker, thereby increasing the number of radical sites per active species molecule to two.[79] Charlton *et al*. instead tested a verdazyl radical, 3-phenyl-1,5-di-*p*-tolylverdazyl, as a symmetric flow cell active species.[80] The verdazyl species exhibited two one-electron redox couples, although the combination of these couples produced a lesser theoretical voltage of 0.98 V when compared to the previous molecules.

Preceding these examples, Potash *et al*. selected a radical-free diaminoanthraquinone compound, 1,4-Bis(isopropylamino)anthraquinone, as a candidate for demonstration of a symmetric RFB.[76] Although the low solubility of this compound was a limitation of its use, it served as a valuable illustration of the electrochemical profile that is required for the active species in a symmetric RFB: the four reversible one-electron reactions that were exhibited in cyclic voltammetry occurred over a potential range of 2.72 V.

The reporting of a symmetric RFB that utilised a porphyrin-based active species further diversified the field.[81] Cyclic voltammetry of the active species, 5,10,15,20-tetraphenylporphyrin (H_2TPP), showed four reversible one-electron redox reactions. For an RFB, one set of two one-electron reactions corresponding to the redox couple $[H_2TPP]^{2-}/H_2TPP$ served as the anode reaction and the second set of two one-electron redox reactions

($[H_2TPP]/[H_2TPP]^{2+}$) was active at the cathode. The potential difference between the most extreme negative and positive redox peaks of H_2TPP was 2.83 V.

Most recently out of all of these examples, a dianion of the croconate dicyanomethylene pseudooxocarbon variety of molecules, croconate violet, was tested as a symmetric RFB species.[82] Croconate violet contained a high proportion of redox-active functional groups and cyclic voltammetry revealed several stable and unstable oxidation states. Using redox reactions in which croconate violet was oxidised to a radical monoanion and reduced to a radical trianion, a symmetric flow cell was possible with a theoretical voltage of 1.82 V. However, capacity loss was observed in flow cell testing which was attributed to a disproportionation of the trianion into the starting species and an unstable species of lower oxidation state, and croconate violet was ultimately deemed unsuitable as a symmetric RFB species.

The separation in redox potentials of the species in some of the examples outlined so far furnished cells with a theoretical voltage in excess of 1.6 V,[76, 78, 79] necessitating the testing of these materials in non-aqueous solvents such as acetonitrile. Conversely, the approach of Winsberg *et al*. was the joining of cathode-active and anode-active units together in a single molecule, where the separation in formal potential of the redox reactions of these units was within the electrochemical window of water.[83] The ‘combi-molecule’ that was studied consisted of one phenazine subunit that was linked to two TEMPO subunits by triethylene glycol linkers. The cathodic reaction involved the TEMPO subunits while the anodic reaction was the two-electron redox reaction of the phenazine unit. The theoretical voltage for a symmetric cell based on this molecule was 1.2 V. A similar approach was taken in the application of another combi-molecule in an aqueous symmetric cell. This molecule contained a TEMPO unit and an *N,N’*-dialkyl-4,4’-bipyridinium (viologen) unit.[84] The combination of TEMPO and viologen in the same molecule gave a theoretical cell voltage of 1.16 V for a symmetric flow cell based on this species.

Symmetric RFBs where the active species contain inorganic components have utilised metal-organic complexes containing transition metals in which the metal ion is stable in multiple oxidation states. These complexes are soluble in non-aqueous solvents. For instance, vanadium(III) acetylacetonate ($V(acac)_3$, Figure 1.4) was proposed as a possible symmetric RFB active species. The $V(acac)_3$ complex exhibited two redox couples: oxidation of V^{III} to V^{IV} and reduction of V^{III} to V^{II}. The combination of these processes offered a theoretical cell voltage of 2.2 V, although charge/discharge testing of the complex was not extensive and limited to a stationary cell only, where the coulombic efficiency was 50%. Similarly, electrolytes containing $Cr^{III}(acac)_3$ and $Mn^{III}(acac)_3$ have also been examined for application in symmetric RFBs in which the central metal atom in both cases could be reduced to an oxidation state of +2 and oxidised to +4. This corresponded to theoretical cell voltages of 3.4 V in the case of the chromium complex and 1.1 V for the manganese complex.[85, 86] Coulombic efficiencies in stationary cell tests using $Cr^{III}(acac)_3$ were below 60% and an unknown side reaction reportedly occurred in the case of $Mn^{III}(acac)_3$. With a comparable approach but a different metal ion and ligands, Zhang *et al*. investigated a bis(acetylacetone)ethylenediamine cobalt(II) complex, [Co(acacen)], in which the cobalt atom could be reduced to cobalt(III) and oxidised to cobalt(I) leading to a theoretical cell potential of 2.0 V for this system, which was tested in a stationary cell.[87]

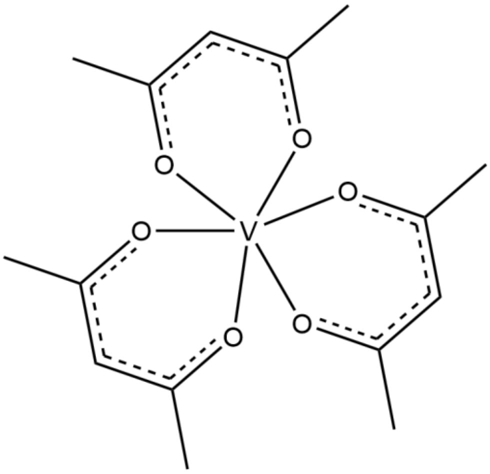

Figure 1.4 - An example of metal-organic complex that has been investigated as a symmetric RFB active species, vanadium(III) acetylacetonate.

In their investigation of 'redox non-innocent' ligands as components of RFB active species, Capillino *et al*. studied vanadium complexes of the maleonitriledithiolate (mnt) ligand. The tris(mnt)vanadium(IV) complex $[V(mnt)_3]^{2-}$ (Figure 1.5) was the species placed under test.[88] $[V(mnt)_3]^{2-}$ underwent two one-electron reductions of the vanadium center to generate $[V(mnt)_2]^{4-}$ and a one-electron oxidation of the ligands to yield $[V(mnt)_3]^{-}$, thereby making it a possible symmetric RFB active species. The separation in redox potential between the ligand-centred oxidation and the second one-electron metal-centred reduction was 2.3 V. In charge/discharge testing in a stationary cell, the coulombic efficiency was ~90% and a decrease in capacity of ~20% was observed over 16 cycles. Hogue *et al*. extended the study of mnt complexes as non-aqueous symmetric RFB active species by also analysing the electrochemistry and charge/discharge performance of several bis-mnt complexes: $[(TEA)Fe_{mnt}]$, $[(TEA)_2Co_{mnt}]$, $[(TEA)_2Ni_{mnt}]$ and $[(TEA)_2Cu_{mnt}]$.[89] The Fe, Co, Ni and Cu mnt complexes would potentially have led to symmetric RFBs with a theoretical voltage in the range of 1.12–1.92 V, due to the occurrence of both metal-centred and ligand-centred redox reactions, but it was ultimately found that not all oxidation states of the complexes were stable which caused poor capacity retention in flow cell testing. Some of these species could, however, be suitable for study in asymmetric RFBs.

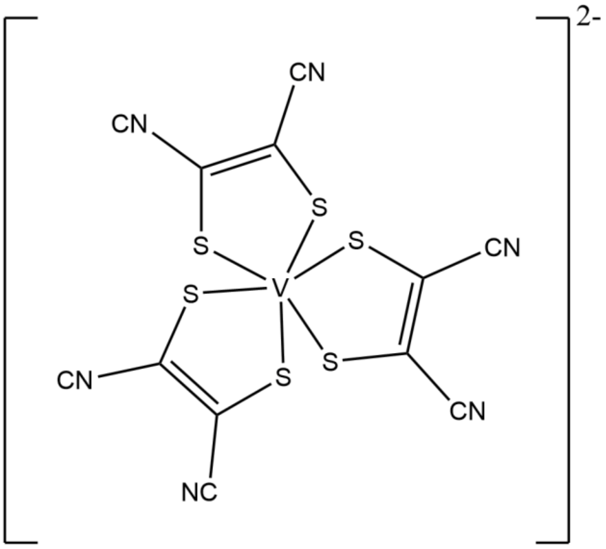

Figure 1.5 - A tris-maleonitriledithiolate vanadium(IV) complex, tested as a symmetric RFB active species, with redox non-innocent ligands.

Cabrera *et al*. also investigated a coordination complex with non-innocent ligands, in this instance a complex of chromium and ester-substituted bipyridine ligands.[90] Cyclic voltammetry showed that this complex exhibited six one-electron redox couples with a separation between the first and sixth peak of ~1.8 V. There was potential to access three redox reactions of this complex at the anode and three redox reactions at the cathode in an RFB, which could lead to a multi-electron symmetric RFB, although only two electrons were accessed in practice when the species was subjected to charge/discharge testing in a stationary cell. It was also shown that a range of cobalt(II) complexes with azole-pyridine ligands exhibited ‘ligand-centric’ reduction in addition to cobalt redox processes.[91] Separation between the Co^{II}/Co^{III} redox process and the oxidation/reduction process of the ligands was as high as 2.17 V. The tunability of the redox properties of the complexes was also highlighted: for instance, the replacement of up to two pyridine sites in the ligands with 3,5-dimethylpyrazole units correlated with a positive shift of the Co^{II}/Co^{III} redox couple and thus an increase in the theoretical voltage for an RFB that used this reaction.

Thus, it is illustrated that there has been investigation of several species which display the multiple oxidation states that are required for the active species of a symmetric RFB. The application of several organic redox-active molecules has been presented, some being aromatic molecules and others being molecules that can exist as stable radical species. Further, a range of metal-organic complexes have been described, all with the property that the central metal ion can switch between different oxidation numbers, and some with the involvement of redox reactions of the ligands which can provide further oxidation states.

Considering these examples, the ideal symmetric RFB chemistry remains to be seen and there are factors that warrant consideration for both organic and metal-organic species if any were to be taken beyond the proof-of-concept stage that was presented. For instance, some of the metal-organic species did not exhibit stability in all redox states[89] or instability of the active species was postulated as a reason for poor charge/discharge performance[90] or low coulombic efficiencies were obtained.[85, 92] Thus, while these species exhibited an electrochemical profile in cyclic voltammetry that could suit the operation of a symmetric RFB, obtaining charge/discharge results without questions arising over stability did not always follow. Further, each metal-organic complex referred to was soluble in non-aqueous solvent and non-aqueous RFBs are, in general, trailing state-of-the-art aqueous RFBs in terms of properties and development. As noted in the previous section on asymmetric RFBs, the ionic conductivity is lower for organic electrolytes which is a factor contributing to high internal resistance and poor voltage efficiency.[70] Further, membranes for use with organic solvents are not yet available which adds a further challenge to the use of non-aqueous electrolytes.[89] The ionic conductivity of commercial ion exchange membranes is reduced in non-aqueous solutions compared to in aqueous solutions, which contributes to heightened internal resistance.[70]

In a comprehensive review of RFBs based on redox active organic active species, both symmetric and asymmetric, it was noted that the chemical stability of free radical species is a major challenge for long-term cycling and storage stability.[93] One study provided insight into the sources of performance loss observed in non-aqueous flow cells that utilise organic radical active species.[94] It was found that solvent and choice of supporting electrolyte affected the lifetime of the radicals under investigation (2,5-di-*tert*-butyl-1-methoxy-4-[2'-methoxyethoxy]benzene and 9-fluorenone). In particular, 9-fluorenone was less stable in acetonitrile compared to 1,2-dimethoxyethane, which was perhaps attributable to side reactions with the acetonitrile molecule. The $[BF_4]^-$ anion, present as part of the supporting electrolyte, caused fast quenching of both radicals suggesting this anion had a high reactivity with each species, while cation choice (use of the tetraethylammonium cation instead of Li^+) was thought to inhibit the formation of dimers from 9-fluorenone.

While deleterious effects of side reactions of TEMPO and TEMPO derivatives have not been reported in previous RFB studies,[57-59] other organic radical active species (indeed, amongst the symmetric RFB examples previously discussed) have exhibited possible issues with stability. Flow cells based on the aforementioned PTIO active species exhibited capacity loss during cycling, speculatively associated with chemical instability of charged species,[78] and a capacity fade of around 50% was observed after 11 charge/discharge cycles for the diradical nitronyl nitroxide species which was thought to be attributable to side reactions or decomposition of the active species through radicals reacting together.[79] The verdazyl radical species studied showed capacity fade, with 98% of the theoretical capacity accessed in a stationary cell in early cycles but ~30% accessed by cycle 50, which was attributed to decomposition of the active species on the anode side.[80] Thus, as for asymmetric RFBs, the use of organic radical species in symmetric RFBs requires that consideration be given to the inherent reactivity of these molecules.

1.3 Polyoxometalate Redox Flow Batteries

Polyoxometalates (POMs) are anionic metal-oxygen clusters containing early transition metals, commonly vanadium, molybdenum and tungsten. POMs can undergo multiple reversible redox reactions. This electrochemistry is one of the properties of POMs that spurs the investigation of these species in areas such as catalysis and biomedicine,[95, 96] as well as in energy storage. For instance, in the area of energy storage, POMs have been investigated as charge carriers in hybrid fuel cells powered with biomass,[97] as a constituent of electrodes in supercapacitors[98] and as the anode material in a sodium-ion battery.[99] As RFB active species, POMs straddle the divide between organic and inorganic compounds. Being composed of transition metals, POMs are inorganic species, but the identity of the metal in the structure can be changed and POMs can be functionalised with organic units meaning that, as for organic species, there are an indefinite number of POM structures and it is possible to modify properties by making structural alterations.

POMs that contain more than one redox-active metal have been identified as candidates for the active species of symmetric RFBs. Pratt *et al*. were the first in the field to publish charge/discharge results for the operation of a POM RFB, with the data obtained from their symmetric aqueous flow cell based on $[SiV_3W_9O_{40}]^{7-}$.[100] The vanadium in this POM cycled between V^{IV} and V^{V} at the cathode and the tungsten cycled between W^{VI} and W^{V} at the anode, with a coulombic efficiency of >95% observed over 100 cycles. Two plateaus were shown in the charge/discharge plot with representative voltaic efficiencies of 99% and 30%. 90% of the theoretical capacity was accessed initially. The capacity loss after 100 cycles was 10% but the authors report no evidence of decomposition of $[SiV_3W_9O_{40}]^{7-}$ in UV-visible, infrared or NMR spectra of the solutions after their removal from the cell following cycling. $[SiV_3W_9O_{40}]^{7-}$ was also tested in non-aqueous electrolyte (propylene carbonate) by using the tetra-*n*-butyl ammonium salt of $[SiV_3W_9O_{40}]^{7-}$ (soluble in organic solvent) which was prepared by carrying out cation exchange of the potassium salt of $[SiV_3W_9O_{40}]^{7-}$. This shows that POMs can be studied for application in both aqueous and non-aqueous RFBs. However, performance was poorer for the non-aqueous flow cell, with a lower coulombic efficiency (≤85%) and a capacity loss of 50% after 10 cycles.

Liu *et al*. used $[CoW_{12}O_{40}]^{6-}$ in a symmetric RFB that coupled the Co^{II}/Co^{III} reaction of the central cobalt atom at the cathode with the W^{VI}/W^{V} reactions of the tungsten atoms at the anode.[101] The coulombic efficiency was 99% over 100 cycles and the POM concentration in the electrolytes was 0.8 M in water (compared to 0.02 M for the symmetric POM flow cell reported by Pratt *et al*.), with 78.5% of the theoretical capacity accessed. The voltaic efficiency for this concentration was around 84%. Energy efficiencies were 85.4%, 73.8% and 54.9% at a current density of 25, 50 and 100 mA cm^{-2}, respectively. The energy density was 15.4 Wh L^{-1}. However, the number of electrons involved in the positive and negative half-cell reactions were not balanced, meaning that the RFB required asymmetric electrolyte volumes. A single electron is transferred per cobalt atom at the cathode whereas two tungsten redox reactions can occur at the anode, each involving two electrons. The volume of catholyte was four times greater than the volume of anolyte to allow the tungsten to be oxidised and reduced by four electrons.

These two POM RFB concepts were similar in that they used POMs with more than one redox-active metal in the structure, with the result that both POM flow cells cycled between the oxidation states of a different metal at the anode and cathode. The theoretical voltages for the symmetric RFBs based on $[SiV_3W_9O_{40}]^{7-}$ and $[CoW_{12}O_{40}]^{6-}$ were 0.8 V and 1.2–1.4 V, respectively. Other examples of symmetric POM RFBs switched between different oxidation states of the same metal at the anode and cathode. Chen and Barteau used electrolytes of $[PMo_{12}O_{40}]^{3-}$ to create an RFB based on the redox reactions of molybdenum only, which can be reduced from molybdenum(VI) to molybdenum(V). The RFB cycled between $[PMo_{12}O_{40}]^{4-}$ and $[PMo_{12}O_{40}]^{3-}$ at the cathode and $[PMo_{12}O_{40}]^{4-}$ and $[PMo_{12}O_{40}]^{5-}$ at the anode.[102] This combination of half-cell reactions had a relatively low theoretical voltage of 0.36 V and only one electron was transferred between half-cells compared to three electrons and four electrons in the previous examples. The solvent used for the system was acetonitrile, again highlighting the possibility of using POMs in both aqueous and non-aqueous RFBs.

The preceding three symmetric POM RFB examples all used POMs that have the Keggin structure, which is the archetypal POM structure with a general formula of $[XM_{12}O_{40}]^{n-}$. VanGelder *et al*. investigated another type of POM structure, the Lindqvist structure.[103] The general formula of the Lindqvist polyoxovanadate-alkoxide species that were investigated was $[V_6O_7(OR)_{12}]$, where R = CH_3 or C_2H_5. The POMs were soluble in acetonitrile (solubility of 0.1 M–0.2 M) and exhibited four one-electron redox reactions. The use of the most positive and negative of these four redox reactions in an RFB corresponded to a theoretical voltage of ~1.7 V. $[V_6O_7(OC_2H_5)_{12}]$ was found to be the most stable species in charge/discharge testing. Two electrons were cycled at the anode and cathode and coulombic efficiencies were around 97%. In later work, the polyoxovanadate-alkoxide species were shown to be modifiable: substitution of a vanadium atom in the POM framework with titanium could increase the theoretical voltage of the system by 0.5 V,[104] and the incorporation of alternative organic ligands in the structures could increase solubility up to 0.934 M in acetonitrile,[105, 106] although reversible electrochemistry was not always retained after this modification.

Asymmetric RFBs in which either one or both electrolytes contain a POM as the active species have also been investigated. Friedl *et al*. reported an asymmetric RFB that used $[PV_{14}O_{42}]^{9-}$ in the catholyte and $[SiW_{12}O_{40}]^{4-}$ in the anolyte.[107] $[PV_{14}O_{42}]^{9-}$ was reducible by up to seven electrons, but only four electrons were used in practice to create an RFB that transferred four electrons between half-cells during charge and discharge. Coulombic efficiencies were around 94%, and up to 96% of the theoretical capacity was accessed. Over 150 cycles, the capacity decayed by 0.16% per cycle which was attributed to atmospheric oxygen entering the electrolytes. The peak power density, after correction for the potential drop of the cell, was 100 mW cm^{-2} at a current density of 160 mA cm^{-2}. At this current density, the ohmic resistance of the cell caused 73% of the potential drop. When the ohmic resistance was corrected for, the calculated peak power density was 150 mW cm^{-2}. In a crossover study, it was found that $[SiW_{12}O_{40}]^{4-}$ did not cross commercial cation exchange membranes, which was explained by the large size of $[SiW_{12}O_{40}]^{4-}$ compared to simple metal ions as well as electrostatic repulsion due to the high negative charge of this species. The size of $[SiW_{12}O_{40}]^{4-}$ was reported to be 2 nm with the hydration shell included (calculated from the Stokes-Einstein equation).[107] For comparison, the monovalent, bivalent, and trivalent metal ions Na^+, Mg^{2+} and Al^{3+} have hydrated radii of 0.36 nm, 0.43 nm and 0.48 nm, respectively.[108] For further comparison, common ions in a supporting electrolyte such as H_3O^+, Li^+ and Cl^- that will cross ion exchange membranes for charge balance in RFBs have hydrated radii of 0.28 nm, 0.38 nm and 0.33 nm respectively.[108] However, it should be noted that it has been reported that $[SiW_{12}O_{40}]^{4-}$ has minimal solvation due to the calculation of a hydrodynamic radius that is similar to its crystallographic radius in other work.[109, 110]

The same asymmetric POM RFB system underwent 1400 cycles in a scaled-up cell.[111] The size of the cell was increased from a cell with a membrane surface area of 25 cm^2 in the original work to a cell with a membrane surface area of 1400 cm^2. A higher coulombic efficiency of ~99% was observed in the scaled-up testing, with an average capacity loss of 0.011% per cycle. The energy efficiency at a current density of 4 mA cm^{-2} was around 86%, dropping to 40% when the cell was operated at 43 mA cm^{-2} for a proportion of the 1400 cycles. Post-cycling analysis of the electrolytes (using NMR spectroscopy and cyclic voltammetry) indicated that neither POM had decomposed after 1400 cycles. An EIS study revealed that the resistance that could be related to diffusion, referred to as R_{diff}, was the largest contributor to the total resistance for each of the flow rates used in the study (R_{CT} and R_{ohm} were independent of flow rate). The energy efficiency of the cell with a membrane surface area of 1400 cm^2 was greater (86%) than for a laboratory cell with a membrane surface area of 25 cm^2 (64%) that was cycled with the same POM electrolytes at the same concentration. This was attributed to the different cell design. R_{ohm} was similar for both cells but R_{diff} was smaller for the scaled-up cell which was thought to be attributable to improved distribution of the electrolyte in the graphite felt electrodes of the larger cell. This EIS study illustrates that voltaic efficiency can be related to the design of an RFB cell.

Chen *et al*. demonstrated an asymmetric RFB in which only one of the electrolytes contained a POM.[112] The anolyte contained $[P_2W_{18}O_{62}]^{6-}$, a Wells-Dawson structure, and was combined with the Br_2/HBr redox couple in the catholyte. It was found that increasing the POM concentration (from 2 mM to 100 mM) and lowering the pH (changing the supporting electrolyte from 1 M Li_2SO_4 at pH 7 to 1 M H_2SO_4) facilitated the reduction of the POM by 18 electrons. In a bulk electrolysis study that used a 100 mM $[P_2W_{18}O_{62}]^{2-}$ solution, 96% of the charge supplied during an 18-electron reduction could be recovered during reoxidation. In a flow cell test that used a 0.5 M $[P_2W_{18}O_{62}]^{6-}$ anolyte, the coulombic efficiency was 98% over 20 cycles and the energy density, based on the discharge capacity, was 225 Wh L^{-1}. The energy efficiency was 76%.

A further asymmetric RFB with a POM-based anolyte was reported by Feng *et al.* which used $[PW_{12}O_{40}]^{3-}$ and the I_3^-/I^- redox couple.[113] $[PW_{12}O_{40}]^{3-}$ could undergo three reversible redox reactions in which a total of four electrons were transferred, whereas the I_3^-/I^- redox couple is a two-electron reaction. Different concentrations of active species were used to counter this (a 1:6 mole ratio which corresponded to an anolyte concentration of 0.4 M and a catholyte concentration of 2.5 M). However, the differing ion concentrations were thought to cause an imbalanced osmotic pressure and changes in the volume of the electrolytes during flow cell testing. The iodide ion was also found to permeate the Nafion membrane that was used as a separator. Using mixed electrolytes to counter these issues (a catholyte of 0.25 M $[PW_{12}O_{40}]^{3-}$/1.6 M hydrogen iodide and an anolyte of 0.25 M $[PW_{12}O_{40}]^{3-}$/1.1 M hydrogen iodide), a flow cell ran for 700 cycles during which coulombic efficiencies were 99.6% and the capacity retention was 99.99% per hour. A charge cut-off voltage of 0.92 V was used to inhibit the hydrogen evolution reaction, which had been a source of low coulombic efficiency in earlier flow cell tests, and this allowed $[PW_{12}O_{40}]^{3-}$ to undergo a redox reaction that involved two electrons. The operating current density was 100 mA cm^{-2} and the peak power density was 224.7 mW cm^{-2}. The energy efficiency was around 80%.

In the most recent work out of all these examples, $[PMo_{12}O_{40}]^{3-}$ (the subject of work discussed earlier[102]) was further studied as an RFB active species.[114] Switching solvent from acetonitrile to dimethylformamide allowed the access of a further two-electron redox reaction, in addition to the two one-electron redox reactions used in previous charge/discharge tests. The cell voltage was 0.7 V for a symmetric cell using 10 mM solutions in dimethylformamide, which cycled between $[PMo_{12}O_{40}]^{5-}$ and $[PMo_{12}O_{40}]^{3-}$ at the cathode and $[PMo_{12}O_{40}]^{5-}$ and $[PMo_{12}O_{40}]^{7-}$ at the anode, compared to 0.35 V for a cell that used the POM in acetonitrile (in which only a one-electron transfer was possible). A $[PMo_{12}O_{40}]^{3-}$ concentration of 0.1 M in dimethylformamide was also tested, the highest concentration used in a non-aqueous POM flow cell to date, along with an asymmetric flow cell that used $[PMo_{12}O_{40}]^{3-}$ as the catholyte species and $[P_2W_{18}O_{62}]^{6-}$ in the anolyte. Four-electron transfers of both POMs were utilised in the asymmetric cell, and the cell voltage was increased to 1.3 V.

These POM RFB concepts highlight some of the properties of POMs that make them attractive candidates as RFB active species. POMs are soluble in aqueous and non-aqueous solvents, meaning that the investigation of POMs for RFBs can extend across aqueous and non-aqueous solutions.[100, 102, 103] Solubility can be altered by switching the counterion (e.g. substituting a potassium counterion for the tetra-*n*-butyl ammonium ion[100]) or tuned through structural modification of a POM, as in the example of the polyoxovanadate-alkoxide species that were functionalised with organic units.[105, 106] The structural versatility and tunability of POMs is an asset in the search for new RFB active species, as there is the potential to alter properties and substitute species that are found to have undesirable properties for alternatives.

The electrochemical properties of POMs, specifically the multi-electron redox reactions, have led to the design of RFBs which transfer more than one electron between half-cells; up to four electrons have been reported in flow cell tests[101, 107] and it was later shown that the choice of electrolyte could facilitate the reduction of $[P_2W_{18}O_{62}]^{6-}$ by up to 18 electrons.[112] In a 2016 article about the direction of RFB research and development, it was highlighted that “the most attractive future RFB chemistries are likely to be ones that offer multi-electron redox reactions per active-species molecule, since this can enable high energy densities at modest concentrations.”[115] If an active species can undergo multi-electron redox reactions, more electrons can be stored per volume of electrolyte. This could increase the volumetric energy density relative to a system that uses one-electron redox reactions. As

POMs exhibit multi-electron redox reactions, energy density is one parameter that POM RFB development can target for improvement, providing that the concentration of POM electrolytes can be made comparable to the concentrations that mature RFBs currently use (e.g. ~1.5 M for the VRFB which has an energy density of ~25 Wh L^{-1}). However, voltaic efficiency is an RFB parameter that may be negatively impacted by utilising the sequential multi-electron transfers that species such as POMs undergo. Plateaus of unequal length in voltage-time plots during charge and discharge for multi-electron systems can mean that a higher voltage is maintained for longer during charging whilst a lower voltage is maintained for longer during discharging.[116] This increases the average charging voltage and decreases the average discharging voltage which lowers the voltaic efficiency and, thus, the energy efficiency. Causes of unequal plateau durations can be the continued reaction of active species from the initial stage of a sequential electron transfer (that were not entirely consumed during the first plateau) when the voltage of the plateau corresponding to the next electron transfer in the sequence has been reached.[116] This extends the duration of charge or discharge at the voltage of this later plateau.

Differing mass transfer rates for species in different oxidation states could also cause asymmetric charge and discharge curves, which have charging plateaus of differing length to the corresponding discharging plateau, by affecting the relative fluxes of different species to the electrode surface.[116] For instance, the rate of reactant delivery to the electrode surface is influenced by the diffusion coefficient of the active species, among other factors that affect the rate of mass transport such as concentration[117] (mass transport is discussed in a later section) and species in different oxidation states can have differing diffusion coefficients.[118] Thus, when using multi-electron species, an increase in energy density may not result if the transfer of extra electrons is offset by a poorer voltaic efficiency due to asymmetric charge/discharge curves. This should be kept in mind when investigating POMs for RFBs.

Reported energy efficiencies for the aqueous POM RFBs previously discussed were 64%–86%. Coulombic efficiencies were >94%, indicating that the energy efficiency of these POM systems was lowered by the voltaic efficiency of the cells (as energy efficiency = coulombic efficiency × voltaic efficiency). As noted in Section 1.2, the voltaic efficiency is lowered by several resistances in a cell which add up to the total resistance, R_{total} (Equation 1.3).

$$R_{total} = R_{ohm} + R_{CT} + R_{mass} \qquad 1.3$$

R_{ohm} includes the electronic resistance between the various cell components (such as between current collector and electrode) and the resistance of the membrane, R_{CT} is the charge transfer resistance (which is inversely proportional to the electron transfer constant, k^0) and R_{mass} is the mass transport resistance.

Friedl *et al*. determined values for the various resistances in two POM flow cells and showed that the biggest contributor to the total resistance of the cells was the ohmic resistance and the component of the resistance that could be related to diffusion, rather than R_{CT} which is the only parameter of the three that is related to the active species used.[111] The resistance pertaining to mass transport was largest in their flow cell experiments and relates to the availability of active material in the electrodes, being influenced by factors such as concentration, flow rate and how effectively electrolyte is distributed in the electrodes. As will be discussed in Chapter 4, the electron transfer kinetics of POMs are facile. The contribution of R_{CT} to R_{total} can be expected to be small when the electron transfer kinetics of the active species are fast.[111] Thus, the voltaic efficiencies of POM RFBs that are quoted could be influenced more by the cell design or operational choices (e.g. the membrane used or the flow rate), rather than the POM active species.

Further, peak power densities reported for aqueous POM RFBs in laboratory-scale testing are comparable to typical power density values of the VRFB.[107, 113] This suggests that, at the very least, the use of POMs will not limit the power density of RFBs to below the values of state-of-the-art RFBs. Further, as will be discussed in later chapters, POMs could even be a route to improving the power density of RFBs, if the electron transfer kinetics are facile.

1.4 Concluding Remarks

To summarise, the advantageous aspects of studying POMs as RFB active species includes the array of different structures, with the potential for modification of properties, and the multi-electron redox reactions. POMs could also match or improve the power density of current RFBs. POMs can be made soluble in both water and organic solvents and, as the performance of non-aqueous RFBs does not yet match the performance of aqueous RFBs, this allows a focus on the use of aqueous electrolytes, thereby utilising the desirable properties of water such as non-flammability and higher ionic conductivity.

The aim of the work described in this thesis was to investigate a symmetric aqueous POM RFB. A common cycle of investigating an RFB active species involves the identification of a candidate, synthesis of this material, characterisation, preliminary investigation of electrochemical properties, in-depth study of electrochemical reactions through bulk electrolysis experiments, and testing in a laboratory-scale RFB. This cycle of investigation describes the general activity that took place during this work. A study of the kinetics of electron transfer in a POM redox reaction and the testing of a POM as an anolyte species in an asymmetric POM RFB were carried out in addition to the symmetric POM RFB work.

This chapter has introduced RFBs, giving an indication of the current status of research into both asymmetric and symmetric RFBs, as well as providing a section distinct from this to highlight POM RFBs. Chapter 2 provides background information and theory about POMs, from their origin to their electrochemical properties, as well as sections dedicated to general electrochemical techniques and characterisation techniques suitable for POMs. Chapter 3 summarises a study of a symmetric POM RFB, highlighting properties of the mixed-metal POM species $[SiV_3W_9O_{40}]^{7-}$ that warrant consideration for its application as an RFB active species. Chapter 4 describes a study of the electron transfer kinetics of $[SiW_{12}O_{40}]^{4-}$. Chapter 5 is an investigation into the application of $[CoW_{12}O_{40}]^{6-}$ in an asymmetric POM RFB. Chapter 6 concludes this thesis with a summary of results and the possible direction of future work, a summation of the status of POMs for RFBs generally and a discussion of the limitations of POM RFBs.

1.5 References

1. M. R. Allen, O. P. Dube, W. Solecki, F. Aragón-Durand, W. Cramer, S. Humphreys, M. Kainuma, J. Kala, N. Mahowald, Y. Mulugetta, R. Perez, M. Wairiu and K. Zickfeld, in *Global Warming of 1.5°C. An IPCC Special Report on the impacts of global warming of 1.5°C above pre-industrial levels and related global greenhouse gas emission pathways, in the context of strengthening the global response to the threat of climate change, sustainable development, and efforts to eradicate poverty*, Intergovernmental Panel on Climate Change, 2018, pp. 47-92.
2. *WMO Provisional Statement of the State of the Climate*, World Meteorological Organization, 2019.
3. What is the Paris Agreement?, https://unfccc.int/process-and-meetings/the-paris-agreement/what-is-the-paris-agreement, (accessed 20 January, 2020).
4. J. Rogelj, D. Shindell, K. Jiang, S. Fifita, P. Forster, V. Ginzburg, C. Handa, H. Kheshgi, S. Kobayashi, E. Kriegler, L. Mundaca, R. Séférian and M. V. Vilariño, in *Global Warming of 1.5°C. An IPCC Special Report on the impacts of global warming of 1.5°C above pre-industrial levels and related global greenhouse gas emission pathways, in the context of strengthening the global response to the threat of climate change, sustainable development, and efforts to eradicate poverty*, Intergovernmental Panel on Climate Change, 2018, pp. 93-174.
5. O. Hoegh-Guldberg, D. Jacob, M. Taylor, M. Bindi, S. Brown, I. Camilloni, A. Diedhiou, R. Djalante, K. L. Ebi, F. Engelbrecht, J. Guiot, Y. Hijioka, S. Mehrotra, A. Payne, S. I. Seneviratne, A. Thomas, R. Warren and G. Zhou, in *Global Warming of 1.5°C. An IPCC Special Report on the impacts of global warming of 1.5°C above pre-industrial levels and related global greenhouse gas emission pathways, in the context of strengthening the global response to the threat of climate change, sustainable development, and efforts to eradicate poverty*, Intergovernmental Panel on Climate Change, 2018, pp. 175-312.
6. H. d. Coninck, A. Revi, M. Babiker, P. Bertoldi, M. Buckeridge, A. Cartwright, W. Dong, J. Ford, S. Fuss, J.-C. Hourcade, D. Ley, R. Mechler, P. Newman, A. Revokatova, S. Schultz, L. Steg and T. Sugiyama, in *Global Warming of 1.5°C. An IPCC Special Report on the impacts of global warming of 1.5°C above pre-industrial levels and related global greenhouse gas emission pathways, in the context of strengthening the global response to the threat of climate change, sustainable development, and efforts to eradicate poverty*, Intergovernmental Panel on Climate Change, 2018, pp. 313-444.

7. *2017 UK Greenhouse Gas Emissions, Final Figures*, Department for Business, Energy & Industrial Strategy, London, 2019.
8. *UK Renewable electricity capacity and generation, July to September 2019*, Department for Business, Energy & Industrial Strategy, London, 2019.
9. *New Energy Outlook 2019 - Executive Summary*, Bloomberg New Energy Finance, 2019.
10. *European Energy Storage Technology Development Roadmap Towards 2030*, European Association for Storage of Energy/European Energy Research Alliance, 2013.
11. *European Energy Storage Technology Development Roadmap - 2017 Update*, European Association for Storage of Energy/European Energy Research Alliance, 2017.
12. Energy Storage Investments Boom as Battery Costs Halve in the Next Decade, https://about.bnef.com/blog/energy-storage-investments-boom-battery-costs-halve-next-decade/, (accessed 22 January, 2020).
13. A. Z. Weber, M. M. Mench, J. P. Meyers, P. N. Ross, J. T. Gostick and Q. H. Liu, *Journal of Applied Electrochemistry*, 2011, **41**, 1137-1164.
14. M. L. Perry, R. M. Darling and R. Zaffou, *ECS Transactions*, 2013, **53**, 7-16.
15. *Vanadium Redox Flow Batteries: An In-Depth Analysis*, Electric Power Research Institute, Palo Alto, 2007.
16. A. A. Akhil, G. Huff, A. B. Currier, B. C. Kaun, D. M. Rastler, S. B. Chen, A. L. Cotter, D. T. Bradshaw and W. D. Gauntlett, *DOE/EPRI 2013 Electricity Storage Handbook in Collaboration with NRECA*, Sandia National Laboratories, Albuquerque, 2013.
17. Y. A. Gandomi, D. S. Aaron, J. R. Houser, M. C. Daugherty, J. T. Clement, A. M. Pezeshki, T. Y. Ertugrul, D. P. Moseley and M. M. Mench, *J Electrochem Soc*, 2018, **165**, A970-A1010.
18. J. Luo, B. Hu, M. Hu, Y. Zhao and T. L. Liu, *ACS Energy Letters*, 2019, **4**, 2220-2240.
19. M. Skyllas-Kazacos, G. Kazacos, G. Poon and H. Verseema, *Int. J. Energy Res.*, 2010, **34**, 182-189.
20. S. F. Tie and C. W. Tan, *Renewable and Sustainable Energy Reviews*, 2013, **20**, 82-102.
21. M. Skyllas-Kazacos, M. H. Chakrabarti, S. A. Hajimolana, F. S. Mjalli and M. Saleem, *J Electrochem Soc*, 2011, **158**, R55-R79.

22. *United States of America Pat.*, 3 996 064, 1976.
23. L. H. Thaller, *Electrically Rechargeable Redox Flow Cells*, National Aeronautics and Space Administration, 1974.
24. J. Noack, N. Roznyatovskaya, C. Menictas and M. Skyllas-Kazacos, *Journal*, 2019, **21**.
25. N. H. Hagedorn, *NASA Redox Storage System Development Project - Final Report*, U.S Department of Energy - Conservation and Renewable Energy Division of Energy Storage Systems, Cleveland, 1984.
26. P. Kelly-Detwiler, EnerVault Unveils First of Its Kind Iron-Chromium Megawatt-Scale Flow Battery, https://www.forbes.com/sites/peterdetwiler/2014/05/30/enervault-unveils-first-of-its-kind-iron-chromium-megawatt-scale-flow-battery/#253caddd1030, (accessed 23 January, 2020).
27. E. Wesoff, Flow Battery Startup EnerVault Files for Assignment Before Creditors, https://www.greentechmedia.com/articles/read/flow-battery-startup-enervault-files-for-assignment-before-creditors, (accessed 28 January, 2020).
28. M. Skyllas-Kazacos, M. Rychcik, R. G. Robins, A. G. Fane and M. A. Green, *J Electrochem Soc*, 1986, **133**, 1057-1058.
29. redT energy storage, https://www.redtenergy.com/, (accessed 23 January, 2020).
30. Rongke Power, http://www.rongkepower.com/?lang=en, (accessed 23 January, 2020).
31. Department of Energy Global Energy Storage Database, https://energystorageexchange.org/, (accessed 24 January, 2020).
32. N. Roznyatovskaya, T. Herr, M. Küttinger, M. Fühl, J. Noack, K. Pinkwart and J. Tübke, *J Power Sources*, 2016, **302**, 79-83.
33. *Vanadium - Mineral Commodity Summary 2019*, U.S. Geological Survey, 2019.
34. *United States of America Pat.*, 4 485 154, 1984.
35. F. C. Walsh, *Pure and Applied Chemistry*, 2001, **73**, 1819.
36. *Review of Electrical Energy Storage Technologies and Systems and of their Potential for the UK*, Department of Trade and Industry/Future Energy Solutions, United Kingdom, 2004.
37. C. Ponce de León, A. Frías-Ferrer, J. González-García, D. A. Szánto and F. C. Walsh, *J Power Sources*, 2006, **160**, 716-732.
38. *United States of America Pat.*, 312 802, 1885.
39. R. A. Putt, *Development of zinc bromide batteries for stationary energy storage. Final report, November 1979-December 1981*, EPRI-EM-2497, Gould, Inc., United States, 1982.

40. R. Bellows, H. Einstein, P. Grimes, E. Kantner, P. Malachesky, K. Newby, H. Tsien and A. Young, *Development of a circulating zinc-bromine battery, Phase II. Final report,* SAND-83-7108, Exxon Research and Engineering Co., United States, 1983.
41. Redflow - Advanced Energy Storage, https://redflow.com/, (accessed 24 January, 2020).
42. Primus Power, http://www.primuspower.com/en/, (accessed 28 January, 2020).
43. J. Noack, N. Roznyatovskaya, T. Herr and P. Fischer, *Angewandte Chemie International Edition*, 2015, **54**, 9776-9809.
44. *United States of America Pat.,* 7 625 663, 2009.
45. B. Li, Z. Nie, M. Vijayakumar, G. Li, J. Liu, V. Sprenkle and W. Wang, *Nature Communications*, 2015, **6**, 6303.
46. Y. Xu, Y. Wen, J. Cheng, G. Cao and Y. Yang, *Electrochemistry Communications*, 2009, **11**, 1422-1424.
47. Y. Xu, Y.-H. Wen, J. Cheng, G.-P. Cao and Y.-S. Yang, *Electrochim Acta*, 2010, **55**, 715-720.
48. B. Huskinson, M. P. Marshak, C. Suh, S. Er, M. R. Gerhardt, C. J. Galvin, X. Chen, A. Aspuru-Guzik, R. G. Gordon and M. J. Aziz, *Nature*, 2014, **505**, 195-198.
49. B. Huskinson, M. P. Marshak, M. R. Gerhardt and M. J. Aziz, *ECS Transactions*, 2014, **61**, 27-30.
50. K. Lin, Q. Chen, M. R. Gerhardt, L. Tong, S. B. Kim, L. Eisenach, A. W. Valle, D. Hardee, R. G. Gordon, M. J. Aziz and M. P. Marshak, *Science*, 2015, **349**, 1529-1532.
51. D. G. Kwabi, K. Lin, Y. Ji, E. F. Kerr, M.-A. Goulet, D. De Porcellinis, D. P. Tabor, D. A. Pollack, A. Aspuru-Guzik, R. G. Gordon and M. J. Aziz, *Joule*, 2018, **2**, 1894-1906.
52. Z. Yang, L. Tong, D. P. Tabor, E. S. Beh, M.-A. Goulet, D. De Porcellinis, A. Aspuru-Guzik, R. G. Gordon and M. J. Aziz, *Advanced Energy Materials*, 2018, **8**, 1702056.
53. Z. Li, S. Li, S. Liu, K. Huang, D. Fang, F. Wang and S. Peng, *Electrochemical and Solid-State Letters*, 2011, **14**, A171-A173.
54. B. Yang, L. Hoober-Burkhardt, F. Wang, G. K. Surya Prakash and S. R. Narayanan, *J Electrochem Soc*, 2014, **161**, A1371-A1380.
55. B. Yang, L. Hoober-Burkhardt, S. Krishnamoorthy, A. Murali, G. K. S. Prakash and S. R. Narayanan, *J Electrochem Soc*, 2016, **163**, A1442-A1449.
56. L. Hoober-Burkhardt, S. Krishnamoorthy, B. Yang, A. Murali, A. Nirmalchandar, G. K. S. Prakash and S. R. Narayanan, *J Electrochem Soc*, 2017, **164**, A600-A607.

57. T. Liu, X. Wei, Z. Nie, V. Sprenkle and W. Wang, *Advanced Energy Materials*, 2016, **6**, 1501449.
58. T. Janoschka, N. Martin, M. D. Hager and U. S. Schubert, *Angewandte Chemie International Edition*, 2016, **55**, 14427-14430.
59. B. Hu, Y. Tang, J. Luo, G. Grove, Y. Guo and T. L. Liu, *Chemical Communications*, 2018, **54**, 6871-6874.
60. B. Hu, C. DeBruler, Z. Rhodes and T. L. Liu, *Journal of the American Chemical Society*, 2017, **139**, 1207-1214.
61. C. DeBruler, B. Hu, J. Moss, X. Liu, J. Luo, Y. Sun and T. L. Liu, *Chem*, 2017, **3**, 961-978.
62. J. Luo, B. Hu, C. Debruler and T. L. Liu, *Angewandte Chemie International Edition*, 2018, **57**, 231-235.
63. B. Hu and T. L. Liu, *Journal of Energy Chemistry*, 2018, **27**, 1326-1332.
64. K. Lin, R. Gómez-Bombarelli, E. S. Beh, L. Tong, Q. Chen, A. Valle, A. Aspuru-Guzik, M. J. Aziz and R. G. Gordon, *Nature Energy*, 2016, **1**, 16102.
65. A. Orita, M. G. Verde, M. Sakai and Y. S. Meng, *Nature Communications*, 2016, **7**, 13230.
66. A. Hollas, X. Wei, V. Murugesan, Z. Nie, B. Li, D. Reed, J. Liu, V. Sprenkle and W. Wang, *Nature Energy*, 2018, **3**, 508-514.
67. T. Janoschka, N. Martin, U. Martin, C. Friebe, S. Morgenstern, H. Hiller, M. D. Hager and U. S. Schubert, *Nature*, 2015, **527**, 78-81.
68. J. Winsberg, T. Janoschka, S. Morgenstern, T. Hagemann, S. Muench, G. Hauffman, J.-F. Gohy, M. D. Hager and U. S. Schubert, *Advanced Materials*, 2016, **28**, 2238-2243.
69. J. Winsberg, T. Hagemann, S. Muench, C. Friebe, B. Häupler, T. Janoschka, S. Morgenstern, M. D. Hager and U. S. Schubert, *Chemistry of Materials*, 2016, **28**, 3401-3405.
70. K. Gong, Q. Fang, S. Gu, S. F. Y. Li and Y. Yan, *Energy & Environmental Science*, 2015, **8**, 3515-3530.
71. M. Duduta, B. Ho, V. C. Wood, P. Limthongkul, V. E. Brunini, W. C. Carter and Y.-M. Chiang, *Advanced Energy Materials*, 2011, **1**, 511-516.
72. X. Wei, W. Xu, M. Vijayakumar, L. Cosimbescu, T. Liu, V. Sprenkle and W. Wang, *Advanced Materials*, 2014, **26**, 7649-7653.
73. K. Wedege, E. Dražević, D. Konya and A. Bentien, *Scientific Reports*, 2016, **6**, 39101.

74. A. Orita, M. G. Verde, M. Sakai and Y. S. Meng, *J Power Sources*, 2016, **321**, 126-134.
75. M. Zhang, M. Moore, J. S. Watson, T. A. Zawodzinski and R. M. Counce, *J Electrochem Soc*, 2012, **159**, A1183-A1188.
76. R. A. Potash, J. R. McKone, S. Conte and H. D. Abruña, *J Electrochem Soc*, 2016, **163**, A338-A344.
77. S. H. Oh, C. W. Lee, D. H. Chun, J. D. Jeon, J. Shim, K. H. Shin and J. H. Yang, *Journal of Materials Chemistry A*, 2014, **2**, 19994-19998.
78. W. Duan, R. S. Vemuri, J. D. Milshtein, S. Laramie, R. D. Dmello, J. Huang, L. Zhang, D. Hu, M. Vijayakumar, W. Wang, J. Liu, R. M. Darling, L. Thompson, K. Smith, J. S. Moore, F. R. Brushett and X. Wei, *Journal of Materials Chemistry A*, 2016, **4**, 5448-5456.
79. T. Hagemann, J. Winsberg, B. Häupler, T. Janoschka, J. J. Gruber, A. Wild and U. S. Schubert, *Npg Asia Materials*, 2017, **9**, e340.
80. G. D. Charlton, S. M. Barbon, J. B. Gilroy and C. A. Dyker, *Journal of Energy Chemistry*, 2019, **34**, 52-56.
81. M. Ting, P. Zeng, M. Licheng, C. Chengcheng, H. Mo, S. Zhenfeng and C. Jun, *Angewandte Chemie International Edition*, 2018, **57**, 3158-3162.
82. C. G. Armstrong, R. W. Hogue and K. E. Toghill, *J Power Sources*, 2019, **440**, 227037.
83. J. Winsberg, C. Stolze, S. Muench, F. Liedl, M. D. Hager and U. S. Schubert, *ACS Energy Letters*, 2016, **1**, 976-980.
84. T. Janoschka, C. Friebe, M. D. Hager, N. Martin and U. S. Schubert, *ChemistryOpen*, 2017, **6**, 216-220.
85. Q. Liu, A. A. Shinkle, Y. Li, C. W. Monroe, L. T. Thompson and A. E. S. Sleightholme, *Electrochemistry Communications*, 2010, **12**, 1634-1637.
86. A. E. S. Sleightholme, A. A. Shinkle, Q. Liu, Y. Li, C. W. Monroe and L. T. Thompson, *J Power Sources*, 2011, **196**, 5742-5745.
87. D. Zhang, H. Lan and Y. Li, *J Power Sources*, 2012, **217**, 199-203.
88. P. J. Cappillino, H. D. Pratt, N. S. Hudak, N. C. Tomson, T. M. Anderson and M. R. Anstey, *Advanced Energy Materials*, 2014, **4**, 1300566-n/a.
89. R. W. Hogue, C. G. Armstrong and K. E. Toghill, *ChemSusChem*, **0**.
90. P. J. Cabrera, X. Yang, J. A. Suttil, K. L. Hawthorne, R. E. M. Brooner, M. S. Sanford and L. T. Thompson, *The Journal of Physical Chemistry C*, 2015, **119**, 15882-15889.
91. C. G. Armstrong and K. E. Toghill, *J Power Sources*, 2017, **349**, 121-129.

92. Q. Liu, A. E. S. Sleightholme, A. A. Shinkle, Y. Li and L. T. Thompson, *Electrochemistry Communications*, 2009, **11**, 2312-2315.

93. P. Leung, A. A. Shah, L. Sanz, C. Flox, J. R. Morante, Q. Xu, M. R. Mohamed, C. Ponce de León and F. C. Walsh, *J Power Sources*, 2017, **360**, 243-283.

94. X. Wei, W. Xu, J. Huang, L. Zhang, E. Walter, C. Lawrence , M. Vijayakumar, W. A. Henderson, T. Liu, L. Cosimbescu, B. Li, V. Sprenkle and W. Wang, *Angewandte Chemie International Edition*, 2015, **54**, 8684-8687.

95. M. Sadakane and E. Steckhan, *Chem. Rev.*, 1998, **98**, 219-237.

96. M. T. Pope and A. Müller, *Angewandte Chemie International Edition in English*, 1991, **30**, 34-48.

97. W. Liu, W. Mu, M. Liu, X. Zhang, H. Cai and Y. Deng, 2014, **5**, 3208.

98. H.-Y. Chen, R. Al-Oweini, J. Friedl, C. Y. Lee, L. Li, U. Kortz, U. Stimming and M. Srinivasan, *Nanoscale*, 2015, **7**, 7934-7941.

99. S. Hartung, N. Bucher, H.-Y. Chen, R. Al-Oweini, S. Sreejith, P. Borah, Z. Yanli, U. Kortz, U. Stimming, H. E. Hoster and M. Srinivasan, *J Power Sources*, 2015, **288**, 270-277.

100. H. D. Pratt Iii, N. S. Hudak, X. Fang and T. M. Anderson, *J Power Sources*, 2013, **236**, 259-264.

101. Y. Liu, S. Lu, H. Wang, C. Yang, X. Su and Y. Xiang, *Advanced Energy Materials*, 2017, **7**, 1601224.

102. J.-J. J. Chen and M. A. Barteau, *Journal of Energy Storage*, 2017, **13**, 255-261.

103. L. E. Vangelder, A. M. Kosswattaarachchi, P. L. Forrestel, T. R. Cook and E. M. Matson, *Chemical Science*, 2018, **9**, 1692-1699.

104. L. E. VanGelder and Ellen M. Matson, *Journal of Materials Chemistry A*, 2018, **6**, 13874-13882.

105. L. E. VanGelder, B. E. Petel, O. Nachtigall, G. Martinez, W. W. Brennessel and E. M. Matson, *ChemSusChem*, **0**.

106. L. E. VanGelder, H. D. Pratt, T. M. Anderson and E. M. Matson, *Chemical Communications*, 2019, **55**, 12247-12250.

107. J. Friedl, M. V. Holland-Cunz, F. Cording, F. L. Pfanschilling, C. Wills, W. McFarlane, B. Schricker, R. Fleck, H. Wolfschmidt and U. Stimming, *Energy & Environmental Science*, 2018, DOI: 10.1039/C8EE00422F.

108. J. N. Israelachvili, in *Intermolecular and Surface Forces (Third Edition)*, ed. J. N. Israelachvili, Academic Press, San Diego, 2011, DOI: https://doi.org/10.1016/B978-0-12-375182-9.10004-1, pp. 71-90.

109. L. C. W. Baker and M. T. Pope, *Journal of the American Chemical Society*, 1960, **82**, 4176-4179.
110. A. Horky, N. P. Kherani and G. Xu, *J Electrochem Soc*, 2003, **150**, A1219.
111. J. Friedl, F. L. Pfanschilling, M. V. Holland-Cunz, R. Fleck, B. Schricker, H. Wolfschmidt and U. Stimming, *Clean Energy*, 2019, DOI: 10.1093/ce/zkz019.
112. J.-J. Chen, M. D. Symes and L. Cronin, *Nature Chemistry*, 2018, DOI: 10.1038/s41557-018-0109-5.
113. T. Feng, H. Wang, Y. Liu, J. Zhang, Y. Xiang and S. Lu, *J Power Sources*, 2019, **436**, 226831.
114. Y. Cao, J.-J. J. Chen and M. A. Barteau, *Journal of Energy Chemistry*, 2020, **50**, 115-124.
115. M. L. Perry and A. Z. Weber, *J Electrochem Soc*, 2016, **163**, A5064-A5067.
116. B. J. Neyhouse, A. M. Fenton and F. R. Brushett, *J Electrochem Soc*, 2021, **168**, 050501.
117. J. D. Milshtein, K. M. Tenny, J. L. Barton, J. Drake, R. M. Darling and F. R. Brushett, *J Electrochem Soc*, 2017, **164**, E3265-E3275.
118. J. A. Kowalski, M. D. Casselman, A. P. Kaur, J. D. Milshtein, C. F. Elliott, S. Modekrutti, N. H. Attanayake, N. Zhang, S. R. Parkin, C. Risko, F. R. Brushett and S. A. Odom, *Journal of Materials Chemistry A*, 2017, **5**, 24371-24379.

Chapter 2 - Background and Theory

2.1 Polyoxometalates

2.1.1 Formation of Polyoxometalates

Polyoxometalates (POMs) are anionic metal-oxygen clusters of early transition metals. They can be subdivided into isopolyoxometalates which have a general formula of $[M_mO_y]^{p-}$ or heteropolyoxometalates of general formula $[X_XM_mO_y]^{q-}$ where the identity of the element 'M', termed an addenda atom, is a d-block metal in its highest oxidation state. The addenda atoms are commonly tungsten, molybdenum or vanadium, but the occurrence of niobium and tantalum in POMs is also known.[1] The 'X' element in heteropolyoxometalates is termed the heteroatom, which has a much more varied identity. Upwards of 50 different elements have been incorporated into POMs as heteroatoms,[2] of which silicon, phosphorous, germanium and boron are common examples.

The structure of POMs may be illustrated by using ball and stick or polyhedral representations. The most well-known POM is the Keggin structure, a heteropolyoxometalate with a formula of $[XM_{12}O_{40}]^{q-}$. Ball and stick and polyhedral representations of the Keggin structure are shown in Figure 2.1. In the polyhedral representation, the POM is shown as being composed of octahedral MO_6 units, with a central tetrahedral unit that contains the heteroatom.

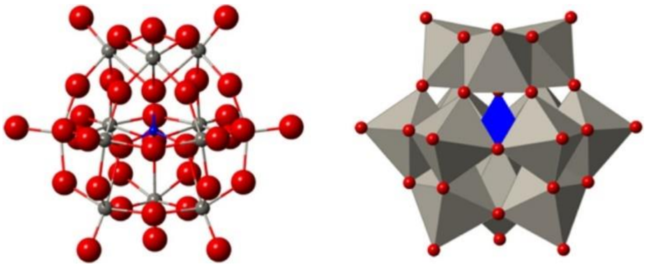

Figure 2.1 - Left: a ball and stick representation of the Keggin structure (red = oxygen atom, grey = addenda atom and blue = heteroatom). Right: a polyhedral representation of the Keggin structure.[3] (Reprinted with permission from I. A. Weinstock, R. E. Schreiber, and R. Neumann, Chem. Rev., 2018, 118, 5, 2680–2717. Copyright 2018 American Chemical Society.)

In addition to isopolyoxometalates and heteropolyoxometalates, a third division of POM structure exists. Structures in this group are termed Mo-blue and Mo-brown reduced POM clusters.[4] These are high nuclearity clusters of molybdenum, the composition of which was uncovered by Müller *et al*. who reported $[Mo_{154}(NO)_{14}O_{420}(OH)_{28}(H_2O)_{70}]^{(25\pm5)-}$.[5] This species was described as a "big wheel" structure and contained more than 700 atoms.

It has been noted that there are two 'essential' requirements for transition metals if they are to be the constituents of POMs,[6] which restricts the identity of the addenda atoms to only a small number of elements. The first requirement concerns the radius of the metal cation. When tungsten, molybdenum and vanadium are incorporated into a POM, their coordination number is expanded from four to six.[6] Cations that are of a smaller size than V^{5+} may only display a maximum coordination number of four,[6] making them unsuitable starting species.

The second requirement for consideration is the strength of a metal's ability to be an acceptor of p-orbital π electrons when bonding with oxygen. In polyoxomolybdates and polyoxotungstates, the metal atoms in octahedral environments are displaced from the centre of their octahedra, occupying a position that is closer to the exterior of the structure.[6] The oxygen atoms in these structures can be divided into two types depending on whether they are shared with another addenda atom or not: terminal and bridging (Figure 2.2). Terminal oxygen atoms are bonded to one addenda atom only.

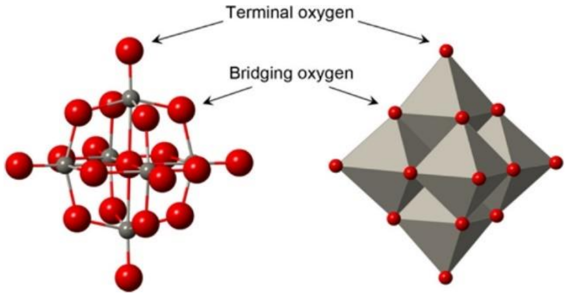

Figure 2.2 - The types of oxygen atoms in the Lindqvist structure ($[M_6O_{19}]^{p-}$).[3] (Reprinted with permission from I. A. Weinstock, R. E. Schreiber, and R. Neumann, Chem. Rev., 2018, 118, 5, 2680–2717. Copyright 2018 American Chemical Society.)

In terminal metal-oxygen bonds, strong ion-to-induced-dipole attractions between addenda atoms and their unshared oxygen atoms causes shortening of these M-O bonds whereas interior, bridging oxygen atoms shared with other addenda atoms are less polarisable.[7] For instance, the difference in W-O bond distances between interior oxygen atoms and exterior oxygen atoms can be 0.7 Å to 1.0 Å.[7] This creates short M-O bonds on the exterior of the anion in which strong metal-oxygen π-bonding is present.[6] The terminal oxygen atoms in the shortened M-O bonds are polarised towards the interior of the structure rendering them with a low degree of basicity and promoting a structure that is stable to protonation and further polymerisation.[6] This ensures that discrete complexes are formed rather than "insoluble extended solid matrixes".[7] Cations of a greater size than Nb^{5+} are too large to exhibit the same structural displacements in an octahedral environment, reducing the capability of these elements to form strong π bonds with terminal oxygen atoms.

POMs are commonly prepared by acidifying an aqueous solution of oxoanions, which promotes polycondensation of the oxoanions into large anionic species. The formal sequence of hydrolysis reactions that results in the formation of POMs is shown in Scheme 2.1.[8]

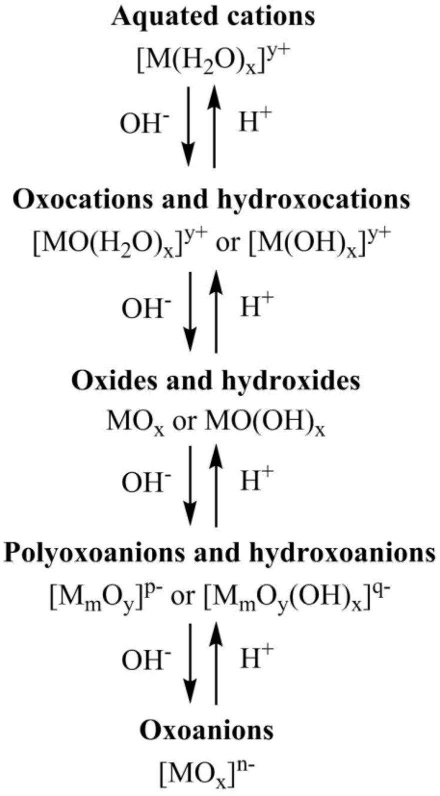

Scheme 2.1 - The formal sequence of hydrolysis reactions that links oxoanions and polyoxoanions.[8]

Formation of an isopolyoxometalate occurs under circumstances where only the same oxoanion is present, for instance, in the formation of paratungstate (Equation 2.1).[8] If another oxoanion that contains a heteroatom is present, formation of a heteropolyoxometalate can occur (Equation 2.2).[9]

$$7[WO_4]^{2-} + 8H^+ \rightarrow [W_7O_{24}]^{6-} + 4H_2O \qquad 2.1$$

$$12[WO_4]^{2-} + [HPO_4]^{2-} + 23H^+ \rightarrow [PW_{12}O_{40}]^{3-} + 12H_2O \qquad 2.2$$

Careful control of pH, concentration and temperature may be required for POM formation. Isolation of the POM species can be achieved by addition of a counterion supplied by an alkali metal, ammonium or tetraalkylammonium salt.[9] Isolation of POMs in free acid form as heteropoly acids, e.g. $H_3PMo_{12}O_{40}$, involves extracting the POM from a strongly acidified solution into an ‘etherate’ phase by using diethyl ether.[10] The etherate species that is produced can be decomposed by the addition of water and allowed to crystallise via evaporation following removal of the ether.[9]

2.1.2 Early Developments and the Discovery of the Keggin Structure

The formation of a POM was first noted by Berzelius in 1826 who found that a yellow precipitate was produced after addition of phosphoric acid to ammonium molybdate ($(NH_4)_2MoO_4$).[11] This compound is now known to be ammonium 12-molybodophosphate, $(NH_4)_3PMo_{12}O_{40}$. Preparation of the first heteropolytungstate, 12-tungstosilicic acid, was later reported by Marignac in 1862.[1, 7] This preceded a fruitful period of development in the field, with around 60 different types of heteropoly compounds detailed by the first decade of the 20th century.[1]

The desire to understand the structure of POMs led to development of the Miolati-Rosenheim theory, which was a progression of the earlier work of Werner[12] and Miolati and Pizzighelli.[13] Based on Werner's theory of coordination complexes, a structural hypothesis was put forward by Miolati with research efforts into proving the structure led later by Rosenheim,[7] thereby giving rise to the Miolati-Rosenheim view of the structure of heteropoly compounds. This theory supposed that the heteropoly acids of molybdenum and tungsten could be separated into two classes, '12-class' and '6-class', depending on whether the central atom had 12 or six molybdenum or tungsten atoms surrounding it.[14] The 12-class species contained a six-coordinate central group $[XO_6]^{n-}$ (e.g. X = Si and n = 8) in which the oxygen atoms were replaced by Mo_2O_7 or W_2O_7 groups leading to, for example, a structure of formula $H_8[Si(W_2O_7)_6]$. The 6-class species were also composed of a six-coordinate central group but each oxygen atom was substituted with MoO_4 or WO_4 units instead.

However, it was later discussed by Pauling that the structures determined using the Miolati-Rosenheim theory did not account for the observed properties of the 12-heteropoly acids, for instance, the number of replaceable hydrogen atoms.[14] Noting that the crystal radii of Mo^{6+} and W^{6+} suggested an octahedral coordination environment with oxygen, Pauling proposed that the 12-heteropoly acids contained MO_6 octahedral units and a central tetrahedral XO_4 group, with the octahedra arranged in such a way that they shared corners. This led to a structure for 12-tungstosilicic acid being written as $H_4[SiO_4W_{12}O_{18}(OH)_{36}]$ (Figure 2.3a). The 36 oxygen atoms that did not share corners in Pauling's proposed structure were protonated in order to oppose their negative charges.

In 1933, Keggin solved the structure of $H_3PW_{12}O_{40}\cdot 5H_2O$ by X-ray crystallography, thereby finally elucidating the correct structure for the 12-heteropoly compounds and giving rise to the eponymous Keggin structure.[15] Keggin's work confirmed that the $[PW_{12}O_{40}]^{3-}$ anion contained octahedral MO_6 units but these units shared edges as well as corners, unlike in Pauling's proposed structure (Figure 2.3b).

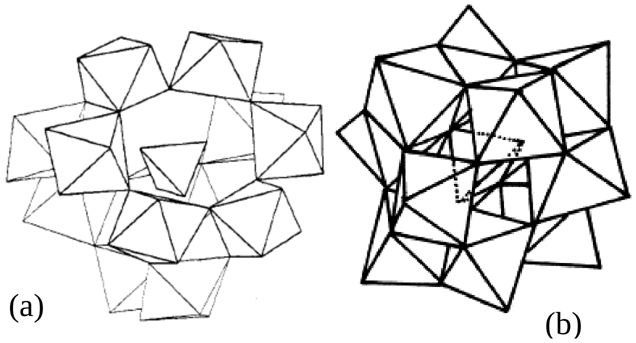

Figure 2.3 - (a) The structure proposed by Pauling for $H_4[SiO_4W_{12}O_{18}(OH)_{36}]$ in 1929.[14] *(Reprinted with permission from L. Pauling, J. Am. Chem. Soc., 1929, 51, 2868–2880. Copyright 1929 American Chemical Society.) (b) The Keggin structure.*[16] *(Reprinted from F. Cavani, Catalysis Today, 1998, 41, 73–86, Copyright 1998, with permission from Elsevier.)*

The Keggin structure can be viewed as consisting of four M_3O_{13} groups. MO_6 octahedra share edges within each M_3O_{13} group but share corners with octahedra from different M_3O_{13} groups. The structure was later confirmed in a second X-ray crystallography study of $H_3PW_{12}O_{40}\cdot 29H_2O$ by Bradley and Illingworth.[17] Several other complexes containing 12 addenda atoms, including the metatungstate anion $[H_2W_{12}O_{40}]^{6-}$, were also confirmed to have the Keggin structure by Signer and Gross.[7, 18]

2.1.3 Other Polyoxometate Subclasses

The structures of further families of POMs were later elucidated. Along with the Keggin structure, the other main subclasses of heteropolyoxometalates are the Anderson-Evans structure and the Wells-Dawson structure. The Anderson-Evans structure (Figure 2.4b) was first proposed by Anderson for the species $[IMo_6O_{24}]^{5-}$ and other 6-heteropoly compounds by using the Miolati-Rosenheim theory for 6-heteropoly species, and later confirmed crystallographically in 1948 by Evans in the study of $[TeMo_6O_{24}]^{6-}$.[19, 20] The heteroatom in the Anderson-Evans structure is in an octahedral environment and is surrounded by six edge-sharing MO_6 units.

Following earlier study of a dimeric 9-molybdophosphate anion[21] and an investigation into ‘phospho-18-tungsto acids and phospho-18-molybdic acids’ by Wu,[22] a structure of $[P_2W_8O_{62}]^{6-}$ was suggested by Wells for a dimeric 9-tungstophosphate anion in 1945.[23] The structure was confirmed later by Dawson in 1953 using X-ray crystallography.[24] The Wells-Dawson structure (Figure 2.4d) can be viewed as a dimer of XM_9O_{34} units. The structure contains two heteroatoms with tetrahedral coordination which are each linked to an M_3O_{13} group and three M_2O_{10} groups, leading to the assignment of two types of addenda atoms in the structure: six polar addenda atoms and 12 equatorial addenda atoms.[25] A further notable subclass of heteropolyoxometalate is the Preyssler structure, $[P_5W_{30}O_{110}]^{n-}$ (Figure 2.4e), which is a by-product of the synthesis of the Wells-Dawson structure.[26] A common isopolyoxometalate subclass is the Lindqvist structure (Figure 2.4a), with a formula of $[M_6O_{19}]^{n-}$. This was first reported in 1950 and consists of six MO_6 octahedra that participate in both edge-sharing and corner-sharing.[27]

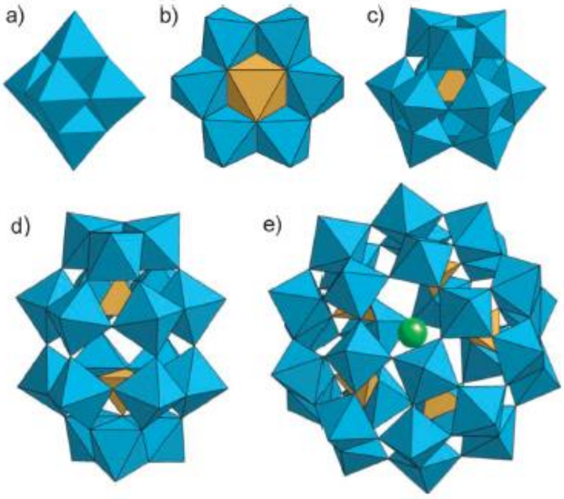

Figure 2.4 - Polyhedral representations of well-known POM subclasses.[28] *(a) The Lindqvist structure. (b) The Anderson-Evans structure. (c) The Keggin structure. (d) The Wells-Dawson structure. (e) The Preyssler structure. (Reproduced from Ref. 28 with permission from The Royal Society of Chemistry.)*

2.1.4 Isomerism of the Keggin Structure

There are other possible structural arrangements of the Keggin structure in addition to that shown in Figure 2.3b, giving rise to four other isomers. The occurrence of these isomers was predicted by Baker and Figgis.[29] The Baker-Figgis isomers of the Keggin structure are obtained through the 60° rotation of one, two, three or all four M_3O_{13} groups. In the β isomer, one edge-shared M_3O_{13} unit is rotated 60°, meaning that it now shares corners with the adjacent M_3O_{13} groups. The structure of the β isomer was confirmed using $[SiW_{12}O_{40}]^{4-}$ by Matsumoto in 1975.[30] Figure 2.5 shows how sequential rotation of further M_3O_{13} units generates γ, δ and ε isomers.

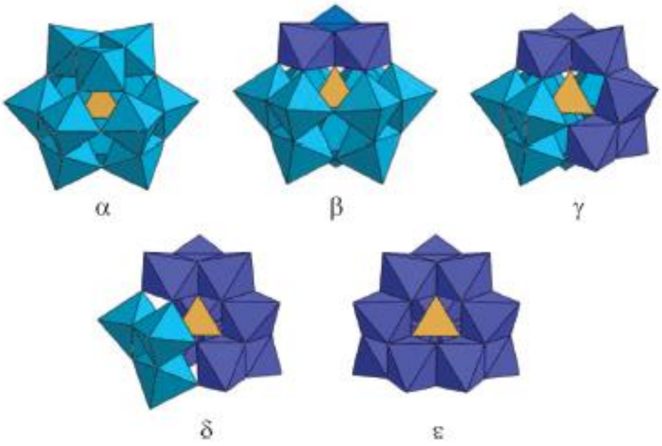

Figure 2.5 - The Baker-Figgis isomers of the Keggin structure.[28] *(Reproduced from Ref. 28 with permission from The Royal Society of Chemistry.)*

The γ, δ and ε isomers become progressively more unstable as a result of the increasing number of edge-shared linkages between M_3O_{13} groups. In the α and β isomers, the M_3O_{13} groups are linked by corner sharing and these structures are, theoretically, of similar stability.[31] Rotation of additional M_3O_{13} units leads to the replacement of some of the 12 corner-shared links in the α and β isomer with 1–6 edge-shared links in the γ, δ and ε isomers and situates metal atoms closer together, increasing electrostatic repulsion.[31]

The γ isomer of $[SiW_{12}O_{40}]^{4-}$ was prepared by Tézé *et al.* in 1996 who reported no decrease in stability relative to the α isomer in organic solvents, but an increased sensitivity to hydrolysis in aqueous solution.[32] Sartzi *et al.* reported the first isolation of a δ-Keggin structure in 2015 through the incorporation of a triethanolamine ligand that was coordinated to the three 60°-rotated M_3O_{13} units.[33] The attachment of the triethanolamine ligand was found to stabilise or "lock" the arrangement of the structure. The first instance of a preparation of the ε isomer was an oxomolydenum(V) complex, a cation of formula $[(C_5Me_5Rh)_8(Mo^{V}{}_{12}O_{36})(Mo^{VI}O_4)]^{2+}$, which was reported in 1992.[34] The core of the complex, a tetrahedral $[Mo^{VI}O_4]^{2-}$ unit in a $[Mo^{V}{}_{12}O_{36}]^{12-}$ cage, adopted the ε-Keggin structure and was capped by eight Rh^{III} centers. An ε-Keggin core also featured in later work,[35, 36] including in the polyoxomolybdate $[Mo^{V}{}_{12}O_{30}(\mu_2\text{-}OH)_{10}H_2\{Ni^{II}(H_2O\}_3)_4]$ and the polyoxocation $[PMo_{12}O_{36}(OH)_4\{La(H_2O)_4\}_4]^{5+}$ which were capped by electrophilic nickel and lanthanide units, respectively, for stability.[37, 38] An all-vanadium ε-Keggin structure was reported in 2012, $H_3[\{Bi(dmso)_3\}_4V_{13}O_{40}]$·ca. 4 DMSO, which contained an $[\varepsilon\text{-}V_{12}O_{40}]^{15-}$ unit capped by Bi^{III} centers.[39]

2.1.5 Lacunary Polyoxometalate Species

For tungstosilicates (and tungstogermanates) with the Keggin structure, the generation of a variety of lacunary anions is possible.[2] Scheme 2.2 illustrates how the structures interconvert through addition of acid or base. An addenda atom or atoms, and the oxygen atoms not shared with other addenda atoms, have been removed in the lacunary Keggin structures.

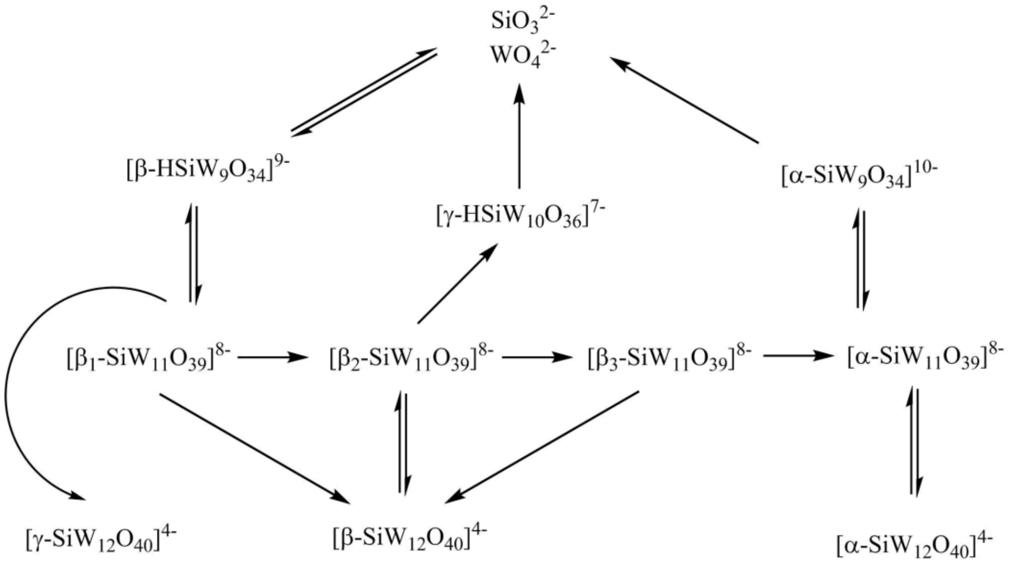

Scheme 2.2 - The general route for synthesis of the dodecatungstosilicate anion, $[SiW_{12}O_{40}]^{4-}$, and the related lacunary species.[40]

The formation of the lacunary structures of $[SiW_{12}O_{40}]^{4-}$ is achieved by increasing the pH of a solution of the parent anion. At pH ≈ 4.5 the undecatungstosilicate, $[SiW_{11}O_{39}]^{6-}$, forms by hydrolysis of W-O bonds.[2] In $[SiW_{11}O_{39}]^{6-}$, four oxygen atoms are exposed and, as discussed later, these oxygen atoms can undergo additional reactions. Increasing the pH further causes additional cleavage of W-O bonds and results in $[\gamma\text{-}SiW_{10}O_{36}]^{8-}$ or the α or β isomer of the nonatungstosilicate species, depending on which isomer was the precursor.[40] To generate a trivacant structure, tungsten atoms can either be removed from three different W_3O_{13} groups or removed from the same W_3O_{13} group which leads to A-type and B-type structures respectively.[41] A different, and perhaps more convenient, synthesis route to the $[SiW_{11}O_{39}]^{6-}$ and $[SiW_9O_{34}]^{10-}$ anions is through acidification of solutions of SiO_3^{2-} and WO_4^{2-}, as reported by Tézé and Hervé.[40] Polyhedral representations of the structures of $[SiW_{11}O_{39}]^{6-}$, $[\gamma\text{-}SiW_{10}O_{36}]^{8-}$, A-$[SiW_9O_{34}]^{10-}$ and B-$[SiW_9O_{34}]^{10-}$ are shown in Figure 2.6.

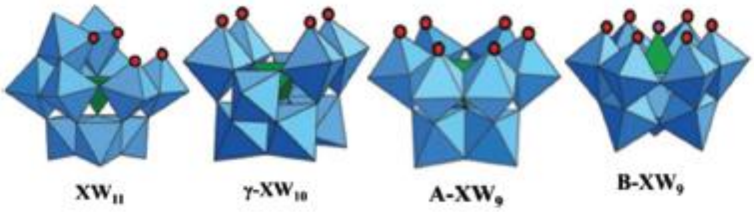

Figure 2.6 - (a) The structure of $[SiW_{11}O_{39}]^{6-}$, (b) $[\gamma\text{-}SiW_{10}O_{36}]^{8-}$, (c) A-$[SiW_9O_{34}]^{10-}$ and (d) B-$[SiW_9O_{34}]^{10-}$.[42] *(Reproduced from Ref. 42 with permission from The Royal Society of Chemistry.)*

Lacunary species of other Keggin anions, as well as lacunary Wells-Dawson structures, can be prepared. $[PW_{12}O_{40}]^{3-}$ undergoes an analogous transformation into $[PW_{11}O_{39}]^{7-}$ and $[PW_9O_{34}]^{9-}$ anions.[2] Several lacunary structures of the Wells-Dawson structure are known: $[P_2W_{17}O_{61}]^{10-}$, in which either a single equatorial tungsten or polar tungsten atom is missing, and the $[P_2W_{15}O_{56}]^{12-}$ anion which is deficient of three polar tungsten atoms. These structures can be obtained by the degradation of $[P_2W_{18}O_{62}]^{6-}$ in alkaline conditions.[25, 43]

Such lacunary structures show an enhanced reactivity compared to the parent anion. The negative charge of non-lacunary, or plenary, POMs is delocalised over the whole structure,[44] and these structures lack strongly nucleophilic sites. In the lacunary derivatives, the nucleophilicity of the oxygen atoms at the surface of the defect site is increased.

The enhanced reactivity of lacunary POMs is evidenced by work in the area of organic-inorganic POM hybrids, in which the vacant sites are occupied by organometal or organometalloidal groups. This includes electrophilic groups such as organophosphate, organosilyl, organoarsonate and organotin groups.[44] Ho and Klemperer were the first to report the preparation of a POM bound to an organometallic group by reaction of the $[PW_{11}O_{39}]^{8-}$ anion with $(\eta^5\text{-}C_5H_5)TiCl_3$ to generate $[(\eta^5\text{-}C_5H_5)Ti(PW_{11}O_{39})]^{4-}$, with the titanium atom taking the place of a tungsten atom.[45] A later advance in this area was presented by Judeinstein who reported the polymerisation of organic-functionalised POM units by free radical polymerisation. The organic-inorganic POM monomers with a formula of $[SiW_{11}O_{40}(SiR)_2]^{4-}$ were obtained by the reaction of $[SiW_{11}O_{39}]^{8-}$ with compounds such as $RSiCl_3$, where R = vinyl ($CH{=}CH_2$), allyl ($CH_2CH{=}CH_2$) or a 3-(methacryloxyl)propyl group ($(CH_2)_3OC(O)C(CH_3){=}CH_2$).[46] The variety of structures and applications of organic-inorganic POM hybrids is beyond the scope of this introductory section but such functionalisation of lacunary species can alter the properties of POMs, allowing the tuning of electrochemistry, acidity/basicity and solubility. Functionalisation of POMs could be a means of improving the efficiency and selectivity of catalysis[47] and opening up new possibilities for POMs in materials chemistry through, for instance, incorporation of organic-functionalised POMs as polymer constituents or surface interactions of POMs with materials such as nanoparticles.[44]

Transition metal cations can also be incorporated into the structure of lacunary POMs, and it was this work that preceded the development of POM organic-inorganic hybrids. In 1966, Baker *et al*. established that a metal ion of lower valency (Co^{II}, Co^{III}, Ga^{III}) could occupy one of the octahedral tungsten sites in the Keggin structure.[48] Weakley and Malik later reported a range of Keggin structures described as containing two types of addenda atoms with a general formula of $[XZW_{11}O_{40}H_2]^{n-}$ where X is a heteroatom and Z = Co^{II}, Co^{III} or Ni^{II} (the formula included two non-acidic hydrogen atoms attached to exterior oxygen atoms).[49] A structure in which Co^{II} had substituted a molybdenum site, $[SiCo^{II}Mo_{11}O_{40}H_2]^{6-}$, was also reported. The synthesis procedure for each complex consisted of partial degradation of the parent 12-heteropoly compound with base to remove one tungsten or molybdenum in the presence of a salt of the metal that would take its place. The same authors reported the preparation of derivatives of the Wells-Dawson structure $[P_2W_{18}O_{62}]^{6-}$ by analogous methods to form $[X_2YW_{17}O_{62}H_2]^{8-}$, where X = P or As and Y = Mn^{II}, Co^{II} or Ni^{II}.[50]

Further contributions of note in this period came from Ripan and co-workers who reported nickel-substituted 11-tungstozincate and 11-tungstoferrate anions[7] and the preparation of $K_6[NiSiW_{11}O_{40}H_2]\cdot nH_2O$ and $K_5[NiPW_{11}O_{40}H_2]\cdot nH_2O$.[51] Tourné *et al*. also prepared a range of Keggin structures of general formula $[XZW_{11}O_{40}H_2]^{n-}$ (Z = Mn^{II}, Mn^{III} and Cu^{II}) and $[XZMo_{11}O_{40}H_2]^{n-}$ (Z = Mn^{II}, Cu^{II}), as well as two copper(II)-substituted Wells-Dawson structures, $[P_2CuW_{17}O_{62}H_2]^{8-}$ and $[As_2CuW_{17}O_{62}H_2]^{8-}$.[52] Lacunary Keggin and Wells-Dawson polyoxotungstates substituted with a trivalent ion of aluminium, gallium, indium or thallium[53] and iron or rhodium[54] were also reported. The structure of a metal-substituted Keggin structure is shown in Figure 2.7.

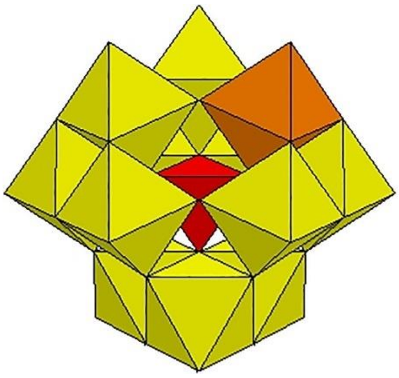

Figure 2.7 - The structure of a metal-substituted Keggin structure ($[SVW_{11}O_{40}]^{3-}$, yellow: tungsten, orange: vanadium, red: sulphur).[55] (Reprinted from J. Li, C. L. Bentley, T. Ueda, A. M. Bond, J. Zhang, Journal of Electroanalytical Chemistry, 2018, 819, 193–201, Copyright 2018, with permission from Elsevier.)

Reaction of lacunary POMs that have more than one vacant site with an alternative metal also results in substituted structures. Disubstituted anions are less numerous but it was shown that the reaction of the $[\gamma\text{-}HSiW_{10}O_{36}]^{7-}$ anion that is obtained from the hydrolysis of $[\beta_2\text{-}SiW_{11}O_{39}]^{8-}$ (shown in Scheme 2.2) with vanadium(V) generates $[\gamma\text{-}SiV_2W_{10}O_{40}]^{6-}$.[56] Finke *et al*. studied trisubstituted heteropoly compounds extensively.[7] This included the study of $[SiNb_3W_9O_{40}]^{7-}$, a structure in which Nb^{5+} comes to occupy the three vacant sites in $[A\text{-}\beta\text{-}HSiW_9O_{34}]^{9}$.[57] Mossoba *et al*. described the vanadium-substituted $[\alpha\text{-}SiV_3W_9O_{40}]^{7-}$ anion in 1980[58] and Finke *et al*. later published the synthesis protocol for $[\beta\text{-}SiV_3W_9O_{40}]^{7-}$.[59] Preparation of a mixed Mo/W Keggin structure, $[\alpha\text{-}SiMo_3W_9O_{40}]^{4-}$, along with two mixed V/Mo/W species, $[\alpha\text{-}SiMo_2VW_9O_{40}]^{5-}$ and $[\alpha\text{-}SiMoV_2W_9O_{40}]^{6-}$, is also possible through the use of $[\alpha\text{-}SiW_9O_{34}]^{10-}$ as the starting material.[60] An array of other transition metals were shown to form trisubstituted Keggin structures, in which the identity of the 'M' atom in the general formula $[SiW_9M_3O_{40}]^{n-}$ was Al, Ga, Cr^{III}, Fe^{III}, Co^{II}, Ni^{II} and Cu^{II}.[61] Trisubstituted Wells-Dawson structures ($[P_2M_3W_{15}O_{62}]^{y-}$) have also been studied.[62, 63]

Further noteworthy in this area of work is the combination of lacunary species to create "sandwich-type" structures and larger POM complexes. The first sandwich-type POM based on two Keggin-based fragments, $[P_2Co_4(H_2O)_2W_{18}O_{68}]^{10-}$, was described by Weakley *et al*. in 1973.[64] This structure consists of two PW_9O_{34} fragments linked by four Co^{II} centers. Finke *et al*. later reported that two lacunary Well-Dawson structures can also be combined to form a dimer containing two $P_2W_{15}O_{56}$ fragments linked by four 'M' atoms, $[P_4M_4(H_2O)_2W_{30}O_{112}]^{16-}$, where M = Co^{II}, Cu^{II} or Zn^{II}.[65] Since this early work, the reporting of manifold structures composed of lacunary POM fragments has ensued, examples of which can be found in the following review articles,[4, 66, 67] illustrating how the existence and utility of lacunary species diversifies the range of possible POM structures.

2.1.6 Redox Activity

A much-studied property of POMs is their redox activity. The reduction of the addenda atoms of POMs is accompanied by a distinctive colour change to dark blue, which gained these species the alternative moniker of 'heteropoly blues' (Figure 2.8). The concomitant electrochemical profile of the formation of heteropoly blues is a series of one-electron and two-electron reversible reduction waves.

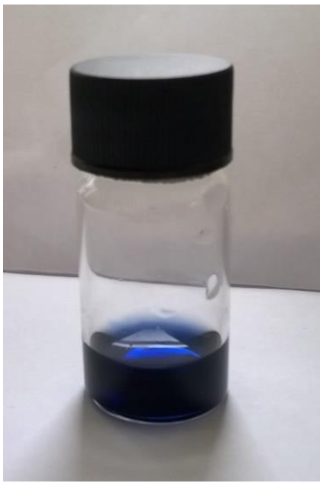

Figure 2.8 - A solution of a heteropolyoxometalate ($[SiV_3W_9O_{40}]^{7-}$) after electrochemical reduction.

The reason that reversible reduction waves are exhibited by some POMs is structural. Pope distinguished between two classes of MO_6 octahedra in POMs depending on the number of unshared oxygen atoms: type I and type II.[68] Type I octahedra ('mono-oxo' structures) have one unshared, or terminal, M-O bond and are characterised by displacement of the central metal atom in each octahedron towards one terminal oxygen. In type II octahedra ('cis dioxo' structures), the central metal atom is displaced towards two terminal oxygen atoms which have a cis arrangement to one another.

A requirement for the observation of reversible redox reactions and the formation of heteropoly blues is that the MO_6 octahedra are type I. In this instance, the lowest unoccupied molecular orbital (LUMO) is non-bonding (a largely metal-centred d_{xy} orbital[69]) and it follows that addition of an electron does not result in large changes in bond length. In type II octahedra, the LUMO is anti-bonding and electron addition is accompanied by substantial structural changes.[70] Thus, it can be rationalised why reversible reduction waves are observed for structures composed of type I octahedra, such as Keggin and Wells-Dawson species, and why the reduction of type II structures is irreversible: structures based on type I octahedra retain their structure upon reduction whereas the reduction of species containing type II octahedra is accompanied by structural changes.

It has been demonstrated that the electrons added to POMs when the addenda atoms are reduced do not remain localised on specific metal atoms. In a one-electron-reduced type I species, the added electron undergoes a temperature-dependent hopping mechanism, being localised on one metal atom at lower temperatures and undergoing thermally-activated hopping between addenda atoms at higher temperatures.[71] This process, which is fast on the timescale of Electron Spin Resonance (ESR) and NMR spectroscopy, has been indicated by ESR studies of one-electron-reduced species of Keggin anions such as $[\alpha\text{-}PMo_{12}O_{40}]^{n-}$, as well as in studies of $[SiW_{12}O_{40}]^{4-}$ that used ^{17}O NMR spectroscopy.[72-74] Analysis of the product of a two-electron reduction of $[\alpha\text{-}SiW_{12}O_{40}]^{4-}$ by using ^{183}W NMR spectroscopy showed a single signal for the addenda atoms, indicating delocalisation of the added electrons over all 12 tungsten atoms, whereas the two electrons added to reduce $[\alpha\text{-}P_2W_{18}O_{62}]^{8-}$ were delocalised over the six equatorial tungsten atoms.[75] It was later indicated that a 'ring current' of the electrons added to various tungsten-based Keggin and Wells-Dawson structures was set up in an applied magnetic field, which was indicated by the detection of the "excess diamagnetism of a $2e^-$ blue" due to the opposing magnetic field that was generated by the ring currents.[76] The delocalised electrons added to $[\alpha\text{-}SiW_{12}O_{40}]^{4-}$ circulate almost spherically whereas in $[\alpha\text{-}P_2W_{18}O_{62}]^{8-}$, the added electrons circulate throughout the two arrays of equatorial tungsten atoms.

For mixed-addenda POMs, electrons added upon reduction remain localised on the most reducible addenda atom, the reducibility decreasing in the order V > Mo > W. For instance, the reduced product of a one-electron reduction of $[P_2V_3W_{15}O_{62}]^{9-}$ exhibits an ESR spectrum consistent with the occurrence of electron hopping involving three equivalent ^{51}V nuclei at high temperature (350 K) and a spectrum corresponding to the trapping of an electron on a single vanadium atom at a lower temperature (5 K).[62] The ^{183}W NMR spectrum of $[P_2Mo_3W_{15}O_{62}]^{6-}$, reduced by two electrons, indicated that the added electrons were delocalised over the three Mo atoms (at 299 K).[75]

The reversible electrochemical reductions exhibited by type I POM species spurs investigation into the application of redox-active POMs in areas such as electrocatalysis and energy storage. Further, the incorporation of another type of metal into a lacunary POM species can alter its redox properties relative to the plenary structure, increasing the range of possible applications. As discussed, different addenda atoms (W, Mo, V) have different oxidising abilities and incorporation of a second type of addenda atom into a Keggin or Wells-Dawson structure can serve as the active site for POM-catalysed reactions.[77]

2.2 Techniques for the Study of Polyoxometalates

2.2.1 NMR Spectroscopy

In writing this section, the text by Lampman *et al.* was consulted.[78]

Some atomic nuclei possess the property of spin. Examples include ${}^{1}_{1}H$, ${}^{13}_{6}C$ and ${}^{17}_{8}O$. Each of these nuclei contain an odd number of protons and/or neutrons and, as a result of this, have a quantized spin angular momentum and a magnetic moment. The presence of such nuclei in a chemical species make it suitable for analysis by NMR Spectroscopy, a technique referred to previously in Section 2.1.6.

Nuclei with spin have a defined number of 'spin states' which are degenerate under conditions where there is no magnetic field. However, the energy of the spin states is no longer equivalent in a magnetic field due to the magnetic moment of the nucleus which can oppose the direction of the applied magnetic field. The number of spin states of a nucleus depends on its nuclear spin quantum number *I*. For a spin quantum number of *I*, there are $2I + 1$ possible spin states that range from $+I$ to $-I$ (Equation 2.3).

$$+I, (I-1), \dots, (-I+1), -I \qquad 2.3$$

The simplest case is a ${}^{1}_{1}H$ nucleus for which $I = \frac{1}{2}$, leading to $+\frac{1}{2}$ and $-\frac{1}{2}$ spin states. The spin states of the ${}^{1}_{1}H$ nucleus can be considered to correspond to the nucleus spinning in a manner aligned with ($+\frac{1}{2}$) or opposed to ($-\frac{1}{2}$) the applied magnetic field. The $+\frac{1}{2}$ spin state is of lower energy than the $-\frac{1}{2}$ spin state. Upon absorption of an amount of incoming energy in the radiofrequency range of the electromagnetic spectrum that matches the energy difference between spin states, termed the resonance frequency, a ${}^{1}_{1}H$ nucleus can be excited to the higher energy spin state, thereby flipping its spin. The energy differences between the spin states of a nucleus depend on the strength of the magnetic field and the type of nucleus. For a ${}^{1}_{1}H$ nucleus, the energy levels for the $+\frac{1}{2}$ and $-\frac{1}{2}$ spin state are both populated at room temperature but there is a slight excess of nuclei in the lower energy spin state. The excess population of nuclei in the lower energy spin state that can be promoted to the higher energy spin state is responsible for the observation of a signal in ^{1}H NMR spectroscopy. For nuclei with $I > \frac{1}{2}$, the spin states can have orientations and energy levels that are intermediate between being aligned with or opposed to the applied magnetic field.

The absolute resonance frequency of a signal is not reported in NMR spectroscopy. Instead, the chemical shift, δ, is used: (Equation 2.4).

$$\delta = \frac{Frequency\ difference\ between\ signal\ and\ reference\ signal\ (Hz)}{Frequency\ of\ spectrometer\ (MHz)} \qquad 2.4$$

Chemical shift values indicate how far a signal is shifted from the signal of a reference compound relative to the spectrometer’s operating frequency and are reported in parts per million (ppm). The resonance frequency of a signal for a given nucleus is dependent on the strength of the applied magnetic field, which varies between NMR spectrometers. Therefore, different spectrometers have a different operating frequency that is used to induce nuclear spin transitions. The absolute frequency of a signal will vary depending on the spectrometer but by including the operating frequency of the spectrometer as the divisor in Equation 2.4, the chemical shift becomes independent of magnetic field strength, and therefore the NMR spectrometer that is used to analyse a sample.

Nuclei in different environments have differences in their surrounding electron density and differing values of chemical shift. In an applied magnetic field, the electrons surrounding a nucleus are induced to circulate and generate a secondary magnetic field that opposes the applied field. This results in the ‘shielding’ of a nucleus from the applied magnetic field, an effect termed diamagnetic shielding, and nuclei with shielding experience a weaker net applied magnetic field. A shielded nucleus located in a region of high electron density will absorb radiation of a lower frequency than a nucleus in an environment with minimal shielding. This results in differing chemical shifts for ‘non-equivalent’ nuclei which are in different chemical environments.

NMR spectroscopy can be used for identification of a species by analysing the characteristic chemical shift values that result from the unique chemical environments of the nuclei in a molecule. For nuclei with $I = \frac{1}{2}$, spin-spin splitting can be observed whereby a single signal for a nucleus is split into a characteristic pattern of smaller signals of higher and lower frequency by the spin state of nearby nuclei, which can diminish or reinforce the strength of the applied magnetic field. Nuclei exhibiting spin-spin splitting are said to be coupled.

Nuclei with $I > \frac{1}{2}$ are said to have a quadrupole moment. Whereas nuclei with $I = \frac{1}{2}$ are surrounded by charge that is distributed symmetrically, nuclei possessing a quadrupole moment have a distribution of charge that is ellipsoidal. These nuclei undergo rapid spin transitions as a result of their charge distribution, such that they exhibit an averaged spin state which decouples them from adjacent nuclei.[78] Spin-spin splitting is thus not observed and peaks are also typically broader than for nuclei with $I = \frac{1}{2}$.

Several nuclei are of interest to the characterisation of POMs by NMR spectroscopy. These include ^{29}Si, ^{31}P and ^{183}W ($I = \frac{1}{2}$), ^{17}O ($I = \frac{5}{2}$) and ^{51}V ($I = \frac{7}{2}$). In this work, ^{51}V NMR spectroscopy was used for characterisation and analysis of POMs. Vanadium-based POMs exhibit chemical shifts of between -400 ppm and -600 ppm in ^{51}V NMR spectroscopy.[1]

2.2.2 Other Techniques

While not used extensively in this work, other techniques that can be used to analyse POMs include Infrared Spectroscopy and UV-Visible Spectroscopy. The most useful region of an infrared spectrum in the analysis of POMs is 1000–400 cm^{-1} where absorption due to metal-oxygen stretching occurs.[1] Metal-to-metal or oxygen-to-metal charge transfers and the occurrence of ligand field splitting for POMs that contain heteroatoms with partially filled d- or f-shells can result in absorption of light in the visible range by POMs, meaning UV-Visible Spectroscopy can also be a suitable tool to use for analysis.[1]

2.3 Electrochemical Methods

2.3.1 Introduction

Within the field of electrochemistry is the study of reactions occurring at the interface between two phases: an electrode and an electrolyte. When an electrochemical reduction or oxidation occurs at this electrode/solution interface, the heterogeneous transfer of electrons from or to the electrode brings about a change in the chemical species in solution. A key area of study in electrochemistry is the use of equilibrium electrode potentials of species of interest, in which the electron transfer occurring at the electrode/solution interface is at equilibrium, to calculate thermodynamic parameters. This is in contrast to kinetic electrochemical experiments where currents are induced to flow at electrodes driven away from their equilibrium potential value. These experiments are discussed in more detail in Sections 2.3.6, 2.3.8 and 2.3.9.

2.3.2 The Nernst Equation

The source of an equilibrium electrode potential is the equilibrium attained at an electrode by the species in the electrolyte that can accept charge. For a solution containing species A and B and the electrode as the source of electrons, an equilibrium is set up (Equation 2.5) where ν_A and ν_B are stoichiometric coefficients.

$$\nu_A A^{n+} + e^- \rightleftharpoons \nu_B B^{(n-1)+} \qquad 2.5$$

Once the equilibrium is established there is a net electrical charge on each phase, the sign and magnitude of which depends on the position of equilibrium.[79] If the position of equilibrium lies to the left, then a net negative charge exists on the electrode and a net positive charge exists in the solution. If the position of equilibrium lies to the right, the electrode will be positively charged compared to the solution. Thus, both the electrode, e.g, a metal wire, and the solution bear an electrical potential, termed ϕ_M and ϕ_S, and a potential difference at the electrode/solution interface exists.[79]

The potential difference has a dependence on the ratio of the concentration of A and B in solution, a relation which was formulated into an equation by Nernst. This expression which is central to electrochemistry, the Nernst equation, allows for the calculation of a potential difference at an electrode/solution interface using the ratio of the concentration of the species involved in the acquisition of equilibrium (termed A and B in this discussion). A derivation of the Nernst equation is found in the following reference.[79] This derivation leads to the Nernst equation for the potential difference at a single electrode/solution interface:

$$\phi_M - \phi_S = \Delta\phi^0 - \frac{RT}{F} ln \frac{[B]}{[A]} \qquad 2.6$$

In Equation 2.6, $\Delta\phi^0$ is a constant containing two standard chemical potential values and the chemical potential of the electron in the electrode:

$$\Delta\phi^0 = \frac{1}{F}(\mu_A^0 + \mu_{e^-} - \mu_B^0) \qquad 2.7$$

It is not possible to measure an absolute value for the potential drop ($\phi_M - \phi_S$ or $\Delta\phi_{M/S}$) across a single electrode/solution interface, or half-cell. A second half-cell is required to complete the circuit and form a complete electrochemical cell. For this purpose, the universal standard reference electrode is the Standard Hydrogen Electrode (SHE) (described later in Section 2.3.7). This provides a fixed interfacial potential difference to which the potential of the other half-cell can be reported relative to. If the voltage of such an electrochemical cell was measured, then this would be reported as the difference between $\Delta\phi_{M/S}$ of the electrode/solution interface of interest and $\Delta\phi_{M/S}$ of the SHE, the latter being a constant value that is 0 by convention. The measured potential difference or equilibrium electrode potential, E_{eq}, is thus:[80]

$$E_{eq} = \Delta\phi_{M/S}\,(A^{n+}/B^{(n-1)+}) - \Delta\phi_{\,SHE} = \Delta\phi_{M/S}(A^{n+}/B^{(n-1)+}) - 0 \qquad 2.8$$

The Nernst equation can be written in an alternative form, shown in Equation 2.9, using ionic activities instead of concentrations.[81] E_{eq} values that are calculated using the Nernst equation are reported relative to the SHE.

$$E_{eq} = E^0 + \frac{RT}{nF} ln \frac{a_A}{a_B} \qquad 2.9$$

The Nernst equation illustrates that the potential difference of an electrode/solution interface at equilibrium is a result of the standard electrode potential, E^0, and the concentrations of the species involved in the equilibrium (A and B). A system is said to be Nernstian (thermodynamically or electrochemically reversible[81]) if the potential established at equilibrium follows the potential that is predicted by the Nernst equation.

2.3.3 Standard Electrode Potentials and Formal Potentials

E^0 is the potential difference measured between the electrode of interest and the SHE when all the chemical species involved in the equilibrium at each electrode have an activity (or pressure for gases) of unity.[79] The activity, a, of an ion is shown in Equation 2.10, where γ_i is the activity coefficient and $[i]$ is the concentration of the ion.

$$a_i = \gamma_i [i] \qquad 2.10$$

As activity coefficients are usually unknown, their use can be avoided by using the formal potential, $E^{0'}$. $E^{0'}$ is the measured potential of a half-cell when the ratio of [A] to [B] is unity and any other species present are at designated concentrations. The relation between $E^{0'}$ and E^0 is shown in Equations 2.11, 2.12 and 2.13.[81]

$$E_{eq} = E^0 + \frac{RT}{nF} ln \frac{\gamma_A [A]}{\gamma_B [B]} \qquad 2.11$$

$$E_{eq} = E^{0\prime} + \frac{RT}{nF} ln \frac{[A]}{[B]} \qquad 2.12$$

$$E^{0\prime} = E^0 + \frac{RT}{nF} ln \frac{\gamma_A}{\gamma_B} \qquad 2.13$$

Values of E^0 are determined by measuring $E^{0'}$ at different ionic strengths and extrapolating to where the activity coefficients are equal to unity at zero ionic strength.[81] E^0 values are all reported relative to the SHE and are tabulated for a multitude of half-cell reactions. These values can be used to predict the potential of an electrochemical cell, such as the Daniell Cell.[82] In this cell, the negative half-cell (anode) and positive half-cell (cathode) reactions are as follows:

$$\text{Anode: } Zn^{2+}\,(aq) + e^- \rightarrow Zn(s) \qquad 2.14$$

(E^0 = -0.76 V vs SHE)

$$\text{Cathode: } Cu^{2+}(aq) + e^- \rightarrow Cu(s) \qquad 2.15$$

(E^0 = +0.34 V vs SHE)

The cell is shown in cell notation below, in which the anode is on the left and the cathode is on the right. The two bars separating the anode and cathode represent a salt bridge which allows the conduction of ions between half-cells in order to complete the circuit.

$$Zn|Zn^{2+}(aq)(a = 1)||Cu^{2+}(aq)(a = 1)|Cu$$

Using E^0 for each reaction, the potential of a cell that consists of these two half-cells can be predicted using:

$$E^0_{cell} = E^0_{right} - E^0_{left} \qquad 2.16$$

This leads to E^0 = 1.1 V for the overall cell reaction, which is:

$$Zn(s) + Cu^{2+}(aq) \rightarrow Cu(s) + Zn^{2+}(aq) \qquad 2.17$$

2.3.4 Further Application of the Nernst Equation

The Nernst equation has been described for a cell where there is a single half-cell of interest, allowing the calculation of E_{eq} using E^0 and the ratio of the activities of the reactants and products. It can also be used to predict the cell potential of two half-cells of interest where the species involved are at another known activity rather than their activities at E^0. The Nernst equation for the Daniell cell under these conditions is shown in Equation 2.18.[79] This contains E^0 for the cell reaction and the ratio of the activities of the species from the right side (cathode) to the activities of the species from the left side (anode) in the cell notation shown previously. Pure solids have an activity of unity so do not appear in the logarithmic term.

$$E_{cell} = E^0_{cell} + \frac{RT}{2F} ln \frac{a_{Cu^{2+}}}{a_{Zn^{2+}}} \qquad 2.18$$

It has also been shown that through using Equation 2.16, E^0 values provide a convenient way of calculating the cell potential for two half-cell reactions in which the concentrations or partial pressures are all unity. Aside from being a means of predicting the cell potential of myriad combinations of half-cells, the utility of E^0 values becomes further evident when considering the relation between E^0 and the standard Gibbs free energy, ΔG_0, shown in Equation 2.19.

$$\Delta G_0 = -nFE^0 \qquad 2.19$$

If all substances do not have an activity of unity, then Equation 2.20 applies:

$$\Delta G = -nFE \qquad 2.20$$

This implies that a positive E_{eq} value corresponds to a negative ΔG value, and therefore a spontaneous reaction. Linking the cell potential with ΔG allows for other quantities to be determined, such as equilibrium constants or reaction entropy changes. Taking measurements of the cell potential under conditions of equilibrium is therefore a route to the determination of thermodynamic data, and is the principle of studying equilibrium electrochemistry in which no sustained currents flow.[79] This is in contrast to kinetic electrochemistry, which is the subject of Section 2.3.6, where a potential is applied that is different to E_{eq}. This induces the exchange of electrons between the electrode and the species in solution and, therefore, the flow of current.

2.3.4.1 Sequential Electron Transfer

As noted in Section 2.1.6, which covered the redox activity of POMs, POMs undergo multiple electron transfers. These can be one-electron or two-electron reactions and occur in sequence. For sequential reactions, each electron transfer can be represented by the Nernst equation. For the following sequential reductions of a species, A:

$$A^{n+} + e^- \rightleftharpoons A^{(n-1)+}$$

$$A^{(n-1)+} + e^- \rightleftharpoons A^{(n-2)+}$$

the Nernst equation can be written as follows:[83]

$$E_{eq} = E_1^{0\prime} + \frac{RT}{F} ln \frac{[A^{n+}]}{[A^{(n-1)+}]} \qquad 2.21$$

$$E_{eq} = E_2^{0\prime} + \frac{RT}{F} ln \frac{[A^{(n-1)+}]}{[A^{(n-2)+}]} \qquad 2.22$$

$E_1^{0\prime}$ and $E_2^{0\prime}$ are the formal potentials of the first and second reductions, respectively.

2.3.5 The Electrical Double Layer

At the electrode/solution interface there is a separation of charge: the electrode side of the interface carries an excess of charge that is balanced by a charge of equal and opposite magnitude on the solution side. The charge on the electrode is constituted by an excess or deficiency of electrons in a thin layer on the surface (<0.1 Å).[84] In the solution, an excess of cations or anions in the vicinity of the electrode surface balances this charge. The layer of charge on the electrode surface that is equally matched by an area of opposing charge in the solution is termed the electrical double layer.

The solution layer of the electrical double layer is thought to consist of several regions: an inner layer closest to the electrode containing solvent molecules and specifically adsorbed ions which have lost their solvation shell, and an outer layer of nonspecifically adsorbed ions which is termed the diffuse layer. The thickness of the diffuse layer varies with the ionic concentration of the solution but is less than ~100 Å for concentrations greater than 10^{-2} M.[84] Ions can occupy two distinct regions in the vicinity of the electrode: the inner Helmholtz plane in the inner layer, or the closest point of approach for nonspecifically adsorbed ions that is known as the outer Helmholtz plane (Figure 2.9).[84]

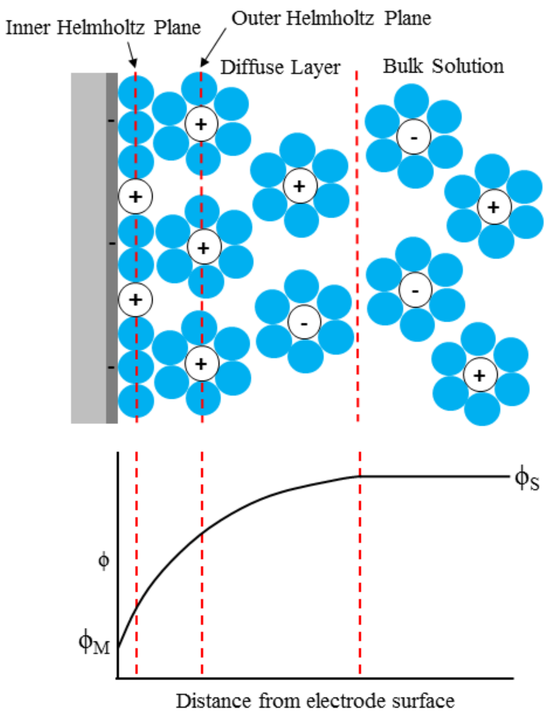

Figure 2.9 - A schematic diagram of the electrical double layer and potential profile for a negatively charged electrode.

When the potential of the electrode is changed, the electrical double layer responds in a manner that is akin to a parallel plate capacitor in which the electrode can be envisaged as one plate and the layer of opposing charge in solution is the other plate. A charging current known as non-faradaic current flows as the composition of the electrical double layer adjusts to the change in applied potential.

The behaviour of a capacitor is given by Equation 2.23, which shows that the capacitance, C, (unit of farads, F) is equal to the charge stored on the capacitor, q, divided by the voltage across the capacitor. At the electrical double layer, a non-faradaic current will flow until the characteristic value of the double-layer capacitance, C_{DL}, for a given potential is reached. The charges of the electrode and the solution are often expressed as charge densities by dividing by the area of the electrode and these values are of the order of 10^{-6} C cm^{-2}. A typical range of values for the capacitance of the electrical double layer is 10–40 µF cm^{-2}.[84]

$$C = \frac{q}{V} \qquad 2.23$$

2.3.6 Electrochemical Kinetics

Application of a potential greater than E_{eq} to an electrochemical cell will induce current flow and it is this type of experiment that is central to the following discussion. Electrochemical reactions involve heterogeneous electron transfer at an electrode/solution interface. The electron transfer occurs at a characteristic rate that depends on the chemical species involved and the reaction mechanism. Through experimentation, kinetic parameters can be determined which indicate if electron transfer is a facile or sluggish process.

A key term in this discussion is the overpotential, η, (Equation 2.24) which is the potential applied above E_{eq}.

$$\eta = E - E_{eq} \qquad 2.24$$

Using the general one-step one-electron reaction shown in Equation 2.25, it can be shown that the rate of the forward and reverse reaction is related to η.

$$A + e^- \underset{k_r}{\overset{k_f}{\rightleftharpoons}} B \qquad 2.25$$

An expression for the net current for the above reaction, i, can be derived and is shown in Equation 2.26.[85] k_f and k_r are the rate constants for the reduction of A to B and the oxidation of B to A, respectively. The concentrations of A and B are represented by the terms $[A]_{x=0}$ and $[B]_{x=0}$, where x is the distance from the surface of the electrode.

$$i = nFA(k_f[A]_{x=0} - k_r[B]_{x=0}) \qquad 2.26$$

Figure 2.10 shows the standard Gibbs free energy along the reaction coordinate at two potentials, $E^{0'}$ and E, for the reaction shown in Equation 2.25. In this scenario, E is more positive than $E^{0'}$. At $E^{0'}$ the activation energies for the forward and reverse processes are equal. More specifically, the change in Gibbs free energy on going from A or B to the transition state ($\Delta G^{\ddagger}_{0f}$ and $\Delta G^{\ddagger}_{0r}$ respectively) are equivalent. If the potential is changed from $E^{0'}$ to the new value E, then the Gibbs free energy change that occurs upon the reactants adopting the transition state changes to $\Delta G^{\ddagger}_{f}$ by a value equal to $-F(E-E^{0'})$.[82] It can also be seen that $\Delta G^{\ddagger}_{r}$ is now smaller than $\Delta G^{\ddagger}_{0r}$.

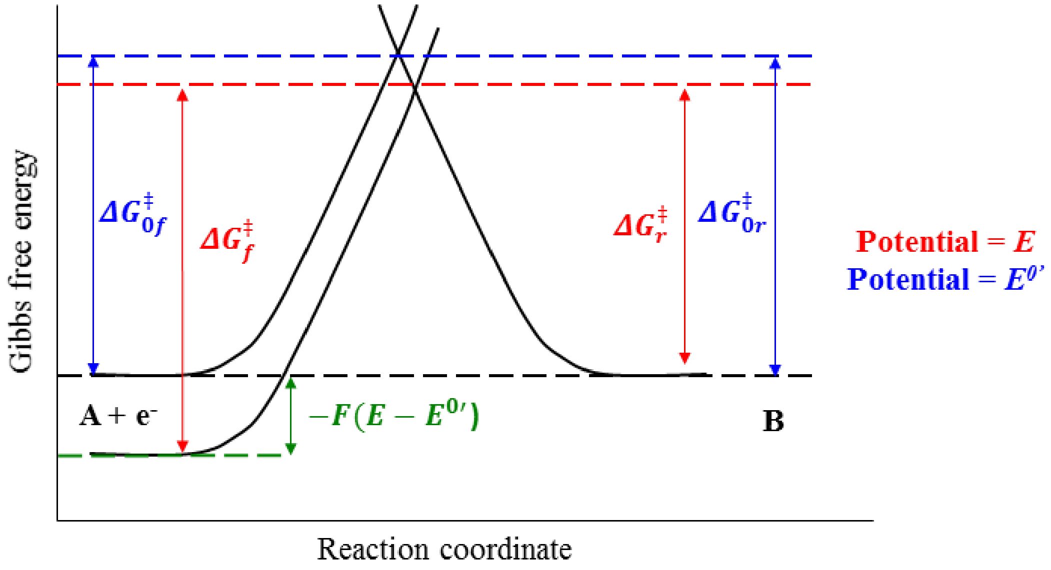

Figure 2.10 - The change in Gibbs free energy upon moving to the transition state when the reaction occurs at a potential of $E^{0'}$ *and when changed to a new potential, E. (The following reference was consulted when preparing this figure.*[85]*)*

Introducing the transfer coefficient, α, $\Delta G^{\ddagger}_{0r}$ decreases by a fraction of $F(E-E^{0'})$ equal to $(1-\alpha)F(E-E^{0'})$ (Equation 2.27). The value of $\Delta G^{\ddagger}_{f}$ increases above $\Delta G^{\ddagger}_{f0}$ by a fraction equal to $\alpha F(E-E^{0'})$, as shown in Equation 2.28.[85]

$$\Delta G^{\ddagger}_{r} = \Delta G^{\ddagger}_{0r} - (1-\alpha)F(E-E^{0\prime}) \qquad 2.27$$

$$\Delta G^{\ddagger}_{f} = \Delta G^{\ddagger}_{0f} - \alpha F(E-E^{0\prime}) \qquad 2.28$$

The value of the transfer coefficient is between 0 and 1. It lies between 0.3 and 0.7 in most systems and can be approximated to 0.5 if not deduced from measurement.[85] It depends on the shape of the intersection region of the two curves shown in Figure 2.10 and is indicative of the symmetry of the transition state.

Using transition state theory, the rate constants k_f and k_r can be defined as:

$$k_f = Aexp\left(\frac{-\Delta G^{\ddagger}_{f}}{RT}\right) \qquad 2.29$$

$$k_r = Aexp\left(\frac{-\Delta G^{\ddagger}_{r}}{RT}\right) \qquad 2.30$$

Substituting in Equations 2.27 and 2.28, leads to Equations 2.31 and 2.32.

$$k_f = Aexp\left(\frac{-\Delta G^{\ddagger}_{0f}}{RT}\right)\exp\left(\frac{-\alpha F(E-E^{0\prime})}{RT}\right) \qquad 2.31$$

$$k_r = Aexp\left(\frac{-\Delta G^{\ddagger}_{0r}}{RT}\right)\exp\left(\frac{(1-\alpha)F(E-E^{0\prime})}{RT}\right) \qquad 2.32$$

For an electrode/solution interface at equilibrium where [A] = [B] (the constitution of the solution at $E^{0'}$ by definition) so that $E = E^{0'}$, Equation 2.33 applies:

$$Aexp\left(\frac{-\Delta G_{0f}^{\ddagger}}{RT}\right) = Aexp\left(\frac{-\Delta G_{0r}^{\ddagger}}{RT}\right) \qquad 2.33$$

Or represented another way:

$$k_f = k_r \qquad 2.34$$

Instead of distinguishing between k_f and k_r which have the same value at $E^{0'}$, the standard rate constant, k^0, can be referred to. The expressions for the rate constants at other potentials can also be written in terms of k^0:

$$k_f = k^0 \exp\left(\frac{-\alpha F(E - E^{0\prime})}{RT}\right) \qquad 2.35$$

$$k_r = k^0 \exp\left(\frac{(1-\alpha) F(E - E^{0\prime})}{RT}\right) \qquad 2.36$$

Substituting Equations 2.35 and 2.36 into the equation for the net current of the reaction, Equation 2.26, yields Equation 2.37. This current-potential relationship is used extensively in the study of heterogeneous electron transfer kinetics. It is known as the Butler-Volmer treatment of electrode kinetics, being named after J. A. V. Butler and M. Volmer.[86, 87]

$$i = FAk^0\left[[A]_{x=0}\, exp\frac{-\alpha F(E - E^{0\prime})}{RT} - [B]_{x=0}\, exp\frac{(1-\alpha) F(E - E^{0\prime})}{RT}\right] \qquad 2.37$$

2.3.6.1 The Standard Rate Constant and the Exchange Current

The value of k^0 indicates whether the rate of electron transfer in a redox couple is a fast or sluggish process. A reaction with a large value of k^0 reaches equilibrium rapidly and only a slight overpotential is required to induce current flow.[85] In considering the kinetics of a reaction, the definition of a Nernstian reaction from Section 2.3.2 can be elaborated upon, from a reaction for which the potential established at equilibrium follows the potential predicted by the Nernst equation, to a reaction with kinetics that are so facile that the electrode/solution interface is always at equilibrium. Reported values of k^0 for different reactions cover several orders of magnitude, for example, 10^{-1} cm s^{-1} for the $[Fe(CN)_6]^{3-}$/$[Fe(CN)_6]^{4-}$ redox couple to 10^{-6} cm s^{-1} for the VO_2^+/VO^{2+} redox couple.[88, 89] These are considered as facile and sluggish electrochemical reactions respectively.

The magnitude of the anodic and cathodic current is equal at equilibrium, with the result that there is no net current flowing. The underlying current at equilibrium is known as the exchange current, i_0, and is given by Equation 2.38. As the reaction is at equilibrium, the bulk concentration of A and B are the same as the concentrations at the electrode surface, so $[A]_{x=0} = [A]$ and $[B]_{x=0} = [B]$.

$$i_0 = FAk^0[A]^{(1-\alpha)}[B]^{\alpha} \qquad 2.38$$

i_0 is proportional to the rate of electron transfer and is thus an indicator of whether the kinetics of a reaction are facile or sluggish. The value of i_0 is often normalised to the exchange current density, j_0, using the electrode area ($j_0 = i_0/A$). In the special case of a reaction at equilibrium where [A] = [B], the relation between i_0 and k^0 is as follows, where c now represents concentration:

$$i_0 = FAk^0c \qquad 2.39$$

2.3.6.2 Tafel Analysis

Determination of i_0, and therefore of k^0, can be achieved through a Tafel analysis. This uses the Butler-Volmer equation (Equation 2.40), which is derived from Equation 2.37. The Butler-Volmer equation gives the contribution of the cathodic and anodic reaction to the total current at any potential. In working with i_0 instead of k^0, the deviation from the equilibrium potential (the overpotential, η) instead of the deviation from $E^{0'}$ is used. The equation therefore shows how the current varies with the overpotential and the transfer coefficient. (The derivation of Equation 2.40, including the steps taken to allow replacement of $E^{0'}$ with η, has been omitted. This is available in the following reference.[85])

$$i = i_0\left[\frac{[A]_{x=0}}{[A]} exp\frac{-\alpha F\eta}{RT} - \frac{[B]_{x=0}}{[B]} exp\frac{(1-\alpha)F\eta}{RT}\right] \qquad 2.40$$

Under conditions where the concentrations of reactants at the electrode surface do not differ from their bulk solution values, such as in a well-stirred solution, Equation 2.40 simplifies to Equation 2.41:

$$i = i_0\left(exp\frac{-\alpha F\eta}{RT} - exp\frac{(1-\alpha)F\eta}{RT}\right) \qquad 2.41$$

At small overpotentials, there is a linear relationship between the net current and η (Equation 2.42).

$$i = -i_0\frac{F}{RT}\eta \qquad 2.42$$

At large overpotentials, the relationship between the current and the overpotential is exponential:

$$i = i_0e^{-\frac{\alpha\eta F}{RT}} \qquad 2.43$$

Equation 2.43 leads to the Tafel equation:

$$\eta = \frac{RT}{\alpha F}\ln{(i_0)} + \frac{RT}{\alpha F}\log{(i)} \qquad 2.44$$

By plotting log(i) against η, a Tafel plot can be constructed (Figure 2.11).

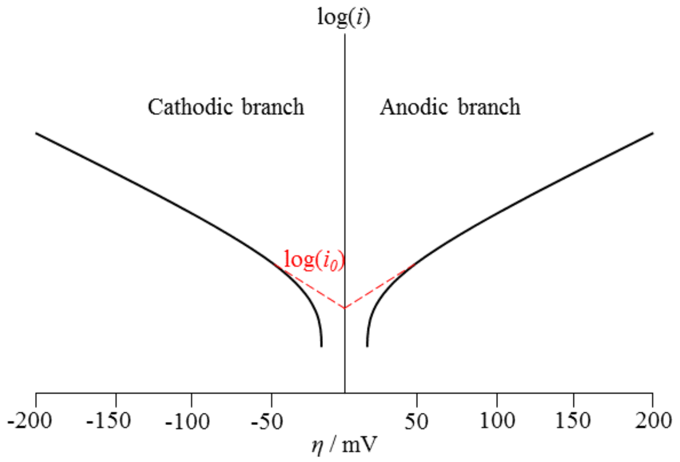

Figure 2.11 - An example of a Tafel plot.

In a Tafel analysis, overpotentials that are both positive and negative of E_{eq} are applied leading to an anodic and cathodic branch when the data in plotted in a Tafel plot. Extrapolation of the linear portion of each branch to $y = 0$ yields $\log(i_0)$ and α can be calculated from the slope.

The use of the Tafel equation is limited to conditions where the opposing current (e.g. an oxidising current in the case of a net reduction) is less than 1% of the current of the forward reaction.[90] Suggested values for the overpotential that will yield a linear region in a Tafel plot that is suitable for determining kinetic data are values greater than 50 mV but less than several hundred mV.[90] At small overpotentials, the Tafel plot deviates from linearity due to the current from the reverse reaction increasing above 1%, which is shown by curvature of the plot at less extreme overpotentials in Figure 2.11. A deviation from linearity will also be observed at large overpotentials where the current recorded is limited by mass transport. Different regions of a Tafel plot can therefore be distinguished depending on whether the current is under charge transfer control or mass transport control.[91] In the charge transfer region, the reaction is solely under charge transfer control and its response to the increasing overpotential is an exponential rise in the current, shown as a region of linearity in a Tafel plot. The recorded current is the kinetic current and can be used to determine kinetic parameters.

In the region of a Tafel plot where the reaction is under mass transport control, the current is independent of the overpotential and its magnitude is determined by the rate of transport of reactants from the bulk of the solution to the electrode surface instead. The recorded current is limited by mass transport and the slope of the line will deviate from the value predicted by the Tafel equation. The slopes of the anodic branch and cathodic branch are equal to Equation 2.45 and Equation 2.46, respectively.

$$\frac{(1-\alpha)F}{2.3\ RT} \qquad 2.45$$

$$-\frac{\alpha F}{2.3\ RT} \qquad 2.46$$

If the number of electrons exchanged is 1 and α is 0.5, the theoretical value of the slope is -8.5 V or 118 mV decade^{-1} at 298 K. This value can be a useful indicator of the number of electrons exchanged in a reaction, and whether the slope is truly a 'Tafel slope' that can be used to deduce i_0.

Sluggish reactions often show good Tafel behaviour because current flow is small unless large overpotentials are applied, in which case the current is, in effect, unidirectional.[85] Reactions with facile kinetics pose more of a challenge in capturing a truly kinetic current in a Tafel analysis as mass transport can become an influence at relatively small overpotentials.

2.3.6.3 Techniques

There are a range of techniques used to study electrochemical kinetics. Principally, these are potential step (potentiostatic) or current step (galvanostatic) techniques. In a potentiostatic technique, the potential of a system is stepped from 0 to a constant value and the resultant current transient recorded. In a galvanostatic technique, the current is instead stepped from 0 to a constant value and the potential profile is recorded. Collection of the current or potential response of a system to these perturbations over a range of values and use of the Butler-Volmer treatment of electrochemical kinetics is a route to the determination of i_0 and k^0. Other techniques that can yield values for kinetic parameters, such as Electrochemical Impedance Spectroscopy (Section 2.3.10), apply a periodic perturbation of potential or current to the system and analyse the characteristic response of the system to variation in the frequency of the perturbation.

2.3.7 Electrochemical Cells

Two classifications of electrochemical cell exist: galvanic cells and electrolytic cells. In a galvanic cell, electrical current flow occurs due to the spontaneous reaction that takes place. The Daniell cell that was discussed in Section 2.3.3 is an example of a galvanic cell. In an electrolytic cell, a non-spontaneous reaction is induced through the application of a potential that is greater than the open circuit potential (OCP) of the cell, that is, the potential difference measured for the cell when no current is flowing.

By driving a non-spontaneous reaction to occur in an electrolytic cell, insight can be gained into its current/potential relationship. Typically, only a reaction at a single electrode/solution interface is of interest and so the second electrode in an electrolytic electrochemical cell can be standardised to allow the process at the other electrode to be studied. Thus, two different types of electrode can be distinguished:

- A working electrode where the reaction of interest occurs.
- A reference electrode with a fixed potential to which the potential of the working electrode is reported relative to.

With the potential of the working electrode at E_{eq} relative to the reference electrode, a positive or negative overpotential needs to be applied to induce an oxidising or reducing current and observe how the current changes as a function of the potential. However, the potential applied to the working electrode contains an additional term, the ohmic drop or iR_S, which is equal to the product of the current, i, and the solution resistance, R_s. R_s is characteristic of the supporting electrolyte and the iR_s term is the portion of the applied potential that is required to induce the flow of current as ions in the supporting electrolyte as electrons flow through the external circuit. The potential applied to the cell relative to the reference electrode, E_{appl}, is a sum of E_{eq}, η and iR_S, as shown in Equation 2.47.[84]

$$E_{appl} = E_{eq} + \eta + IR_S \qquad 2.47$$

Under conditions where iR_s is small (e.g. <1 mV[84]) and the passage of current does not affect the potential of the reference electrode, a two-electrode cell with a working electrode and reference electrode can be a suitable experimental set-up for electrochemical studies. However, under high-current conditions in large-scale experiments where iR_s is substantial, or where the potential of the reference electrode is likely to change, a three-electrode cell is necessary. In this instance, a third electrode termed the counter electrode is introduced so that the current flow is between the working and counter electrode while the potential of the working electrode is measured relative to the reference electrode. Close positioning of the working electrode and reference electrode ensures that iR_S is minimised. This experimental set-up is termed a three-electrode cell (Figure 2.12) and is a common arrangement for electrochemical studies.

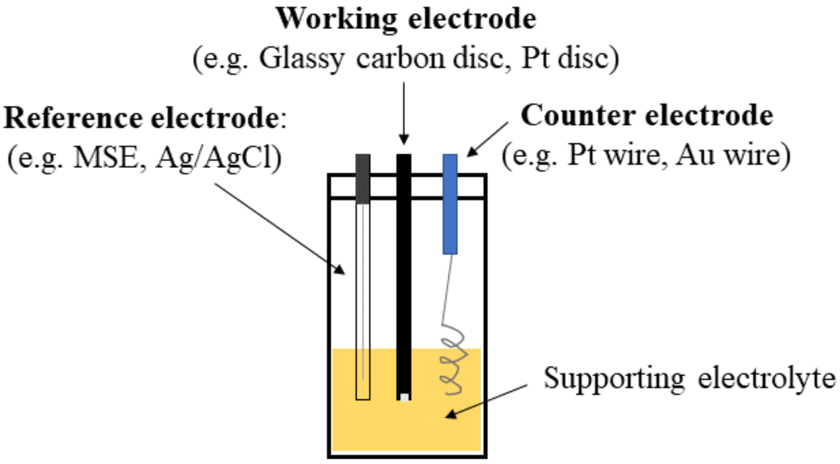

Figure 2.12 - A schematic of a three-electrode cell, used to study a redox-active species of interest that is dissolved in a supporting electrolyte.

Commercial working electrodes come with a defined surface area which allows conversion of the current to current density *(i/A)*. A common material is glassy carbon which can be polished prior to analysis to yield a uniform surface that will be the site of the electrochemical reaction under study. A criterion for choosing a counter electrode is that no substances are produced under current flow that can impede the process at the working electrode.[84] The reference electrode introduced previously in Section 2.3.2 was the SHE. This consists of an electrode of platinised platinum over which H_2 gas is bubbled, which is in contact with an aqueous solution of HCl with a proton activity of 1. The equilibrium that is the source of the stable potential of the SHE is shown in Equation 2.48.

$$H^+ \,(aq) + \, e^- \, \rightleftharpoons \, \tfrac{1}{2}H_2 \,(g) \tag{2.48}$$

It is, however, difficult to use the SHE experimentally and other reference electrodes are available, the potential of which is a known value reported relative to the SHE. Common examples are the mercury/mercurous sulfate electrode (MSE) and silver/silver chloride electrode (Ag/AgCl). The potential-determining equilibria for these reference electrodes are as follows:

$$Hg_2SO_4 + \, 2e^- \rightleftharpoons 2Hg + \, SO_4^{2-} \tag{2.49}$$

$$AgCl + \, e^- \rightleftharpoons \, Ag + Cl^- \tag{2.50}$$

Small variations in the potential of a reference electrode are seen with different filling solutions. Examples of potentials for the MSE and Ag/AgCl electrode are 0.674 V vs SHE for the MSE with 1 M H_2SO_4 as filling solution and 0.209 V vs SHE for a Ag/AgCl electrode with a filling solution of 3 M NaCl.[92] Reference electrode potentials are sometimes quoted as relative to the Normal Hydrogen Electrode (NHE). The terms NHE and SHE can be used with equivalence.[84] All potentials in this work are reported relative to the SHE.

2.3.8 Cyclic Voltammetry

A commonly employed electrochemical technique is cyclic voltammetry. In this technique, the potential is cycled between two values continuously. This generates a cyclic voltammogram (CV) in which the current that is recorded is plotted against the applied potential. In a typical CV showing a reversible reduction of a species (Figure 2.13), the potential is swept from its initial value to a more negative potential (a cathodic scan). During this sweep, the potential becomes negative enough to reduce the sample and a current is recorded, reaching a maximum at the peak current, i_{pc}, at a cathodic peak potential of E_{pc}. After this maximum is reached, the reducible species are depleted at the electrode surface and the magnitude of the current is dependent on the delivery of reactants to the electrode by diffusion. Upon reversal of the direction of the scan (an anodic scan), when the potential becomes sufficiently positive to oxidise the sample, a current is recorded which reaches a peak current, i_{pa}, at an anodic peak potential of E_{pa} before becoming diffusion limited.

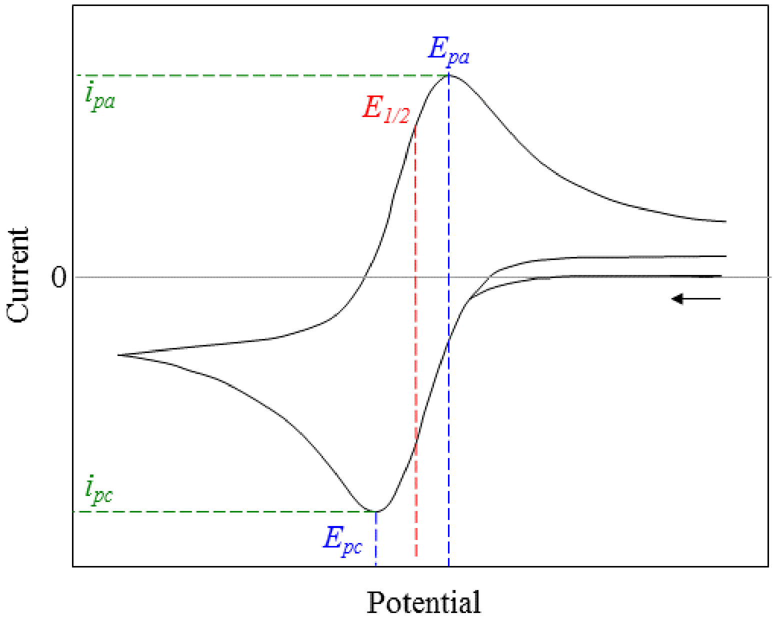

Figure 2.13 - A schematic of a cyclic voltammogram for a reversible one-electron reduction when the potential is scanned in the negative direction and then returned to the initial value.

The ratio of the peak current, i_{pa}/i_{pc}, and the separation of the peak potentials, $E_{pa} - E_{pc}$ (ΔE_p), are two parameters of interest that can be obtained from a CV.[93] For a Nernstian reaction:

$$\frac{i_{pa}}{i_{pc}} = 1 \qquad 2.51$$

$$\Delta E_p = \frac{2.3\,RT}{nF}(59/\text{n mV at }25°\text{C}) \qquad 2.52$$

A deviation of i_{pa}/i_{pc} from 1 indicates "homogenous kinetic or other complications in the electrode process".[93] For an irreversible reaction with sluggish electron transfer kinetics, the value of ΔE_p shifts from the Nernstian value as more negative or more positive potentials must be applied in order to observe a redox reaction.[94] In the context of cyclic voltammetry, the terms reversible and irreversible refer to "limiting cases according to whether the electrode kinetics are fast or slow relative to the mass transport conditions of the electrode of interest".[80] A reversible cyclic voltammogram indicates that the current is limited by mass transport (diffusion) only. When the rate of mass transport is great relative to the rate of electron transfer, ΔE_p increases and the reverse peak becomes less pronounced, tending to a complete disappearance in the limiting case of a very slow electron transfer rate, so that only the peak resulting from the forward scan is visible.[95]

The rate of the potential sweep is variable and altering the scan rate, v, can reveal characteristics of the electrochemical reaction under study. For a reversible wave, E_p values are independent of scan rate and i_p is proportional to the square root of the scan rate, $v^{1/2}$. The dependence of the peak current on the scan rate is described by the Randles-Sevcik equation:[93]

$$i_p = (2.69 \times 10^5) n^{3/2} A D_O^{1/2} c_O^* v^{1/2} \tag{2.53}$$

Equation 2.53 applies at 25°C, where A is the geometric surface area of the electrode, D_O is the diffusion coefficient of the oxidised species and c_O^* is the bulk concentration of the oxidised species. For an irreversible process, the size of the peak on the reverse scan compared to the forward scan depends on the scan rate, decreasing at higher scan rates.

A linear plot of i_p versus $v^{1/2}$ is obtained for electron transfer processes of freely diffusing redox species that are electrochemically reversible.[94] If species are adsorbed on the electrode, the current response should instead vary linearly with scan rate. Equation 2.54 shows that for an adsorbed species, the peak current increases with the scan rate (where Γ is the maximum coverage for the species in oxidised form).[95]

$$i_p = \frac{n^2 F^2}{4RT} v A \Gamma \tag{2.54}$$

The deviation from linearity of i_p vs $v^{1/2}$ for species that are thought to be freely diffusing suggests a quasi-reversible process or electron transfer that is occurring through species adsorbed on the electrode surface.[94]

Cyclic voltammetry can also be used to locate $E_{1/2}$, which corresponds to the potential at the half-way point between the anodic and cathodic peak where the concentrations of oxidised and reduced species are equal (as shown in Figure 2.13). It is determined by calculating the average of E_{pa} and E_{pc} and can be used to estimate $E^{0'}$ (Equation 2.55).

$$E_{1/2} = \frac{(E_{pa} + E_{pc})}{2} \qquad 2.55$$

In the context of POM characterisation, cyclic voltammetry can be used for “fingerprinting purposes”, as a large number of POMs undergo a series of characteristic reversible reductions involving one or two electrons.[1]

2.3.9 Bulk Electrolysis

Methods such as cyclic voltammetry probe electrochemical reactions by using an electrode of small surface area compared to the solution volume. Changes to the bulk solution are therefore slight. In some circumstances, a substantial change to the bulk solution is sought and a bulk electrolysis method is required. A working electrode that is large relative to the solution volume is used in bulk electrolysis, through which currents flow that are substantially higher than those in voltammetry methods. This leads to a complete change in the composition of the bulk solution as the species of interest is reduced or oxidised to another oxidation state. The counter electrode should also have a large surface area as the same current flows at the counter electrode as at the working electrode.

In the bulk electrolysis method employed, either the current (chronoamperometry) or the potential (chronopotentiometry) is controlled. In chronoamperometry, a constant current is applied to the cell and the potential is recorded. The potential shifts during the course of the experiment as the ratio of oxidised to reduced species changes. In chronopotentiometry, a constant potential is applied and the current is recorded, which decreases with time as the amount of oxidised material in the solution is depleted.

In such experiments, diffusion alone is not sufficient to supply a continuous supply of fresh reactant to the electrode and mass transport must be enhanced through forced convection. Thus, the reaction is continuously stirred in a typical electrolysis experiment. Substantial currents also flow at the counter electrode which is often placed in a different compartment and separated from the main cell by a separator such as a sintered glass frit. A schematic of a cell used for bulk electrolysis is shown in Figure 2.14, which is based on the cell used in this work that was purchased commercially. By monitoring the number of coulombs passed to the sample during a bulk electrolysis technique, the extent of the reduction or oxidation of the sample can be determined.

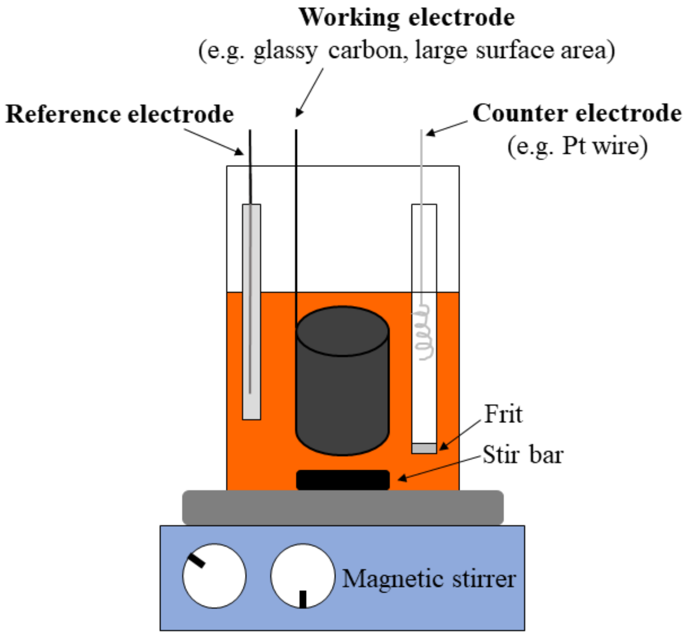

Figure 2.14 - A schematic of a bulk electrolysis cell used in this work. The working electrode is a glassy carbon cylinder with a high surface area.

2.3.10 Electrochemical Impedance Spectroscopy

The frequency-dependent resistance to current flow of an element in a circuit is termed its impedance, *Z*, and is defined as:[95]

$$Z_{cell} = \frac{E_{cell}}{I_{cell}} \qquad 2.56$$

E_{cell} is the voltage across the cell and I_{cell} is the current. *Z* has units of Ohms (Ω).

In a circuit with a DC voltage applied, the resistance is technically the impedance with zero phase angle,[96] that is to say, the current response is in phase with the applied voltage. However, in AC circuits with capacitive and/or inductive effects, voltage and current are no longer in phase with each other and the opposition to electrical current displayed by elements of the circuit, now termed the impedance, depends on frequency.

In a common EIS experiment, a fixed sinusoidal voltage is applied to a three-electrode cell normally containing a solution of electrolyte and the species under investigation.[96] The response of the electrode to the potential perturbation is a current that is also sinusoidal but different in phase to the applied signal. A range of perturbation frequencies are applied and the electrical response recorded. Summarised, an EIS experiment consists of four steps.[95]

1. Application of a small amplitude sinusoidal potential perturbation.
2. Acquisition of the electrical response over a range of frequencies of perturbation.
3. Deduction of an equivalent circuit.
4. Relation of “key physical or chemical characteristics of the electrochemical system”[95] to the equivalent circuit components.

An important step in the experiment is the construction of the equivalent circuit. In the simplest case, impedance arises from the solution resistance (R_S), charging of the electrical double layer at the electrode (C_{DL}), the charge transfer resistance (R_{CT}) and the Warburg impedance (Z_W).[96] This combination of circuit elements is known as a Randles circuit (Figure 2.15).

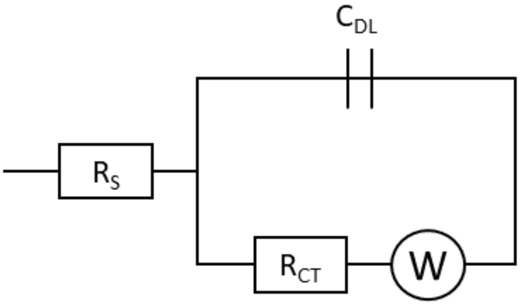

Figure 2.15 - A Randles circuit.

The solution conductivity and the geometry of the cell determine R_S. The nature of the electrode and its area and the electrolyte ionic strength and permittivity are reflected in C_{DL}.[95] R_{CT} represents the kinetics of electron transfer and the Warburg impedance represents the rate of diffusion of reactants to and from the electrode.

In order to deduce true values for the impedance, manipulation of complex numbers is required.[96] The overall impedance of a cell is given by Equation 2.57, where $j = \sqrt{-1}$.[95]

$$Z_{cell} = Z_{Re} + jZ_{Im} \qquad 2.57$$

The data obtained can be presented in different ways. In a Nyquist plot, $-Z_{im}$ is plotted against Z_{Re}. In a Bode plot, the logarithm of the impedance ($\log(|Z|)$) and the phase angle are plotted against frequency. These plots can be considered complementary as frequency values are not evident in a Nyquist plot whereas Bode plots do show frequency information.

For a Randles circuit, the Nyquist plot shows a semicircle. At high frequencies, the impedance of C_{DL} is low, short-circuiting the ‘charge transfer branch[97]’ that contains R_{CT} and Z_W in series, and the impedance is determined by R_S. At low frequencies, the impedance of C_{DL} is large and the current flows through the charge transfer branch. The Warburg impedance presents as a straight line with a slope of 45° in the low frequency region of a Nyquist plot, reflecting the concentration changes due to the greater allowance for diffusion of the reactants away from the electrode surface at low frequencies. In a Nyquist plot, R_S can be extracted from the high frequency intercept on the ‘real’ axis and R_{CT} from the diameter of the semicircle. C_{DL} can be estimated from the frequency (ω) at the maximum of the circle (Figure 2.16a).

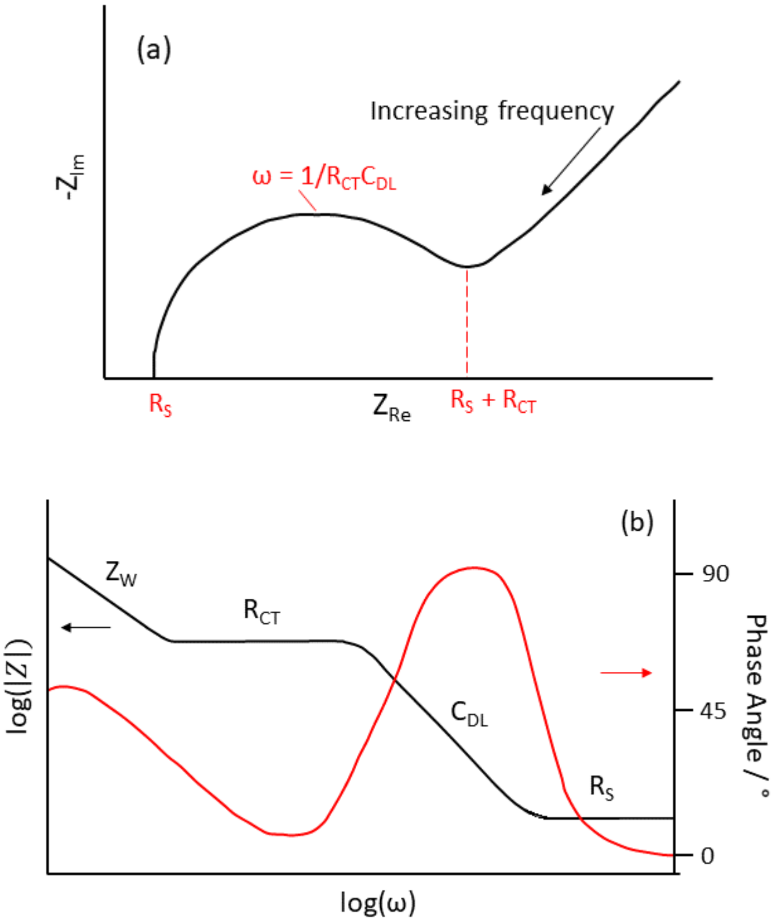

Figure 2.16 - A schematic of a Nyquist plot (a) and a Bode plot (b) that correspond to the equivalent circuit shown in Figure 2.15. (In order to draw the Bode plot, the following reference was consulted.[98])

In the Bode plot for a Randles circuit (Figure 2.16b), a horizontal line is observed in the plot of log($|Z|$) versus log(ω) where resistance behaviour dominates and the phase angle is close to 0°.[98] Capacitive behaviour is also shown by a straight line in the log($|Z|$) versus log(ω) plot that has a slope of -1, with a phase angle of 90°, and the Warburg impedance exhibits as a straight line with a slope of $-\frac{1}{2}$ and a phase angle of 45°.[98]

Under circumstances where the capacitance for an electrode/electrolyte interface shows a dependency on the frequency, termed ‘frequency dispersion of capacitance’, a constant phase element (CPE) is used instead of C_{DL}. The CPE is “a specific circuit element that successfully describes the non-trivial frequency dependence of the interfacial capacitance”.[99] The origins of the frequency dispersion of capacitance that have been discussed in literature include surface roughness and heterogeneities and electrode porosity, among other proposed factors.[100] The CPE is expressed as:[101]

$$Z_{CPE} = \frac{1}{(j\omega)^{\alpha}Q} \qquad 2.58$$

In this equation, j is the imaginary unit, ω is the angular frequency and Q and α are frequency-independent constants. If $\alpha = 1$, the CPE simplifies to a capacitance,[102] i.e. the CPE behaves like a capacitor.

2.3.11 Mass Transport

The rate of a reaction may be controlled by how fast reactant is transported to or from the electrode surface by mass transport. Mass transport can be divided into three transport processes:

- Diffusion
- Migration
- Convection

Diffusion is the movement of a species due to a concentration gradient and is discussed in Section 2.3.11.2. Migration is the movement of a charged species in an electric field and is discussed in 2.3.11.3. Convection can refer to natural convection or forced convection.

2.3.11.1 Convection

Natural convection arises from thermal gradients and differences in density within a solution. Forced convection can be achieved by stirring or bubbling a gas through a solution. The flow field, the electrolyte flow rate, and the electrodes of an RFB can be selected so as to enhance convective mass transport.[103] For instance, flow fields that promote convection through porous electrodes can be selected such as interdigitated flow fields (discussed in Section 2.3.13) in which channels are alternately blocked at the inlet and outlet of the flow field to encourage perpendicular flow of electrolyte into the adjacent electrode.[104] Houser *et al*. studied mass transport by convection in RFBs and found that interdigitated flow fields performed better than serpentine flow fields at lower flow rates for cells discharged to a point where mass transport polarisation dominated, as a greater proportion of the theoretical capacity was accessed when using interdigitated flow fields.[105] This was attributed to superior transport of reactant within the electrodes due to improved convection, although the improvement vanished at higher flow rates, with a similar proportion of the theoretical capacity accessed in a cell that used a serpentine flow field. Increasing the flow rate enhances the mass transport of active species in the pores of a porous electrode by increasing the electrolyte velocity but has an associated energy penalty due to the requirement for higher pumping power.[106]

2.3.11.2 Diffusion

For a solution with a high concentration of solute in one region, the rate of diffusion of the molecules of solute is proportional to the concentration gradient in the solution. Fick’s first law of diffusion states this, showing that the flux of a species *B* (e.g. an ion diffusing linearly to an electrode surface) at a given point (*x*) and time (*t*) is proportional to its concentration gradient (∂[B]/∂x):[107]

$$-J(x,t) = D_B \frac{\partial [B](x,t)}{\partial x} \tag{2.59}$$

The flux, *J*, has units of mol s^{-1} cm^{-2} and represents the number of moles of a species that diffuses through a unit area in one second.[80]

Fick's second law describes the change in concentration of a species at a given point with time:

$$\frac{\partial [B](x,t)}{\partial t} = D_B \left(\frac{\partial^2 [B](x,t)}{\partial x^2} \right) \tag{2.60}$$

D_B is the diffusion coefficient of the species *B* and has the units of cm^2 s^{-1}. The value of the diffusion coefficient is specific to a species and the magnitude of *D* indicates how rapidly a species diffuses. The diffusion coefficient can be determined by using the Randles-Sevcik equation (Equation 2.53, previously discussed in Section 2.3.8 on cyclic voltammetry):

$$i_p = (2.69 \times 10^5) n^{3/2} A D_O^{1/2} c_O^* v^{1/2} \tag{2.53}$$

The Stokes-Einstein equation shows that the diffusion coefficient is related to the viscosity of a solution and the hydrodynamic radius of an ion which is the combined radius of an ion and the layer of water molecules associated with it. k_B is Boltzmann's constant, *T* is the temperature, η is the dynamic viscosity and *r* is the hydrodynamic radius:

$$D = \frac{k_B T}{6\pi\eta r} \tag{2.61}$$

Example values of diffusion coefficients are 5.22 ×10^{-6} cm^2 s^{-1} for sucrose in water, 1.24 × 10^{-5} cm^2 s^{-1} for ethanol in water and 2.26 × 10^{-5} cm^2 s^{-1} for H_2O itself in water.[108] Diffusion coefficients for Keggin structures are of the order of 10^{-6} cm^2 s^{-1}, such as $D = 3.9 \times 10^{-6}$ cm^2 s^{-1} for $[SiW_{12}O_{40}]^{4-}$.[109] In an RFB, the rate of delivery of reactant to the electrode surface is related to the diffusion coefficients of the active species, among other factors.

2.3.11.3 Migration

The potential drop across an electrode/solution interface ($\Delta\varphi_{M/S}$) (see Section 2.3.2) results in an external electric field that exerts an electrostatic force on charged species, inducing the movement of ions to or from the electrode.[80] This mass transport process is known as migration.

The use of a background electrolyte of high concentration relative to the concentration of ionic active species can mean that mass transport due to the migration of active species can be neglected. Charge transfer reactions at the electrode surface will result in a change in the concentration of ions in the vicinity of the electrode and a change in the electrical potential of the solution, altering the electric field that is acting on the ions and their resulting migration.[80] However, the high concentration of cations and anions from the background electrolyte ensures that electroneutrality of the bulk solution is maintained despite the ongoing charge transfer reaction, and that gradients in potential are limited to the small region that comprises the electrical double layer.[80] The background electrolyte also ensures a constant ionic strength of the solution (ionic strength is discussed in the next section), meaning that activity coefficients of the active species remain constant.[80]

2.3.12 Debye-Hückel Theory

As noted in Section 2.3.3, the activity, a, of an ion, i, is equal to the activity coefficient γ_i multiplied by the concentration of the ion.

$$a_i = \gamma_i[i] \qquad 2.10$$

In an ideal solution, γ_i is unity and there is an absence of coulombic interactions between ions in solution. Interactions between ions in electrolyte solutions result in a deviation from ideality and the activity coefficient is less than 1. Activity coefficients are usually unknown but can be calculated for dilute electrolyte solutions using Debye-Hückel theory:

$$\log_{10}\gamma_i = -Az_i^{2}\sqrt{I} \qquad 2.62$$

In equation 2.62, z_i is the charge on the ion and A is a temperature and solvent dependent parameter which is 0.5 in water at 25°C.[79] I is the ionic strength of the solution (Equation 2.63) which is obtained by summing the product of the concentration and the squared charge, z, of all the ions in a solution and dividing by two:

$$I = \frac{1}{2}\sum_i [i]z_i^{2} \qquad 2.63$$

Debye-Hückel theory supposes that a cation or anion in solution is surrounded by an ionic atmosphere of opposite charge, with a net charge that is equal in magnitude to the charge on the ion. The size of the ionic atmosphere is given by the Debye length which is the distance between a cation or anion and the average location of the charge in the ionic atmosphere and decreases with increasing ionic strength.[79]

Debye-Hückel theory assumes that ionic interactions are described by Coulombs law for point charges and that the electrolyte is fully dissociated with no significant formation of ion pairs (where a cation and anion occur in solution as a single entity).[79] It is a limiting law that is reliable in dilute solutions, below around 10^{-2} M.[79] At higher concentrations, the extended Debye-Hückel law can be applied instead (Equation 2.64) where B is a constant that is specific to the solvent and temperature and a is the radius of the ion i.[79]

$$\log_{10}\gamma_i = \frac{-Az_i^2\sqrt{I}}{1 + Ba\sqrt{I}} \tag{2.64}$$

As concentration is increased further, deviation from the extended Debye-Hückel law is observed due to the interactions of water molecules with ions.[79] In an aqueous electrolyte, the ions are hydrated, that is, they are surrounded by water molecules which form a hydration shell. The effect of ion-solvent interactions is captured by the Robinson and Stokes equation:

$$\log_{10}\gamma_{\pm} = \left(\frac{-A(z_+z_-)\sqrt{I}}{1 + Ba\sqrt{I}}\right) + CI \tag{2.65}$$

The new second term accounts for the ion-solvent interactions, with *C* being a solute and solvent specific parameter.[79] γ_i has been replaced by $\gamma_{\pm}$ which is the mean activity coefficient (Equation 2.66) where γ_+ and γ_- are the activity coefficients of the cation and anion that make up an electrolyte of general formula MX.[79]

$$\gamma_{\pm} = (\gamma_+\gamma_-)^{1/2} \tag{2.66}$$

The size of the hydration shell affects an ion's migration in solution, as will now be discussed. An ion with a charge *z* in a voltage gradient will be induced to move. However, the motion of the ion will be impeded as it must move past solvent molecules and it thus experiences drag forces acting in the opposite direction.[79] The ion reaches a limiting speed which is determined by the magnitude of the voltage gradient and the mobility of the ion, *u*, the latter of which is given by Equation 2.67:[108]

$$u = \frac{e|z|}{6\pi\eta a} \tag{2.67}$$

e is the charge of an electron, *a* is the radius of the ion, and η is the viscosity of the solution. The greater the viscosity of the solution, the greater the impeding force that an ion moving along a voltage gradient experiences. How well an ion conducts electricity depends on its mobility which is proportional to the molar conductivity, Λ, of an ion (Equation 2.68):[79]

$$\Lambda \propto \frac{e|z|}{6\pi\eta a} \tag{2.68}$$

Equation 2.67 shows that the mobility of an ion, and thus its molar conductivity, depends on its charge, its size, and the viscosity of a solution. Small, highly charged ions (and ions in a solution of low viscosity) should have the greatest mobility. Thus, the conductivity of the group 1 metals would expectedly decrease in the order $Li^+ > Na^+ > K^+$ based on their radii. However, the ionic conductivities of Li^+, Na^+ and K^+ at 25°C are 39 S cm^2 mol^{-1}, 50 S cm^2 mol^{-1} and 74 S cm^2 mol^{-1} respectively based on their molar conductivity at such low concentrations that interactions between ions can be ignored (the limiting molar conductivity).[79] The hydration shell of an ion must move with it and Li^+ ions are the most extensively hydrated while K^+ ions are the least extensively hydrated of the three metal ions. The size of the hydration shell is related to the charge density of an ion which explains why the smaller Li^+ ion has a larger hydration shell than Na^+ and K^+, and a lower ionic conductivity. Li^+ has a crystallographic radius of 0.60 Å and a hydrated radius of 2.4 Å, Na^+ has a crystallographic radius of 0.95 Å and hydrated radius of 1.8 Å and K^+ has a crystallographic radius of 1.33 Å and a hydrated radius of 1.3 Å.[79]

It was found that the Keggin POMs $[SiMo_{12}O_{40}]^{4-}$ and $[SiW_{12}O_{40}]^{4-}$ both had hydrodynamic radii of 5.6 Å when this was calculated from diffusion coefficients.[110] These values were comparable to the crystallographic radii, suggesting minimal solvation of the anions. The same result was obtained in later work, when the hydrodynamic radii of the Keggin structure $[PW_{12}O_{40}]^{3-}$, along with $[SiW_{12}O_{40}]^{4-}$, were also calculated to be 5.6 Å from diffusion coefficients.[111] Horky *et al*. calculated the hydrodynamic radius of $[SiW_{12}O_{40}]^{4-}$ to be 5.78 Å by using the value they determined for the diffusion coefficient and also noted the closeness of this value to the crystallographic radius which suggested minimal solvation of the ion.[109] Based on Equation 2.67, the hydrodynamic radii of Keggin POMs suggests that they may have lower mobilities (and lower conductivities) than simple metal ions. However, Horky *et al*. determined an ionic conductivity for $[SiW_{12}O_{40}]^{4-}$, based on its limiting molar conductivity, of 237 S cm^2 mol^{-1} at 25°C.[109] In other work, the molar conductivity of $[SiW_{12}O_{40}]^{4-}$ was determined to be 305.0 S cm^2 mol^{-1} for the lithium salt, 328.7 S cm^2 mol^{-1} for the sodium salt and 354.8 S cm^2 mol^{-1} for the potassium salt.[112] This molar conductivity was greater than for other salts with identical cations such as LiCl (100.1 S cm^2 mol^{-1}), NaCl (111.0 S cm^2 mol^{-1}), KCl (133.3 S cm^2 mol^{-1}) and KNO_3 (126.3 S cm^2 mol^{-1}) and was linked to the high mobility of Keggin ions due to their low solvation.[112] The ionic mobility, *u*, of $[SiW_{12}O_{40}]^{4-}$ at 25°C (6.1×10^{-4} cm^2 s^{-1} V^{-1} [109]) is also comparable to values for other common anions such as 7.91×10^{-4} cm^2 s^{-1} V^{-1} for Cl^-, 7.40×10^{-4} for NO_3^- and 8.29×10^{-4} cm^2 s^{-1} V^{-1} for SO_4^{2-} at 25°C.[108]

In other work, a 0.4 M solution of the free acid form of $[SiW_{12}O_{40}]^{4-}$, $H_4SiW_{12}O_{40}$, was found to have a conductivity of 0.39 S cm^{-1} which was comparable to the value quoted for 1 M H_2SO_4 (0.40 S cm^{-1}) at 25°C.[113] It was also found that the viscosity of a 0.4 M $H_4SiW_{12}O_{40}$ solution (which was 64.8 wt% POM) was 2.01 mPa·s compared to 1.10 mPa·s for 1 M H_2SO_4 (which is 9.1 wt% H_2SO_4).[113] This would suggest that the larger size of Keggin anions may not impact the viscosity of electrolytes as much as might be expected when the viscosity is compared to other common electrolytes.

2.3.13 Redox Flow Battery Testing

Once species of interest have been identified and their electrochemistry studied, a next step is to determine the theoretical voltage of an RFB that uses these species in the catholyte and anolyte. The theoretical voltage can be calculated from the difference between the standard electrode potentials (E^0) of the anodic and cathodic reactions, or the formal potentials ($E^{0'}$) where E^0 cannot be calculated. As noted in Section 2.3.8, cyclic voltammetry can be used to determine $E_{1/2}$, which corresponds to the potential at the half-way point between the anodic and cathodic peak where the concentrations of oxidised and reduced species are equal. $E_{1/2}$ is determined by calculating the average of E_{pa} (the anodic peak potential) and E_{pc} (the cathodic peak potential) and can be used to estimate $E^{0'}$.

The actual voltage observed upon testing of an RFB is less that the theoretical voltage due to multiple ‘losses’ that occur when current flows. These losses are often individually or collectively termed polarisation.[114] The three primary losses are the activation polarisation, the ohmic polarisation, and the concentration, or mass-transport, polarisation. Each loss always contributes to the deviation from the theoretical voltage when a current is flowing, but different losses dominate at different current densities. This can be illustrated using a polarisation curve which shows the relationship between the voltage and the current density. A polarisation curve for a VRFB is shown in Figure 2.17.

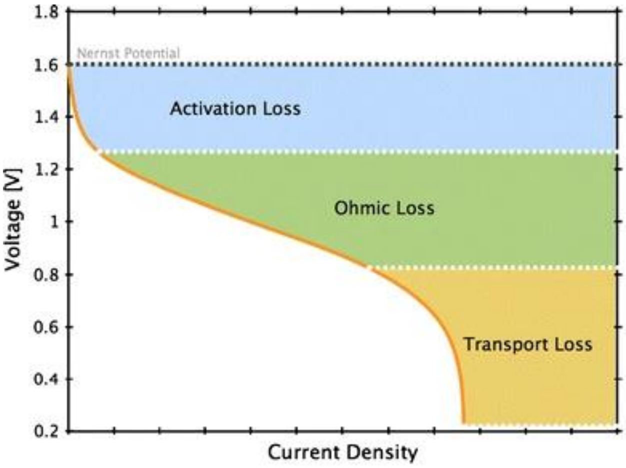

Figure 2.17 - An example of a polarisation curve for a VRFB showing the dominant losses as the current density is increased.[115] *(Reprinted by permission from Springer Nature: Springer, J. Appl. Electrochem., Polarization curve analysis of all-vanadium redox flow batteries, D. Aaron, Z. Tang, A. B. Papandrew and T. A. Zawodzinski, 2011.)*

The activation polarisation is caused by slow charge transfer reactions and dominates at low current densities. The magnitude of the activation polarisation thus depends on the identity of the active species and can be minimised by selecting species with facile electron transfer kinetics or by using a catalyst. The ohmic polarisation is caused by resistance to ionic transport in the electrolyte, within the electrodes and across the membrane, electronic resistance in the electrodes and current collectors, and contact resistances between cell components such as external wires, current collectors, electrodes and flow fields.[115, 116]

Flow fields distribute electrolyte through the electrodes for flow-by RFB configurations. Conversely, in a flow-through RFB design, electrolyte is forced through a porous electrode, which improves convective mass transport relative to a flow-by design but requires relatively thick electrodes which contributes to ohmic polarisation.[106] The flow-by design allows the use of thinner electrodes which are pressed against patterned flow fields that provide channels for the electrolyte to flow through. Flow fields then distribute electrolyte across the electrode by diffusion and convection.[117] A flow cell design that uses a serpentine flow field is shown in Figure 2.18.

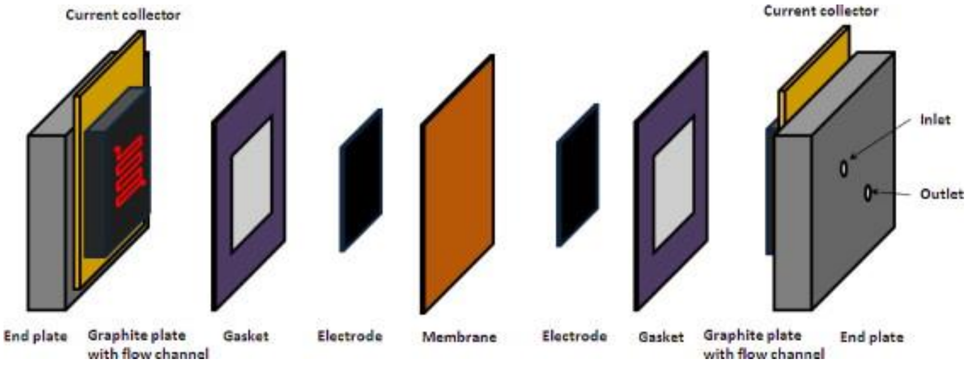

Figure 2.18 - Schematic of an RFB with a serpentine flow field.[117] *(Reprinted from D. S. Aaron, Q. Liu, G. M. Tang, G. M. Grim, A. B. Papandrew, A. Turham, T. A. Zawodsinski and M. M. Mench, J. Power Sources, 2012, 206, 450–453, Copyright 2012, with permission from Elsevier.)*

Cross-sections of flow-by and flow-through configurations, along with other types of flow fields, are shown in Figure 2.19. A flow-through configuration is used in this work so the design of flow fields is not discussed further.

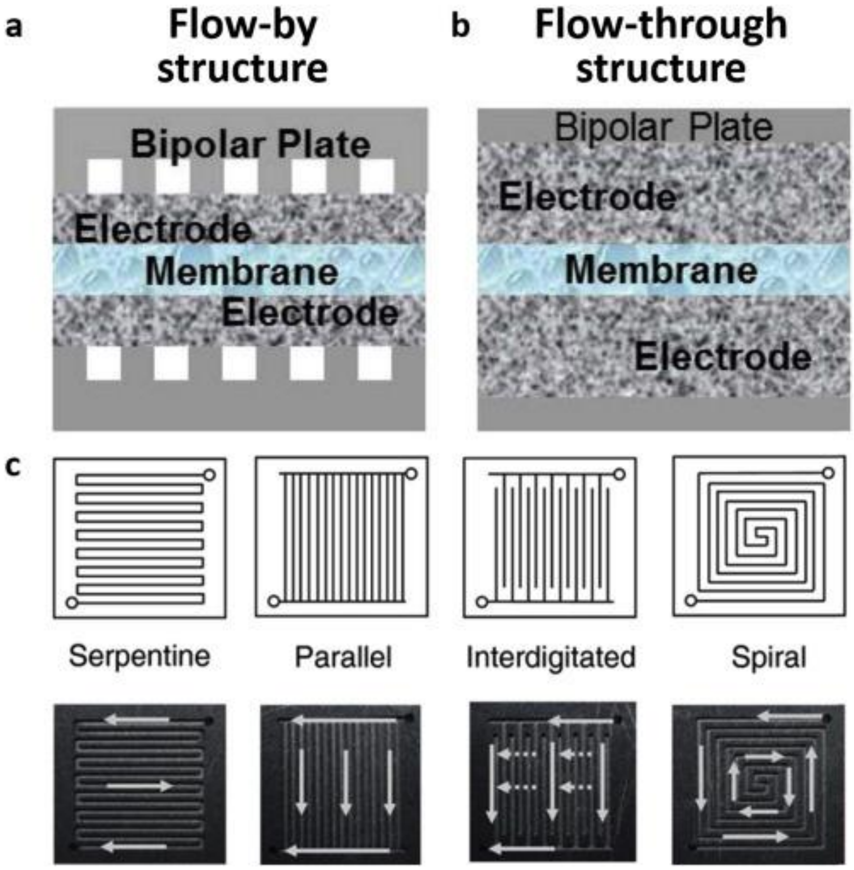

Figure 2.19 - (a) Cross-section of a flow-by RFB structure. (b) Cross-section of a flow-through RFB structure. (c) Four types of flow field for flow-by RFBs.[106] *(Reprinted from X. L. Zhou, T. S. Zhao, L. An, Y. K. Seng and L. Wei, J. Power Sources, 2017, 339, 1-12, Copyright 2017, with permission from Elsevier.)*

Ohmic polarisation dominates in the intermediate region of the polarisation curve and the biggest contributor to this is typically the membrane.[116] Losses due to activation polarisation and ohmic losses due to the membrane tend to be specific to the chemistry employed in an RFB.[103] Modification to the cell design can reduce other ohmic losses, such as by using a "zero-gap" architecture where any gap between the membranes and the electrodes is eliminated and use of relatively thin electrodes is prioritised.[117, 118]

At high current densities, concentration polarisation contributes significantly to the loss of cell potential as the concentration of reactant becomes depleted at the electrode surface. The finite rate of transport of fresh reactant to the electrode surface is insufficient to replenish the concentration, which limits the current density.[115] Concentration polarisation caused by the insufficient delivery of reactant to the electrode surface will occur in all RFBs.[103] However, the region of concentration polarisation may not be observed where the activation polarisation and ohmic polarisation are great enough to cause a cell to reach its voltage limits before concentration polarisation becomes dominant.[116] The rate that reactant is delivered to the electrode surface is related to the concentration of active species and the state of charge of the RFB. At extreme states of charge (near 0% or 100%), the concentration of active species is much depleted in the electrolytes and delivery of reactant to the electrode surface is reduced. The rate of delivery of reactant is also related to the electrolyte velocity, the diffusion coefficients of the active species, the flow field design, and the electrode structure.[103]

Another common technique used to investigate RFBs is galvanostatic cycling which produces charge and discharge curves at constant current. Galvanostatic cycling can be used to assess the voltaic and coulombic efficiencies of an RFB at a selected current. The voltaic efficiency will decrease with current whilst the coulombic efficiency will generally increase (as there is less time for crossover to occur when the charge and discharge of a cell is faster). Thus, galvanostatic cycling can be used to select the range of currents where these efficiencies are at acceptable values.[116] Galvanostatic cycling can also be used to determine the electrochemical yield of an RFB (the proportion of the theoretical capacity that is accessed). The electrochemical yield is affected by the current density, generally decreasing at higher current densities, as well as the polarisation of a cell.[116]

Representative charge/discharge curves from galvanostatic cycling of an iron-chromium RFB are shown in Figure 2.20 in which a voltage cut-off of 1.2 V was selected for charging and 0.8 V for discharging.

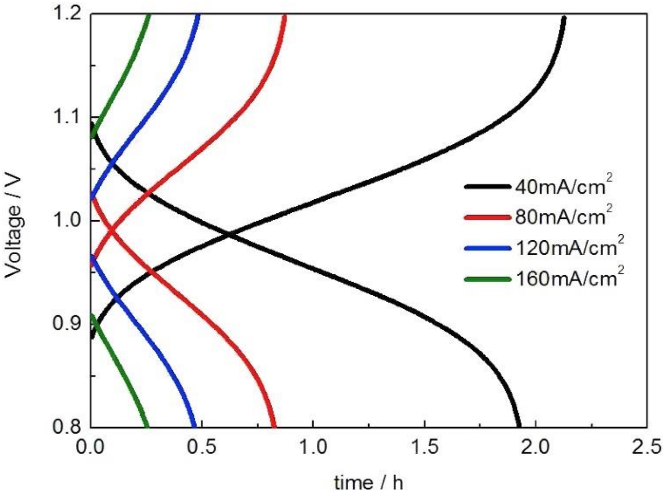

Figure 2.20 - Charge/discharge curves of an iron-chromium RFB.[119] *(Reprinted from Y. K. Zeng, T. S. Zhao, L. An, X. L. Zhou and L. Wei, J. Power Sources, 2015, 300, 438–443, Copyright 2015, with permission from Elsevier.)*

The charge/discharge curves in Figure 2.20 show that a greater capacity can be accessed with improved voltaic efficiency at lower current densities. However, operating at the highest current density that maintains acceptable efficiency values should be the goal for any RFB. The total area of the cell and the membrane make a significant contribution to the cost of an RFB,[115] and the active area of a cell (generally the membrane surface area) is inversely proportional to the power density, as Equation 1.5 showed, where I was the current and V was the cell voltage.

$$Power\ density = \frac{I \times V}{active\ surface\ area} \qquad 1.5$$

The lower the current density, the greater the active surface area required (and the larger the cell required) to deliver a desired power, which decreases the power density. Conversely, the active surface area can be smaller for cells that operate at higher current densities, which will increase the power density.

Galvanostatic cycling is used in this work to assess the coulombic and voltage efficiencies of several POM RFBs.

2.4 References

1. M. T. Pope, in *Heteropoly and Isopoly Oxometalates*, Springer-Verlag, Berlin, 1983, ch. 1, pp. 1-14.
2. M. T. Pope, in *Heteropoly and Isopoly Oxometalates*, Springer-Verlag, Berlin, 1983, ch. 4, pp. 58-90.
3. I. A. Weinstock, R. E. Schreiber and R. Neumann, *Chem. Rev.*, 2018, **118**, 2680-2717.
4. D. L. Long, E. Burkholder and L. Cronin, *Chemical Society Reviews*, 2007, **36**, 105-121.
5. A. Müller, E. Krickemeyer, J. Meyer, H. Bögge, F. Peters, W. Plass, E. Diemann, S. Dillinger, F. Nonnenbruch, M. Randerath and C. Menke, *Angewandte Chemie International Edition in English*, 1995, **34**, 2122-2124.
6. M. T. Pope, in *Heteropoly and Isopoly Oxometalates*, Springer-Verlag, Berlin, 1983, ch. 8, pp. 128-136.
7. L. C. W. Baker and D. C. Glick, *Chem. Rev.*, 1998, **98**, 3-50.
8. B. Keita and L. Nadjo, presented in part at the Encyclopedia of Electrochemistry, 2007.
9. M. T. Pope, in *Heteropoly and Isopoly Oxometalates*, Springer-Verlag, Berlin, 1983, ch. 2, pp. 15-32.
10. G. A. Tsigdinos and C. J. Hallada, *Inorg. Chem.*, 1968, **7**, 437-441.
11. J. J. Berzelius, *Annalen der Physik*, 1826, **82**, 369-392.
12. A. Werner, *Zeitschrift für anorganische Chemie*, 1893, **3**, 267-330.
13. A. Miolati and R. Pizzighelli, *Journal für Praktische Chemie*, 1908, **77**, 417-456.
14. L. Pauling, *Journal of the American Chemical Society*, 1929, **51**, 2868-2880.
15. J. F. Keggin, *Nature*, 1933, **131**, 908-909.
16. F. Cavani, *Catalysis Today*, 1998, **41**, 73-86.
17. A. J. Bradley and J. W. Illingworth, *Proceedings of the Royal Society of London. Series A, Mathematical and Physical Sciences*, 1936, **157**, 113-131.
18. R. Signer and H. Gross, *Helvetica Chimica Acta*, 1934, **17**, 1076-1080.
19. J. S. Anderson, *Nature*, 1937, **140**, 850-850.
20. H. T. Evans, *Journal of the American Chemical Society*, 1948, **70**, 1291-1292.
21. A. Rosenheim and A. Traube, *Zeitschrift für anorganische Chemie*, 1915, **91**, 75-106.
22. H. Wu, *Journal of Biological Chemistry*, 1920, **43**, 189-220.
23. A. F. Wells, *Structural Inorganic Chemistry*, Oxford University Press, 1st edn., 1945.
24. B. Dawson, *Acta Crystallographica*, 1953, **6**, 113-126.

25. R. Contant, in *Inorganic Syntheses*, ed. A. P. Ginsberg, Wiley, 1990, vol. 27, ch. 3, pp. 104-111.
26. M. H. Alizadeh, S. P. Harmalker, Y. Jeannin, J. Martin-Frere and M. T. Pope, *Journal of the American Chemical Society*, 1985, **107**, 2662-2669.
27. I. Lindqvist, *Acta Crystallographica*, 1950, **3**, 159-160.
28. X. López, J. J. Carbó, C. Bo and J. M. Poblet, *Chemical Society Reviews*, 2012, **41**, 7537-7571.
29. L. C. W. Baker and J. S. Figgis, *Journal of the American Chemical Society*, 1970, **92**, 3794-3797.
30. Y. Matsumoto Kazuko, A. Kobayashi and Y. Sasaki, *Bulletin of the Chemical Society of Japan*, 1975, **48**, 3146-3151.
31. M. T. Pope, *Inorg. Chem.*, 1976, **15**, 2008-2010.
32. A. Tézé, J. Canny, L. Gurban, R. Thouvenot and G. Hervé, *Inorg. Chem.*, 1996, **35**, 1001-1005.
33. H. Sartzi, H. N. Miras, L. Vilà-Nadal, D.-L. Long and L. Cronin, *Angewandte Chemie International Edition*, 2015, **54**, 15488-15492.
34. H. K. Chae, W. G. Klemperer, D. E. Paez-Loyo, V. W. Day and T. A. Eberspacher, *Inorg. Chem.*, 1992, **31**, 3187-3189.
35. M. I. Khan, A. Müller, S. Dillinger, H. Bögge, Q. Chen and J. Zubieta, *Angewandte Chemie International Edition in English*, 1993, **32**, 1780-1782.
36. B. Nohra, H. El Moll, L. M. Rodriguez Albelo, P. Mialane, J. Marrot, C. Mellot-Draznieks, M. O’Keeffe, R. Ngo Biboum, J. Lemaire, B. Keita, L. Nadjo and A. Dolbecq, *Journal of the American Chemical Society*, 2011, **133**, 13363-13374.
37. A. Müller, C. Beugholt, P. Kögerler, H. Bögge, S. Bud'ko and M. Luban, *Inorg. Chem.*, 2000, **39**, 5176-5177.
38. P. Mialane, A. Dolbecq, L. Lisnard, A. Mallard, J. Marrot and F. Sécheresse, *Angewandte Chemie International Edition*, 2002, **41**, 2398-2401.
39. J. Tucher, L. C. Nye, I. Ivanovic-Burmazovic, A. Notarnicola and C. Streb, *Chemistry – A European Journal*, 2012, **18**, 10949-10953.
40. A. Tézé and G. Hervé, in *Inorganic Syntheses*, ed. A. P. Ginsberg, John Wiley & Sons, New York, 1990, vol. 27, ch. 3, pp. 85-96.
41. G. Herve and A. Teze, *Inorg. Chem.*, 1977, **16**, 2115-2117.
42. N. Narkhede, S. Singh and A. Patel, *Green Chemistry*, 2015, **17**, 89-107.
43. R. Massart, R. Contant, J. M. Fruchart, J. P. Ciabrini and M. Fournier, *Inorg. Chem.*, 1977, **16**, 2916-2921.

44. A. Dolbecq, E. Dumas, C. R. Mayer and P. Mialane, *Chem. Rev.*, 2010, **110**, 6009-6048.
45. R. K. C. Ho and W. G. Klemperer, *Journal of the American Chemical Society*, 1978, **100**, 6772-6774.
46. P. Judeinstein, *Chemistry of Materials*, 1992, **4**, 4-7.
47. A. Proust, R. Thouvenot and P. Gouzerh, *Chemical Communications*, 2008, DOI: 10.1039/B715502F, 1837-1852.
48. L. C. W. Baker, V. S. Baker, K. Eriks, M. T. Pope, M. S. Orville, W. Rollins, J. H. Fang and L. L. Koh, *Journal of the American Chemical Society*, 1966, **88**, 2329-2331.
49. T. J. R. Weakley and S. A. Malik, *Journal of Inorganic and Nuclear Chemistry*, 1967, **29**, 2935-2944.
50. S. A. Malik and T. J. R. Weakley, *Chemical Communications (London)*, 1967, DOI: 10.1039/C19670001094, 1094-1095.
51. R. Ripan, M. Puscasiu, D. Stanescu and P. Boian, *Zeitschrift für anorganische und allgemeine Chemie*, 1971, **384**, 297-304.
52. C. M. Tourné, G. F. Tourné, S. A. Malik and T. J. R. Weakley, *Journal of Inorganic and Nuclear Chemistry*, 1970, **32**, 3875-3890.
53. F. Zonnevijlle, C. M. Tourne and G. F. Tourne, *Inorg. Chem.*, 1982, **21**, 2742-2750.
54. F. Zonnevijlle, C. M. Tourne and G. F. Tourne, *Inorg. Chem.*, 1982, **21**, 2751-2757.
55. J. Li, C. L. Bentley, T. Ueda, A. M. Bond and J. Zhang, *J Electroanal Chem*, 2018, **819**, 193-201.
56. J. Canny, R. Thouvenot, A. Teze, G. Herve, M. Leparulo-Loftus and M. T. Pope, *Inorg. Chem.*, 1991, **30**, 976-981.
57. R. G. Finke and M. W. Droege, *Journal of the American Chemical Society*, 1984, **106**, 7274-7277.
58. M. M. Mossoba, C. J. O'Connor, M. T. Pope, E. Sinn, G. Herve and A. Teze, *Journal of the American Chemical Society*, 1980, **102**, 6864-6866.
59. R. G. Finke, B. Rapko, R. J. Saxton and P. J. Domaille, *Journal of the American Chemical Society*, 1986, **108**, 2947-2960.
60. E. Cadot, R. Thouvenot, A. Teze and G. Herve, *Inorg. Chem.*, 1992, **31**, 4128-4133.
61. J. Liu, F. Ortega, P. Sethuraman, D. E. Katsoulis, C. E. Costello and M. T. Pope, *Journal of the Chemical Society, Dalton Transactions*, 1992, DOI: 10.1039/DT9920001901, 1901-1906.
62. S. P. Harmalker and M. T. Pope, *Journal of the American Chemical Society*, 1981, **103**, 7381-7383.

63. S. P. Harmalker, M. A. Leparulo and M. T. Pope, *Journal of the American Chemical Society*, 1983, **105**, 4286-4292.
64. T. J. R. Weakley, H. T. Evans, J. S. Showell, G. F. Tourné and C. M. Tourné, *Journal of the Chemical Society, Chemical Communications*, 1973, DOI: 10.1039/C39730000139, 139-140.
65. R. G. Finke and M. W. Droege, *Inorg. Chem.*, 1983, **22**, 1006-1008.
66. D.-L. Long, R. Tsunashima and L. Cronin, *Angewandte Chemie International Edition*, 2010, **49**, 1736-1758.
67. H. N. Miras, J. Yan, D.-L. Long and L. Cronin, *Chemical Society Reviews*, 2012, **41**, 7403-7430.
68. M. T. Pope, *Inorg. Chem.*, 1972, **11**, 1973-1974.
69. M. T. Pope and A. Müller, *Angewandte Chemie International Edition in English*, 1991, **30**, 34-48.
70. M. T. Pope, in *Heteropoly and Isopoly Oxometalates*, Springer-Verlag, Berlin, 1983, ch. 6, pp. 101-117.
71. R. A. Prados, P. T. Meiklejohn and M. T. Pope, *Journal of the American Chemical Society*, 1974, **96**, 1261-1263.
72. J. P. Launay, M. Fournier, C. Sanchez, J. Livage and M. T. Pope, *Inorganic and Nuclear Chemistry Letters*, 1980, **16**, 257-261.
73. C. Sanchez, J. Livage, J. P. Launay, M. Fournier and Y. Jeannin, *Journal of the American Chemical Society*, 1982, **104**, 3194-3202.
74. K. Piepgrass, J. N. Barrows and M. T. Pope, *Journal of the Chemical Society, Chemical Communications*, 1989, DOI: 10.1039/C39890000010, 10-12.
75. M. Kozik, C. F. Hammer and L. C. W. Baker, *Journal of the American Chemical Society*, 1986, **108**, 2748-2749.
76. M. Kozik, N. Casan-Pastor, C. F. Hammer and L. C. W. Baker, *Journal of the American Chemical Society*, 1988, **110**, 7697-7701.
77. M. Sadakane and E. Steckhan, *Chem. Rev.*, 1998, **98**, 219-237.
78. G. M. Lampman, D. L. Pavia, G. S. Kriz and J. R. Vyvyan, in *Spectroscopy (International Edition)*, Brooks Cole, Belmont, 4th edn., 2009, ch. 3, pp. 105-176.
79. R. G. Compton and G. H. W. Sanders, *Electrode Potentials*, Oxford University Press, Oxford, 1996.
80. A. C. Fisher, *Electrode Dynamics*, Oxford University Press, Oxford, 1996.
81. A. J. Bard and L. R. Faulkner, in *Electrochemical Methods - Fundamentals and Applications*, John Wiley & Sons, New York, 2nd edn., 2001, ch. 2, pp. 44-86.

82. John Frederic Daniell, https://makingscience.royalsociety.org/s/rs/people/fst01464106, (accessed 19 June, 2020).
83. B. J. Neyhouse, A. M. Fenton and F. R. Brushett, *J Electrochem Soc*, 2021, **168**, 050501.
84. A. J. Bard and L. R. Faulkner, in *Electrochemical Methods - Fundamentals and Applications*, John Wiley & Sons, New York, 2nd edn., 2001, ch. 1, pp. 1-43.
85. A. J. Bard and L. R. Faulkner, in *Electrochemical Methods - Fundamentals and Applications*, Wiley, New York, 2nd edn., 2001, ch. 3, pp. 87-136.
86. J. A. V. Butler, *Transactions of the Faraday Society*, 1924, **19**, 729-733.
87. T. Erdey-Grúz and M. Volmer, *Journal*, 1930, **150A**, 203.
88. L. M. Peter, W. Dürr, P. Bindra and H. Gerischer, *Journal of Electroanalytical Chemistry and Interfacial Electrochemistry*, 1976, **71**, 31-50.
89. J. Friedl and U. Stimming, *Electrochim Acta*, 2017, **227**, 235-245.
90. M. Ciobanu, J. P. Wilburn, M. L. Krim and D. E. Cliffel, in *Handbook of Electrochemistry*, ed. C. G. Zoski, Elsevier, 2007, ch. 1, pp. 3-29.
91. G. Kear and F. C. Walsh, *Corrosion and Materials*, 2005, **30**, 51-55.
92. T. J. Smith and K. J. Stevenson, in *Handbook of Electrochemistry*, ed. C. G. Zoski, Elsevier, 1st edn., 2007, ch. 4, pp. 73-110.
93. A. J. Bard and L. R. Faulkner, in *Electrochemical Methods - Fundamentals and Applications*, John Wiley & Sons, New York, 2nd edn., 2001, ch. 6, pp. 226-260.
94. N. Elgrishi, K. J. Rountree, B. D. McCarthy, E. S. Rountree, T. T. Eisenhart and J. L. Dempsey, *Journal of Chemical Education*, 2018, **95**, 197-206.
95. G. Denuault, M. Sosna and K.-J. Williams, in *Handbook of Electrochemistry*, ed. C. G. Zoski, Elsevier, 1st edn., 2007, ch. 11, pp. 431-469.
96. E. P. Randviir and C. E. Banks, *Analytical Methods*, 2013, **5**, 1098-1115.
97. W. Schmickler and E. Santos, in *Interfacial Electrochemistry*, Springer-Verlag, Berlin, 2nd edn., 2010, ch. 19, pp. 235-257.
98. C. Fernández-Sánchez, C. J. McNeil and K. Rawson, *Trends in Analytical Chemistry*, 2005, **24**, 37-48.
99. R. S. Neves, E. De Robertis and A. J. Motheo, *Applied Surface Science*, 2006, **253**, 1379-1386.
100. J.-B. Jorcin, M. E. Orazem, N. Pébère and B. Tribollet, *Electrochim Acta*, 2006, **51**, 1473-1479.
101. B. Hirschorn, M. E. Orazem, B. Tribollet, V. Vivier, I. Frateur and M. Musiani, *J Electrochem Soc*, 2010, **157**, C452-C457.

102. P. Zoltowski, *J Electroanal Chem*, 1998, **443**, 149-154.
103. J. D. Milshtein, K. M. Tenny, J. L. Barton, J. Drake, R. M. Darling and F. R. Brushett, *J Electrochem Soc*, 2017, **164**, E3265-E3275.
104. R. M. Darling and M. L. Perry, *J Electrochem Soc*, 2014, **161**, A1381-A1387.
105. J. Houser, J. Clement, A. Pezeshki and M. M. Mench, *J Power Sources*, 2016, **302**, 369-377.
106. X. L. Zhou, T. S. Zhao, L. An, Y. K. Zeng and L. Wei, *J Power Sources*, 2017, **339**, 1-12.
107. A. J. Bard and L. R. Faulkner, in *Electrochemical Methods - Fundamentals and Applications*, John Wiley & Sons, New York, 2nd edn., 2001, ch. 4, pp. 137-155.
108. P. Atkins and J. d. Paula, *Atkins' Physical Chemistry*, Oxford University Press, Oxford, 10th edn., 2014.
109. A. Horky, N. P. Kherani and G. Xu, *J Electrochem Soc*, 2003, **150**, A1219.
110. L. C. W. Baker and M. T. Pope, *Journal of the American Chemical Society*, 1960, **82**, 4176-4179.
111. M. T. Pope and G. M. Varga, *Inorg. Chem.*, 1966, **5**, 1249-1254.
112. H. Gao, A. Virya and K. Lian, *Electrochim Acta*, 2014, **138**, 240-246.
113. N. H. Wisińska, M. Skunik-Nuckowska, S. Dyjak and P. J. Kulesza, *Applied Surface Science*, 2020, **530**, 147273.
114. *Fuel Cell Handbook - Seventh Edition*, National Energy Technology Laboratory, U.S. Department of Energy, United States, 2004.
115. D. Aaron, Z. Tang, A. B. Papandrew and T. A. Zawodzinski, *Journal of Applied Electrochemistry*, 2011, **41**, 1175.
116. Y. A. Gandomi, D. S. Aaron, J. R. Houser, M. C. Daugherty, J. T. Clement, A. M. Pezeshki, T. Y. Ertugrul, D. P. Moseley and M. M. Mench, *J Electrochem Soc*, 2018, **165**, A970-A1010.
117. D. S. Aaron, Q. Liu, Z. Tang, G. M. Grim, A. B. Papandrew, A. Turhan, T. A. Zawodzinski and M. M. Mench, *J Power Sources*, 2012, **206**, 450-453.
118. P. K. Leung, M. R. Mohamed, A. A. Shah, Q. Xu and M. B. Conde-Duran, *J Power Sources*, 2015, **274**, 651-658.
119. Y. K. Zeng, T. S. Zhao, L. An, X. L. Zhou and L. Wei, *J Power Sources*, 2015, **300**, 438-443.

Chapter 3 - The Application of $[SiV_3W_9O_{40}]^{7-}$ in a Symmetric Polyoxometalate Redox Flow Battery

3.1 Introduction

Symmetric RFBs can be defined as "RFBs consisting of a single parent molecule that can be oxidised and reduced to facilitate the positive and negative electrode half-reactions, respectively."[1] An important feature of a symmetric RFB is that the composition of the catholyte and anolyte is the same in the discharged state. The benefit of using electrolytes based on the same parent species is the avoidance of chemical contamination if active material crosses the membrane between half-cells. While the occurrence of crossover in a symmetric RFB will result in a reduction in coulombic efficiency for the current cycle, it does not result in the contamination of the electrolyte with dissimilar chemical species. This means that charge rebalancing is simplified as chemical separations are not required.[1]

The requirement that an active species must satisfy if it is to be used in a symmetric RFB is that it must exhibit different redox reactions at disparate potentials that could be used as the cathode and anode redox reactions in an RFB. A range of organic and inorganic species that satisfy this principle have been the subject of testing in symmetric flow cells which were discussed in Chapter 1. All demonstrated the necessary property for a symmetric RFB species: distinct redox processes separated by an appreciable difference in formal potential. This led to proposed symmetric RFB chemistries with theoretical voltages suitable for aqueous[2, 3] (~1.2 V) or non-aqueous supporting electrolytes (≥1.6 V for these examples[1, 4-11]). However, in spite of displaying an electrochemical profile in cyclic voltammetry that suggested suitability as a symmetric RFB active species, there were issues with stability in all oxidation states[10, 12] and low coulombic efficiencies were reported which meant that the occurrence of side reactions could not be excluded.[6, 7] Further, the reactivity of a radical site in organic active species can be a challenge, causing side reactions,[13] with such occurrences thought to be a factor in the deterioration in capacity in some flow cells that employed this subset of active species.[4, 5, 14] There is scope for further investigation of active species for symmetric flow cells and polyoxometalates (POMs) form another division of materials that have been investigated thus far.

The multi-electron reactions and favourable electron transfer kinetics of POMs have spurred the investigation into their application in RFBs.[15] Some POMs are suitable for application as symmetric RFB active species because they contain more than one redox-active metal. For instance, Pratt *et al*. reported a symmetric flow cell based on $[SiV_3W_9O_{40}]^{7-}$ and Liu *et al*. used $[CoW_{12}O_{40}]^{6-}$.[16, 17] Each POM contained two redox-active metals: $[SiV_3W_9O_{40}]^{7-}$ is a mixed addenda POM containing vanadium and tungsten while the

Co^{II}/Co^{III} redox couple of the heteroatom of $[CoW_{12}O_{40}]^{6-}$ could be used as a cathodic reaction paired with the redox reactions of tungsten for the anode.

The concept of a symmetric POM RFB is the focus of this chapter and the $[SiV_3W_9O_{40}]^{7-}$ anion, previously studied by Pratt *et al.*, was selected as the species that would be used to illustrate this concept. For reasons discussed in the following section, the electrochemical properties of $[SiV_3W_9O_{40}]^{7-}$ make it a candidate for investigation as an active species for a symmetric POM RFB. In their study, Pratt *et al*. used an acidic supporting electrolyte (0.5 M H_2SO_4). In this chapter, it is demonstrated that $[SiV_3W_9O_{40}]^{7-}$ is not stable in all oxidation states in acidic conditions and an alternative supporting electrolyte is tested.

3.2 Experimental

3.2.1 Materials

Sodium tungstate dihydrate (99.0–101.0%) and potassium chloride (99%) were supplied by Alfa Aesar. Sodium metavanadate (≥98%), sodium metasilicate nonahydrate (≥98%), sodium carbonate (anhydrous, ≥99.5%) and hydrochloric acid (37%) were supplied by Sigma Aldrich. Methanol was of general solvent grade and was purchased from Fisher Scientific. Sulphuric acid (95%–98%), used to prepare supporting electrolytes, was supplied by Sigma Aldrich. Anhydrous lithium sulphate (99%), also used to prepare supporting electrolytes, was supplied by ACROS Organics. Sodium L-ascorbate (99%), used as a reducing agent, was supplied by Alfa Aesar.

Samples of $K_4[PVW_{11}O_{40}]$ and $H_6[PV_2Mo_{10}O_{40}]$ were supplied by J. Friedl.

3.2.2 Synthesis of $[SiV_3W_9O_{40}]^{7-}$

For characterisation, ^{51}V NMR spectra were obtained on a Bruker Avance-III 300 Spectrometer. FT-IR spectra were obtained on a Perkin-Elmer Spectrum Two FT-IR spectrometer fitted with an ATR attachment.

3.2.2.1 α isomer

The potassium salt of the α isomer of the $[SiV_3W_9O_{40}]^{7-}$ anion was prepared by following literature procedures.[18, 19]

In a representative procedure, the lacunary precursor, $[\alpha\text{-}SiW_9O_{34}]^{10-}$, was synthesised by following the method of Tézé and Hervé.[20] Sodium tungstate dihydrate (91.0 g, 0.276 mol) and sodium metasilicate nonahydrate (7.11 g, 0.0250 mol) were dissolved in hot water (100 ml, 80–100°C) in a beaker. 6 M HCl (65 mL) was added dropwise over 20–25 minutes while the solution was stirred vigorously using a magnetic stirrer. The solution was boiled until the volume was reduced by ~10%. The solution was left to cool and then filtered to remove unreacted silica. A second solution of anhydrous sodium carbonate (25.0 g, 0.236 mol) dissolved in water (75 mL) was prepared and added slowly to the first solution with stirring. The solution was stirred on a magnetic stirrer for one hour, over which time a white precipitate formed. After one hour, the precipitate was removed by vacuum filtration using a sintered glass frit. The precipitate was washed with portions of 4 M NaCl (5 × 20 mL) on the filter and air-dried to yield 53.3 g of $Na_{10}[\alpha\text{-}SiW_9O_{34}]\cdot xH_2O$ (yield: ~83 %).

Sodium metavanadate (2.70 g, 0.0221 mol) was dissolved in hot water (382 mL, 80–100°C) in a beaker. The solution was cooled to room temperature. $Na_{10}[\alpha\text{-}SiW_9O_{34}]\cdot xH_2O$ (20.0 g, 7.19×10^{-3} mol) was added to the solution and the pH was adjusted to 2.0 with 6 M HCl. A cherry red solution developed during addition of the acid. The solution was stirred for

45 minutes. After this time, potassium chloride (25.4 g, 0.340 mol) was dissolved in the solution with stirring. Methanol (426 mL) was added and an orange precipitate was immediately evident. The precipitate was left to settle for 5–10 minutes then removed using vacuum filtration and dried in air. The product was recrystallised by dissolving it in a minimum amount of hot water (heated to boiling point) and cooling the concentrated solution in an ice bath. This resulted in 10.8 g of red/orange crystals of $K_7[\alpha\text{-}SiV_3W_9O_{40}]\cdot xH_2O$ which were removed using vacuum filtration and air-dried (yield: ~50 %). Based on the yields of $Na_{10}[\alpha\text{-}SiW_9O_{34}]\cdot xH_2O$ in the first step and $K_7[\alpha\text{-}SiV_3W_9O_{40}]\cdot xH_2O$ in the second step, the overall yield was 42%.

3.2.2.2 β isomer

The potassium salt of $[\beta\text{-}SiV_3W_9O_{40}]^{7-}$ was prepared by following a literature procedure.[21]

In a representative procedure, the lacunary precursor, $[\beta\text{-}SiW_9O_{34}]^{10-}$, was synthesised by following the procedure of Tézé and Hervé.[20] Sodium metasilicate nonahydrate (16.2 g, 0.0570 mol) was dissolved in water (250 mL) in a beaker at room temperature, to which sodium tungstate dihydrate (150 g, 0.455 mol) was then added. 6 M HCl (95 mL) was added dropwise slowly with vigorous stirring. A gelatinous precipitate formed during addition of the acid which was removed by filtration using a sintered glass frit after all of the acid had been added. The filtrate was stored in a refrigerator for four days. During this time, a white precipitate formed. Formation of the precipitate was aided by briefly swirling the solution at daily intervals. The white precipitate was collected later using a sintered glass filter, washed with small portions of cold water (4°C) on the filter and dried in air to yield 35.4 g of $Na_9[\beta\text{-}SiW_9O_{34}H]\cdot 23H_2O$ (yield: 33%).

Sodium metavanadate (0.837 g, 6.90×10^{-3} mol) was dissolved in hot water (120 mL, 80–100°C) in a beaker. The solution was cooled to room temperature and 6 M HCl (3 mL) was added with stirring to yield a yellow solution of pH < 1.5 which contained the VO_2^+ anion. To the stirred solution was added $Na_9[\beta\text{-}SiW_9O_{34}H]\cdot 23H_2O$ (6.38 g, 2.24×10^{-3} mol) and a cherry red solution developed. After stirring for 15 minutes, potassium chloride (7.91 g, 0.106 mol) was dissolved in the solution. Methanol (120 mL) was added and a red precipitate was immediately evident. The precipitate was left to settle for 5–10 minutes, then removed by vacuum filtration and dried in air.

The crude product was recrystallised by dissolving it in ~30 mL of a 1:2 methanol/0.03 M HCl mixture heated to 55°C and cooling the solution to 4°C in a refrigerator for six hours. Dark red crystals appeared during this time which were removed by vacuum filtration and air-dried, resulting in 5.04 g of $K_6H[\beta\text{-}SiV_3W_9O_{40}]\cdot 3H_2O$ (yield: 80%). Based on the yields of $Na_9[\beta\text{-}SiW_9O_{34}H]\cdot 23H_2O$ in the first step and $K_6H[\beta\text{-}SiV_3W_9O_{40}]\cdot 3H_2O$ in the second step, the overall yield was 26%.

3.2.3 Electrochemistry

A Biologic SP300 potentiostat was used for cyclic voltammetry and bulk electrolysis experiments.

Cyclic voltammetry was carried out in a custom-built glass cell or a commercial glass cell (BASi). The working electrode was glassy carbon (surface area = 0.02 cm^2) with a gold or platinum wire as counter electrode and an MSE (1 M H_2SO_4) reference electrode (E = 0.674 V vs SHE) or a Ag/AgCl (3 M NaCl) reference electrode (E = 0.209 V vs SHE). Prior to beginning an experiment, solutions were purged with nitrogen for 10 minutes and the working electrode was polished with alumina polish (0.05 μm).

Bulk electrolysis was carried out in a commercial bulk electrolysis cell (BASi, product code MF-1056) with a glassy carbon mesh working electrode, a platinum wire as the counter electrode and a Ag/AgCl (3 M NaCl) reference electrode. The solution was stirred and purged with nitrogen for the entirety of an experiment. CVs of a solution before electrolysis (e.g. Figure 3.21a) were obtained in the electrolysis cell by switching the working electrode to a glassy carbon disc electrode and using the glassy carbon mesh electrode as the counter electrode.

3.2.4 Charge/Discharge Testing

A Biologic BCS-810 battery tester was used for charge/discharge tests.

Stationary cell testing was carried out in a custom-built cell with a Nafion 117 membrane as separator. Membranes were boiled in 1 M Li_2SO_4 for 30 minutes prior to construction of the cell. Graphite felt (GFD 4.6, SGL Carbon) that had been heated in an oven at 400°C for 24 hours was used as the electrode material. Stationary cells were kept in a polycarbonate box purged with nitrogen during operation. Photographs of the stationary cell are shown in Figure 3.1. Two layers of graphite felt, cut to a size of 4×4 cm^2, fitted into each half-cell. The carbon felt was contacted with a carbon paper strip which extended outside of the cell for connection to crocodile clips which led to the battery tester. When the cell was constructed, each half-cell could hold ~13 mL of electrolyte.

A C-Flow LAB 5×5 electrochemical cell was used for flow cell experiments. The membrane, electrode material and treatment of the membrane and electrodes prior to cell construction were as described for the stationary cells. The flow cell and pump were kept in a polycarbonate box during operation and the electrolytes were bubbled with nitrogen for the duration of testing. A photograph of the dismantled flow cell illustrating its components and a photograph of the flow cell after assembly are shown in Figure 3.2.

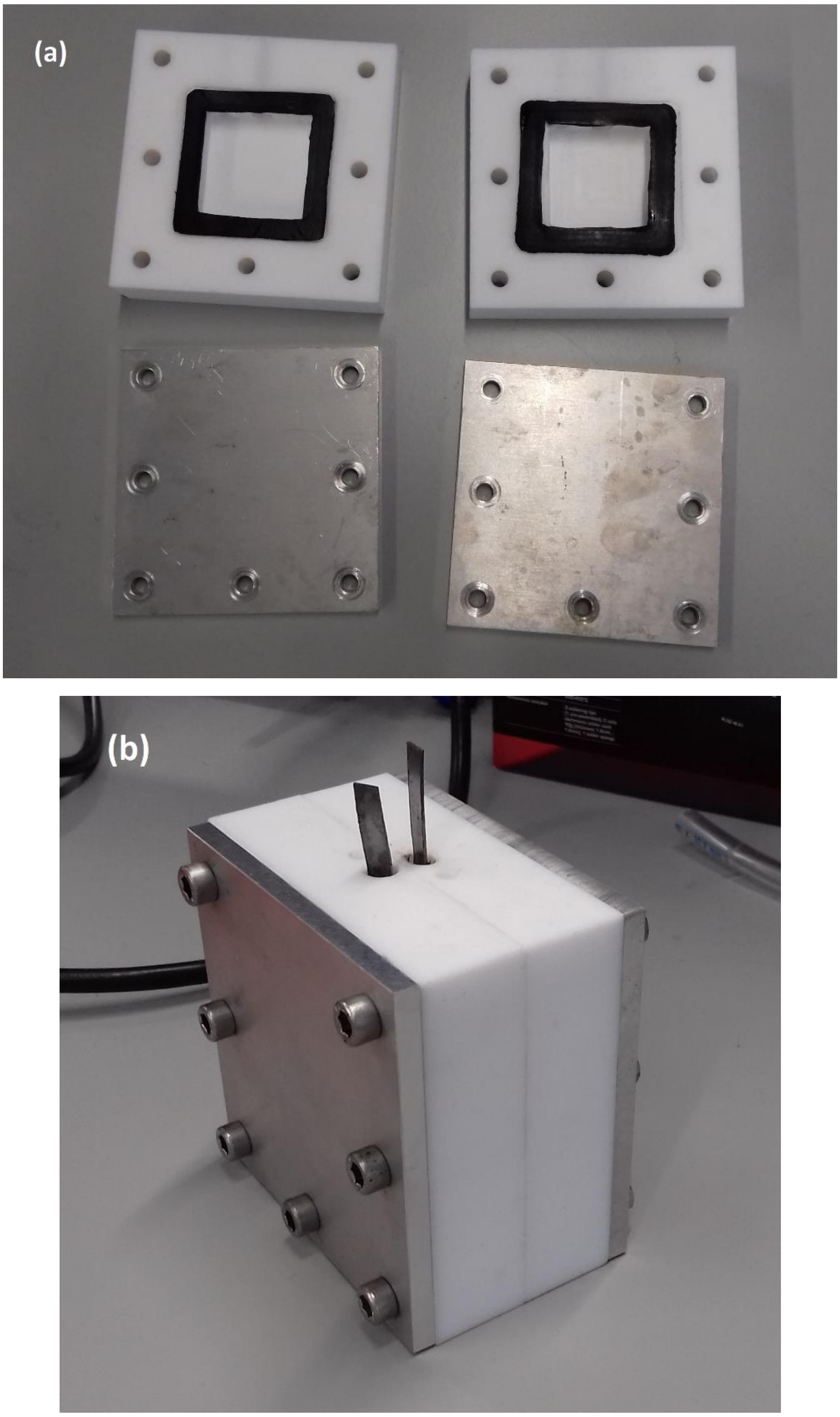

Figure 3.1 - Photographs of the stationary cell used to test **SiV$_3$W$_9$**. *(a) Dismantled cell showing end-plates and two half-cells with gaskets surrounding the cavities into which the carbon felt electrodes were placed. (b) Constructed cell.*

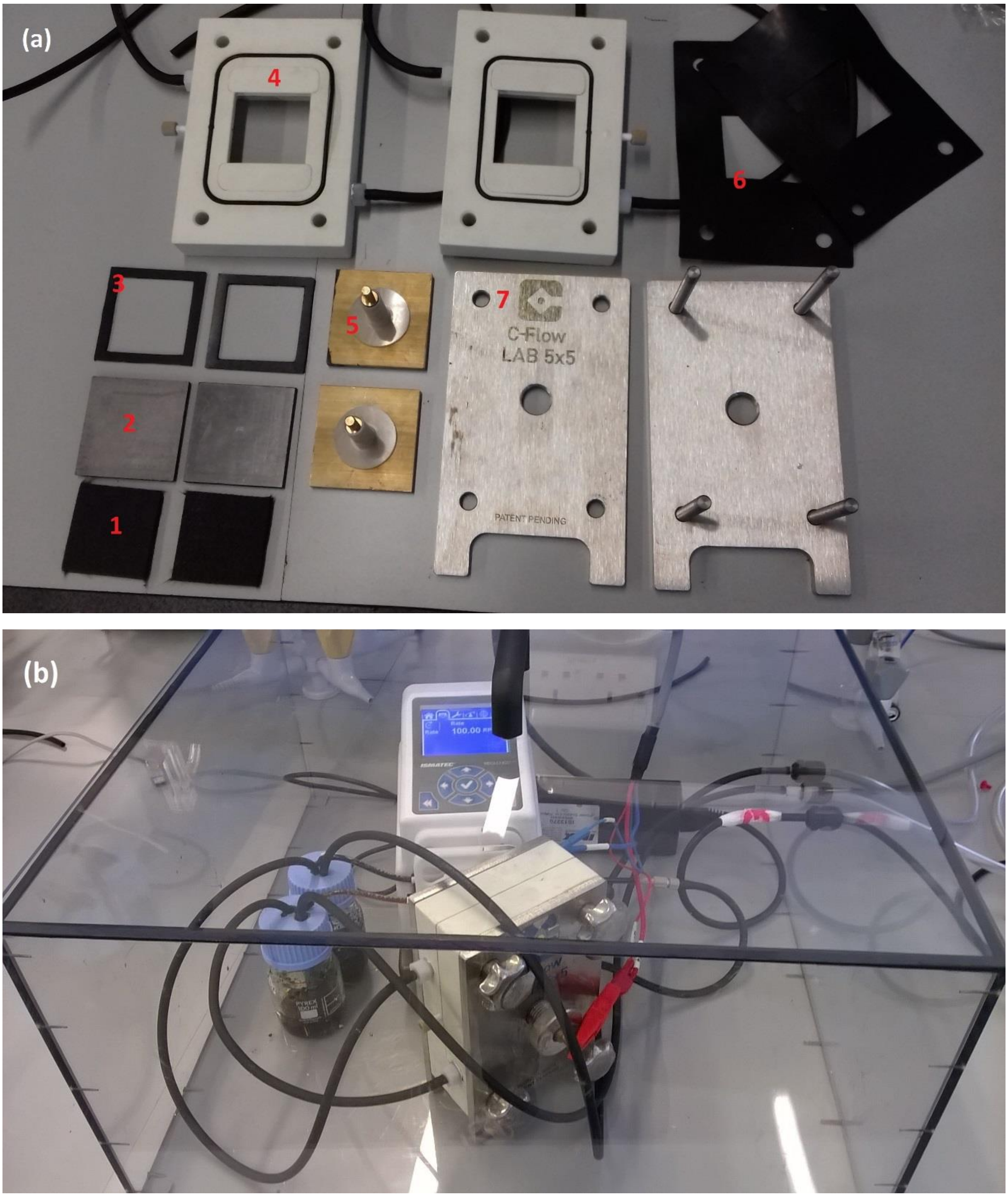

Figure 3.2 - (a) Photograph of the dismantled flow cell. ***1.*** *Graphite felt electrodes.* ***2.*** *Carbon plate electrodes.* ***3.*** *Electrode gaskets.* ***4.*** *Cell frames.* ***5.*** *Brass current collectors.* ***6.*** *Membrane gaskets* ***7.*** *End-plates. (b) Photograph of the flow cell during operation.*

3.3 Polyoxometalates for Symmetric RFBs: Preliminary Investigation

A preliminary investigation of the electrochemistry of several POMs that could have the desired electrochemical properties for a symmetric POM RFB was undertaken. These POMs each contained different addenda atoms that could show redox activity.

For the active species in a symmetric RFB, the number of electrons transferred at high and low potential needs to be considered as these values should be comparable. In addition, to offer a suitable theoretical voltage for an RFB, these redox processes should occur at well-separated potentials. To illustrate these principles, CVs of three mixed-metal POMs containing vanadium and tungsten or vanadium and molybdenum are shown in Figure 3.3. These structures are the mono-vanadium substituted phosphotungstate $[PVW_{11}O_{40}]^{4-}$ (**PVW_{11}**), the di-vanadium substituted phosphomolybdate $[PV_2Mo_{10}O_{40}]^{6-}$ (**PV_2Mo_{10}**) and the tri-vanadium substituted silicotungstate $[SiV_3W_9O_{40}]^{7-}$ (**SiV_3W_9**).

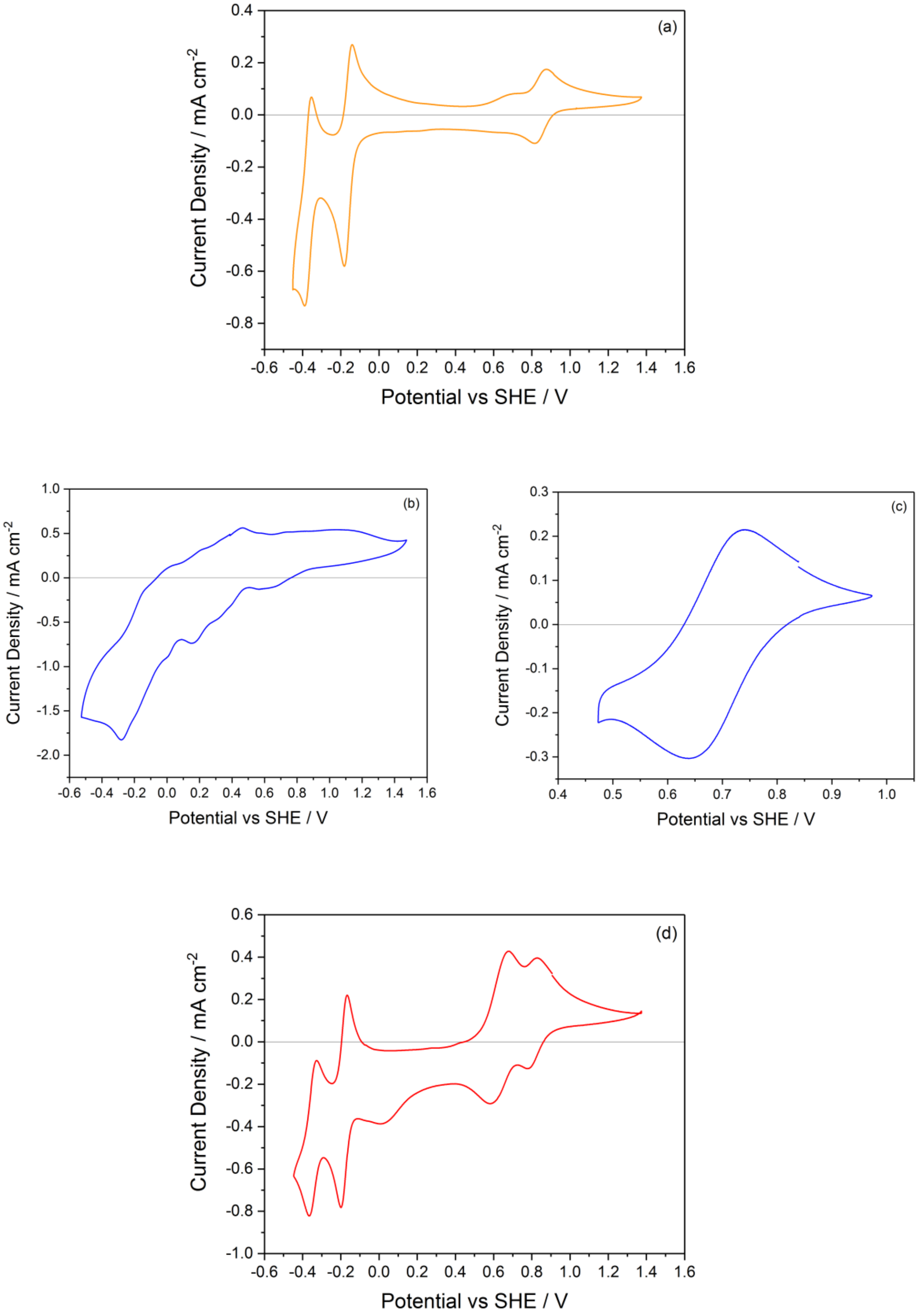

Figure 3.3 - (a) A CV of $[PVW_{11}O_{40}]^{4-}$ *(1 mM) in 1 M* H_2SO_4*. (b) A CV of* $[PV_2Mo_{10}O_{40}]^{6-}$ *(1 mM) in KCl/HCl buffer (pH 2) (c) A further CV of* $[PV_2Mo_{10}O_{40}]^{6-}$ *scanned between 0.974 V vs SHE and 0.474 V vs SHE. (d) A CV of* $[SiV_3W_9O_{40}]^{7-}$ *(1 mM) in 1 M* H_2SO_4*. (WE: glassy carbon, CE: gold wire, RE: MSE (1 M* H_2SO_4*), scan rate: 100 mV/s)*

PVW_{11} has a single vanadium atom in its structure that exhibits redox activity at a more positive potential than the redox processes of the tungsten framework (Figure 3.3a). In accordance with electrochemical data previously reported for the silicon analogue ($[SiVW_{11}O_{40}]^{5-}$ [22]), a single electron is transferred at high potential in a V^{V}/V^{IV} reaction ($E_{1/2}$ = 0.847 V vs SHE) and two two-electron reductions occur at low potential which are W^{VI}/W^{V} processes ($E_{1/2}$ = -0.161 V vs SHE and -0.371 V vs SHE). A peak that is similar in appearance to the peak preceding the V^{V}/V^{IV} peak of **PVW_{11}** is also described in the study of $[SiVW_{11}O_{40}]^{5-}$, where it is assigned to an irreversible V^{IV}/V^{III} process.[22]

PV_2Mo_{10} may have exhibited both vanadium-based and molybdenum-based reactions but the individual redox processes were poorly resolved in the CV (Figure 3.3b). In a previous voltammetric study, it was reported that a redox wave corresponding to the reduction of vanadium(V) to vanadium(IV) was observed at 0.7 V vs SHE in a CV of a vanadium(V)-substituted molybdophosphate complex that had formed in a solution containing the lacunary $[H_3PMo_{11}O_{39}]^{4-}$ anion and vanadium(V) ions.[23] This demonstrates that both vanadium and molybdenum can show redox activity in vanadium-substituted molybdophosphates. Thus, some of the redox processes in the CV in Figure 3.3b could be ascribed to a V^{V}/V^{IV} process. In particular, a peak with $E_{1/2}$ of 0.689 V vs SHE (Figure 3.3c) became clearer when limiting the potential scan range to 0.974 V vs SHE–0.474 V vs SHE which is similar to the previously reported redox potential for the V^{V}/V^{IV} reaction of the aforementioned vanadium(V)-substituted molybodophosphate.[23]

Considering the molybdenum redox processes, it is likely that some of the redox activity observed for **PV_2Mo_{10}** in the CV in Figure 3.3b is attributable to molybdenum. A more positive reduction potential for the molybdenum framework of **PV_2Mo_{10}** than for the reactions of a tungsten-based POM would be expected as it has been shown that reduction potential decreases with increasing electronegativity, and molybdenum is less electronegative than tungsten.[24] For instance, the trend observed in a comparison of the first reduction potential values of $H_nPW_{11}M_1O_{40}$ species, where M = W, Mo or V, was a decrease in reduction potential with increasing electronegativity of the ‘M’ atom in the structure.[24] As an additional example, the redox wave for the first reduced state of the Keggin structure $[PMo_{12}O_{40}]^{3-}$ occurs at around 0.55 V vs SHE,[25] whereas the first reduction peak of $[PW_{12}O_{40}]^{3-}$ occurs at 0.22 V vs SHE.[26]

A disubstituted silicotungstate and phosphotungstate, $[SiV_2W_{10}O_{40}]^{6-}$ and $[PV_2W_{10}O_{40}]^{5-}$, are also possible.[19, 27] These species would be expected to have a greater separation in potential between redox processes than **PV_2Mo_{10}**. For the electrochemistry of $[SiV_2W_{10}O_{40}]^{6-}$, peaks corresponding to the reduction of the vanadium atoms (V^{V}/V^{IV} and

V^{IV}/V^{III}) were described, followed by two two-electron peaks that corresponded to the reduction of tungsten.[27]

Compared to **PVW$_{11}$**, a CV of **SiV$_3$W$_9$** shows additional redox reactions at positive potentials, corresponding to the reduction and oxidation of the three vanadium addenda atoms (Figure 3.3d). The features match a CV of **SiV$_3$W$_9$** shown in previous work.[16] A one-electron wave and a two-electron wave corresponding to V^{V}/V^{IV} reactions and two sets of two-electron waves corresponding to W^{VI}/W^{V} reactions are present.

While this is a limited cross section of mixed addenda POMs, these three CVs illustrate that the POM that exhibits the most desirable electrochemistry for a symmetric RFB species is **SiV$_3$W$_9$**, for reasons summarised below:

- In the CV of **PVW$_{11}$**, the vanadium and tungsten redox reactions are widely spaced by around 1 V but the number of electrons transferred is poorly balanced. Only one electron is transferred in the reversible V^{V}/V^{IV} process that occurs at higher potential compared to the four electrons involved in the tungsten redox reactions.
- **PV$_2$Mo$_{10}$** contains an additional vanadium addenda atom that could contribute an extra electron to the positive potential reactions of an RFB, but the vanadium redox reactions and molybdenum redox reactions were not properly assigned to specific redox processes in this cyclic voltammetry study. The difference in potential that the redox reactions of vanadium and molybdenum occur at is expected to be less compared to vanadium and tungsten, which would reduce the theoretical voltage of a symmetric RFB based on a POM like **PV$_2$Mo$_{10}$**.
- In the CV of **SiV$_3$W$_9$**, three vanadium atoms can contribute electrons at positive potential, unlike in **PVW$_{11}$** which has only one vanadium atom in the structure. Further, the vanadium reactions and tungsten reactions are more widely spaced (there is a difference of ~1 V between $E_{1/2}$ of the first vanadium peaks and the first tungsten peaks) when compared to the redox reactions in **PV$_2$Mo$_{10}$**.

Therefore, due to the three redox-active vanadium atoms and the greater separation in potential between the redox reactions of vanadium and tungsten compared to vanadium and molybdenum, **SiV$_3$W$_9$** exhibits the most desirable electrochemical profile for a symmetric POM RFB out of these examples, making it the most appropriate choice for demonstration of the concept. As mentioned, **SiV$_3$W$_9$** was previously tested in a flow cell by Pratt *et al*. and this work will be referred back to in this study.[16]

3.4 Fundamentals and Electrochemistry of $[SiV_3W_9O_{40}]^{7-}$

The **SiV_3W_9** anion can exist as two isomers, **α-SiV_3W_9** and **β-SiV_3W_9**. As for the parent Keggin anion $[SiW_{12}O_{40}]^{4-}$, rotation of one W_3O_{13} group by 60° results in a β isomer (Figure 3.4).

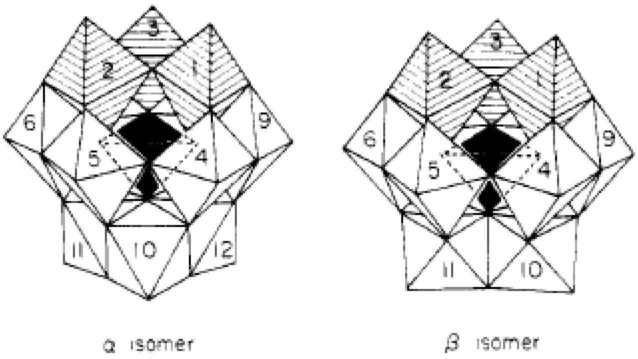

Figure 3.4 - The α and β isomers of ***SiV_3W_9****. The striped octahedra represent VO_6 units. (Reprinted with permission from R. G. Finke, B. Rapko, R. J. Saxton and P. J. Domaille, J. Am. Chem. Soc., 1986, 108(11), 2947–2960. Copyright 1986 American Chemical Society.)*

Each isomer is synthesised from VO_2^+ and the corresponding α or β isomer of the lacunary precursor, $[SiW_9O_{34}]^{10-}$ (**α-SiW_9** or **β-SiW_9**).[21] The preparation of **β-SiV_3W_9** is shown below.[21]

$$[SiO_3]^{2-} + 9[WO_4]^{2-} + 11H^+ \rightarrow \beta(H[SiW_9O_{34}])^{9-} + 5H_2O \tag{3.1}$$

$$3[VO_3]^- + 6H^+ \rightarrow 3[VO_2]^+ + 3H_2O \tag{3.2}$$

$$\beta(H[SiW_9O_{34}])^{9-} + 3[VO_2]^+ \rightarrow H[\beta SiV_3W_9O_{40}]^{6-} \tag{3.3}$$

The α and β isomers can be distinguished by ^{51}V NMR spectroscopy. The **SiV_3W_9** anion exhibits a single vanadium peak corresponding to the three equivalent vanadium(V) atoms in the structure. The chemical shift of this peak is different for each isomer, as shown in Figure 3.5 (-569 ppm for **α-SiV_3W_9** and -576 ppm for **β-SiV_3W_9** at pH 2.0).

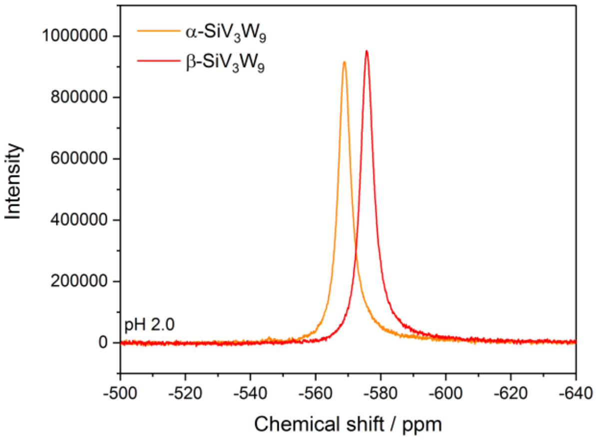

Figure 3.5 - ^{51}V NMR spectra of the α and β isomer of ***SiV_3W_9****.*

The electrochemical properties of **α-SiV_3W_9** are illustrated in Figure 3.6. It can be seen that the single two-electron reduction peak in 1 M H_2SO_4 (shown previously in Figure 3.3d) splits into three peaks when the supporting electrolyte is changed from 1 M H_2SO_4 to acidified 1 M Li_2SO_4 at pH 2.0. As a result, three reduction peaks that correspond to the three vanadium atoms in the **SiV_3W_9** structure are visible.

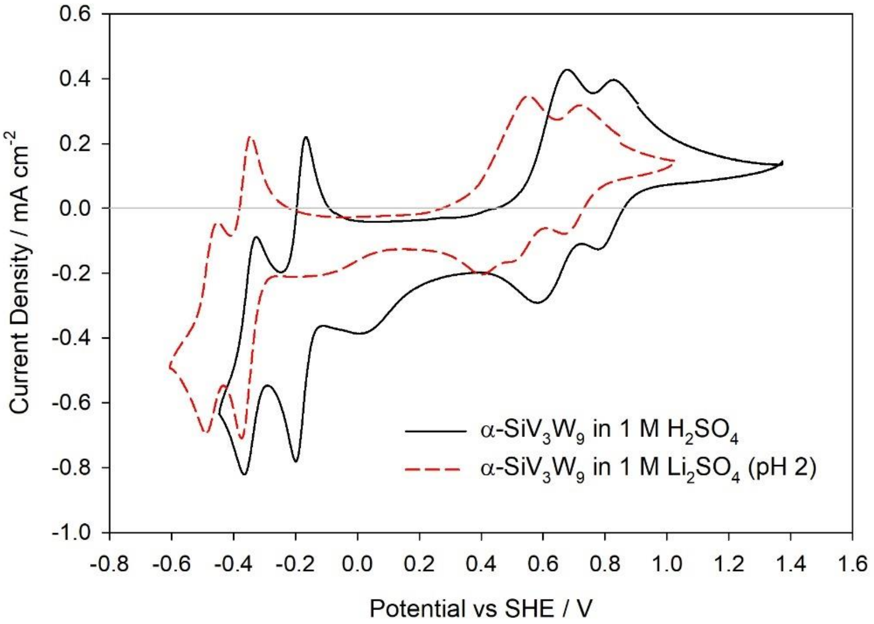

*Figure 3.6 - CVs of **α-SiV_3W_9** (1 mM) in supporting electrolytes of 1 M H_2SO_4 and 1 M Li_2SO_4 that was acidified to pH 2 with 1 M H_2SO_4. (1 M H_2SO_4: WE: glassy carbon, CE: gold wire, RE: MSE (1 M H_2SO_4), scan rate: 100 mV/s. 1 M Li_2SO_4 (pH 2) WE: glassy carbon, CE: platinum wire, RE: MSE (1 M H_2SO_4), scan rate: 100 mV/s)*

CVs focused on the vanadium and tungsten redox processes at different scan rates are shown in Figure 3.7. For the first pair of vanadium peaks ($E_{1/2}$ = 0.695 V vs SHE), the first pair of tungsten peaks ($E_{1/2}$ = -0.359 V vs SHE) and the second pair of tungsten peaks ($E_{1/2}$ = -0.472 V vs SHE), a linear relationship is shown between the peak current and the square root of the scan rate which is indicative of a reversible cyclic voltammogram (Figure 3.8). The addition of data points at higher scan rates to the plots would be desirable to support the presence of a linear relationship but CVs at scan rates of above 100 mV/s were not obtained.

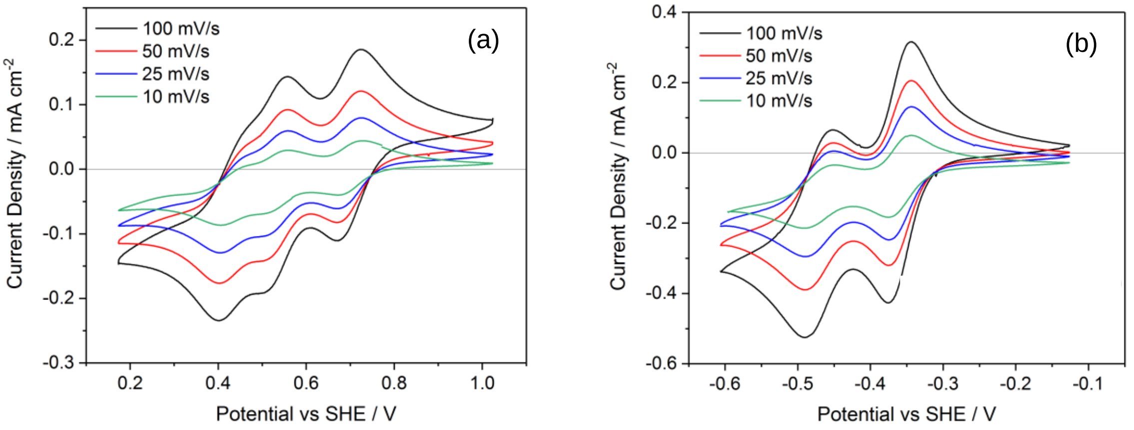

*Figure 3.7 - (a) CVs of 1 mM **α-SiV$_3$W$_9$** in 1 M Li_2SO_4 acidified to pH 2 with 1 M H_2SO_4 at different scan rates focused on the vanadium redox activity. (b) CVs at different scan rates focused on the tungsten redox activity. (WE: glassy carbon, CE: platinum wire, RE: MSE (1 M H_2SO_4), scan rate: 100 mV/s)*

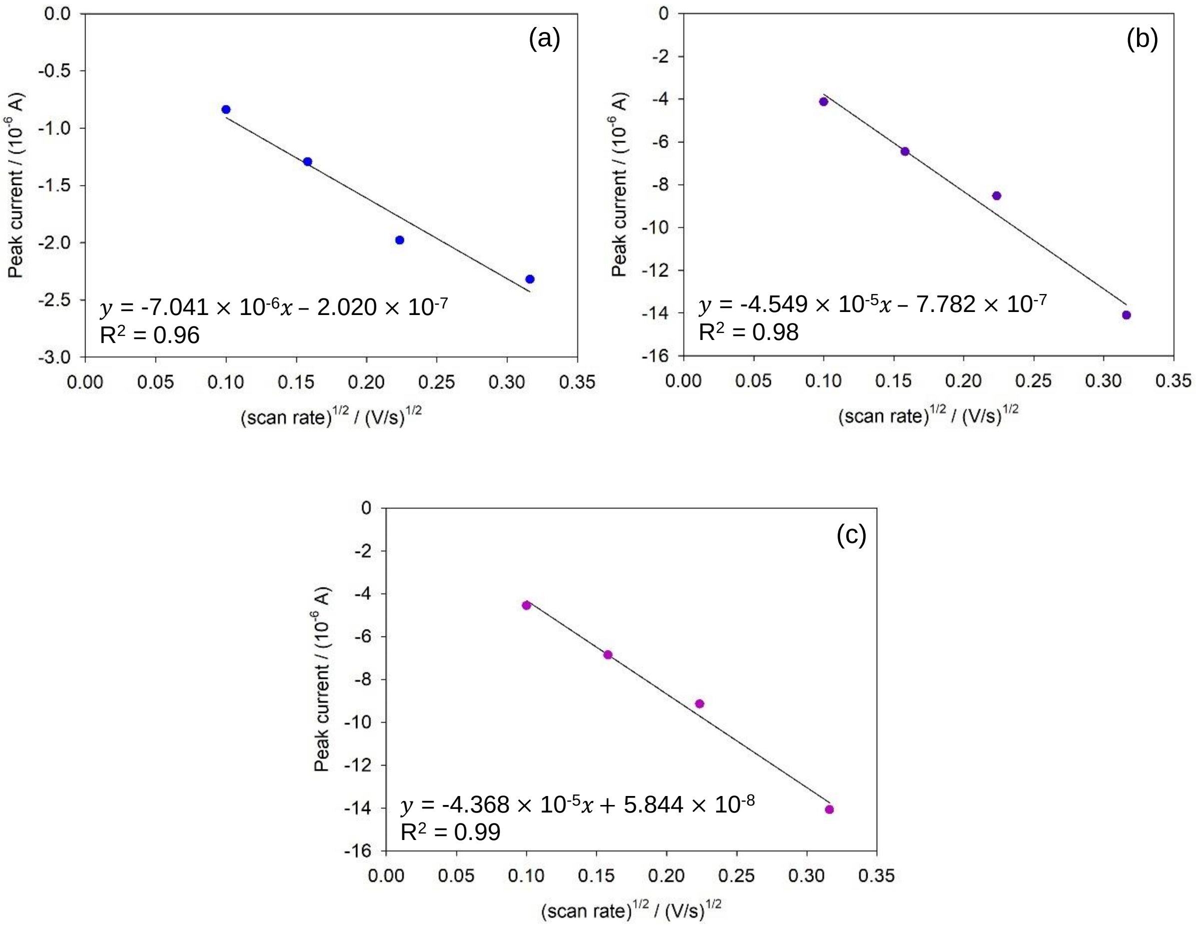

Figure 3.8 - (a) A plot of reduction peak current versus the square root of the scan rate for the first vanadium peak. (b) A plot of reduction peak current versus the square root of the scan rate for the first tungsten peak. (c) A plot of reduction peak current versus the square root of the scan rate for the second tungsten peak. (All currents were measured from the baseline of the first cycle of the CVs shown in Figure 3.7.)

The criteria used to discern a reversible cyclic voltammogram are as follows.[28] Firstly, as noted, the peak current should be proportional to the square root of the scan rate which was indicated in Figure 3.8. Secondly, the peak potential, E_p, should be independent of the scan rate. A shift in E_p was not observed when comparing CVs of **α-SiV$_3$W$_9$** at different scan rates. Thirdly, the following criteria should apply, which were referred to in Section 2.3.8:

$$\frac{i_{pa}}{i_{pc}} = 1 \qquad 2.51$$

$$\Delta E_p = \frac{2.3\,RT}{nF}(0.059/\mathrm{n\ V\ at\ 25°C}) \qquad 2.52$$

For the first redox reaction of vanadium, the ratios of the anodic peak current to the cathodic peak current were 0.96 (10 mV/s), 1.28 (25 mV/s), 1.18 (50 mV/s) and 1.68 (100 mV/s). For the first redox reaction of tungsten, i_{pa}/i_{pc} values were 0.28 (10 mV/s), 0.39 (25 mV/s), 0.48 (50 mV/s) and 0.45 (100 mV/s). For the second redox reaction of tungsten, i_{pa}/i_{pc} was 0.073 for a scan rate of 100 mV/s. A negative current was recorded on the reverse scan for scan rates less than 100 mV/s. In general, pairs of peaks for **α-SiV$_3$W$_9$** were asymmetrical around the baseline and i_{pa}/i_{pc} deviated from 1. This can indicate complications in the electrode process. However, in CVs of **α-SiV$_3$W$_9$**, it was noted that the negative cathodic current on the forward scan was generally larger than the positive anodic current on the reverse scan, perhaps due to **α-SiV$_3$W$_9$** being fully oxidised at the start of the reverse scan, which may result in the deviations of i_{pa}/i_{pc} from 1 that were calculated. Nonetheless, the CVs of **α-SiV$_3$W$_9$** do not meet one of the criteria for a reversible voltammogram.

A chemically reversible and electrochemically reversible process is indicated by closeness to the theoretical value of ΔE_p, where chemical reversibility refers to a species that is stable after reduction and can be reoxidised and electrochemical reversibility refers to a species with kinetics that are so facile that a Nernstian equilibrium is always established at the electrode/solution interface when the potential of the electrode is changed.[29] Unlike the values for i_{pa}/i_{pc}, values of ΔE_p calculated for **α-SiV$_3$W$_9$** were close to the theoretical value. The difference in peak separation, ΔE_p, for the first vanadium reaction was 0.055 V which was close to the theoretical value for a one-electron reaction. For the first tungsten reaction, ΔE_p was 0.031 V which was close to the theoretical value for a two-electron reaction (0.030 V). For the second tungsten reaction, ΔE_p was 0.040 V. This differs from the theoretical value of ΔE_p but is closer to the theoretical value for a two-electron reaction than for a one-electron reaction. The oxidation peak for the second tungsten reaction is noticeably smaller than the oxidation peak for the first tungsten reaction, which does suggest that this reaction is less straightforward.

The diffusion coefficient was estimated by using the slope of the plots of the peak current against the square root of the scan rate. The following equation was used:[29]

$$D = \left(\frac{slope}{0.4463nFAc}\right)^2 \frac{RT}{nF} \qquad 3.4$$

In Equation 3.4, *n* is the number of electrons transferred, *A* is the geometric surface area of the electrode in cm^2, and *c* is the bulk concentration of the species under study in mol cm^{-3}.

Inserting the slope of the plot of reduction peak current versus the square root of the scan rate for the first reduction of **α-SiV$_3$W$_9$** (Figure 3.8a) into Equation 3.4 gave an estimation for the diffusion coefficient of 1.72×10^{-6} cm^2 s^{-1}. The order of magnitude of this value is the same as the diffusion coefficient reported for the parent structure, $[SiW_{12}O_{40}]^{4-}$. Values reported for $[SiW_{12}O_{40}]^{4-}$ include $2.56 \pm 0.15 \times 10^{-6}$ cm^2 s^{-1},(30) 3.9×10^{-6} cm^2 s^{-1},(31) and 2.8×10^{-6} cm^2 s^{-1}.[32] The values for the diffusion coefficient are also comparable to other RFB active species that were recently investigated such as a quinone species (1.58×10^{-6} cm^2 s^{-1}),[33] and a TEMPO derivative and methyl viologen (4.8×10^{-6} cm^2 s^{-1} and 5.7×10^{-6} cm^2 s^{-1}).[34] A diffusion coefficient of $\approx 10^{-6}$ cm^2 s^{-1} is also comparable to the active species of the VRFB. When the diffusion coefficients of V^{3+} and VO^{2+} were measured using electrolytes of between 0% and 80% SOC, it was found that values ranged from 4.02×10^{-7} cm^2 s^{-1} and 7.25×10^{-6} cm^2 s^{-1} for V^{3+} and from 3.55×10^{-7} cm^2 s^{-1} and 2.33×10^{-6} cm^2 s^{-1} for VO^{2+}.[35] The diffusion coefficient of VO_2^+ has been calculated to be 1.4×10^{-6} cm^2 s^{-1}.[36]

Based on $E_{1/2}$ for the second set of vanadium peaks (0.535 V vs SHE) and the first set of tungsten peaks (-0.360 V vs SHE), the theoretical voltage for an RFB based on **α-SiV$_3$W$_9$** is 0.895 V. The maximum theoretical voltage, calculated using $E_{1/2}$ of the first set of vanadium peaks (0.700 V vs SHE) and the second set of tungsten peaks (-0.472 V vs SHE), is 1.12 V. Based on a theoretical voltage of 0.895 V and the maximum concentration of the potassium salt of **α-SiV$_3$W$_9$** in water (determined to be 0.45 M[16]) the theoretical energy density of an **α-SiV$_3$W$_9$** RFB is 16 Wh L^{-1}.

Regarding the vanadium peaks, Cadot *et al*. reported that the first vanadium reduction of **α-SiV$_3$W$_9$** is proton coupled. A potential shift of -60 mV pH^{-1} was observed for the first vanadium peak which corresponded to exchange of one electron and one proton.[37] Below pH 9.5 and above pH 4, a slope of -60 mV pH^{-1} unit was observed, while at values of between pH 3 and 4, the value of the slope decreased which was attributed to protonation of oxidised **α-SiV$_3$W$_9$** in this pH range and no involvement of a proton in the redox reaction. Below pH 3, the slope of -60 mV pH^{-1} unit was observed again.[37]

The proton dependence of POM reactions has been studied. Keita and Nadjo found that when the pH of aqueous solutions was lowered, the first two monoelectronic reactions of

$[SiW_{12}O_{40}]^{4-}$ and $[P_2W_{18}O_{62}]^{6-}$ merged into a single bielectronic process.[38] When the pH of solutions of the same POMs in dimethylformamide was lowered, it was found that additional electrons could be added to the POMs due to single electron transfers becoming multi-electron transfers, the reduction pattern for $[SiW_{12}O_{40}]^{4-}$ changing from an electron ratio of 1:1:2 to 2:2:4 for instance.[38] Pope and Varga suggested that the number of electrons that a series of Keggin structures could be reduced by was limited by the overall charge of the anion, but could be increased if protonation accompanied reduction.[30] In solutions of pH ≥ 5, $[FeW_{12}O_{40}]^{5-}$ could be reduced by three electrons and $[CoW_{12}O_{40}]^{6-}$ and$[H_2W_{12}O_{40}]^{6-}$ could be reduced by two electrons. As the pH was lowered, protonation could begin to accompany reduction and one-electron waves identified using polarography were converted to two-electron waves, such that $[FeW_{12}O_{40}]^{5-}$ could be reduced by five electrons and $[CoW_{12}O_{40}]^{6-}$ and $[H_2W_{12}O_{40}]^{6-}$ by four electrons. Generally, PCET in chemical and biological redox reactions provides “reaction pathways in which electrons and protons are transferred simultaneously, thus avoiding high energy intermediates”.[39] In relation to the proton dependence of POM reactions, the increasing negative charge upon reduction encourages protonation, which counters the negative charge and allows further reduction.[40]

To investigate further whether **α-SiV$_3$W$_9$** undergoes proton-coupled electron transfer (PCET), CVs were obtained in supporting electrolytes of different pH, by dissolving **α-SiV$_3$W$_9$** in solutions of 1 M Li_2SO_4 that had been adjusted to pH values within the range 1.5–3.0 with 1 M H_2SO_4 (Figure 3.9).

The CVs provided evidence that the first vanadium reduction is indeed proton coupled in this pH range. The slope of a graph of $E_{1/2}$ for the first set of vanadium peaks versus the pH was -0.048 V pH^{-1}. This is lower than the theoretical value of -0.059 V pH^{-1} for a one-electron one-proton reaction. The result obtained by Cadot *et al.* was closer to this theoretical value and they investigated a greater pH range.[37] In light of this, determining $E_{1/2}$ values across a larger pH range for **α-SiV$_3$W$_9$** would be desirable to allow a more extensive comparison with their results. However, a dependence of $E_{1/2}$ on the proton concentration is indicated by the linearity of the data points in this work (Figure 3.9b).

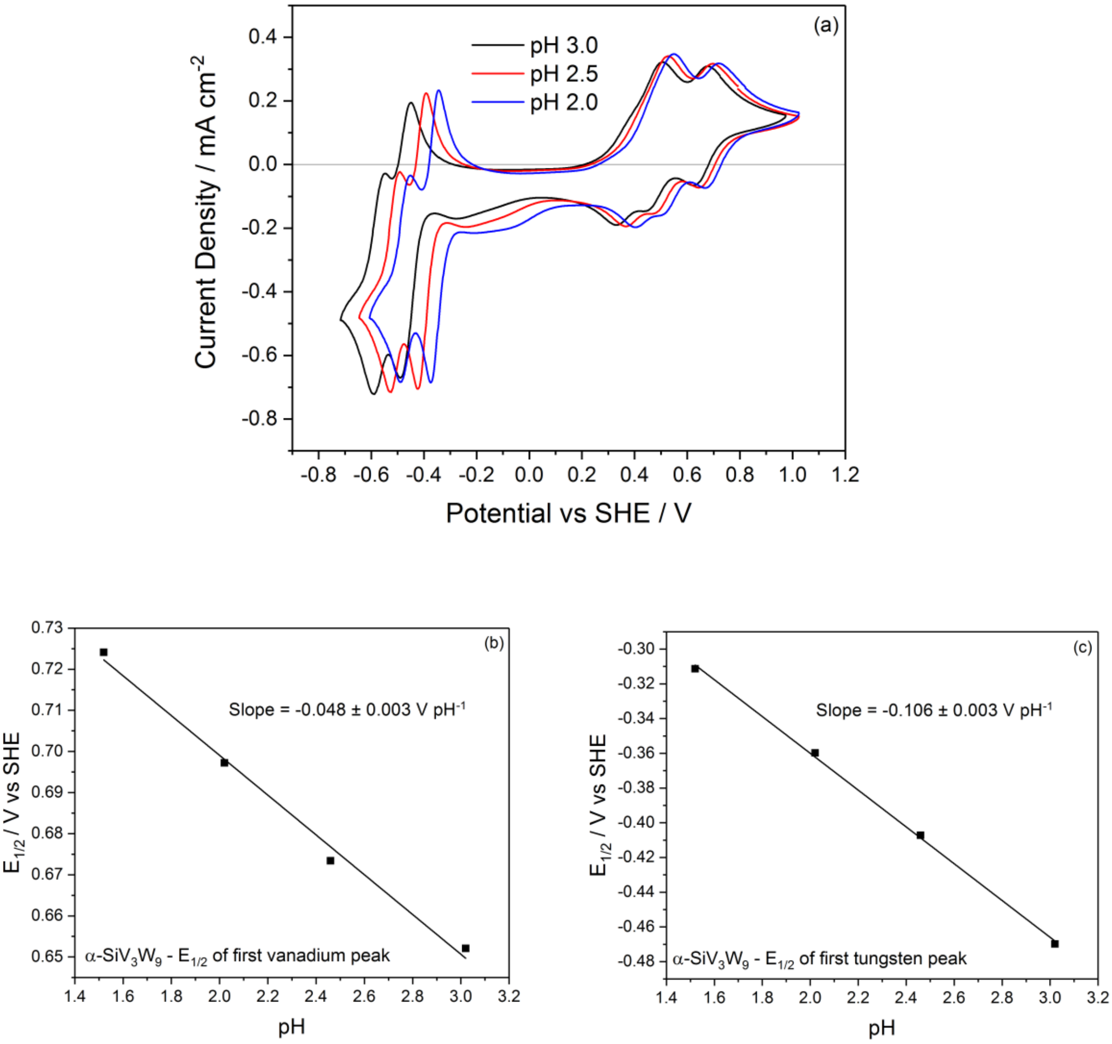

Figure 3.9 - (a) CVs of 1 mM ***α-SiV_3W_9*** *solutions in 1 M Li_2SO_4 acidified to different pH values with 1 M H_2SO_4. (b) A plot of $E_{1/2}$ of the first vanadium reduction peak versus pH. (c) A plot of $E_{1/2}$ of the first tungsten reduction peak versus pH. (WE: glassy carbon, CE: platinum wire, RE: MSE (1 M H_2SO_4), scan rate: 100 mV/s)*

For a reaction in which one proton and one electron are transferred, the equation for the first vanadium reduction of **α-SiV_3W_9** would be as follows:

$$[SiV_3^VW_9O_{40}]^{7-} + H^+ + e^- \rightarrow [HSiV^{IV}V_2^VW_9O_{40}]^{7-} \qquad 3.5$$

The CVs shown in Figure 3.9a that were obtained at different pH indicate that each set of vanadium and tungsten peaks shifts to a more negative potential as the pH increases, suggesting that the potential of all of the vanadium and tungsten redox reactions has a dependence on the proton concentration in this pH range. A slope of -0.106 V pH^{-1} was obtained by plotting $E_{1/2}$ of the first tungsten reduction peak against pH (Figure 3.9c), which is closer to the theoretical value for a two-electron two-proton process (-0.118 V pH^{-1}) than the value for a reaction where one electron and one proton are transferred.[41]

The peaks for the second and third vanadium reactions were less defined as the oxidation peak of the third reaction merges with the oxidation peak of the second reaction as the pH is lowered, but estimation of $E_{1/2}$ for the second vanadium reaction was possible. Recording a CV across a potential range where only the vanadium peaks occur allowed the second and third vanadium reactions to be viewed with more clarity (Figure 3.10).

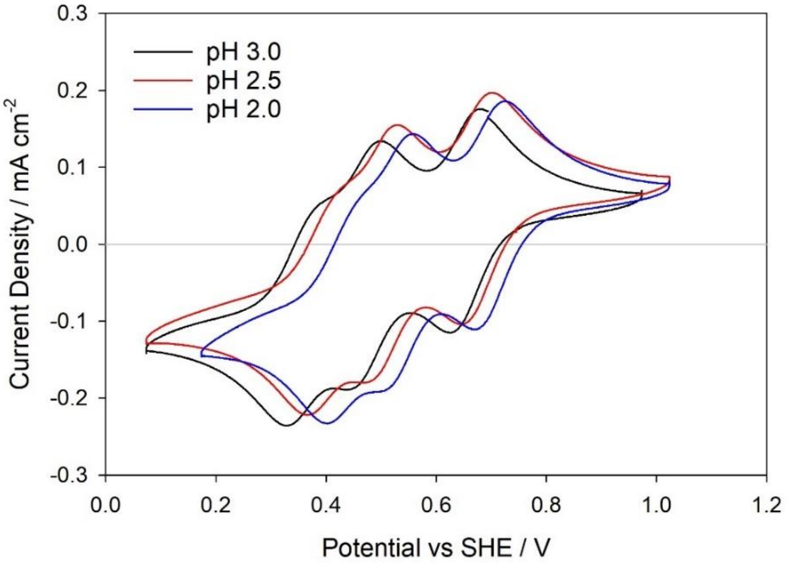

Figure 3.10 - CVs of ***α-SiV₃W₉*** *focused on the vanadium peaks in a supporting electrolyte of 1 M* Li_2SO_4 *acidified to different pH values with 1 M* H_2SO_4*. (WE: glassy carbon, CE: platinum wire, RE: MSE (1 M* H_2SO_4*), scan rate: 100 mV/s)*

The slope of a graph of $E_{1/2}$ of the second set of vanadium peaks versus pH was -0.065 V pH^{-1} which is close to the theoretical value for a reaction in which one proton and one electron are transferred. This suggests that there is additional protonation of the POM after the first vanadium reaction but before the first tungsten reaction. Taking this additional protonation of the POM into account, the equation for the first tungsten reduction of **α-SiV₃W₉** would be as follows, for a reaction in which two protons and two electrons are transferred:

$$[H_3SiV_3^{IV}W_9^{VI}O_{40}]^{7-} + 2H^+ + 2e^- \rightarrow [H_5SiV_3^{IV}W_2^{V}W_7^{VI}O_{40}]^{7-} \qquad 3.6$$

This equation assumes additional protonation of the POM has occurred after the first vanadium redox reaction and before the first tungsten redox reaction.

The dependence of the value of $E_{1/2}$ on proton concentration suggests that the reduced forms of **SiV₃W₉** are protonated species in this pH range, so may be represented as $[SiV_3W_9O_{40}H_3]^{7-}$ after reduction of vanadium and $[SiV_3W_9O_{40}H_7]^{7-}$ after reduction of tungsten. The occurrence of PCET for both the vanadium and tungsten redox reactions would be beneficial if these reactions were used as the high potential and low potential redox reactions of a symmetric flow cell as, upon charge and discharge, protons could be taken up by the active species in one half-cell at the same time as being released by active species in the other half-cell.

3.5 pH Effects on the Stability of $[SiV_3W_9O_{40}]^{7-}$

Further preliminary electrochemical investigations of **SiV_3W_9** were carried out in a supporting electrolyte of 1 M H_2SO_4. CVs of **α-SiV_3W_9** and **β-SiV_3W_9** cycled 100 times in 1 M H_2SO_4 are shown in Figure 3.11.

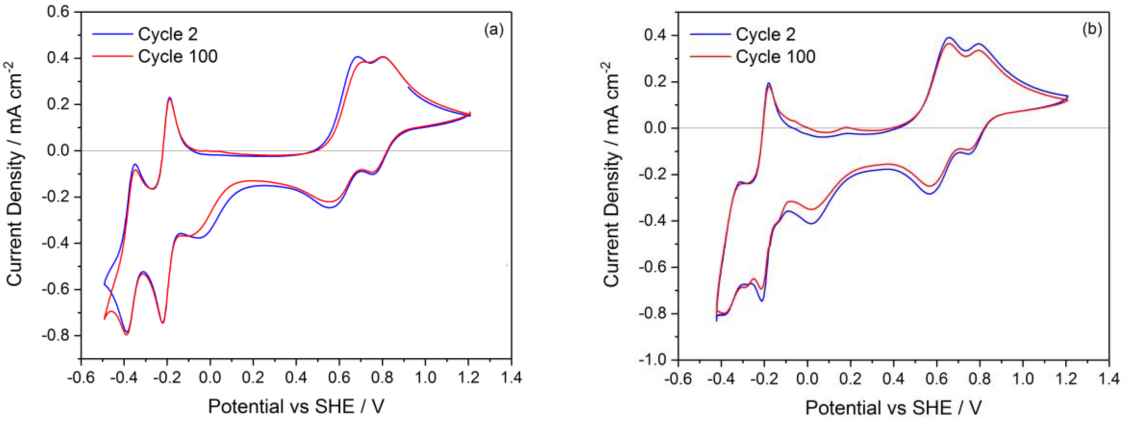

*Figure 3.11 - (a) Initial CV of a 1 mM **α-SiV_3W_9** solution and a CV after cycling 100 times in 1 M H_2SO_4. (b) Initial CV of a 1 mM **β-SiV_3W_9** solution and a CV after cycling 100 times in 1 M H_2SO_4. (WE: glassy carbon, CE: platinum wire, RE: Ag/AgCl (3 M NaCl), scan rate: 100 mV/s)*

Moderate changes in the CVs of **α-SiV_3W_9** and **β-SiV_3W_9** were visible after 100 cycles. The change in appearance of the second tungsten reduction peak centred at -0.367 V vs SHE in the CV of **α-SiV_3W_9** could be due to adsorption of the POM on the surface of the glassy carbon electrode as it was found in practice that the appearance of these peaks could be restored following polishing of the electrode. It has been shown before that the parent species, $[SiW_{12}O_{40}]^{4-}$, modifies glassy carbon surfaces when scanning to potentials where $[SiW_{12}O_{40}]^{4-}$ is in its most reduced state, leading to an earlier onset of the hydrogen evolution reaction.[42] This modification involves the potential-dependent deposition of molecules on the electrode surface which then catalyse the hydrogen evolution reaction.[43] A similar occurrence could take place during cyclic voltammetry of **SiV_3W_9**.

The changes in the CV of **β-SiV_3W_9** were particularly noticeable. Additional peaks have appeared in the potential region where tungsten reduction occurs which could be attributed to decomposition products. Further, in the charge/discharge curves of a preliminary stationary cell test that used electrolytes of **β-SiV_3W_9** in 1 M H_2SO_4, shown in Figure 3.12a, the discharge curves did not have a stable appearance. In spite of coulombic efficiencies of ~96% after cycle 15 (Figure 3.12b), discharge curves with features that change with cycling could indicate that active species are not stable.

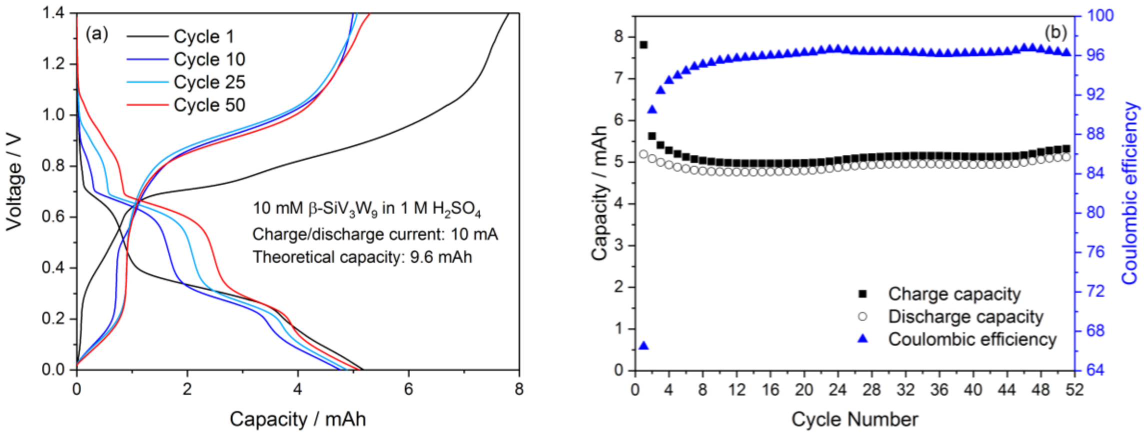

*Figure 3.12 - (a) Charge/discharge curves of a **β-SiV$_3$W$_9$** stationary cell with a 1 M H_2SO_4 supporting electrolyte. (b) A plot of charge capacity, discharge capacity and coulombic efficiency versus cycle number.*

The catholyte was extracted after 51 charge/discharge cycles when the cell was in a charged state and an NMR spectrum was obtained. The anolyte of the cell in the charged state was not subjected to ^{51}V NMR spectroscopy due to the assumed presence of vanadium(IV), which would not provide a signal. The ^{51}V NMR spectrum of the catholyte showed two peaks at -557 ppm and -543 ppm (Figure 3.13). The chemical shift of the first peak at -557 ppm is not characteristic of the chemical shift of **β-SiV$_3$W$_9$**, which is greater than -570 ppm at pH 4 and below (as shown later in Figure 3.18). This suggests that this peak is not attributable to **β-SiV$_3$W$_9$** and could instead be attributable to a decomposition product. The peak at -543 ppm has a chemical shift that is comparable to that of the pervanadyl ion, VO_2^+.[44] Therefore, the NMR spectrum suggested that decomposition products were present in the catholyte and that **β-SiV$_3$W$_9$** was not stable under these charge/discharge conditions.

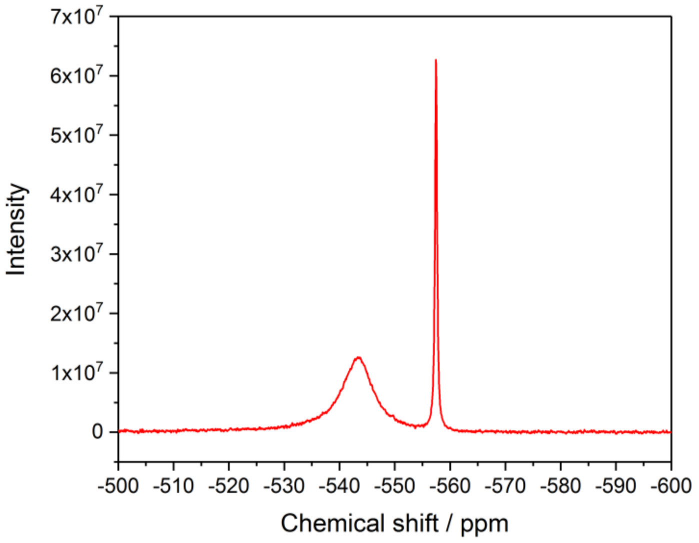

*Figure 3.13 - A ^{51}V NMR spectrum of the catholyte of the **β-SiV$_3$W$_9$** stationary cell from Figure 3.12 after charge/discharge testing.*

The previous results cast doubt on whether **β-SiV_3W_9** could be used as an RFB active species. Therefore, further assessment of the stability of the POM in a supporting electrolyte of 1 M H_2SO_4 was carried out. The method of Controlled Potential Electrolysis (CPE) was selected for this purpose which was carried out in a bulk electrolysis cell. The aim of using CPE was to record the open circuit potential (OCP) of **α-SiV_3W_9** solutions after the reduction of vanadium and tungsten. Given that the OCP varies depending on the ratio of oxidised and reduced species in solution in accordance with the Nernst equation, monitoring this value would be a way of assessing how stable a species is in a particular oxidation state. A stable OCP indicates a stable ratio of oxidised and reduced species in solution.

However, CVs of the solutions after CPE at a potential corresponding to reduction of the tungsten atoms (-0.391 V vs SHE) indicated that a change in the POM species had occurred (Figure 3.14). In both instances, the total charge passed in CPE equalled the charge required for reduction of the POM by six electrons (corresponding to reduction of three V^{V} centres to V^{IV} and three W^{VI} centres to W^{V}).

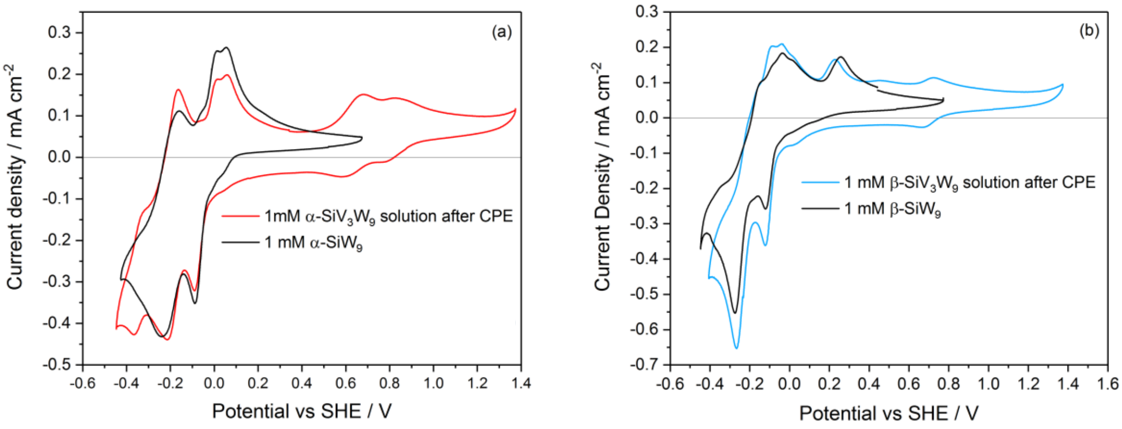

*Figure 3.14 - (a) A CV of **α-SiV_3W_9** in 1 M H_2SO_4 after CPE at -0.391 V vs SHE. (b) A CV of **β-SiV_3W_9** in 1 M H_2SO_4 after CPE at -0.391 V vs SHE. (WE: glassy carbon, CE: gold wire, RE: MSE (1 M H_2SO_4), scan rate: 100 mV/s)*

In a CV of the reduced **α-SiV_3W_9** solution, the vanadium peaks are diminished and additional peaks have appeared in the potential region where reduction of tungsten occurs (Figure 3.14a). The CV of the reduced **β-SiV_3W_9** solution shows a similar result (Figure 3.14b). Further, when overlaid with CVs of the lacunary precursor for each isomer (also shown in Figure 3.14) it was noticed that the new peaks appearing after reduction bore a similarity to the peaks observed in CVs of **α-SiW_9** and **β-SiW_9**. When cycling in a potential region where the VO_2^+/VO^{2+} redox couple would be expected to be observed, a large oxidation peak was present at 1.60 V vs SHE (Figure 3.15). This oxidation peak occurs at a similar potential to values that have been previously reported for the $VO^{2+} \rightarrow VO_2^+$ oxidation peak in the same electrolyte (1.59 V vs SHE).[45] The lack of a reduction peak indicates that the process is irreversible. The presence of this peak suggested that vanadium had been removed from **SiV_3W_9**, reverting it to the corresponding isomer of the precursor species, **SiW_9**, and free vanadium (VO^{2+}).

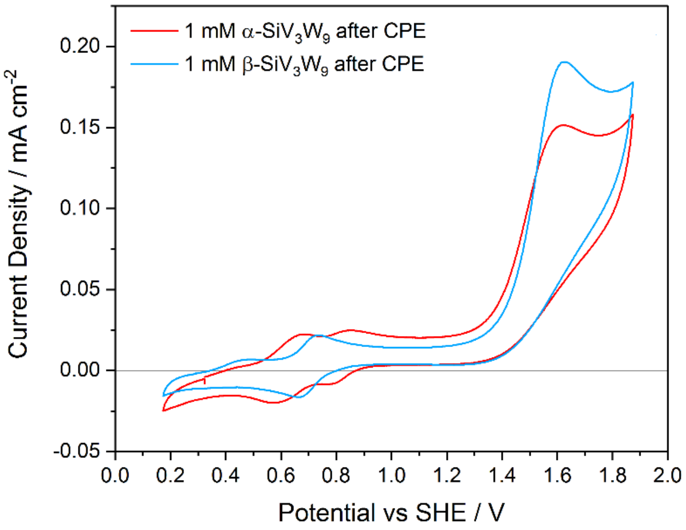

*Figure 3.15 - Overlaid CVs of the reduced **α-SiV_3W_9** and reduced **β-SiV_3W_9** solutions in 1 M H_2SO_4 cycled between 0.174 V vs SHE and 1.870 V vs SHE, showing an additional oxidation peak. (WE: glassy carbon, CE: gold wire, RE: MSE (1 M H_2SO_4), scan rate: 10 mV/s)*

As a potential at which both the tungsten and vanadium would be reduced was used in the CPE procedure previously (-0.391 V vs SHE), an additional CPE experiment was carried out. This time the potential was held at 0.398 V vs SHE, so that only the reduction of vanadium(V) to vanadium(IV) would be expected to occur in **SiV_3W_9**. The aim of this experiment was to determine the extent of reduction that corresponded to destruction of the POM, i.e., could the decomposition to **SiW_9** be associated with reduction solely of vanadium, or was the reduction of both tungsten and vanadium required for this to occur. A CV of the **α-SiV_3W_9** solution after CPE at 0.398 V vs SHE is shown in Figure 3.16. This bears a similarity to the CV in Figure 3.14a, again exhibiting features of the CV of the lacunary precursor, **α-SiW_9**, which is also shown. This result indicates that the instability of **SiV_3W_9** can be associated with reduction of the vanadium only and suggests that there could be a difference in the stability of the vanadium(V) and the vanadium(IV) oxidation states of **SiV_3W_9**. This is significant when considering the application of **SiV_3W_9** in an RFB (as in the work of Pratt *et al.*[16]) because it is a necessity that the active species of an RFB is stable in all oxidation states. Pratt *et al*. did not discuss any issues with the stability of **SiV_3W_9**, stating that there was no evidence of decomposition of **SiV_3W_9** in UV-Visible, infrared and NMR spectra of solutions after charge/discharge testing. The UV-Visible spectra or NMR spectra were not presented by Pratt *et al.*, but an FT-IR spectrum of a sample of $\mathbf{SiV_3W_9}$ obtained by evaporating the electrolyte after charge/discharge testing had the same features as an FT-IR spectrum of a $\mathbf{SiV_3W_9}$ sample that had not been used in a flow cell. However, the result shown in this work in Figure 3.14 suggests that $\mathbf{SiV_3W_9}$ may be unstable in some conditions.

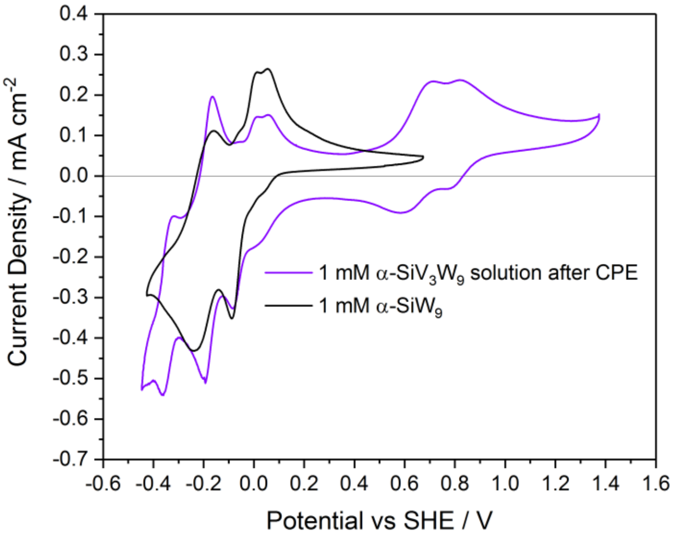

Figure 3.16 - A CV of a reduced $\boldsymbol{\alpha}$**-**$\mathbf{SiV_3W_9}$ *in 1 M* H_2SO_4 *after CPE at 0.398 V vs SHE, overlaid with a CV of* $\boldsymbol{\alpha}$**-**$\mathbf{SiW_9}$ *in the same supporting electrolyte. (WE: glassy carbon, CE: gold wire, RE: MSE (1 M* H_2SO_4*), scan rate: 100 mV/s)*

Surveying the literature on tungsten-based POMs that are substituted with vanadium shows that instability associated with reduction has been observed before: decomposition in solutions of reduced $[PV_3W_9O_{40}]^{6-}$ and $[PV_4W_8O_{40}]^{7-}$ was previously reported.[46] Analysis of the solution composition of $[PV^{IV}_3W_9O_{40}]^{6-}$ after storage under argon for 24 hours showed loss of vanadium from the POM structure had occurred, with a higher proportion of the vanadyl ion present in solutions with lower pH values (1% VO^{2+} in a reduced solution at pH 4.2 compared to 3% VO^{2+} at pH 2.5). The pH effect on stability was more marked for $[PV^{IV}_4W_8O_{40}]^{7-}$, with reduced solutions consisting of 65% VO^{2+} at pH 1.1 and 5% VO^{2+} at pH 4.1. The presence of $[PV_3W_9O_{40}]^{6-}$ in the $[PV_4W_8O_{40}]^{7-}$ solution after it was reoxidised, and $[PV_2W_{10}O_{40}]^{5-}$ in the reoxidised $[PV_3W_9O_{40}]^{6-}$ solution, suggested that formation of structures with the next lowest vanadium content occurred following removal of VO^{2+}.

A difference in stability that could be linked to the valence of metal ions in a substituted POM has been reported previously for a family of tungstosilicates, where pH was a factor that affected the stability of the lower valent species. The free acids of a series of $[Mn^{III}(H_2O)ZW_{11}O_{39}]^{n-}$ anions (Z = B, Zn, P, Si, Ge) could be prepared by using a cation exchange column in H^+ form, but the corresponding $[Mn^{II}(H_2O)ZW_{11}O_{39}]^{n-}$ species were unstable below a pH of 2.1, with Mn^{II} being removed during the cation exchange treatment.[47]

Further, the observation by Müller *et al.* that Mn^{II} and Co^{II} cations were removed from $[Mn^{II}(H_2O)SiW_{11}O_{39}]^{6-}$ and $[Co^{II}(H_2O)SiW_{11}O_{39}]^{6-}$ under acidic conditions followed the theme of low pH being associated with removal of metal ions from tungstosilicate structures in which some of the tungsten atoms had been substituted with other metals.[48] This was attributed to protonation of adjacent oxygen atoms which were more basic in the substituted tungstosilicates due to the substitution of W^{VI} with an M^{II} ion.

These previous studies suggest that POMs substituted with lower valent metals may be less stable under certain conditions and that instability is linked to low pH. Thus, the use of an acidic supporting electrolyte such as 1 M H_2SO_4 could be the factor that leads to decomposition in the reduced **SiV_3W_9** solutions. The results for **SiV_3W_9** were particularly interesting as Pratt *et al.* chose an acidic supporting electrolyte of 0.5 M H_2SO_4 for their **SiV_3W_9** flow cell.[16] Granted, this is half as concentrated as the supporting electrolyte used in the bulk electrolysis experiments here, but the results of these experiments in 1 M H_2SO_4 demonstrate that **SiV_3W_9** may be unstable when reduced and examples from literature studies indicate that instability of POMs substituted with metals that are below the maximum oxidation state (e.g. V^{IV}, Mn^{II}) is associated with low pH.

The instability of reduced **SiV_3W_9** that was observed is contrary to the reporting by Mossoba *et al.* of the isolation of the potassium salt of $[\alpha\text{-}SiV^{IV}{}_3W_9O_{40}H_3]^{7-}$ following electrochemical reduction of the vanadium in the POM.[49] Although the experimental conditions for the electrochemical reduction were not specified, this result suggests that reduced **SiV_3W_9** is stable under some conditions. Thus, the instability observed in this work could be attributable to the conditions that CPE was carried out under (i.e. the pH).

Owing to the acidic supporting electrolyte used in bulk electrolysis, the observations in literature of a lesser stability for POM structures substituted with lower valent metals[47, 48] and the reported isolation of the potassium salt of **$\alpha\text{-}SiV_3W_9$** after reduction,[49] it was proposed that pH was a factor that could affect the stability of reduced **$\alpha\text{-}SiV_3W_9$** and a pH stability study was carried out.

3.5.1 Stability of $[SiV^V{}_3W_9O_{40}]^{7-}$

The stability study was to encompass the investigation of the stability of the vanadium(V) species, **$SiV^V{}_3W_9$**, and the vanadium(IV) species, **$SiV^{IV}{}_3W_9$**, under conditions of different pH.

To investigate the stability of **$SiV^V{}_3W_9$**, ^{51}V NMR spectroscopy was utilised. **$SiV^V{}_3W_9$** solutions of different pH were prepared by dissolving the POM in water and then adjusting the solution to the desired pH. The pH values studied initially were pH 0.3, 1.0, 2.0, 3.0 and 4.0. NMR spectra of the **$\alpha\text{-}SiV^V{}_3W_9$** solutions acquired over one week are shown in Figure 3.17. The chemical shift of the peak for **$\alpha\text{-}SiV^V{}_3W_9$** shifts downfield as the pH is lowered, changing from -563 ppm at pH 4.0 to -575 ppm at pH 0.3. A peak shift that correlated with the lowering of pH was previously observed in ^{51}V NMR spectra of **α-SiV₃W₉** and was attributed to protonation of the anion inducing shielding.[50]

The results of the NMR study show that **α-SiV$^{V}_{3}$W$_{9}$** is stable in this pH range as no additional peaks, which would indicate decomposition, have appeared in any of the spectra after one week. A small peak preceding the **SiV$_3$W$_9$** peak is present in spectra at all pH values which is attributed to free vanadium that is left over from synthesis and not removed by recrystallisation, as the chemical shift of -546 ppm for this small peak at pH 0.3 matches reported chemical shifts values for VO_2^+ under conditions of pH < 1.5.[44] It was previously reported that **α-SiV$^{V}_{3}$W$_{9}$** is stable up to pH 10.[50] In an extension study (Section 3.5.1.1) the pH stability window of **α-SiV$^{V}_{3}$W$_{9}$** was investigated further.

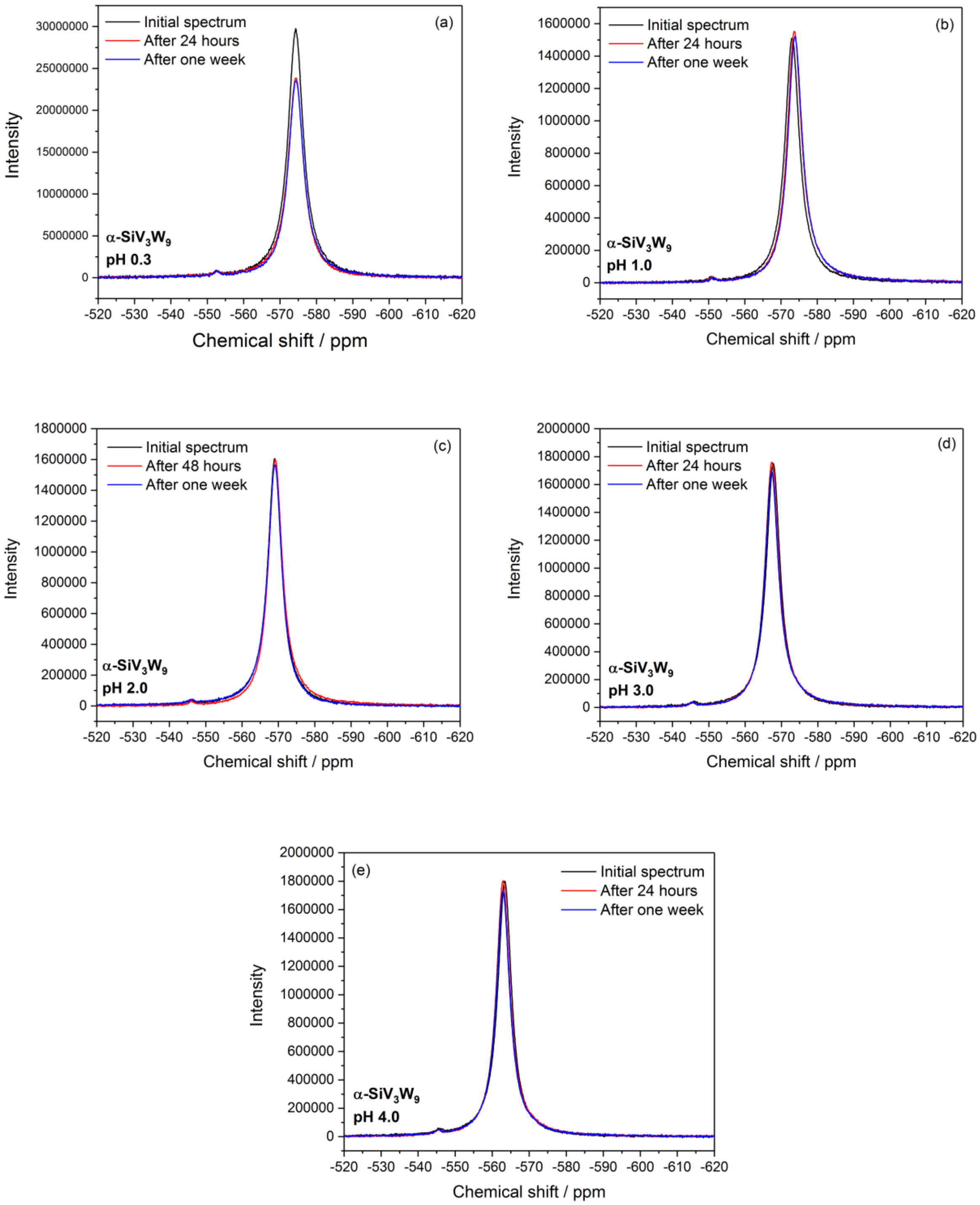

*Figure 3.17 - ^{51}V NMR spectra of **α-SiV$^{V}_{3}$W$_9$** in H_2O at pH 0.3, 1.0, 2.0, 3.0 and 4.0. (Due to differences in peak intensity between spectra for the solution at pH 1.0, the spectra in (b) were autoscaled.)*

An identical study was also carried out for **β-SiV$^{V}_{3}$W$_9$** which is shown in Figure 3.18. In this case, the initial NMR spectrum of **β-SiV$^{V}_{3}$W$_9$** at pH 0.3 showed a single peak at -580 ppm but after 24 hours, a second small peak at -560 ppm has appeared which is also visible in the spectrum after one week. The NMR spectra of **β-SiV$^{V}_{3}$W$_9$** at pH 1.0, 2.0, 3.0 and 4.0 remained clear of additional peaks over one week.

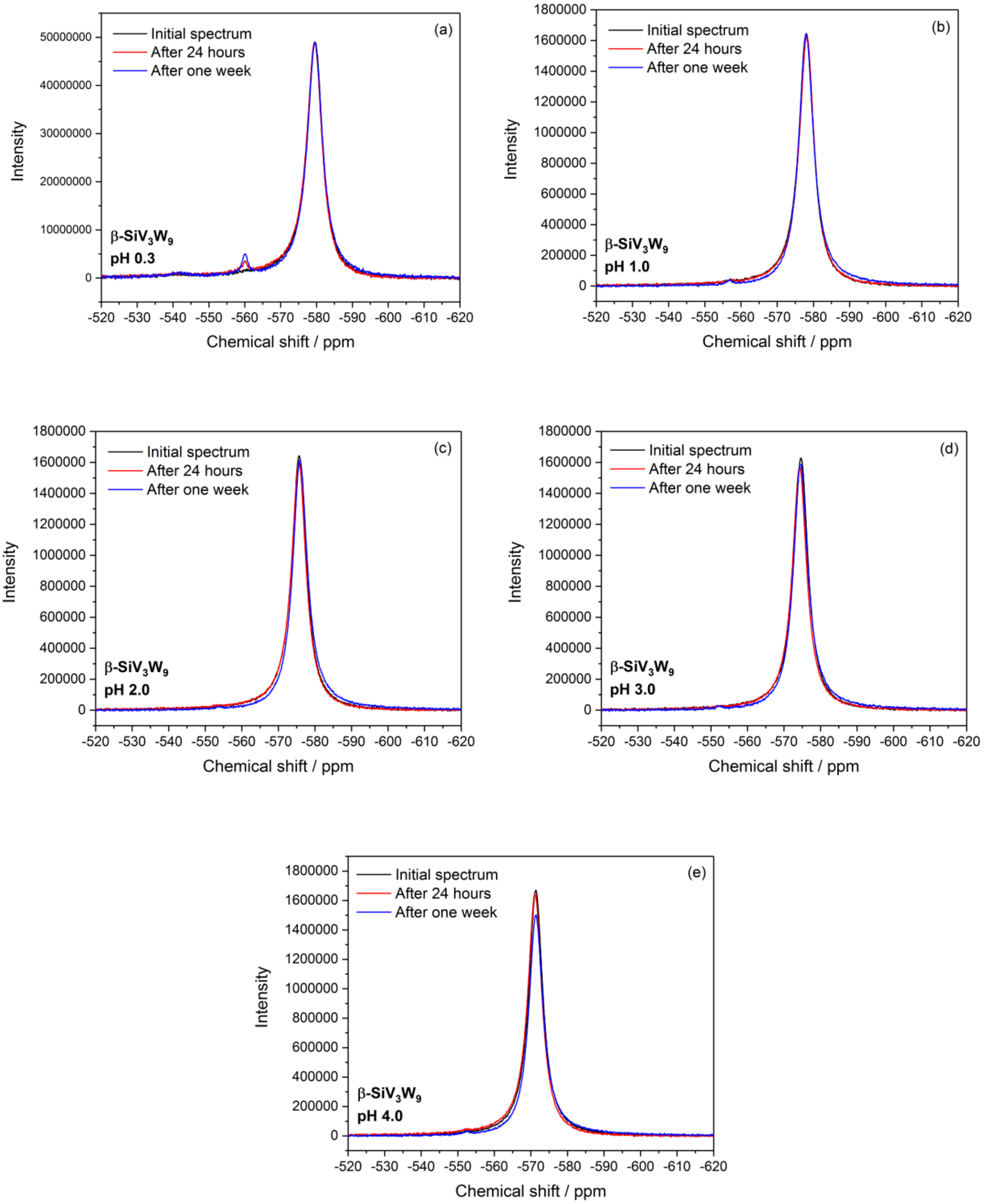

*Figure 3.18 - ^{51}V NMR spectra of **β-SiV$^{V}_{3}$W$_{9}$** in H_2O at pH 0.3, 1.0, 2.0, 3.0 and 4.0. (Due to differences in peak intensity between spectra for the solution at pH 0.3, the spectra in (a) were autoscaled.)*

The spectra demonstrate that aqueous solutions of both **α-SiV$^{V}_{3}$W$_{9}$** and **β-SiV$^{V}_{3}$W$_{9}$** show stability at pH 1.0, 2.0, 3.0 and 4.0, but that **α-SiV$^{V}_{3}$W$_{9}$** is more stable at the lowest pH value investigated (pH 0.3) than **β-SiV$^{V}_{3}$W$_{9}$**. The **β-SiV$^{V}_{3}$W$_{9}$** solution at pH 0.3 showed the development of an, albeit small, additional peak attributable to an unknown newly-formed species. As it could be a decomposition product, this is evidence that **β-SiV$^{V}_{3}$W$_{9}$** is not wholly stable at this pH value. Further, it suggests that instability of **β-SiV$_3$W$_9$** at low pH cannot solely be associated with reduction of the POM. The lesser stability of **β-SiV$^{V}_3$W$_9$** in acidic conditions is also evidenced by the changes in the CV in 1 M H_2SO_4 in Figure 3.11b. Additional peaks appeared with cycling in this CV that did not occur in the corresponding CV for **α-SiV$^{V}_3$W$_9$**.

In the case of **α-SiV$_3$W$_9$**, CVs of solutions after reduction using CPE indicated changes to the POM structure had occurred, even when only the vanadium was reduced, whereas NMR spectra of solutions of the fully oxidised POM were stable over one week. This included a solution of **α-SiV$^{V}_3$W$_9$** that had been adjusted to a pH value in the same range as the 1 M H_2SO_4 supporting electrolyte used in CPE (pH ≈ 0). Only the stability of reduced **α-SiV$_3$W$_9$** was investigated further.

3.5.1.1 Extended Stability Study of [α-SiV$_3$W$_9$O$_{40}$]$^{7-}$

The study of the stability of **α-SiV$^{V}_3$W$_9$** using ^{51}V NMR Spectroscopy was extended to a pH range that encompassed more alkaline values. NMR spectra of **α-SiV$^{V}_3$W$_9$** in water at pH 5.0, 6.0, and 7.0 were obtained over one week and the results are shown in Figure 3.19.

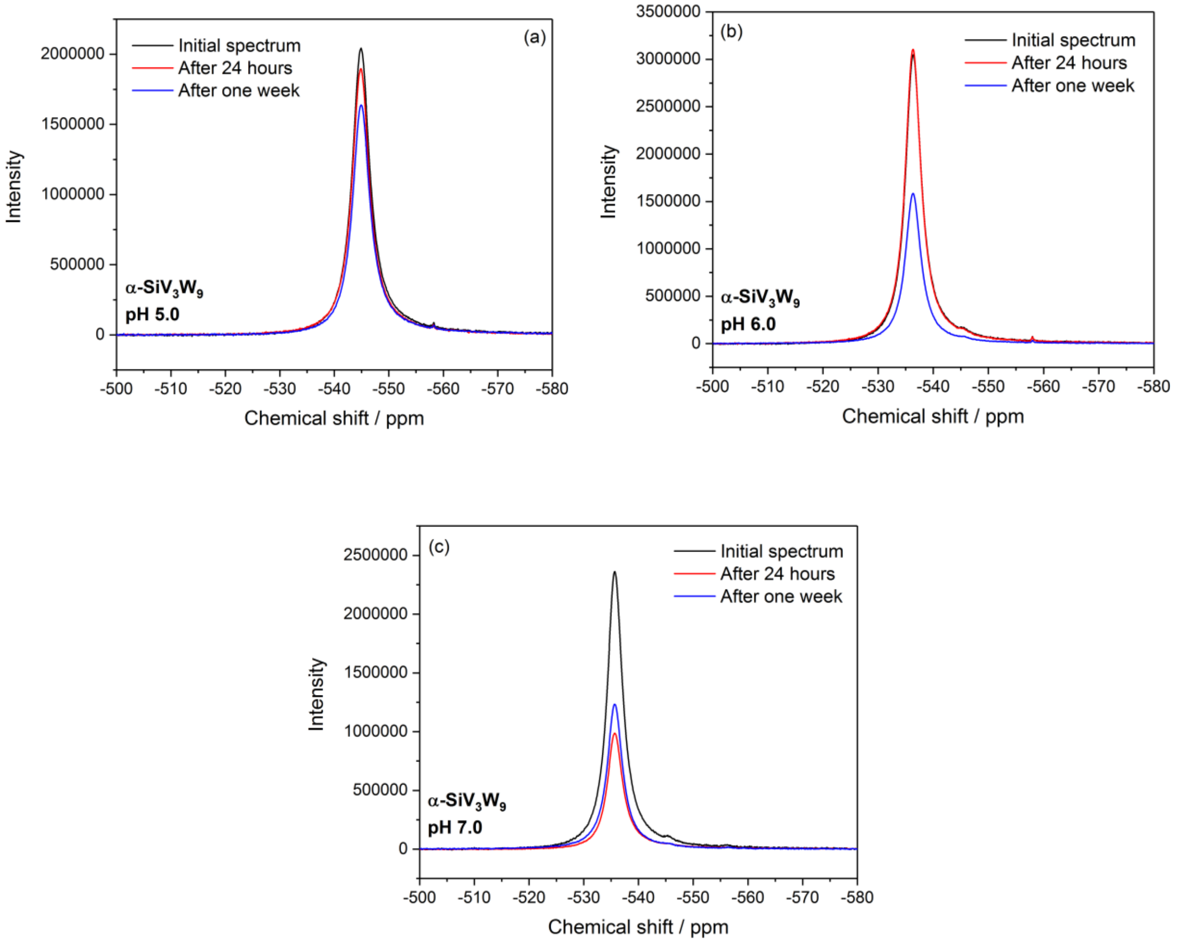

*Figure 3.19 - NMR spectra obtained over one week of solutions of **α-SiV$^{V}_3$W$_9$** in H_2O at pH 5.0, 6.0 and 7.0.*

The peak intensity was variable between spectra obtained on different days for an unknown reason but no further peaks appeared in the spectrum that would indicate instability of the POM at these pH values. Solutions with pH values that were higher still were prepared, with pH values of 11.0 and 12.0. Spectra of these solutions over one week are shown in Figure 3.20. The spectra of solutions at pH 11.0 indicated stability of the POM under these conditions, and as a result of this it is assumed that **α-$SiV^{V}_3W_9$** is also stable at lower pH values of 8, 9 and 10. The spectrum obtained for a solution at pH 12.0 after one week indicated that the POM may be reaching the limit of its stability as an additional peak had developed. Nonetheless, no signs of decomposition were evident after 24 hours and indicate that **α-$SiV^{V}_3W_9$** is stable over a wide pH range. This is in contrast to the parent structure, $[SiW_{12}O_{40}]^{4-}$, which was found to be 100% decomposed at pH 11 when solutions of different pH were monitored over a similar timescale (four days to one week).[51]

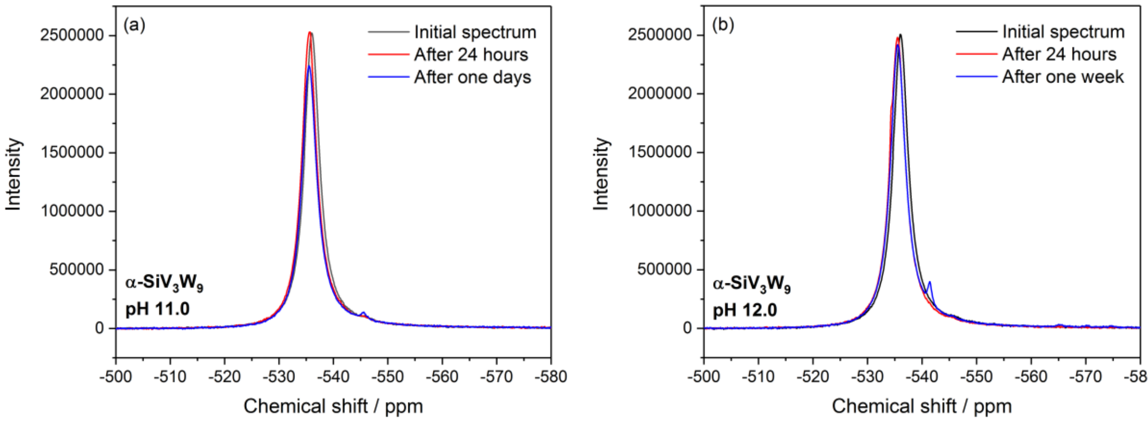

*Figure 3.20 - NMR spectra of **α-$SiV^{V}_3W_9$** solutions with a pH of 11.0 and 12.0, monitored over one week.*

As a side note, the chemical shift of **α-$SiV^{V}_3W_9$** was -545 ppm at pH 5.0 and -536 ppm at pH 6.0, 7.0, 11.0 and 12.0. As noted, **α-$SiV^{V}_3W_9$** is deprotonated as the pH rises. These chemical shift values indicate that the POM is deprotonated at pH 6.0 and above. Values for the chemical shift of **α-$SiV^{V}_3W_9$** were previously reported up to pH 11 and it was also shown that the chemical shift stayed constant at -536 ppm after pH 6.[52] Assuming monoprotonation of **α-$SiV^{V}_3W_9$**, a plot of the chemical shift versus the pH was used to determine a pK_a value for **α-SiV_3W_9** of 4.97.[52]

3.5.2 Stability of $[SiV^{IV}_3W_9O_{40}]^{10-}$

Vanadium(IV) is paramagnetic, meaning that a signal for **$SiV^{IV}_3W_9$** is not observable in ^{51}V NMR spectroscopy.[53] Consequently, ^{51}V NMR spectroscopy could not be used to identify decomposition of **α-$SiV^{IV}_3W_9$**. Therefore, cyclic voltammetry was employed instead, after CPE had been used to reduce **α-$SiV^{V}_3W_9$** to **α-$SiV^{IV}_3W_9$** in supporting electrolytes of different pH. A CV was obtained of the reduced solution one hour and 24 hours after reduction, with the aim of monitoring any evolution in the CVs.

A CV of **α-SiV$_3$W$_9$** taken in the bulk electrolysis cell before CPE is shown in Figure 3.21a in a supporting electrolyte of 1 M H_2SO_4. CPE was then carried out at 0.444 V vs SHE. As shown previously in Figure 3.16, a change in the CV is evident one hour after reduction and further changes were apparent after 24 hours (Figure 3.21b). A reduction in the current associated with the vanadium peaks is evident, along with a diminishing of the tungsten peaks and the appearance of new peaks in this region.

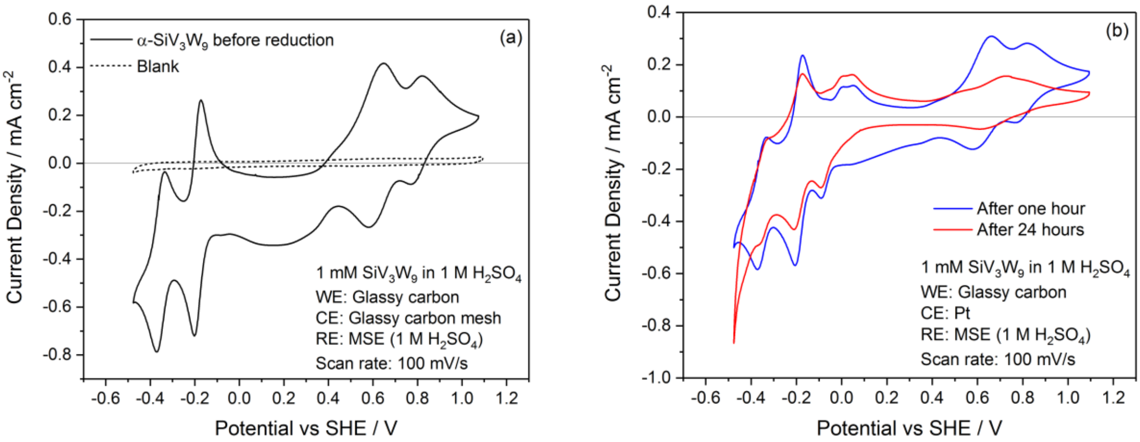

*Figure 3.21 - CVs of an **α-SiV$_3$W$_9$** solution in a supporting electrolyte of 1 M H_2SO_4 before reduction of vanadium(V), (a), and afterwards, (b).*

In a supporting electrolyte of 1 M Li_2SO_4 acidified to pH 1.0 with 1 M H_2SO_4, no changes in the CV were observed after one hour following CPE at 0.324 V vs SHE (Figure 3.22a). However, after 24 hours, instability of **α-SiV$_3$W$_9$** is indicated by a decrease in intensity of the original peaks and the appearance of additional peaks (Figure 3.22b).

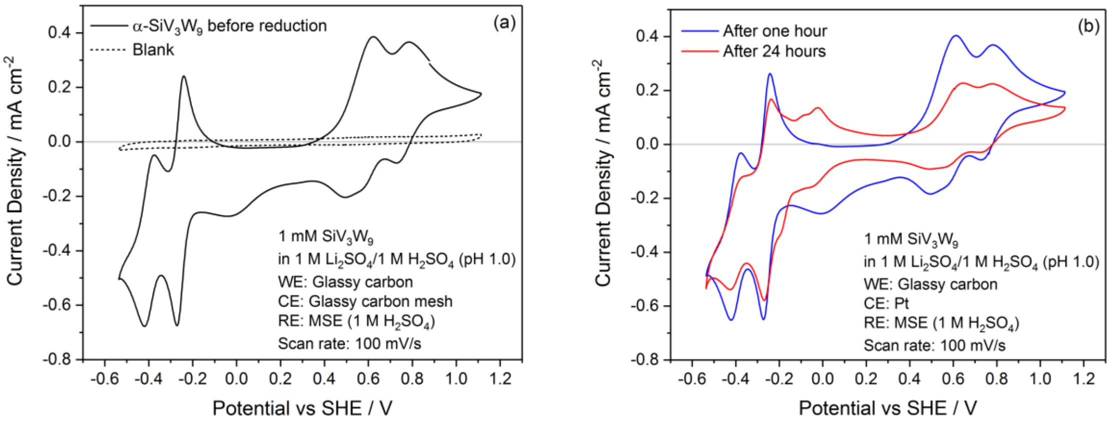

*Figure 3.22 - CVs of an **α-SiV$_3$W$_9$** solution in a supporting electrolyte of a mixture of 1 M Li_2SO_4 (acidified to pH 1.0 with 1 M H_2SO_4) before reduction of vanadium(V), (a), and afterwards, (b).*

In 1 M Li_2SO_4 acidified to pH 2.0 (by addition of 6 M H_2SO_4) no changes in the CV were observed after one hour and after 24 hours following CPE at 0.174 V vs SHE (Figure 3.23a and Figure 3.23b). This indicated that the minimum pH that reduced **α-SiV$_3$W$_9$** was stable at in this study was pH 2.0, which provided a starting point for choosing an appropriate pH for an RFB electrolyte.

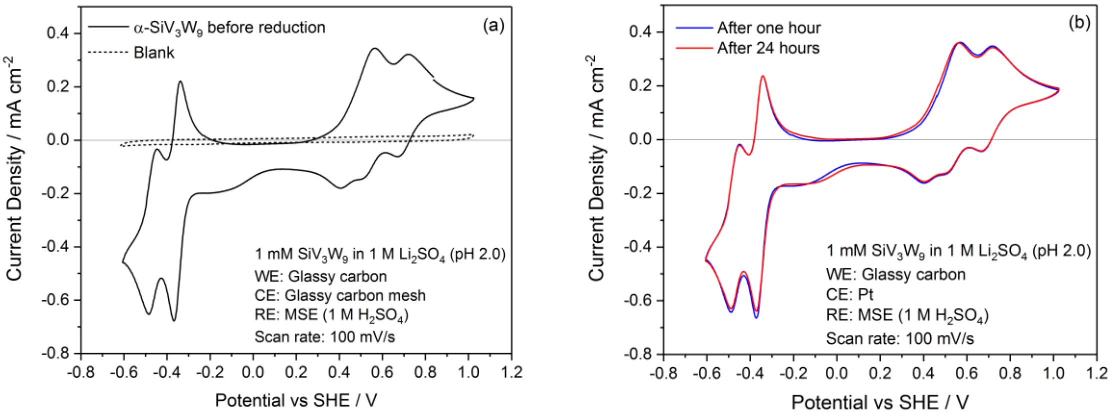

*Figure 3.23 - CVs of an **α-SiV$_3$W$_9$** solution in a supporting electrolyte of 1 M Li_2SO_4 (acidified to pH 2.0) before reduction of vanadium(V), (a), and afterwards, (b).*

A reason for the observation of increased stability of **$SiV^{IV}_3W_9$** at pH 2.0 relative to lower pH values could be similar to the explanation by Müller *et al*. for their observation of the removal of Mn^{II} and Co^{II} from $[Mn^{II}(H_2O)SiW_{11}O_{39}]^{6-}$ and $[Co^{II}(H_2O)SiW_{11}O_{39}]^{6-}$ under acidic conditions.[48] They report that “at too low pH value the substituent atom Z^{II} is removed via protonation of the adjacent oxygen atoms” as the replacement of a $(W{=}O_{terminal})^{4+}$ unit with a more negative Z^{2+} group creates a site of greater basicity.[48] In their explanation, Müller *et al*. also referenced the formulae of a series of rhenium-substituted structures that were studied by Ortéga and Pope as evidence of the greater basicity of sites substituted with metals in lower oxidation states in polyoxotungstates: $[SiRe^{III}(H_2O)W_{11}O_{39}]^{5-}$, $[SiRe^{IV}(OH)W_{11}O_{39}]^{5-}$ and $[SiRe^{V}SiW_{11}O_{40}]^{5-}$.[54] The formulae of these compounds suggests that as the positive charge on rhenium increased, the basicity of the adjacent oxygen atom decreased.

3.6 Symmetric $[SiV_3W_9O_{40}]^{7-}$ Stationary Cells

The principle of a **SiV_3W_9** flow cell is that vanadium is oxidised or reduced at the cathode while tungsten is reduced or oxidised at the anode during charge and discharge of the cell. Pratt *et al*. report that their **SiV_3W_9** flow cell cycles between $[Si\mathbf{V}^{\mathbf{V}}{}_3W^{VI}{}_9O_{40}]^{7-}$ (charged) and $[Si\mathbf{V}^{\mathbf{IV}}{}_3W^{VI}{}_9O_{40}]^{10-}$ (discharged) at the cathode and $[SiV^{IV}{}_3\mathbf{W}^{\mathbf{V}}{}_3W^{VI}{}_6O_{40}]^{13-}$ (charged) and $[SiV^{IV}{}_3\mathbf{W}^{\mathbf{VI}}{}_9O_{40}]^{10-}$ (discharged) at the anode.[16] As evidenced by the PCET shown in section 3.4, it may be that the reduced forms of **SiV_3W_9** reported with ‘-10’ and ‘-13’ charges are protonated, e.g. a formula such as $[H_3SiV^{IV}{}_3W_9O_{40}]^{7-}$ is more appropriate. However, what is indicated by the formulae reported for **SiV_3W_9** in its different stages of reduction is that for a flow cell in the discharged state, **$SiV^{IV}{}_3W_9$** should be present in both half-cells to enable the oxidation of vanadium at the cathode ($V^{IV} \rightarrow V^{V}$) and the reduction of tungsten at the anode ($W^{VI} \rightarrow W^{V}$) upon charging of the cell.

SiV_3W_9 is synthesised with vanadium in an oxidation state of +5. Thus, pre-reduction of **SiV_3W_9** by three electrons is necessary before charge/discharge testing in a cell can begin. As hydrazine has previously been used for the pre-reduction of $[PV_{14}O_{42}]^{9-}$ for subsequent POM RFB testing,[55] this was also tested for the purpose of reducing vanadium(V) to vanadium(IV) in **SiV_3W_9**.

In this test, hydrazine was added to a 15 mM **α-SiV_3W_9** solution in a POM:N_2H_4 mole ratio of 1:1.5 (by assuming two electrons are involved in the oxidation of N_2H_4). The efficacy of the reduction was judged by noting the OCP and obtaining a CV of the solution following hydrazine addition. Using the Nernst equation, a target OCP can be calculated. However, the third set of vanadium peaks are obscured by the second set of vanadium peaks, making estimation of $E^{0'}$ from $E_{1/2}$ for the third vanadium reaction difficult. Instead, a value for $E^{0'}$ can be estimated from $E_{1/2}$ of the first set of vanadium peaks (0.700 V vs SHE). The Nernst equation, applied to the first set of vanadium peaks, is then as follows:

$$E = 0.700 + \frac{RT}{F} ln \frac{[SiV_3^V W_9 O_{40}]}{[SiV_2^V V^{IV} W_9 O_{40}]}$$

$[SiV_3^V W_9 O_{40}]$ and $[SiV_2^V V^{IV} W_9 O_{40}]$ represent the concentration of oxidised **α-SiV_3W_9** and the concentration of **α-SiV_3W_9** after reduction by one electron. Supposing that the reaction has progressed to a point where $[SiV_3^V W_9 O_{40}]$ is 1000 times lower than $[SiV_2^V V^{IV} W_9 O_{40}]$, then the value of E calculated is 0.522 V. Thus, an OCP in the region of 0.522 V vs SHE would be indicative of reduction occurring at least to a point where the first vanadium in **α-SiV_3W_9** is reduced.

Only a partial reduction of **α-SiV_3W_9** was indicated after 30 minutes, with an OCP of 0.676 V vs SHE (Figure 3.24). After leaving the solution for 22 hours, an OCP of 0.649 V vs SHE was recorded. The small change in the OCP 22 hours after hydrazine addition suggests that the rate of reduction could be slow. Previously, a reaction time of 5–20 hours was reported for the oxidation of hydrazine by a range of similar vanadium-substituted phosphotungstates of general formula $[PW_{12-n}V_nO_{40}]^{-(3+n)}$ (n = 1–4), and it was reported that $[PW_{11}VO_{40}]^{4-}$ did not oxidise N_2H_4 at all.[56] Therefore, in spite of its previous use as a reducing agent for $[PV^{V}{}_{14}O_{42}]^{9-}$,[55] hydrazine seemed unsuitable for use in preparing electrolytes for a **SiV_3W_9** flow cell due to reaction times that could be long and which would impede a rapid preparation of flow cell electrolytes.

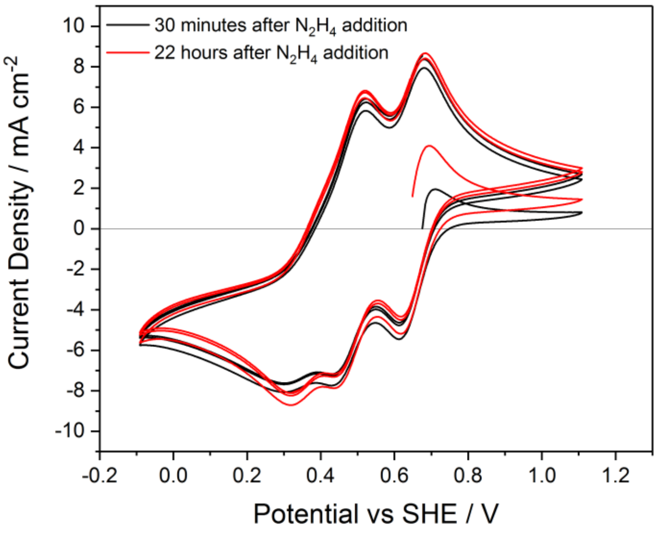

*Figure 3.24 - A CV of **α-SiV$_3$W$_9$** (15 mM) in 1 M Li$_2$SO$_4$ (pH 2) focused on the vanadium peaks, after addition of the stoichiometric amount of hydrazine required to reduce the three V^{IV} centres in the POM. (WE: glassy carbon, CE: platinum wire, RE: Ag/AgCl (3 M NaCl), scan rate: 100 mV/s)*

A further reducing agent reported for the purpose of reducing vanadium(V) to vanadium(IV) in POMs is ascorbic acid, or sodium ascorbate. For instance, ascorbic acid was used for the reduction of $[PV^V{}_2Mo_{10}O_{40}]^{5-}$ and $[PV^VMo_{11}O_{40}]^{4-}$.[57] It was reported to be at least a two-electron reductant, meaning 0.5 moles of ascorbic acid were required to reduce one mole of vanadium(V) to vanadium(IV).[57] A reaction time of 60 minutes for the disubstituted POM and 50 minutes for the monosubstituted POM was stated.

The use of sodium ascorbate for the reduction of $[PV_2Mo_{10}O_{40}]^{5-}$ was also reported.[58] The detection of a one-electron reduced POM species in EPR spectra corresponded to a ratio of $[PV_2Mo_{10}O_{40}]^{5-}$:sodium ascorbate of 1:0.6, suggesting again that the ascorbate species was a two-electron reductant. Further, it has been reported that **α-SiV$_3$W$_9$** itself can be reduced by aqueous ascorbic acid.[59] Therefore, as reports in the literature suggested that ascorbic acid, or the ascorbate anion, could be an efficacious reducing agent for vanadium(V) in several mixed-metal POMs, this was tested with **α-SiV$_3$W$_9$**.

The amount of sodium ascorbate required to reduce three moles of vanadium(V) in **α-SiV$_3$W$_9$** was added to a 5 mM solution of the POM which was then monitored using cyclic voltammetry. Assuming that the sodium ascorbate was a two electron reductant, the reductant:**α-SiV$_3$W$_9$** mole ratio was 1.5:1. A comparison of the OCP of an initial CV of **α-SiV$_3$W$_9$**, focused on the potential region where vanadium reduction occurs, and a CV obtained 30 minutes after addition of sodium ascorbate showed that the OCP value after the ascorbate addition was indicative of vanadium reduction occurring (Figure 3.25). The OCP was 0.768 V vs SHE pre-reduction and 0.287 V vs SHE post-reduction, suggesting the presence of **SiV_3W_9** species that contained vanadium(IV) in the solution.

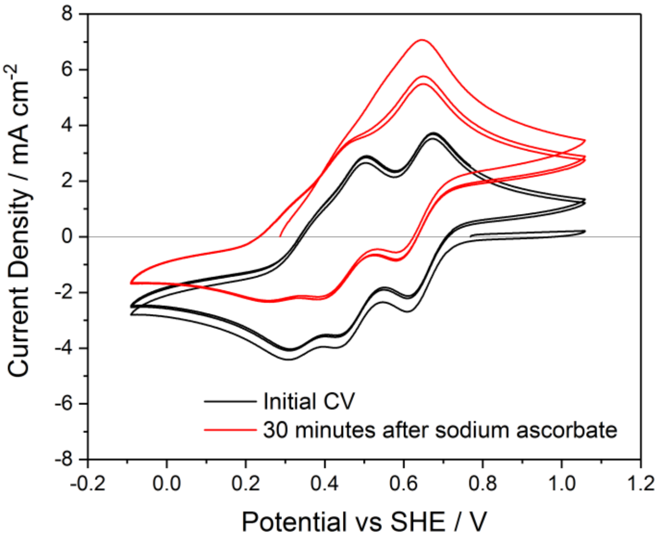

*Figure 3.25 - A CV of **α-SiV_3W_9** (5 mM) in 1 M LiCl (pH 2) after addition of the stoichiometric amount of sodium ascorbate required to reduce three V^V in the POM. (WE: glassy carbon, CE: platinum wire, RE: Ag/AgCl (3 M NaCl), scan rate: 100 mV/s)*

However, a disadvantage of the use of sodium ascorbate as the reducing agent for pre-reduction of a POM electrolyte is that it is not a ‘clean’ reaction. The products of hydrazine oxidation are nitrogen and protons and thus, while the pH of the electrolyte may be affected, the electrolyte is not contaminated with by-products. Conversely, sodium ascorbate is oxidised to dehydroascorbic acid, which means organic molecules remain in solution. There is some thought in the literature that the presence of such organic molecules in an RFB electrolyte is not detrimental: ascorbic acid was added as a complexing agent to prevent the precipitation of iron hydroxides in the negative electrolyte of an iron chloride RFB, which improved RFB performance.[60] For the VRFB, a study deemed ascorbic acid unsuitable as an electrolyte additive for the purpose of increasing the thermal stability of the catholyte but this was due to the propensity of ascorbic acid to be oxidised by VO_2^+ which reduced the state of charge of the catholyte and the usable capacity in a battery.[61] The reducing properties of ascorbic acid are not of concern for its use with **SiV_3W_9** because the POM species containing vanadium(IV) is desired in the pre-reduction step. As addition of ascorbic acid or sodium ascorbate could provide a rapid way of pre-reducing **SiV_3W_9** for an RFB, this was tested when preparing electrolytes for a stationary cell test.

The electrolyte was prepared by dissolving **α-SiV_3W_9** in 1 M Li_2SO_4 (pH 2.0) at a POM concentration of 10 mM. The amount of sodium ascorbate required to reduce three moles of vanadium(IV) was added, plus 5% excess, and the solution was bubbled with nitrogen for one hour. The colour of the solution had changed from red to dark brown after leaving the solution for this amount of time. Following this, the stationary cell was constructed and charge/discharge testing commenced. The stationary cell was kept in a polycarbonate box that was connected to a nitrogen supply in order to minimise oxidation of reduced **α-SiV$_3$W$_9$** by atmospheric oxygen. The results of charge/discharge testing are shown in Figure 3.27.

As noted in Section 3.4, based on $E_{1/2}$ for the second set of vanadium peaks (0.535 V vs SHE) and the first set of tungsten peaks (-0.360 V vs SHE), the theoretical voltage for an RFB based on **α-SiV$_3$W$_9$** is 0.895 V. The maximum theoretical voltage calculated using $E_{1/2}$ of the first set of vanadium peaks (0.700 V vs SHE) and the second set of tungsten peaks (-0.472 V vs SHE) is 1.12 V. A CV with the theoretical voltages indicated in shown in Figure 3.26.

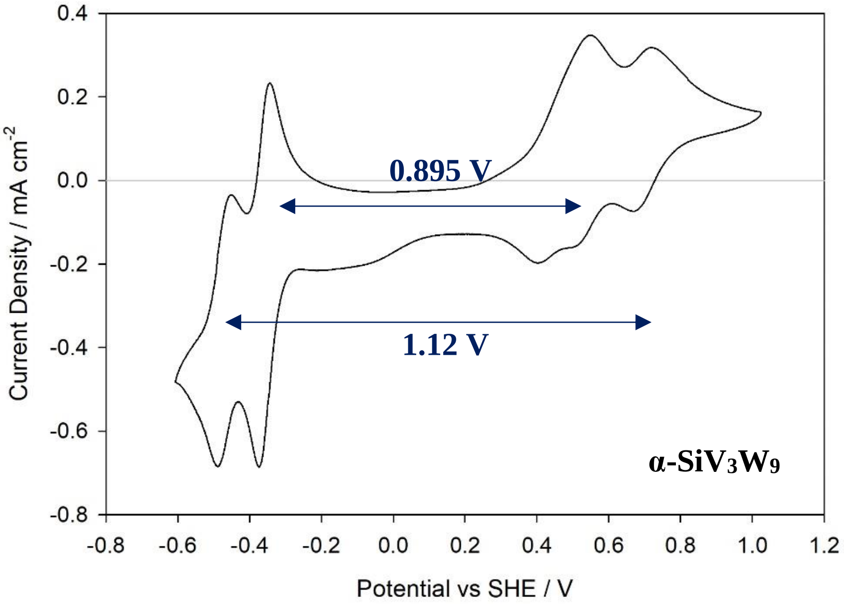

*Figure 3.26 - A CV of **α-SiV$_3$W$_9$** (1 mM) in 1 Li_2SO_4 (pH 2) with theoretical voltages for an RFB indicated (WE: glassy carbon, CE: platinum wire, RE: MSE (1 M H_2SO_4), scan rate: 100 mV/s)*

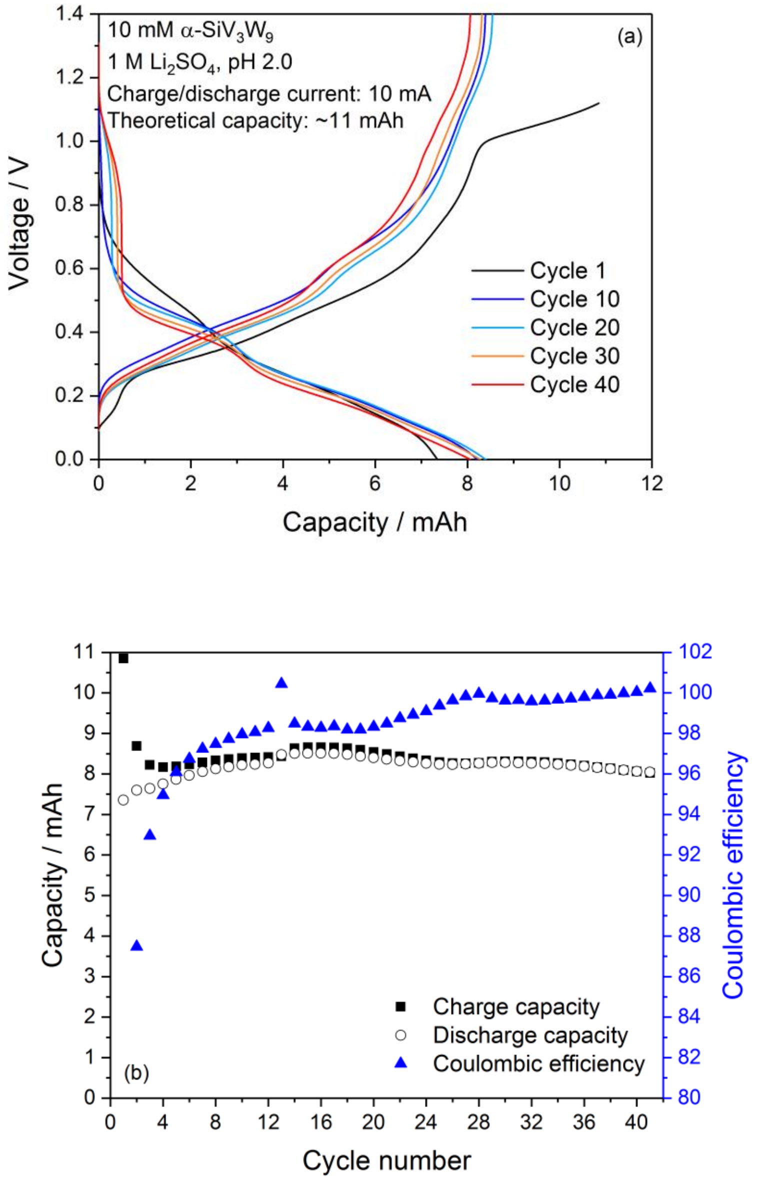

Figure 3.27 - (a) Charge/discharge curves for an **α-SiV$_3$W$_9$** *stationary cell, using electrolytes pre-reduced with sodium ascorbate. (b) Charge capacity, discharge capacity and coulombic efficiency for the* **α-SiV$_3$W$_9$** *stationary cell.*

The stationary cell ran for 41 cycles. Testing could not continue for longer than this due to the electricity supply being lost to the laboratory. Further, the nitrogen supply to the polycarbonate box was lost for several cycles midway through testing (cycle 10 to cycle 23) due to temporary downtime of the house nitrogen system. However, the result of the stationary cell using electrolytes pre-reduced with sodium ascorbate was promising. Apart from the first cycle, stable charge/discharge curves were shown. Coulombic efficiencies were >98% after cycle 10 which indicated that loss of charge to side reactions was low. The capacity fade after the nitrogen supply was lost to the surroundings of the stationary cell was not large. Further, two plateaus were visible in the charge/discharge curves, particularly in the discharge curve, which would suggest that more than one vanadium atom was involved in the charge and discharge reactions of the cell.

Due to the multiple redox reactions, charge/discharge curves with more than one plateau are characteristic of POM RFBs.[17, 55] The shape of the charge/discharge curves in Figure 3.27a match what would be expected based on analysis of the POM by cyclic voltammetry. It would be expected that a first longer plateau would occur upon charging that corresponded to oxidation by two electrons of the two vanadium atoms in the POM for which $E_{1/2}$ is close in value (indicated by overlapping of the peaks in the CV of **α-SiV$_3$W$_9$** in Figure 3.26). The two electrons would be used to reduce the tungsten framework at the anode. A second shorter plateau would then be expected that corresponded to the third vanadium peak that is not obscured by the other peaks in the CV and thus has an $E_{/12}$ value that is distinct from the other vanadium reactions. The electron removed from vanadium would be used to reduce the tungsten framework at the anode. Upon discharge, this latter reaction would be the first to be reversed so a shorter plateau would occur first, followed by a second longer plateau that would correspond to the reaction involving the two vanadium atoms that have overlapping peaks in the CV. However, the observed voltages were different to the theoretical voltages as the first plateau (theoretical voltage of 0.895 V) begins at ~0.20 V when charging the cell. The second charging plateau (theoretical voltage of 1.12 V) begins at ~0.55 V. The observed voltages are not suggestive of the charge/discharge mechanism that was proposed above. A small plateau of unknown origin is also shown to begin at ~1.1 V which grows with time. However, the coulombic efficiencies of >98% that were maintained show that charge was not permanently lost in each cycle to a side reaction that may be responsible for this plateau.

The theoretical capacity based on the volume of electrolyte and the concentration of **α-SiV$_3$W$_9$** that was used was 10.9 mAh. The electrochemical yield based on this value was ~70%, based on the discharge capacity (7.6 mAh) of cycle 2. As the electrolyte was static within the cell, a discrepancy between the observed capacity and theoretical capacity is expected as there was no forced convection of the electrolyte through the electrodes. The voltaic efficiency was 50% based on the average charging voltage and average discharging voltage of cycle 10.

After cycling, the cell was disassembled with the electrolytes in the charged state. The electrolytes were recovered and the pH of each solution was measured. The pH of the charged catholyte was 2.01 and the pH of the charged anolyte was 2.63. The pH of the starting **α-SiV$^{IV}_3$W$_9$** solution before cycling (after addition of sodium ascorbate) was 2.24. The pH changes of the electrolytes measured after cycling could support that PCET occurred during charge/discharge testing. When the cell is charged, protons should be lost from the POM in the positive half-cell as $\mathbf{SiV^{IV}{}_3W_9}$ is oxidised to $\mathbf{SiV^{V}{}_3W_9}$. The charged catholyte had a pH of 2.01 which was more acidic than the pH value before the cell was charged, suggesting protons had been removed from the POM in the positive half-cell. Conversely, protons should be gained by the POM in the negative half-cell when tungsten(VI) is reduced to tungsten(V). The charged anolyte had a pH of 2.63 which is less acidic than before cycling commenced and suggests that the POM was protonated in the negative half-cell during charging. The pH values that were measured also indicate that the stationary cell cycled in the pH range of 2–3, which is the region where PCET was indicated to occur in the previous CV study (Figure 3.9).

As the catholyte should contain vanadium(V) when charged, a ^{51}V NMR spectrum was obtained (Figure 3.28a). This showed the expected peak at -569 ppm for $\boldsymbol{\alpha}$-$\mathbf{SiV_3W_9}$ at pH 2. An additional small peak at -546 ppm was present but this was also observed in a spectrum of an $\boldsymbol{\alpha}$-$\mathbf{SiV_3W_9}$ solution that was freshly prepared. Therefore, decomposition in the catholyte was not indicated by these spectra. As the anolyte contained reduced $\boldsymbol{\alpha}$-$\mathbf{SiV_3W_9}$, analysis with ^{51}V NMR spectroscopy was unsuitable and cyclic voltammetry was used instead. A CV of the anolyte compared with a CV of the catholyte is shown in Figure 3.28b. The vanadium peaks were less resolvable in the CV of the anolyte, but the positions of the tungsten peaks were the same. Thus, the analysis of the recovered electrolytes indicated that the solution contained intact $\boldsymbol{\alpha}$-$\mathbf{SiV_3W_9}$ after charge/discharge testing.

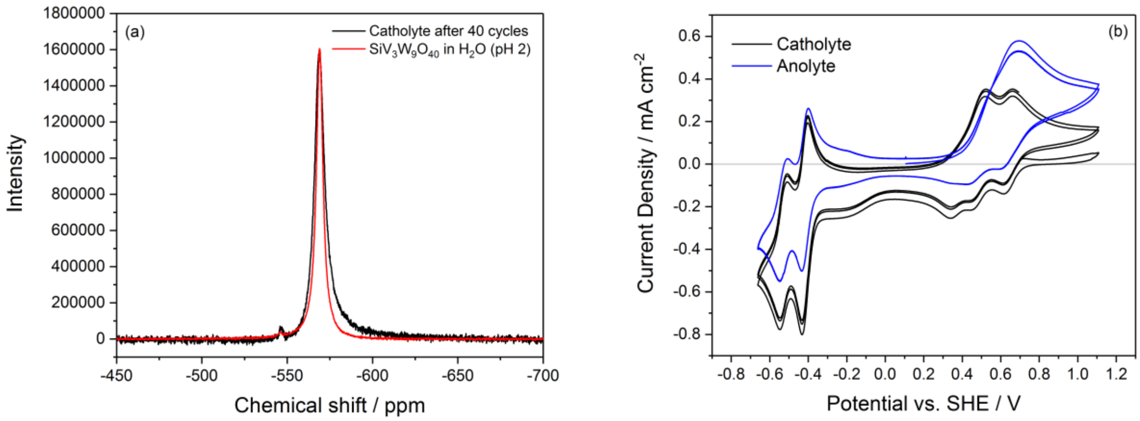

Figure 3.28 - (a) ^{51}V NMR spectrum of the charged $\boldsymbol{\alpha}$-$\mathbf{SiV_3W_9}$ *stationary cell catholyte compared with a spectrum of a freshly prepared* $\boldsymbol{\alpha}$-$\mathbf{SiV_3W_9}$ *solution. (The NMR spectra were autoscaled when overlaid due to differences in peak intensity.) (b) CVs of the* $\boldsymbol{\alpha}$-$\mathbf{SiV_3W_9}$ *catholyte and anolyte diluted with 1 M Li_2SO_4 (pH 2) to a concentration of 1 mM. (WE: glassy carbon, CE: platinum wire, RE: Ag/AgCl (3 M NaCl), scan rate: 100 mV/s)*

A further stationary cell test was prepared in order to obtain charge/discharge data for the β isomer of $\mathbf{SiV_3W_9}$. The preparation procedure that was followed was analogous to that of the $\boldsymbol{\alpha}$-$\mathbf{SiV_3W_9}$ cell, with the electrolyte prepared by dissolving $\boldsymbol{\beta}$-$\mathbf{SiV_3W_9}$ at a concentration of 10 mM in 1 M Li_2SO_4 at pH 2.0. The amount of sodium ascorbate required to reduce three moles of vanadium(V) was then added, plus 5% excess, and the solution was bubbled with nitrogen for one hour before being split between the anode and cathode of the stationary cell. A CV of **β-SiV$_3$W$_9$** is shown in Figure 3.29 which was used to calculate the theoretical voltage of the stationary cell.

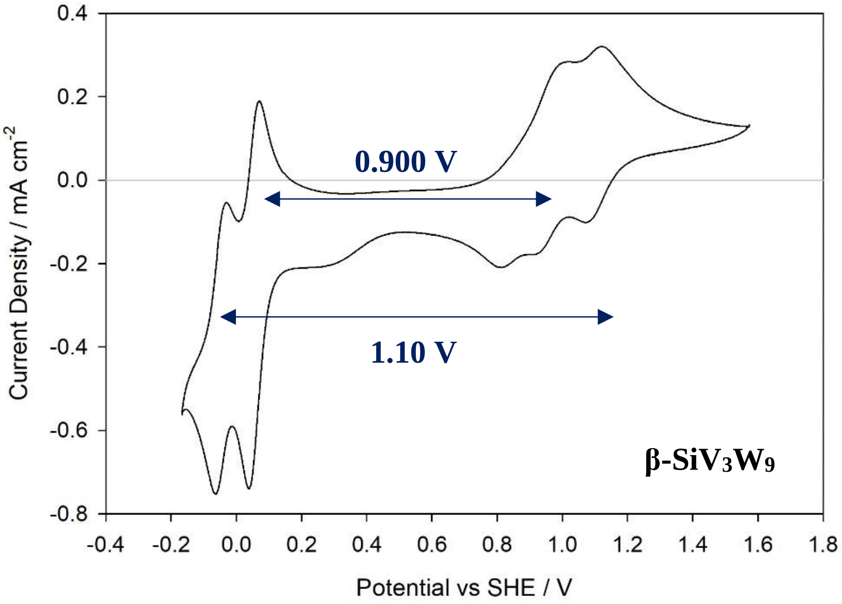

*Figure 3.29 - A CV of **β-SiV$_3$W$_9$** (1 mM) in 1 M Li_2SO_4 (pH 2) with theoretical voltages for an RFB shown. (WE: glassy carbon, CE: platinum wire, RE: Ag/AgCl (3 M NaCl), scan rate: 100 mV/s)*

The theoretical voltage based on $E_{1/2}$ of the second set of vanadium peaks which mask the set of peaks for the third one-electron vanadium reaction of **β-SiV$_3$W$_9$** (0.487 V vs SHE) and $E_{1/2}$ of the first set of tungsten peaks (-0.411 V vs SHE) is 0.900 V. The maximum theoretical voltage, if the third vanadium reaction of **β-SiV$_3$W$_9$** were accessed and was coupled with the second tungsten reaction, is 1.1 V based on $E_{1/2}$ values of 0.633 V vs SHE (V^{IV}/V^{V}) and -0.515 V vs SHE (W^{IV}/W^{V}). The results of the stationary cell are shown in Figure 3.30.

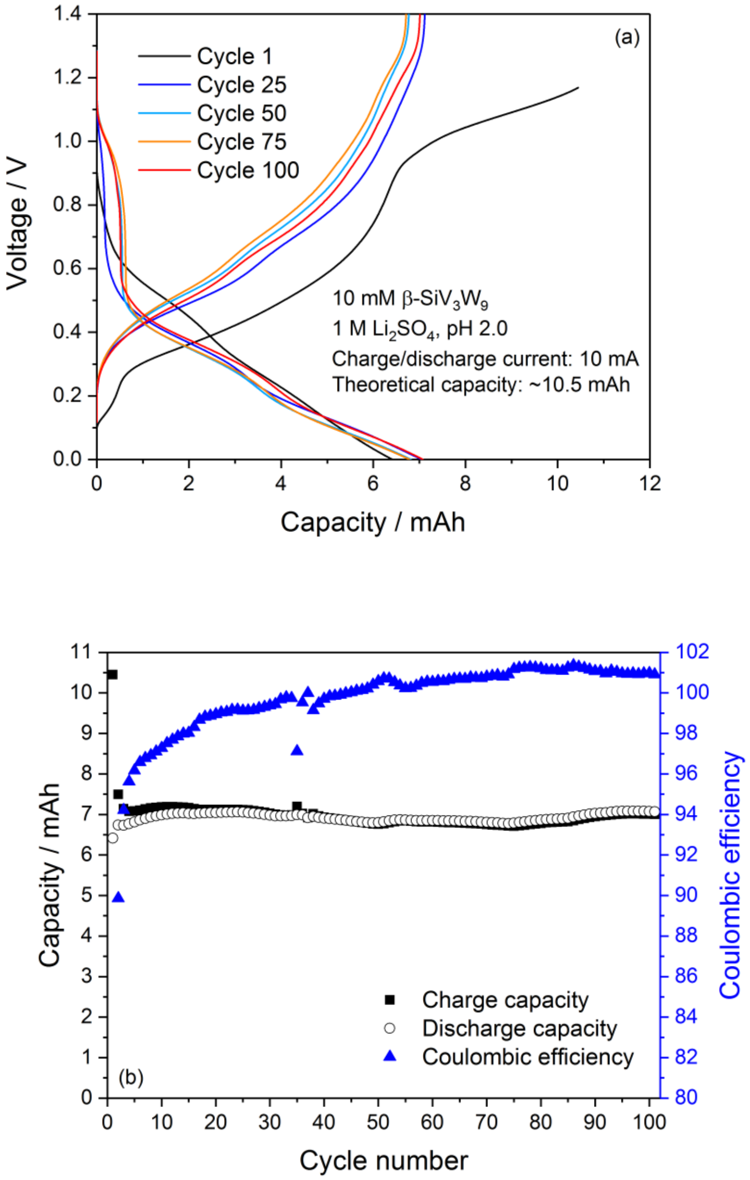

*Figure 3.30 - (a) Charge/discharge curves for a **β-SiV$_3$W$_9$** stationary cell, using electrolytes pre-reduced with sodium ascorbate. (b) Charge capacity, discharge capacity and coulombic efficiency for the **β-SiV$_3$W$_9$** stationary cell.*

The appearance of the charge/discharge curves was similar to the results from the **α-SiV$_3$W$_9$** stationary cell. The curves stabilised after cycle 1 and two plateaus were visible in the discharge curves in particular. The features of a CV of **β-SiV$_3$W$_9$** (Figure 3.29) are comparable to that of **α-SiV$_3$W$_9$** and so the occurrence of two plateaus was expected. The **β-SiV$_3$W$_9$** stationary cell ran for 101 cycles and during that time, coulombic efficiencies of >98% were obtained after cycle 14. The coulombic efficiency rose to greater than 100% (100–101%) after cycle 45. This could suggest incomplete discharge occurred in earlier cycles that subsequently discharged in later cycles. Capacity fade was not evident over 101 cycles.

The electrochemical yield was 64% based on the discharge capacity of cycle 2 (6.7 mAh) and a theoretical capacity of 10.5 mAh.

After cycling, the stationary cell was disassembled with the electrolytes in the charged state. The catholyte was subjected to ^{51}V NMR spectroscopy and the results are shown in Figure 3.31a. While the peak at -576 ppm matches the peak expected for **β-SiV$_3$W$_9$**, there are two other peaks in the spectrum at -534 ppm and -553 ppm. These peaks are not present in a spectrum of a **β-SiV$_3$W$_9$** solution that was not subjected to charge/discharge testing which is also shown. The presence of these peaks could suggest that the formation of other vanadium-containing species had occurred during charge/discharge cycling of **β-SiV$_3$W$_9$**.

It was previously shown by using ^{31}P NMR spectroscopy that small amounts of $[PV_2W_{10}O_{40}]^{5-}$ and $[PVW_{11}O_{40}]^{4-}$ formed when $[\alpha\text{-}PV_3W_9O_{40}]^{6-}$ was subjected to charge/discharge testing in a flow cell, due to the appearance of two additional peaks in the NMR spectrum of the cycled electrolyte.[62] It could be that the additional peaks seen in the ^{51}V NMR spectrum of **β-SiV$_3$W$_9$** after cycling are due to a similar reason: the formation of other vanadium-containing POMs.

A CV of the anolyte after cycling, shown by the blue line in Figure 3.31b, differs in overall appearance to that of a freshly prepared solution but some of the peaks at more negative potentials match the position of tungsten redox peaks in an uncycled solution and show that the POM was not completely decomposed during charge/discharge cycling.

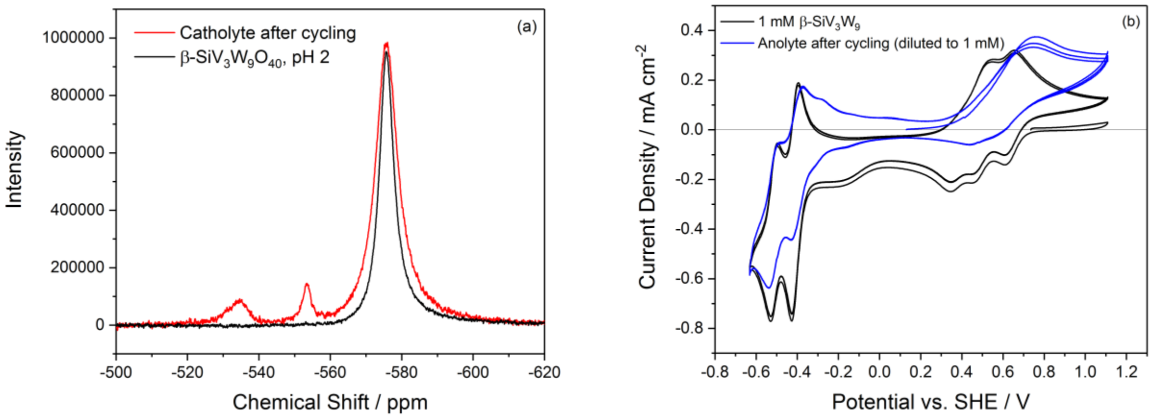

*Figure 3.31 - (a) ^{51}V NMR spectrum of the charged **β-SiV$_3$W$_9$** catholyte from the stationary cell overlaid with a spectrum of a freshly prepared **β-SiV$_3$W$_9$** solution. (b) A CV of the **β-SiV$_3$W$_9$** anolyte after diluting to 1 mM with 1 M Li_2SO_4 (pH 2) overlaid with a CV of a 1 mM **β-SiV$_3$W$_9$** solution that had not undergone charge/discharge testing. (WE: glassy carbon, CE: platinum wire, RE: Ag/AgCl (3 M NaCl), scan rate: 100 mV/s)*

While no capacity fade was evident in the **β-SiV$_3$W$_9$** stationary cell over 101 cycles, the appearance of additional peaks in the NMR spectrum of the cycled catholyte indicates instability of the POM that could be attributable to charge/discharge testing. While the

α-SiV_3W_9 stationary cell underwent fewer cycles, the NMR spectrum of the catholyte after cycling had remained clear of additional peaks which indicated no formation of other vanadium-containing species had occurred. Therefore, **α-SiV_3W_9** was selected as the most suitable isomer to take forward into flow cell testing.

The choice of the use of **α-SiV_3W_9** in flow cell testing is also supported by the difference in the yields reported for the **SiW_9** precursors in literature. These values concur with the yields obtained in this work. In the synthesis of [α-SiW_9O_{34}]$^{10-}$ (**α-SiW_9**), described by Tézé and Hervé, the POM is prepared in 85% yield, the end step being the precipitation of **α-SiW_9** which is filtered after one hour.[20] The same authors report the synthesis of **β-SiW_9**, which is prepared in 35% yield and collected following crystallisation at 5°C for two to three days.[20] This indicates that **α-SiW_9** can be prepared in higher yield and on a shorter timescale. A representative yield for **β-SiW_9** in this work is 22% and for **α-SiW_9** is 77%. Therefore, the results obtained here also indicate that the yield of **α-SiW_9** is higher which supports the continued use of **α-SiV_3W_9** over **β-SiV_3W_9** for further study of a **SiV_3W_9** RFB. A shorter synthesis time with higher yields is clearly preferable.

3.7 Flow cell testing of [$SiV_3W_9O_{40}$]$^{7-}$

The preparation of the **α-SiV_3W_9** electrolytes for flow cell testing was analogous to the method employed in the preparation of the stationary cell electrolytes. The POM was dissolved at a concentration of 10 mM in 1 M Li_2SO_4 at pH 2.0 and the amount of sodium ascorbate required to reduce three moles of vanadium(V) was added. After bubbling the solution for one hour with nitrogen, the solution was split equally between the two tanks of the flow cell, meaning the composition of the anolyte and catholyte was **$SiV^{IV}_3W_9$** before charge/discharge testing commenced. The results of the flow cell test are shown in Figure 3.32.

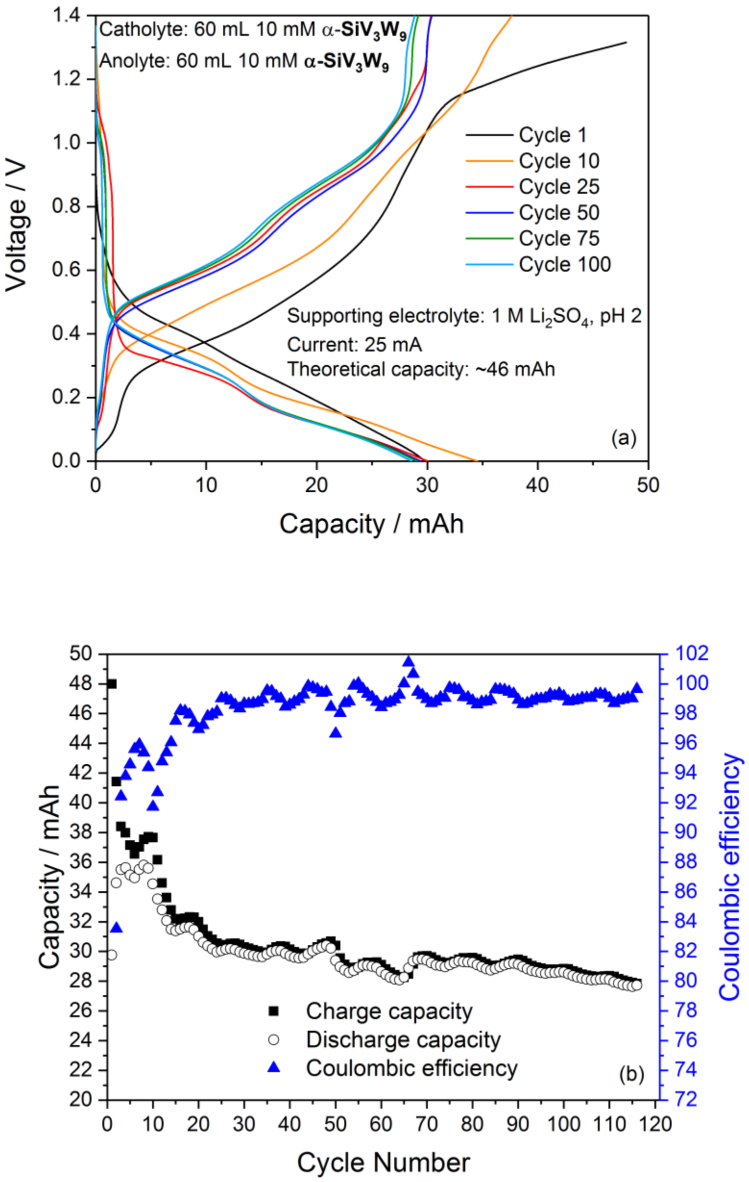

*Figure 3.32 - The results of an **α-SiV$_3$W$_9$** flow cell test. (a) Charge/discharge curves. (b) Charge capacity, discharge capacity and coulombic efficiency versus cycle number.*

A stable appearance of the charge/discharge curves is evident in later cycling and, as for the previous stationary cell test, two plateaus are visible indicating that more than one vanadium atom was active during the charge/discharge cycling. As for the stationary cell, the voltages of the plateaus differed to the theoretical voltages predicted for an **α-SiV$_3$W$_9$** cell (0.895 V and 1.12 V). The first charging plateau began at ~0.4 V and a second charging plateau began at ~0.7 V. During discharge, plateaus began at ~0.4 V and then ~0.2 V. A small plateau beginning at ~1.1 V is similar in appearance to a plateau observed in the **α-SiV$_3$W$_9$** stationary cell (Figure 3.27a) which could be attributable to a side reaction. However, the coulombic efficiency was >98% from cycle 24 onwards indicating that the discrepancy between the charge capacity and discharge capacity was small. Out of a theoretical capacity of

46 mAh, around 30 mAh was accessed during the 116 cycles, corresponding to an electrochemical yield of ~65%. The voltaic efficiency calculated for cycle 10 was 31%.

Capacity fade was evident as the discharge capacity decreased from 29.4 mAh for cycle 50 to 28.6 mAh for cycle 100. One cause of this could be the permeation of atmospheric oxygen into the electrolytes. Each electrolyte was bubbled continuously with nitrogen but the polycarbonate box that the flow cell was housed in was not completely airtight, meaning that oxygen could not be excluded completely from entering the electrolytes. It was previously found that the loss of nitrogen supply during operation of a POM flow cell corresponded with an increase in the rate of capacity fade from 0.16% per cycle to 0.56% per cycle.[55] Therefore, the oxidation of the reduced POM species by atmospheric oxygen in this experiment, resulting in a loss of capacity, is credible and could be investigated further. A slow leakage of electrolyte was also observed from one of the flow ports of the flow cell, due to insufficient sealing with PTFE tape, but this amounted to loss of a few drops of solution over several days so is not thought to have caused a substantial loss of electrolyte volume and capacity.

Figure 3.32b shows that the charge and discharge capacity of the cell oscillated. A similar occurrence was observed in a POM flow cell previously.[55] It was shown that the capacity oscillated in a day and night cycle, the maxima in the capacity values occurring at intervals of 24 hours, which was attributed to temperature changes in the lab.[55] Thus, temperature changes of the surroundings could also be the cause of the oscillation in capacity observed for this flow cell.

During cycling, the colour of the catholyte was seen to change from orange/red when charged to dark brown when discharged. The colour change is illustrated in Figure 3.33. As the colour of fully oxidised **α-SiV$_3$W$_9$** is orange/red, this colour change supported that the POM was cycling between **$SiV^V{}_3W_9$** and **$SiV^{IV}{}_3W_9$** on the cathode side. The colour change of the anode solution was not obvious.

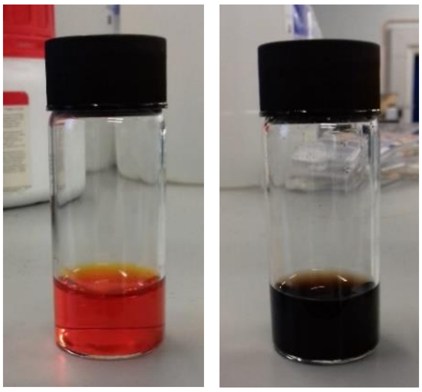

*Figure 3.33 - 10 mM solutions of fully oxidised **α-SiV$^V{}_3$W$_9$** (left image) and reduced **α-SiV$^{IV}{}_3$W$_9$**, (right image) after the addition of 1.5 molar equivalents of sodium ascorbate.*

After 116 charge/discharge cycles, the electrolytes were collected in the discharged state and a CV was obtained of each solution to see if this had evolved in any way that would suggest instability of the POM (Figure 3.34). Both CVs showed features of **α-SiV$_3$W$_9$** and therefore did not indicate that **α-SiV$_3$W$_9$** was unstable during charge/discharge testing in the flow cell.

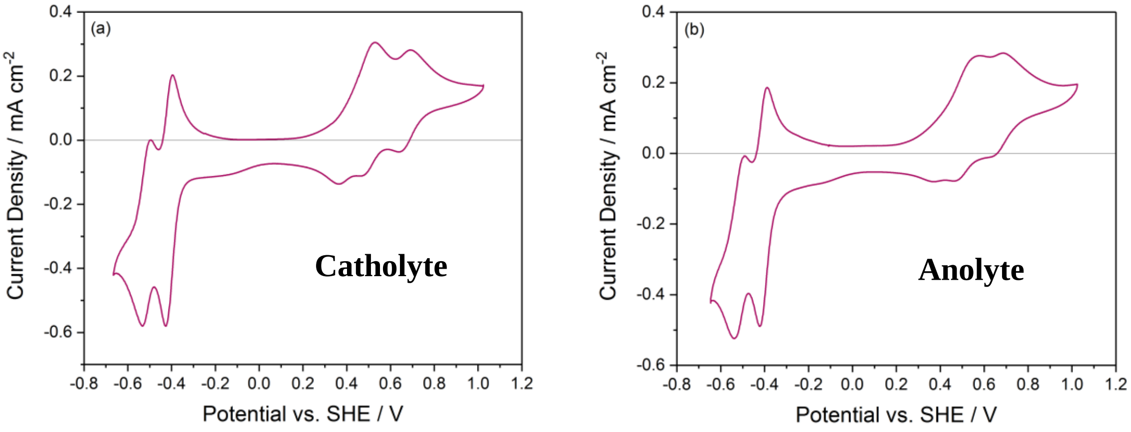

Figure 3.34 - CVs of ***α-SiV$_3$W$_9$*** *after charge/discharge testing in a flow cell. (a) Catholyte diluted to 1 mM with 1 M Li_2SO_4 (pH 2.6). (b) Anolyte diluted to 1 mM with 1 M Li_2SO_4 (pH 2.6). (WE: glassy carbon, CE: platinum wire, RE: MSE (1 M H_2SO_4), scan rate: 100 mV/s)*

As noted in Section 3.6, a disadvantage of using sodium ascorbate as a reducing agent prior to flow cell testing is the persistence of oxidation products in the electrolytes. In spite of the ease with which the reduced electrolytes can be prepared, this is not desirable. Therefore, it was decided that electrochemical reduction would be employed for the preparation of **α-SiV$_3$W$_9$** electrolytes for further flow cell testing.

A bulk electrolysis cell was used to reduce a 10 mM **α-SiV$_3$W$_9$** solution in 1 M Li_2SO_4 at pH 2.0. Chronopotentiometry was employed in which a current was applied to the working electrode (-45 mA) until the amount of charge passed corresponded to three electrons per molecule (96 mAh for 120 mL of solution) and an OCP of 0.3 V vs SHE was recorded. The OCP was indicated by obtaining a CV of the reduced solution and noting the starting potential. The reduced solution was then divided into two portions to make the anolyte and catholyte of the flow cell.

The results from the flow cell with electrochemically-reduced **α-SiV$_3$W$_9$** electrolytes are shown in Figure 3.35. The charging cut-off voltage was reduced from 1.40 V to 1.25 V during cycle 12 which was associated with a decrease in the charge and discharge capacity, but the appearance of the charge/discharge curves stabilised as cycling continued. The plateau that was previously discussed, which began at ~1.1 V in the flow cell in which electrolytes were pre-reduced with sodium ascorbate, was not visible in this test.

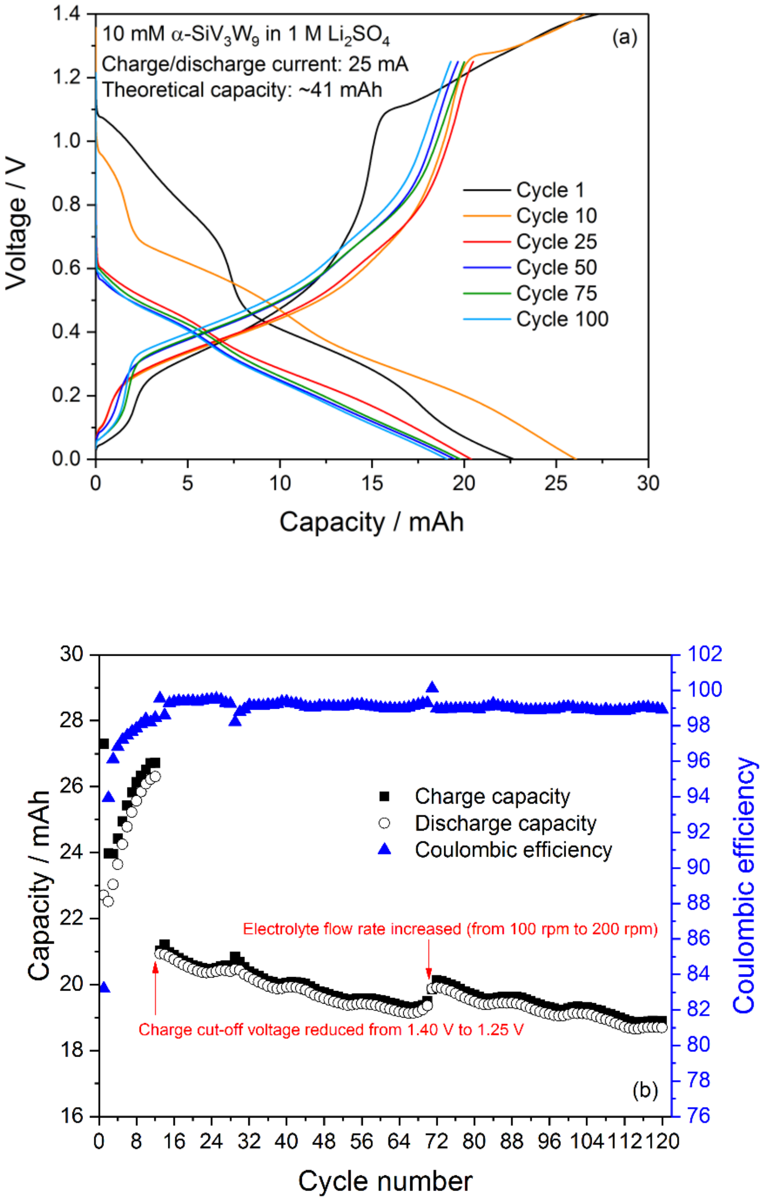

Figure 3.35 - The results of an ***α-SiV₃W₉*** *flow cell test in which the electrolyte was pre-reduced by using electrochemical reduction. (a) Charge/discharge curves. (b) Charge capacity, discharge capacity and coulombic efficiency versus cycle number.*

From cycle 72, the flow rate of the pump was doubled to 200 rpm. This caused a small increase in charging capacity from 19.9 mAh to 20.1 mAh, indicating that more active material was being accessed due to the increase in electrolyte flow rate. Coulombic efficiencies were >98% from cycle 9 onwards. Out of a theoretical capacity of 41 mAh, around 20 mAh were accessed, corresponding to an electrochemical yield of 50%. The discharge capacity decreased from 19.5 mAh in cycle 50 to 19.1 mAh in cycle 100 showing that capacity fade occurred. The voltaic efficiency calculated for cycle 12, after the charging cut-off voltage was altered, was 60%. EIS was carried out and the Nyquist spectrum (see

Appendix) indicated a value of R_{ohm} for the cell in the region of 0.5 Ω. Upon deconstructing the cell when charge/discharge cycling ceased, it was found that one of the gaskets had failed, causing electrolyte to leak into the space between the graphite electrode and brass current collector, and also between the cell frame and stainless-steel endplate. Therefore, electrolyte leakage cannot be ruled out as a contributor to the observed capacity fade. As mentioned previously, if flow cell testing were continued then the nitrogen supply could be turned off to see if this affects the rate of capacity fade.

The results of the initial flow cell testing in this study support that **α-SiV_3W_9** is a suitable species for further investigation of a symmetric POM RFB. It was demonstrated that the POM was stable to a relatively prolonged period of charge/discharge testing (>100 cycles), as CVs of **α-SiV_3W_9** after flow cell testing showed no new features. A greater percentage of the theoretical capacity was accessed in the **α-SiV_3W_9** flow cell in which sodium ascorbate was used to reduce **$SiV^{V}{}_3W_9$** to **$SiV^{IV}{}_3W_9$** prior to cycling, compared to the flow cell prepared with electrochemically reduced electrolytes. Using the discharge capacity of cycle 20 of each flow cell test for comparison, the electrochemical yield was 67% for the flow cell with chemically reduced electrolytes compared to 50% for the flow cell with electrochemically reduced electrolytes. However, the benefit of using chronopotentiometry to reduce the **α-SiV_3W_9** electrolyte is that there are no by-products of the reaction, and no organic molecules with unknown effects, e.g. dehydroascorbic acid, remaining in the electrolyte solutions. For this reason, further testing with electrochemically reduced **α-SiV_3W_9** electrolytes would be desirable.

It is unfortunate that electrolyte leakage could not be prevented in the flow cell tests, and that the source of the capacity fade could not be ascertained. Any future flow cell tests should encompass a period of cycling in which the nitrogen supply to the electrolytes is switched off to see the effect this has on the capacity loss of the cell. It would also be interesting to ascertain if the temperature of the surroundings is responsible for the oscillating charge and discharge capacity that was observed.

3.8 Synthesis Difficulties

The methods used to synthesise **α-SiV_3W_9** and **β-SiV_3W_9** follow the common method used to prepare POMs in water, in which aqueous solutions of oxoanions are acidified in the presence of heteroatoms to form heteropolyoxometalates like **SiV_3W_9**. The equilibrium constants and rates of formation of POMs prepared in this way are generally large enough to allow crystallisation as salts at room temperature.[63] Addition of the appropriate counterion allows isolation of the desired salt (e.g. the potassium salt of the POM) from the solution although the lithium and sodium salts of POMs are more water-soluble.[63] This may add difficulty to this step. However, it is the less-soluble potassium salt of **SiV_3W_9** that is prepared in this work.

In order to prepare the desired POM species, control of temperature and pH may be necessary, the heteroatom may need to be present in excess, and the order in which reagents are added may be significant.[63] The formation of **SiV_3W_9** is not sensitive to the order that reagents are added, although temperature affects which isomer of the precursor **SiW_9**, forms: **β-SiW_9** can be formed from acidifying a cold solution of WO_4^{2-} and SiO_3^{2-} and **α-SiW_9** can be formed from boiling the cold solution of **β-SiW_9**.[63] The ratio of moles of SiO_3^{2-} to moles of WO_4^{2-} in the synthesis of **α-SiW_9** and **β-SiW_9** also differs.

Both **α-SiV_3W_9** and **β-SiV_3W_9** form through the acidification of a solution containing vanadium oxoanions and **α-SiW_9** or **β-SiW_9**. Addition of potassium chloride allows the precipitation of the potassium salt of the POM when methanol is added. Of the methods followed, the **β-SiV_3W_9** synthesis contains more steps, beginning with formation of VO_2^+ by addition of sodium metavanadate ($NaVO_3$) to hot water followed by acidification to pH 1.5.[20] After cooling the VO_2^+ solution, the formation of **β-SiV_3W_9** is immediately evident upon addition of **β-SiW_9** (mole ratio of VO_2^+ to **α-SiW_9** = 3:1) to the solution by a colour change from pale yellow to red. One synthesis of **α-SiV_3W_9** suggests mixing **α-SiW_9** and $NaVO_3$ as dry powders in a 3:1 mole ratio followed by the addition of water, thus cutting out the step of forming a solution of VO_2^+.[19] The formation of **α-SiV_3W_9** is evident upon acidification of the mixture to pH 1.5 by development of a clear “wine red” solution.[19] Alternatively, **α-SiV_3W_9** was prepared by adjusting a solution of $NaVO_3$ and **α-SiW_9** to pH 2.0, with less methanol required for precipitation in this procedure.[18] A 1:1.5 water/methanol mixture is suggested for the recrystallisation of **β-SiV_3W_9**,[20] whereas the suggested recrystallisation solvent for **α-SiV_3W_9** is water.[50]

Despite the simplicity of the procedure, during numerous attempts to synthesise **α-SiV_3W_9** there were difficulties experienced which are recorded in this section. The method followed initially was the method reported by Domaille[19] which proved successful in several attempts early on in this project. In one exemplary synthesis shown in Figure 3.36, a ^{51}V NMR spectrum of a crude **α-SiV_3W_9** sample shows the expected peak for the POM species at -567 ppm, and only a trace of a peak attributable to an impurity at -546 ppm.

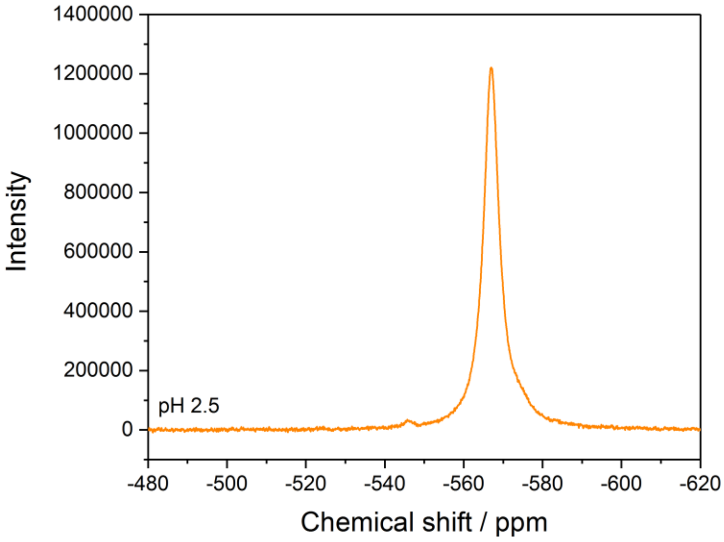

*Figure 3.36 - ^{51}V NMR spectra of a sample of **α-SiV$_3$W$_9$** (crude) from an exemplary synthesis.*

However, following this a new feature of the synthesis emerged: the presence of two peaks in the NMR spectrum, the second at a higher chemical shift of -576 ppm which matched the chemical shift value for **β-SiV$_3$W$_9$**. This showed that, for an unknown reason, the synthesis method had produced two isomers (Figure 3.37).

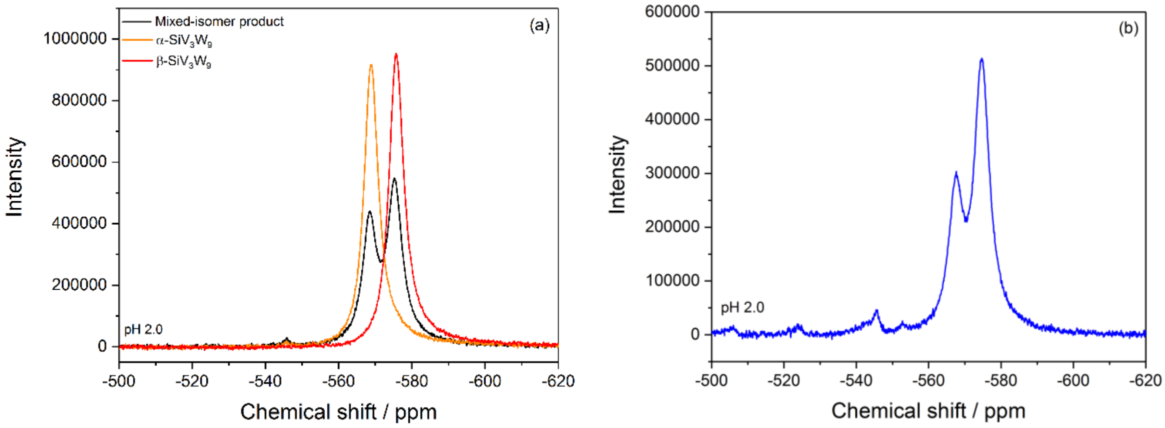

*Figure 3.37 - ^{51}V NMR spectra of products obtained by following the method of synthesis for **α-SiV$_3$W$_9$**. (a) Initial occurrence of the β isomer impurity and comparison with previous isomerically pure samples. (b) A second occurrence of the presence of **β-SiV$_3$W$_9$** (taller peak) after the synthesis was repeated.*

The cause of the presence of two isomers in the samples analysed in Figure 3.37 is unknown. The protocol for synthesising **α-SiV$_3$W$_9$** is an example of a one-pot synthesis. The steps are simple, leaving little room for error or modification: addition of **α-SiW$_9$** and sodium metavanadate to water in a 1:3 molar ratio, acidification to pH 1.5 and the addition of potassium chloride, with a final step of the addition of methanol to precipitate the potassium salt of the POM. A difference in reaction conditions that could favour production of one isomer over another is not indicated. For instance, in both of the synthesis procedures used for the α and β isomer of **SiV_3W_9**, the final pH of the reaction solution was 1.5.

Temperature is one parameter that is different in the conditions of the synthesis of **α-SiW_9** and **β-SiW_9**: the **α-SiW_9** reaction solution is heated to boiling point while the **β-SiW_9** reaction solution remains at room temperature.[20] This suggests that temperature can influence the formation of the α or β isomer of **SiW_9**. However, in the syntheses of **α-SiV_3W_9** and **β-SiV_3W_9**, the reaction solution is at room temperature during the mixing of **SiW_9** and sodium metavanadate in both cases.[19, 64]

One cause could be contamination of the **α-SiW_9** precursor with **β-SiW_9**. To investigate this, FT-IR spectroscopy of several samples of **SiW_9** was carried out. Spectra were obtained of the **α-SiW_9** sample used in a synthesis that resulted in an isomerically pure **SiV_3W_9** sample (from Figure 3.36), the **α-SiW_9** sample used in the synthesis of the impure **SiV_3W_9** sample (from Figure 3.37b) and a sample of **β-SiW_9**. The spectra are shown in Figure 3.38. Granted, these FT-IR spectra are not an indicator of purity, but both of the **α-SiW_9** samples share features, most noticeably bands at ~980 cm^{-1}, 554 cm^{-1} and 525 cm^{-1} which are similar to previously reported band positions for **α-SiW_9**[20] and different to the bands for the sample of **β-SiW_9**. Therefore, there was not an indication from these spectra that the **α-SiW_9** sample used in the synthesis was the source of the production of both **SiV_3W_9** isomers.

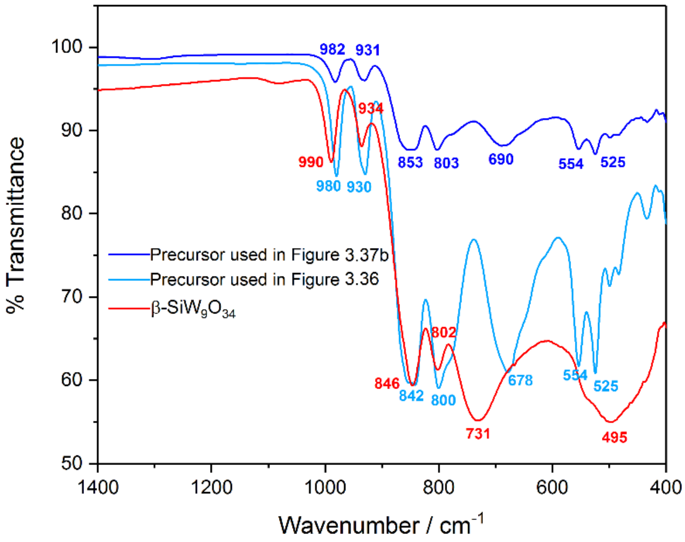

*Figure 3.38 - FT-IR spectra of several **SiW_9** samples.*

Other synthesis protocols reported for **α-SiV_3W_9** in the literature are lacking but it was decided that one such method, which differs slightly to the method previously employed in this work, would be attempted to see if this produced similar results.[18] Upon surveying this procedure, the differences are slight compared to the procedure reported by Domaille,[19] such as a reduction in pH to 2.0 instead of 1.5 and a differing volume of methanol added to precipitate the POM. The result of the two separate synthesis procedures are shown in Figure 3.39.

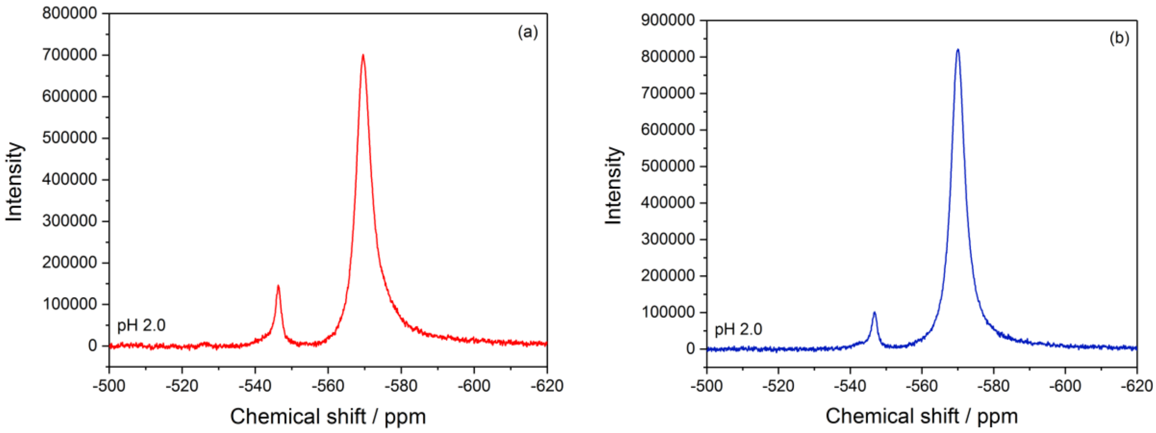

Figure 3.39 - ^{51}V NMR spectra (recrystallised samples) of further attempts to synthesise ***α-SiV$_3$W$_9$****, with reference to a different synthesis procedure.*[18] *(a) First attempt. (b) Second attempt.*

The NMR spectrum in Figure 3.39a indicates that only one isomer is present, with the peak at -570 ppm ascribed to **α-SiV$_3$W$_9$**. The second peak at -546 ppm (of far lower chemical shift than the expected position for the peak for **β-SiV$_3$W$_9$** at this pH) is attributed to VO_2^+ that has not been incorporated into the POM during synthesis. The intensity of this peak lessened after recrystallisation, showing that this impurity could be removed from the sample. A second synthesis afforded a sample with a similar spectrum (Figure 3.39b). Thus, while the source of the formation of both isomers in the previous synthesis attempts is not known, synthesising **α-SiV$_3$W$_9$** with reference to a slightly different method led to a sample which contained a single **SiV$_3$W$_9$** isomer.

Unfortunately, further difficulties were later experienced, when several **α-SiV$_3$W$_9$** samples that were pure of **β-SiV$_3$W$_9$** were found to contain multiple other impurities instead. The results of a series of further **α-SiV$_3$W$_9$** syntheses are shown in Figure 3.40.

Figure 3.40a is the result of a synthesis carried out with reference to the procedure by Bonfim *et al.*,[18] while Figure 3.40b was carried out with reference to the procedure reported by Domaille.[19] Figure 3.40c shows the result of a synthesis carried out by following the same procedure as Figure 3.40b but with a new **α-SiW$_9$** precursor, in case an impure **SiW$_9$** sample was a cause of the impurities in the final **SiV$_3$W$_9$** sample. Multiple peaks are present in each ^{51}V NMR spectrum. The two most prominent peaks are at -570 ppm and -546 ppm, the former is attributable to **α-SiV$_3$W$_9$** and the latter is assigned to VO_2^+. The presence of such a high proportion of VO_2^+ in the sample was not observed in NMR spectra of previous **SiV_3W_9** samples.

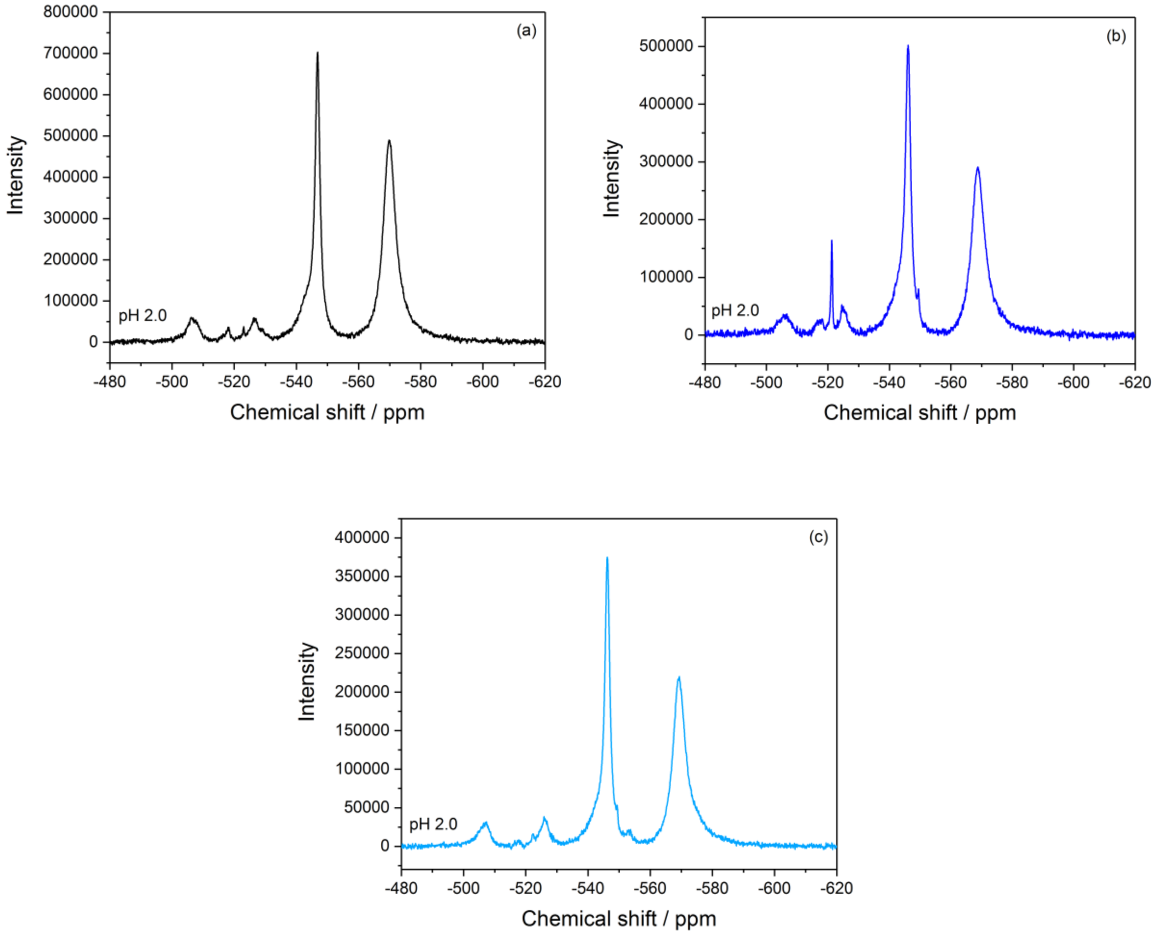

*Figure 3.40 - The result of several syntheses of **α-SiV_3W_9**. (a) Synthesised by referring to ref. 18. (b) Synthesised by following the procedure in ref. 19 and using the same **α-SiW_9** sample as in (a). (c) Synthesised using a different **α-SiW_9** sample to (a) and (b), following the procedure in ref. 19.*

In another repeat of the synthesis, using a further freshly prepared **α-SiW_9** sample that was different to the sample used in Figure 3.40c, a similar spectrum was obtained (Figure 3.41). The impurities in the **α-SiV_3W_9** sample proved difficult to remove by recrystallisation in water, the suggested recrystallisation solvent in the literature procedures. A spectrum of a recrystallised sample is also illustrated in Figure 3.41, showing that the peaks persisted after two recrystallisation steps. Each recrystallisation step incurs a loss of **α-SiV_3W_9** product which added difficulty to obtaining enough sample for the electrolyte of a flow cell. A logical next step in the flow cell testing of **α-SiV_3W_9** would be the preparation of a 20 mM flow cell, which would represent a doubling of the POM concentration compared to the previous flow cell tests. However, the continued preparation of an impure sample added difficulty to furthering the testing of **α-SiV_3W_9**. A reason for the ineffectiveness of the synthesis could not be ascertained at the time.

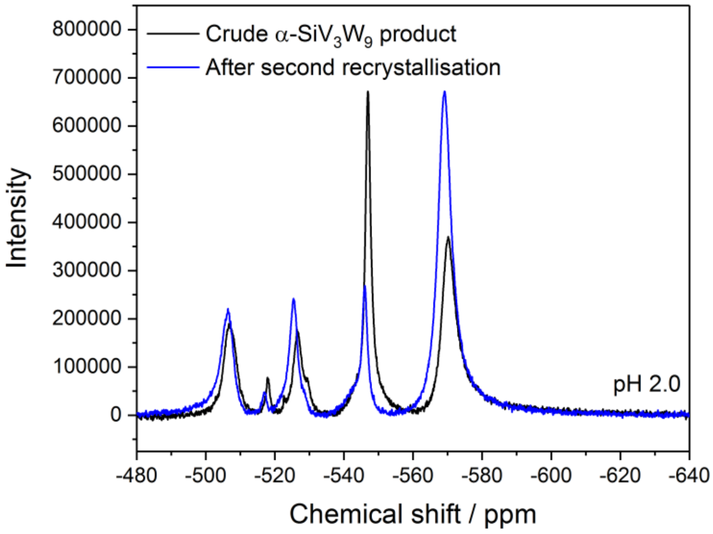

Figure 3.41 - The results of a further attempt to synthesise and recrystallise ***α-SiV$_3$W$_9$****.*

It was later realised that the chemical supplier of the vanadium source had changed from the supplier used in initial syntheses, such as that shown in Figure 3.36 (sodium metavanadate with a purity of ≥98%), Sigma Aldrich), to another chemical supplier (sodium metavanadate with a purity of 'typically 96%', Alfa Aesar). The sodium metavanadate of lower purity was used in later procedures. It was not possible to test whether the change in supplier and purity of the sodium metavanadate was responsible for the issues described but the purity of the vanadium source may need to be considered when preparing **α-SiV$_3$W$_9$**. However, the sodium metavanadate with lower purity was also used to prepare **β-SiV$_3$W$_9$** (see below) and the same issues were not experienced.

To investigate the efficacy of the **β-SiV$_3$W$_9$** synthesis and compare this to the results of the **α-SiV$_3$W$_9$** synthesis, a batch of **β-SiV$_3$W$_9$** was synthesised using 1 g of **β-SiW$_9$** as starting material. The synthesis procedure by Finke *et al*. was followed.[21] A ^{51}V NMR spectrum of the crude sample was obtained (Figure 3.42a) which shows a peak at -576 ppm, attributable to **β-SiV$_3$W$_9$**, and indicates that this was a far cleaner synthesis. The synthesis was repeated on a larger scale (using 33 g of **β-SiW$_9$** as starting material) and the result is shown in Figure 3.42b. Again, the spectrum of even a crude sample of **β-SiV$_3$W$_9$** shows a single peak without impurities.

The methods used to prepare **α-SiV$_3$W$_9$** and **β-SiV$_3$W$_9$** differ. In the procedure for the preparation of **β-SiV$_3$W$_9$**, a solution of VO_2^+ is prepared in a separate step by adding $NaVO_3$ to hot water and lowering the pH. **β-SiW$_9$** is then added to form **β-SiV$_3$W$_9$**. The preparation of a solution of VO_2^+ is omitted when preparing **α-SiV$_3$W$_9$**. The significance, if any, of the extra step of preparing a separate solution containing VO_2^+ is not known but the synthesis of **β-SiV_3W_9** was more effective and this is a notable difference between the two methods.

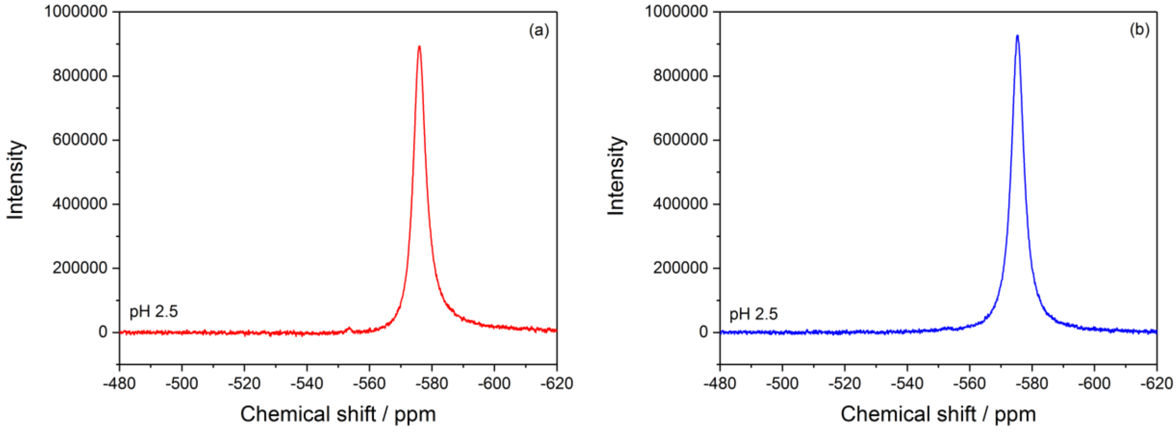

*Figure 3.42 - The results of two separate syntheses of **β-SiV_3W_9**.*

The source of the difficulties experienced in synthesising **α-SiV_3W_9**, both the presence of two isomers in the sample and the occurrence of multiple impurities, is not known but the results are recorded in case they will be of use for future work with **SiV_3W_9.** Based on the results here, the synthesis of **β-SiV_3W_9** is less problematic which could be kept in mind if work on **SiV_3W_9** is revisited. However, the difference in the yield of the two isomers should be considered. The yield of **β-SiV_3W_9** in the second step of the synthesis was 80% but the yield of **β-SiW_9** in the first step was 33%. Thus, the overall yield of **β-SiV_3W_9** is lowered by the poorer yield of **β-SiW_9**. A similar result was reported in a literature synthesis of **β-SiV_3W_9**, in which the yield of **β-SiW_9** was 14–23% and the yield of **β-SiV_3W_9** was 82%.[64] The yield of **β-SiW_9** would be a downside of the use of the β isomer as it lowers the overall yield of **β-SiV_3W_9**. Thus, the effect of the chemical supplier of sodium metavanadate on the purity of the product could be investigated as a next step before investigating **β-SiV_3W_9** further.

3.9 Summary and Conclusions

An investigation was carried out into the application of the tri-vanadium substituted Keggin anion **α-SiV_3W_9** as the active species in a symmetric RFB. A study using cyclic voltammetry illustrated the properties of this species that make it a candidate for a symmetric flow cell. The vanadium and tungsten redox activity described in previous work was observed.[16]

Bulk electrolysis of **SiV_3W_9** led to the discovery that reduction of **$SiV^{V}_3W_9$** to **$SiV^{IV}_3W_9$** could be associated with destruction of the POM, as CVs of reduced solutions showed the same features as CVs of the lacunary precursor **SiW_9**. This was attributed to the acidic conditions under which the experiment was carried out. It was previously shown that instability of polyoxotungstates substituted with metal species that were not in their maximum oxidation state was associated with acidic conditions.[47, 48]

A pH stability study was proposed that encompassed **$SiV^{V}{}_3W_9$** and **$SiV^{IV}{}_3W_9$**. ^{51}V NMR spectra of **α-SiV_3W_9** solutions at different pH (pH 0.3–4.0) illustrated that **α-$SiV^{V}{}_3W_9$** was stable for an extended period (one week) at each pH. Bulk electrolysis and subsequent CVs of **α-$SiV^{IV}{}_3W_9$** solutions in 1 M H_2SO_4 (pH ≈ 0) and at pH 1.0 showed that the reduced **α-$SiV^{IV}{}_3W_9$** species was not stable on the timescale of one hour after reduction in 1 M H_2SO_4 and 24 hours after reduction at pH 1.0. Conversely, **α-SiV_3W_9** that had been reduced in a pH 2.0 solution showed stability after 24 hours. This pH was selected as the minimum pH for the supporting electrolytes in charge/discharge testing.

The testing of a symmetric **α-SiV_3W_9** stationary cell supported the stability of the α isomer to charge/discharge testing, whereas the stability of **β-SiV_3W_9** in an analogous test was not satisfactory. Flow cells based on **α-SiV_3W_9** electrolytes were constructed and exhibited a sustained coulombic efficiency of >98% but capacity fade was evident. CVs of the catholyte and anolyte after charge/discharge testing did not indicate decomposition of **α-SiV_3W_9** had occurred. Electrolyte leakage could, unfortunately, not be prevented in this work and therefore is not excluded as a contributor to the capacity fade of the flow cells, but the permeation of oxygen into flow cell electrolytes solutions could also contribute to capacity fade.[55] Further work could test a (water-tight) **SiV_3W_9** flow cell with and without nitrogen purging of the electrolytes to see the effect of this on the rate of capacity fade. Further investigation of the half-cell reactions of a **SiV_3W_9** flow cell could also be carried out as observed voltages in charge/discharge testing did not match the theoretical voltages calculated for the coupling of the vanadium redox reactions with the tungsten redox reactions.

Efforts to continue flow cell testing of **α-SiV_3W_9**, at increased concentration for instance, were marred by synthesis difficulties. This included the presence of impurities of unknown source in **α-SiV_3W_9** samples, indicated by ^{51}V NMR spectroscopy. In contrast, **β-SiV_3W_9** could be prepared in higher purity. Continued work could investigate further flow cell electrolytes that use **β-SiV_3W_9** as an alternative to **α-SiV_3W_9** if the synthesis problems with **α-SiV_3W_9** persist. Instability of **β-SiV_3W_9** was indicated in a stationary cell test with electrolytes with a pH of 2, but electrolytes of higher pH could be tested to see if the POM is more stable at a different pH. The preparation of **β-SiV_3W_9** samples of higher purity could allow flow cell testing of **SiV_3W_9** to continue, which could include the testing of electrolytes that contain a higher concentration of the POM than the electrolytes already studied.

3.10 References

1. R. A. Potash, J. R. McKone, S. Conte and H. D. Abruña, *J Electrochem Soc*, 2016, **163**, A338-A344.
2. J. Winsberg, C. Stolze, S. Muench, F. Liedl, M. D. Hager and U. S. Schubert, *ACS Energy Letters*, 2016, **1**, 976-980.
3. T. Janoschka, C. Friebe, M. D. Hager, N. Martin and U. S. Schubert, *ChemistryOpen*, 2017, **6**, 216-220.
4. W. Duan, R. S. Vemuri, J. D. Milshtein, S. Laramie, R. D. Dmello, J. Huang, L. Zhang, D. Hu, M. Vijayakumar, W. Wang, J. Liu, R. M. Darling, L. Thompson, K. Smith, J. S. Moore, F. R. Brushett and X. Wei, *Journal of Materials Chemistry A*, 2016, **4**, 5448-5456.
5. T. Hagemann, J. Winsberg, B. Häupler, T. Janoschka, J. J. Gruber, A. Wild and U. S. Schubert, *Npg Asia Materials*, 2017, **9**, e340.
6. Q. Liu, A. E. S. Sleightholme, A. A. Shinkle, Y. Li and L. T. Thompson, *Electrochemistry Communications*, 2009, **11**, 2312-2315.
7. Q. Liu, A. A. Shinkle, Y. Li, C. W. Monroe, L. T. Thompson and A. E. S. Sleightholme, *Electrochemistry Communications*, 2010, **12**, 1634-1637.
8. D. Zhang, H. Lan and Y. Li, *J Power Sources*, 2012, **217**, 199-203.
9. P. J. Cappillino, H. D. Pratt, N. S. Hudak, N. C. Tomson, T. M. Anderson and M. R. Anstey, *Advanced Energy Materials*, 2014, **4**, 1300566-n/a.
10. P. J. Cabrera, X. Yang, J. A. Suttil, K. L. Hawthorne, R. E. M. Brooner, M. S. Sanford and L. T. Thompson, *The Journal of Physical Chemistry C*, 2015, **119**, 15882-15889.
11. C. G. Armstrong and K. E. Toghill, *J Power Sources*, 2017, **349**, 121-129.
12. R. W. Hogue, C. G. Armstrong and K. E. Toghill, *ChemSusChem*, **0**.
13. X. Wei, W. Xu, J. Huang, L. Zhang, E. Walter, C. Lawrence , M. Vijayakumar, W. A. Henderson, T. Liu, L. Cosimbescu, B. Li, V. Sprenkle and W. Wang, *Angewandte Chemie International Edition*, 2015, **54**, 8684-8687.
14. G. D. Charlton, S. M. Barbon, J. B. Gilroy and C. A. Dyker, *Journal of Energy Chemistry*, 2019, **34**, 52-56.
15. J. Friedl, F. L. Pfanschilling, M. V. Holland-Cunz, R. Fleck, B. Schricker, H. Wolfschmidt and U. Stimming, *Clean Energy*, 2019, DOI: 10.1093/ce/zkz019.
16. H. D. Pratt Iii, N. S. Hudak, X. Fang and T. M. Anderson, *J Power Sources*, 2013, **236**, 259-264.
17. Y. Liu, S. Lu, H. Wang, C. Yang, X. Su and Y. Xiang, *Advanced Energy Materials*, 2017, **7**, 1601224.

18. R. d. P. F. Bonfim, L. C. de Moura, J.-G. Eon, O. Mentré, H. Vezin and S. Caldarelli, *Journal of Solid State Chemistry*, 2014, **213**, 9-16.
19. P. J. Domaille, *Journal of the American Chemical Society*, 1984, **106**, 7677-7687.
20. A. Tézé and G. Hervé, in *Inorganic Syntheses*, ed. A. P. Ginsberg, John Wiley & Sons, New York, 1990, vol. 27, ch. 3, pp. 85-96.
21. R. G. Finke, C. A. Green and B. Rapko, in *Inorganic Syntheses*, ed. A. P. Ginsberg, John Wiley & Sons, New York, 1990, vol. 27, ch. 3, pp. 128-135.
22. C. Li, Y. Zhang, K. P. O'Halloran, J. Zhang and H. Ma, *Journal of Applied Electrochemistry*, 2009, **39**, 421-427.
23. S. Himeno and N. Ishio, *J Electroanal Chem*, 1998, **451**, 203-209.
24. I. K. Song and M. A. Barteau, *Journal of Molecular Catalysis A: Chemical*, 2004, **212**, 229-236.
25. M. Robinson, K. Ounnunkad, J. Zhang, D. Gavaghan and A. Bond, *ChemElectroChem*, 2018, **5**, 3771-3785.
26. B. Keita and L. Nadjo, *Journal of Electroanalytical Chemistry and Interfacial Electrochemistry*, 1987, **227**, 77-98.
27. J. Canny, R. Thouvenot, A. Teze, G. Herve, M. Leparulo-Loftus and M. T. Pope, *Inorg. Chem.*, 1991, **30**, 976-981.
28. G. Denuault, M. Sosna and K.-J. Williams, in *Handbook of Electrochemistry*, ed. C. G. Zoski, Elsevier, 1st edn., 2007, ch. 11, pp. 431-469.
29. N. Elgrishi, K. J. Rountree, B. D. McCarthy, E. S. Rountree, T. T. Eisenhart and J. L. Dempsey, *Journal of Chemical Education*, 2018, **95**, 197-206.
30. M. T. Pope and G. M. Varga, *Inorg. Chem.*, 1966, **5**, 1249-1254.
31. A. Horky, N. P. Kherani and G. Xu, *J Electrochem Soc*, 2003, **150**, A1219.
32. K. Bano, J. Zhang, A. M. Bond, P. R. Unwin and J. V. Macpherson, *The Journal of Physical Chemistry C*, 2015, **119**, 12464-12472.
33. D. G. Kwabi, K. Lin, Y. Ji, E. F. Kerr, M.-A. Goulet, D. De Porcellinis, D. P. Tabor, D. A. Pollack, A. Aspuru-Guzik, R. G. Gordon and M. J. Aziz, *Joule*, 2018, **2**, 1894-1906.
34. T. Janoschka, N. Martin, M. D. Hager and U. S. Schubert, *Angewandte Chemie International Edition*, 2016, **55**, 14427-14430.
35. S. Yin, L. Zhou, X. Du and Y. Yang, *Ionics*, 2019, **25**, 593-606.
36. E. Sum, M. Rychcik and M. Skyllas-kazacos, *J Power Sources*, 1985, **16**, 85-95.
37. E. Cadot, M. Fournier, A. Tézé and G. Hervé, *Inorg. Chem.*, 1996, **35**, 282-288.

38. B. Keita and L. Nadjo, *Journal of Electroanalytical Chemistry and Interfacial Electrochemistry*, 1987, **227**, 77-98.
39. M. H. V. Huynh and T. J. Meyer, *Chem. Rev.*, 2007, **107**, 5004-5064.
40. D. M. Way, A. M. Bond and A. G. Wedd, *Inorg. Chem.*, 1997, **36**, 2826-2833.
41. J. Friedl, R. Al-Oweini, M. Herpich, B. Keita, U. Kortz and U. Stimming, *Electrochim Acta*, 2014, **141**, 357-366.
42. B. Keïta and L. Nadjo, *Journal of Electroanalytical Chemistry and Interfacial Electrochemistry*, 1985, **191**, 441-448.
43. B. Keita and L. Nadjo, *J Electroanal Chem*, 1993, **354**, 295-304.
44. A. Selling, I. Andersson, L. Pettersson, C. M. Schramm, S. L. Downey and J. H. Grate, *Inorg. Chem.*, 1994, **33**, 3141-3150.
45. M. V. Holland-Cunz, J. Friedl and U. Stimming, *J Electroanal Chem*, 2018, **819**, 306-311.
46. L. I. Kuznetsova, R. I. Maksimovskaya and K. I. Matveev, *Inorganica Chimica Acta*, 1986, **121**, 137-145.
47. C. M. Tourné, G. F. Tourné, S. A. Malik and T. J. R. Weakley, *Journal of Inorganic and Nuclear Chemistry*, 1970, **32**, 3875-3890.
48. A. Müller, L. Dloczik, E. Diemann and M. T. Pope, *Inorganica Chimica Acta*, 1997, **257**, 231-239.
49. M. M. Mossoba, C. J. O'Connor, M. T. Pope, E. Sinn, G. Herve and A. Teze, *Journal of the American Chemical Society*, 1980, **102**, 6864-6866.
50. E. Cadot, R. Thouvenot, A. Teze and G. Herve, *Inorg. Chem.*, 1992, **31**, 4128-4133.
51. A. Jürgensen and J. B. Moffat, *Catalysis Letters*, 1995, **34**, 237-244.
52. M. A. Leparulo-Loftus and M. T. Pope, *Inorg. Chem.*, 1987, **26**, 2112-2120.
53. X. Lu, W. D. Johnson and J. Hook, *Environmental Science & Technology*, 1998, **32**, 2257-2263.
54. F. Ortega and M. T. Pope, *Inorg. Chem.*, 1984, **23**, 3292-3297.
55. J. Friedl, M. V. Holland-Cunz, F. Cording, F. L. Pfanschilling, C. Wills, W. McFarlane, B. Schricker, R. Fleck, H. Wolfschmidt and U. Stimming, *Energy & Environmental Science*, 2018, DOI: 10.1039/C8EE00422F.
56. L. I. Kuznetsova, Y. V. Chernyshova and R. I. Maksimovskaya, *Inorganica Chimica Acta*, 1990, **167**, 223-231.
57. A. Rudnitskaya, J. A. F. Gamelas, D. V. Evtuguin and A. Legin, *New Journal of Chemistry*, 2012, **36**, 1036-1042.

58. I. Kaminker, H. Goldberg, R. Neumann and D. Goldfarb, *Chemistry – A European Journal*, 2010, **16**, 10014-10020.
59. K. Mizuno, T. Mura and S. Uchida, *Crystal Growth & Design*, 2016, **16**, 4968-4974.
60. A. K. Manohar, K. M. Kim, E. Plichta, M. Hendrickson, S. Rawlings and S. R. Narayanan, *J Electrochem Soc*, 2016, **163**, A5118-A5125.
61. T. D. Nguyen, A. Whitehead, G. G. Scherer, N. Wai, M. O. Oo, A. Bhattarai, G. P. Chandra and Z. J. Xu, *J Power Sources*, 2016, **334**, 94-103.
62. H. D. Pratt Iii and T. M. Anderson, *Dalton Trans.*, 2013, **42**, 15650-15655.
63. M. T. Pope, in *Heteropoly and Isopoly Oxometalates*, Springer-Verlag, Berlin, 1983, ch. 2, pp. 15-32.
64. R. G. Finke, B. Rapko, R. J. Saxton and P. J. Domaille, *Journal of the American Chemical Society*, 1986, **108**, 2947-2960.

3.11 Appendix

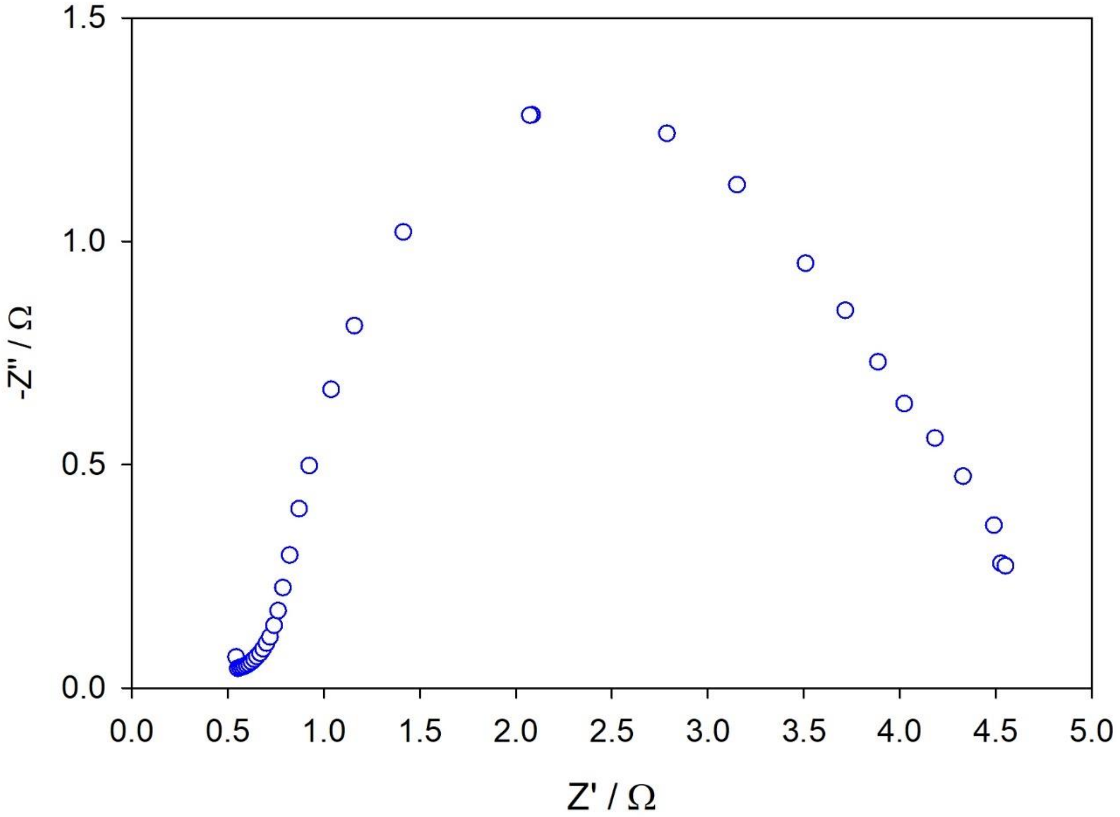

A Nyquist spectrum of the flow cell used in Section 3.7 when the cell was discharged. EIS was carried out over a frequency range of 10 kHz–10 mHz using an amplitude of 10 mV.

Chapter 4 - A Kinetics Study of $[SiW_{12}O_{40}]^{4-}$

4.1 Introduction

The only asymmetric RFB to use POMs in both electrolytes that has been reported currently is the system presented by Friedl *et al*. which uses $[PV_{14}O_{42}]^{9-}$ (**PV_{14}**) and $[SiW_{12}O_{40}]^{4-}$ (**SiW_{12}**).[1] Vanadium is the redox-active metal at the cathode and tungsten is the redox-active metal at the anode. As a side note, this mirrors the working principle of a symmetric POM RFB based on $[SiV_3W_9O_{40}]^{7-}$ (described in the previous chapter), as vanadium and tungsten are the metals that cycle between different oxidation states at the cathode and anode respectively. CVs and ball-and-stick structures of **PV_{14}** and **SiW_{12}** are shown in Figure 4.1.

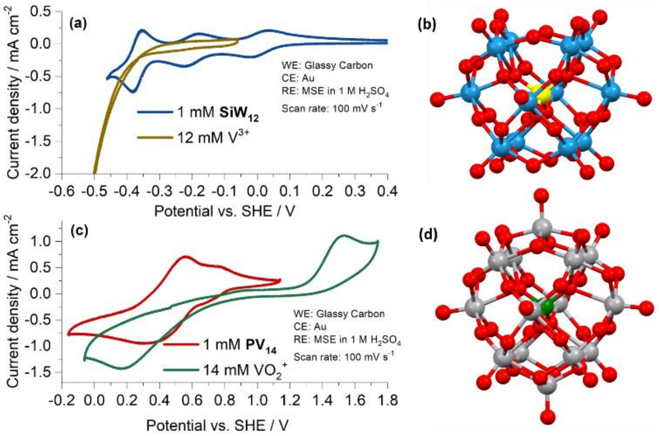

*Figure 4.1 - (a) A CV of **SiW_{12}** (blue line) (overlaid with a CV of V^{3+}). (b) Ball-and-stick representation of **SiW_{12}** and **PV_{14}**. (c) A CV of **PV_{14}** (red line) (overlaid with a CV of VO_2^+). (d) Ball-and-stick representation of **PV_{14}**.[1] (Reproduced by permission of the Royal Society of Chemistry.)*

SiW_{12} has a Keggin structure and its redox properties consist of multiple reversible diffusion-controlled waves. At a concentration of 1 mM, a CV of **SiW_{12}** consists of five reduction waves with approximate electron ratios of 1:1:2:8:12.[2] When scanning to a potential where all of the reduction waves are observed, the reoxidation waves are ill-defined.[2] For stable observation of the reduction pattern in the CV of **SiW_{12}**, it has been found that the potential cannot be scanned further than after the third wave, which is shown in Figure 4.1a, as modification of the electrode surface (glassy carbon) occurs in the potential domain after the third wave, accompanied by catalysis of the hydrogen evolution reaction.[3] Electrolysis at the potential of the third wave also resulted in electrode derivatization.[3] Accordingly, it was found that only the first two one-electron redox reactions of **SiW_{12}** could be used in the **SiW_{12}-PV_{14}** RFB.[1]

In the study by Friedl *et al*. it was highlighted that there are several properties of POMs which make them candidates for the active species in RFB electrolytes, the first of which is “electrons added to POMs by reduction are often delocalised over several metal atoms, and this will facilitate fast electron transfer which enables high current densities”.[1]

Increasing the current density that can be obtained at a given cell voltage leads to an increase in the power density of an RFB (power density = current density × discharge voltage). One way to increase the current that is obtainable from the electrode of a battery is to increase the exchange current density, j_0, as the higher the value of j_0, the lower the overpotential for a given current.[4, 5] Fast redox reactions, where j_0 is high, reduce the contribution of the kinetic overpotential to the total overpotential which must be applied above the theoretical voltage of a battery in order to get a current to flow. This makes species that exhibit fast kinetics attractive candidates for RFB active materials.

The kinetics of redox reactions are characterised by the electron transfer constant, k^0. An estimate given for the order of magnitude of k^0 for a practical RFB was 10^{-5} cm s^{-1} by Weber *et al*. (several assumptions were made in calculating this value which are specified in this reference, for instance, a target kinetic overpotential was given as a value <150 mV for the operation of an RFB at a practical current density of ≥50 mA cm^{-2}).[6] Out of various common redox couples used in RFBs, Weber *et al*. highlighted that the VO_2^+/VO^{2+} redox couple, a CV of which is overlaid with **PV_{14}** in Figure 4.1c, has a “clear kinetic limitation” with a relatively small indicative order of magnitude of 10^{-7} cm s^{-1} referenced for k^0.[6] The large peak separation of 1.37 V in the CV with a scan rate of 100 mV s^{-1} in Figure 4.1c is typical of a sluggish redox reaction.[1]

Similar orders of magnitude have been reported for the V^{3+}/V^{2+} redox couple.[4] The slow kinetics of this reaction are supported by the negligible current in the CV of V^{3+}/V^{2+} that is overlaid with **SiW_{12}** in Figure 4.1a, with comparable current density obtained for **SiW_{12}** despite the twelve-fold higher concentration of V^{3+}. In water, V^{2+} and V^{3+} exist as octahedral complexes that contain six molecules of water.[7]

An inner-sphere reaction mechanism involves specific adsorption of species at the electrode surface, or electron transfer occurs through the formation of a ligand bridge between a specifically adsorbed ion and another ion or between ions. Outer-sphere reaction mechanisms do not involve strong interactions between reacting species or products and the electrode surface or formation of a ligand bridge. The V^{3+}/V^{2+} reaction is thought to proceed by the more complicated inner-sphere mechanism, given its sensitivity to electrode surface modifications.[8, 9] Specifically, the reaction is catalysed by surface carbonyl groups on carbon electrodes but exhibits outer-sphere behaviour if carbonyl groups are not present.[10] It was found that the oxidation of V^{2+} to V^{3+} at a glassy carbon surface involved an adsorbed intermediate.[11] The proposed mechanism in H_2SO_4 involved substitution of a water molecule for an -OH group at the electrode surface to form a ligand bridge, followed by electron transfer. The V^{3+} complex then desorbs from the electrode surface and regains a ligand. In contrast, POMs are likely to undergo outer-sphere electron transfers[12] including the electron transfer of $[SiW_{12}O_{40}]^{4-}$ which was studied as an outer-sphere mechanism.[13]

Given the reported order of magnitude of the k^0 values for the vanadium redox couples of the VRFB, slow redox kinetics can be considered a disadvantage of the use of this chemistry, necessitating the use of porous graphite felt electrodes with a high surface area in order to draw practical currents.

A study that aims to elucidate k^0 values for **SiW_{12}** could yield information in support of its application as the anolyte of an asymmetric POM RFB if the kinetics are found to be fast. Due to the larger size of POMs relative to simpler anions, a weaker interaction with solvent molecules and a resultant low reorganisation energy can be expected, so enabling fast electron transfer kinetics.[14] The basis of transition state theory is that reactants progress through a transition state or activated complex en route to the products. The standard free energy change from reactants to the activated complex, $\Delta G_f^{\ddagger}$, is shown in Equation 4.1, where ΔG_0 is the Gibbs standard reaction energy and λ is the reorganisation energy.[15]

$$\Delta G_f^{\ddagger} = \frac{\lambda}{4}\left(1 + \frac{\Delta G_0}{\lambda}\right)^2 \qquad 4.1$$

The value of λ represents the energy required to convert the nuclear configurations within the reactant and solvent to their configuration in the products.[15] This contains an inner component (λ_i) for the contribution from reorganisation of the reactants and an outer component (λ_o) for the reorganisation of the solvent (Equation 4.2). Thus, it is shown that a change in solvation makes an energetic contribution to $\Delta G_f^{\ddagger}$.

$$\lambda = \lambda_i + \lambda_o \qquad 4.2$$

For an electrode at E^0 (where k_f for the forward reaction = k_r for the reverse reaction = k^0), $\Delta G_f^{\ddagger} \approx \lambda/4$ and k^0 can thus be predicted to be larger when:[15]

- The internal reorganisation is smaller (e.g. the oxidised and reduced species have similar structures resulting in no large changes in bond lengths or angles).
- The molecule is large, so exhibiting lower solvation energies and consequent smaller changes in solvation.

Resultantly, electron transfer reactions involving small molecules can be expected to be slower than the reduction of large aromatic molecules.[15]

Values of k^0 that have been determined for POMs include a value of 0.0032 cm s^{-1} for a manganese-substituted Keggin structure, $[Mn^{III}_3(OH)_3(H_2O)_3SiW_9O_{34}]^{4-}$, and 0.015 cm s^{-1}

for $[PW_{12}O_{40}]^{3-}$.[16, 17] If k^0 values are relatively high for **SiW_{12}**, then this could be an advantage of its use as an anolyte species over other species that are used in traditional RFB chemistries like the VRFB. Two techniques were attempted in the study of the kinetics of **SiW_{12}**. The first method was chronoamperometry, or the potential step method, in which an electrode is perturbed from its equilibrium potential (E_{eq}) by applying a potential step and then measuring the resulting current. In the second method, Electrochemical Impedance Spectroscopy (EIS), “a sinusoidally varying potential with a small amplitude is applied to the interface [the region where electrode and electrolyte meet] and the resulting response of the current measured”.[18]

4.2 Experimental

4.2.1 Materials

$H_4[\alpha\text{-}SiW_{12}O_{40}]\cdot xH_2O$ was purchased as tungstosilicic acid hydrate from Sigma Aldrich and used as received in all experiments. Sulphuric acid (95%–98%), used to prepare supporting electrolytes, was supplied by Sigma Aldrich.

4.2.2 Chronoamperometry

A Biologic SP300 potentiostat was used for chronoamperometry. The three-electrode cell was of a custom-built design with a glassy carbon working electrode (surface area = 0.02 cm^2), a gold wire counter electrode and an MSE (1 M H_2SO_4) reference electrode (E = 0.674 V vs SHE). **SiW_{12}** was dissolved in 1 M H_2SO_4 to make a 10 mM solution and the solution was purged with nitrogen for 10 minutes before measurements began. The working electrode was polished with alumina polish (0.05 μm) prior to the experiment.

The potential of the working electrode was held at 0.274 V vs SHE for 100 ms and then stepped to a new value within a potential range of 0.264 V vs SHE to -0.126 V vs SHE, and held at the new value for 100 ms. The value of the second potential was increased by 10 mV each time. The same set of potentials steps were also carried out for a blank solution of 1 M H_2SO_4.

4.2.3 Electrochemical Impedance Spectroscopy

A Biologic SP300 potentiostat was used for EIS. **SiW_{12}** was dissolved in 1 M H_2SO_4 to make a 20 mM solution. A commercial bulk electrolysis cell (BASi) was used to prepare 50:50 mixtures of $[SiW_{12}O_{40}]^{4-}$/$[SiW_{12}O_{40}]^{5-}$ and $[SiW_{12}O_{40}]^{5-}$/$[SiW_{12}O_{40}]^{6-}$. The cell consisted of a glassy carbon mesh working electrode, a platinum wire counter electrode and a Ag/AgCl (3 M NaCl) reference electrode (E = 0.209 V vs SHE). A constant current of -50 mA was applied to the working electrode until passage of the desired amount of charge to reduce the **SiW_{12}** solution by 0.5 electrons and 1.5 electrons occurred. The solution was continuously stirred and purged with nitrogen during the experiment.

When the desired amount of charge had been passed, the OCP was checked to be equal to $E_{1/2}$ for the first or second reduction of **SiW_{12}** by obtaining a CV of the solution and noting the OCP. The working electrode was switched to a glassy carbon disc electrode (surface area = 0.07 cm^2) and the glassy carbon mesh electrode was used as the counter electrode in order obtain a CV.

EIS was conducted at OCP values of 0.016 V vs SHE for the first reduction of **SiW_{12}** and -0.197 V vs SHE for the second reduction of **SiW_{12}** with an amplitude of 10 mV and a frequency range of 2 MHz–100 mHz.

4.3 Chronoamperometry

Chronoamperometry was previously used to study the kinetics of the oxidation of Mn^{III} to Mn^{VI} in the tri-manganese substituted Keggin structure $[Mn^{III}_3(OH)_3(H_2O)_3SiW_9O_{34}]^{4-}$.[16] As mentioned previously, the k^0 value determined was 0.0032 cm s^{-1}, a value that is several orders of magnitude higher than values reported for the reactions of the VRFB and which supports that POM species could have relatively fast charge transfer kinetics.

It was decided that chronoamperometry would also be used to study **SiW_{12}**. In this technique, a potential step is applied to an electrode that is at E_{eq} at time $t < 0$. After the potential step is applied at $t = 0$, the current is measured with respect to time. Initially, charging of the electrical double layer takes place (non-faradaic current) but, if the decay of the faradaic current is relatively slow, the observed current that becomes relatively constant after charging of the electrical double layer can be accepted as the faradaic current without the effect of diffusion control.[19] The faradaic current is equivalent to the current predicted by the Butler-Volmer equation with a second term ($\exp[\Lambda^2 t]\ \mathrm{erfc}[\Lambda\sqrt{t}]$) correcting for diffusion and carrying the time dependence of the current, where Λ is a constant containing the diffusion coefficients of the redox species, D_{ox} and D_{red} (Equation 4.3).[19]

$$Faradaic\ current = i_0\left(\exp\left[\frac{\alpha_a nF}{RT}\eta\right] - \exp\left[\frac{\alpha_c nF}{RT}\eta\right]\right) * \left(\exp[\Lambda^2 t]\ \mathrm{erfc}\left[\Lambda\sqrt{t}\right]\right) \qquad 4.3$$

For short times ($\Lambda\sqrt{t} << 1$) a plot of i against $\sqrt{t}$ can be extrapolated back to $t = 0$ to yield the underlying faradaic current in the absence of diffusion control.[19]

In voltammetric experiments, **SiW_{12}** can be reduced by four electrons but only study of the first one-electron reduction was undertaken using chronoamperometry. During the experiment, the potential was initially held at a value that was positive of the half-wave potential ($E_{1/2}$) of the first reduction of **SiW_{12}** where no current was recorded (0.274 V vs SHE). The potential was then stepped to a new value in the range of 0.264 V vs SHE to -0.126 V vs SHE, a potential range that encompassed the first reduction of **SiW_{12}** and so induced the flow of a reducing current. This potential range is illustrated in Figure 4.2.

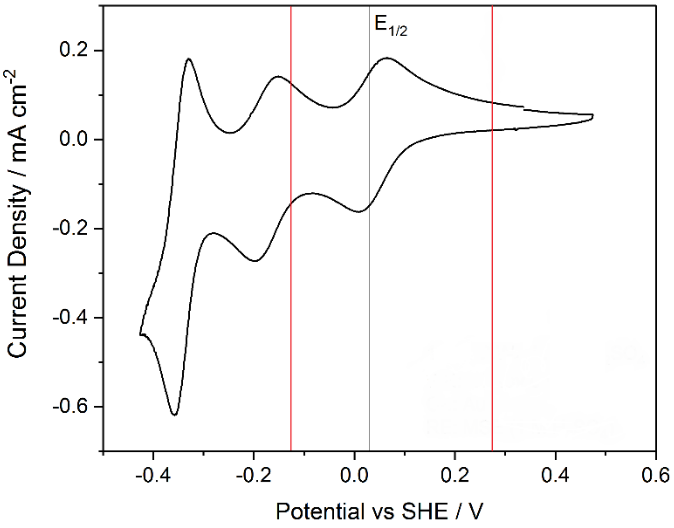

Figure 4.2 - A CV of ***SiW12*** *(1 mM) in 1 M* H_2SO_4 *showing* $E_{1/2}$ *and the range of potentials applied in chronoamperometry (area within the red lines). (WE: glassy carbon, CE: gold wire, RE: MSE (1 M* H_2SO_4*), scan rate: 100 mV/s)*

A representative current transient is shown in Figure 4.3a after the potential was stepped to a more negative value, from 0.274 V vs SHE to 0.014 V vs SHE. To improve the current transients, the non-faradaic current (black data points in Figure 4.3a) can be measured in blank electrolyte and then subtracted. This was carried out and the result of the subtraction is shown by the red data points in Figure 4.3a.

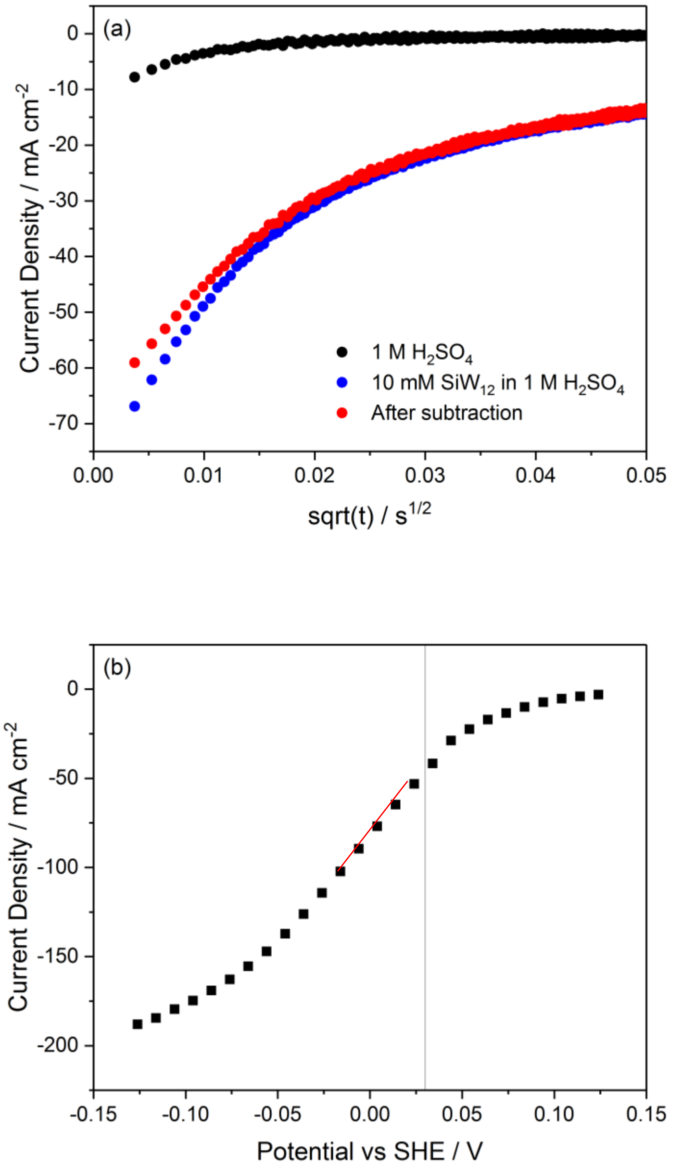

Figure 4.3 - (a) A plot of the current density versus $\sqrt{t}$ after the potential was stepped from 0.274 V vs SHE to 0.014 V vs SHE. The current obtained in blank supporting electrolyte, in a 10 mM solution of $\mathbf{SiW_{12}}$ *and the result of subtracting the current for the blank supporting electrolyte from that of the POM solution are all shown. (b) The extrapolated current, taken to be the faradaic current, at each potential.*

A plot of the faradaic current that was determined by extrapolating to $t = 0$ for each current transient against the potential at which it was obtained is shown in Figure 4.3b. $E_{1/2}$ of the first reduction of $\mathbf{SiW_{12}}$, measured using a CV, is indicated by the grey line (0.030 V vs SHE). Only potential values after and including 0.124 V vs SHE are plotted, as the current recorded was minimal when the potential was stepped to values more positive than this.

The plot shows curvature as the potential becomes more negative. This could indicate the onset of mass transport limitation, as the supply of reactant at the electrode/solution interface would be depleted faster at more negative potentials. The current would expectedly stop increasing as the size of the potential step is increased, as diffusion control becomes predominant. At this point, the current is determined by the rate of transport of the reactants from the bulk solution to the electrode by diffusion and not the reaction kinetics.

The slope of the line indicated in Figure 4.3b (using data points before the curvature was evident) was extrapolated to $E_{1/2}$ of **SiW12** (0.030 V vs SHE). This indicated that the value for the exchange current, i_0, was -1.24 mA which can be converted to a value for k^0 using Equation 4.4, where n is the number of electrons transferred, F is the Faraday constant, A is the area of the electrode and c is the concentration:

$$k_0 = \frac{i_0}{nFAc} \tag{4.4}$$

A value of 0.064 cm s^{-1} was obtained for k^0. An order of magnitude of 10^{-2} cm s^{-1} for this value would support that the kinetics of the reduction of **SiW12** are fast. In the spirit of carrying out a Tafel analysis, a log$_{10}$ plot of the extrapolated current values versus potential is shown in Figure 4.4. For the same data points used for the linear fit in Figure 4.3b, the slope is -162 mV decade^{-1}, but a definitive region where a Tafel slope could exist is not evident in this plot. Problems with this method and the technique overall will now be discussed.

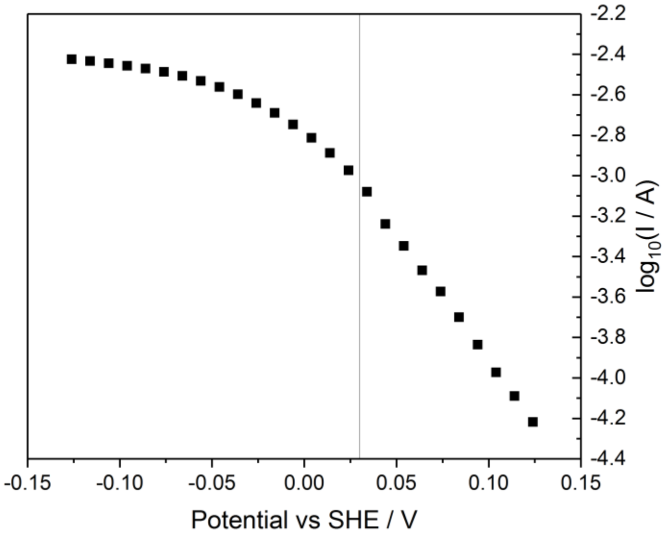

Figure 4.4 - A plot of log$_{10}$ of the extrapolated current values, from Figure 4.3b, versus potential.

Although the procedure for this experiment was similar to the chronoamperometry procedure carried out by Friedl *et al*. in the study of $[Mn^{III}_3(OH)_3(H_2O)_3SiW_9O_{34}]^{4-}$,[16] it was not a textbook Tafel analysis. Only a cathodic branch was recorded and the potential of the electrode before a potential step was applied did not equal the value of E_{eq} for which [oxidised species] = [reduced species], which is the condition for use of Equation 4.4. Instead, a fully oxidised solution of **SiW12** was used and the potential was initially stepped to values that were more positive than $E_{1/2}$. This resulted in some of the data collected being of no use in the analysis. An improved method could be to start with a solution that is a 50:50 mixture of fully oxidised **SiW₁₂** and one-electron reduced **SiW₁₂** (which could be obtained using bulk electrolysis) so that the condition of [oxidised species] = [reduced species] applies at E_{eq}. Both positive and negative overpotentials could then be applied, more akin to a classical Tafel analysis.

Even if the experimental procedure was changed, and in spite of a limit given for the range of rate constants that can be determined using chronoamperometry of $k^0 \leq 1$ cm s^{-1},[18, 19] there are difficulties with this method that led to the decision that it could not be used to determine k^0 for **SiW₁₂** accurately, a species for which fast electron transfer kinetics are anticipated.

Firstly, and a factor that is unrelated to the species under study, is the solution resistance (R_S) and the resultant ohmic potential drop (iR_S) between the working electrode and the reference electrode. The ohmic drop leads to an error in the potential at the working electrode. In determining this potential, the iR_S term must be subtracted from the potential applied to the cell, E_{app} (Equation 4.5).[20] If the ohmic drop is not minimised, then there is a sizeable discrepancy between the applied potential and the actual potential at the working electrode.

$$E = E_{app} - iR_S \qquad 4.5$$

Using EIS, a value of 33 Ω for R_S was determined for a 10 mM **SiW₁₂** solution in 1 M H_2SO_4 in the three-electrode cell used for this experiment. Amongst the higher potential values studied (e.g. applying a potential of 0.014 V vs SHE) currents of -1.5 mA and above were recorded. If R_S = 33 Ω and i = 1.5 mA, iR_S for this experimental set-up would be 50 mV, which indicates the magnitude of the error in the potential at the working electrode that is possible. Since chronoamperometry is a technique in which the potential is controlled and the current varies with time, the iR_S term and the potential error are variable too. The ohmic drop is thus difficult to correct for in chronoamperometry.

Secondly, the shrouding of the faradaic current by the charging of the electrical double layer at the onset of the potential step means that, for a fast reaction, the surface concentrations of reacting species change appreciably while the electrical double layer charges.[18] Thus, the onset of diffusion control could occur before cessation of the double layer charging, meaning that it is not possible to capture purely kinetic current. In spite of the subtraction of the current response for the blank electrolyte from the current response for **SiW₁₂**, which was carried out as a measure to counteract this, there was still an element of arbitrariness in selecting which data points to use in the current transients in order to create a line of best fit that could be used for extrapolation. This led to a distrust that the extrapolated currents at each potential were truly the kinetic current for **SiW12**.

It was decided that another technique should be investigated for the purposes of determining k^0 for **SiW12** and EIS was selected.

4.4 Electrochemical Impedance Spectroscopy

The relative ease with which EIS can be carried out compared to chronoamperometry and other current pulse techniques is one benefit of this method and it is reported that the upper limit of k^0 values measurable by EIS is "about the same as for potential and current pulse methods".[18] In EIS, the heterogeneous charge transfer kinetics mainly determine the charge transfer resistance (R_{CT})[15] and k^0 can therefore be obtained from this. R_{CT} can be considered as "the ratio of overpotential to current in the absence of mass transfer limitation"[21] and goes through a maximum at E_{eq}. When the system is perturbed around the value of E_{eq}, the current-potential relationship can be linearised and R_{CT} can be related to i_0 as shown in Equation 4.6.[21]

$$R_{CT} = \frac{RT}{nFi_0} \tag{4.6}$$

Both the first and second reductions of **SiW12** were studied using EIS. For the first reduction, bulk electrolysis was used to generate a solution of 10 mM **SiW12** and 10 mM $[SiW_{12}O_{40}]^{5-}$ (**SiW12$^-$**) by adding 0.5 electrons per molecule. For the second reduction, a solution containing 10 mM **SiW12$^-$** and 10 mM $[SiW_{12}O_{40}]^{6-}$ (**SiW12^{2-}**) was produced by adding 1.5 electrons per molecule. After bulk electrolysis, the OCP for the EIS measurement was equal to $E_{1/2}$ for the first reduction of **SiW12** (0.016 V vs SHE) or $E_{1/2}$ for the second reduction of **SiW12** (-0.197 V vs SHE). The spectra were fitted to a Randles circuit, shown in Figure 4.5. The inductivity of the setup was accounted for by including an inductor. Inductivities can be caused by electromagnetic interference from other electronic devices due to unshielded cables used for EIS,[22] or by the inductance of the cables themselves.[23] The latter inductance can be reduced by minimising the length of the cables used for EIS. Inductivities result in the measurement of positive -Z'' components which present as a vertical line that cuts the *x* axis at high frequencies in a Nyquist plot and affects the determination of the ohmic resistance. The parameters determined from the fits are shown in Table 4.1.

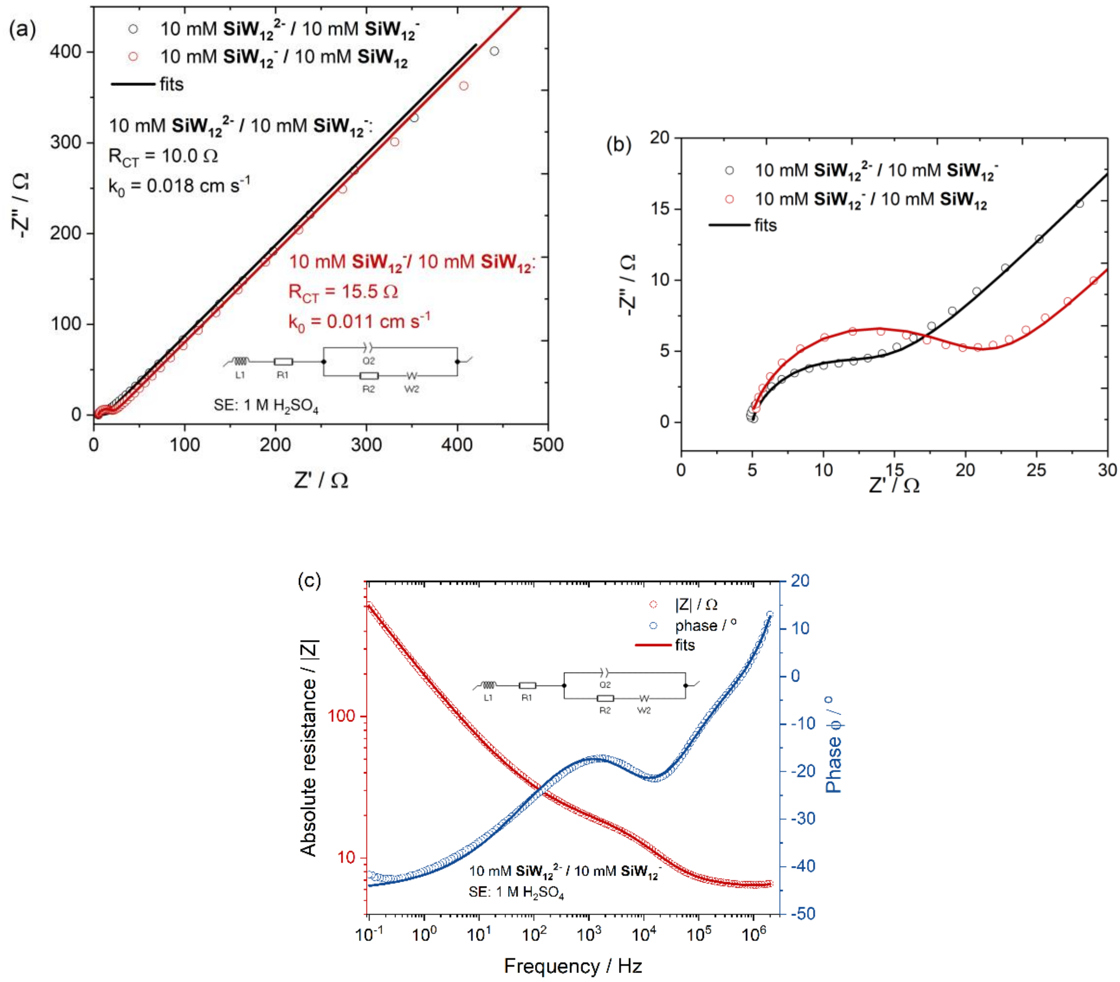

Figure 4.5 - The results of EIS of ***SiW_{12}*****. This experiment was carried out by Faye Cording and Felix L. Pfanschilling***. *(a) Nyquist plots with fits and the equivalent circuit used. (b) Detail of the Nyquist plots from (a). (c) Bode plot for a solution containing a 50:50 mixture of one-electron-reduced and two-electron-reduced* ***SiW_{12}****. (Reproduced by permission of The Royal Society of Chemistry.)*

	R_S / Ω	R_{CT} / Ω	Constant Phase Element / F $s^{(\alpha-1)}$	α	k^0 / cm s^{-1}	C_{DL} / µF
First reduction (SiW_{12}/SiW_{12}^-)	4.8	15.5	2.6×10^{-6}	0.85	0.011	0.31
Second reduction (SiW_{12}^-/SiW_{12}^{2-})	4.6	10.0	21.2×10^{-6}	0.76	0.018	1.0

Table 4.1 - The parameters determined from EIS by fitting the experimental data to the equivalent circuit shown in Figure 4.5. ***The EIS data fitting was carried out by Jochen Friedl***.

The electrical double layer capacitance (C_{DL}) was calculated from the constant phase element for the system using the formula given by Hirschorn *et al*. for a surface with a distribution of time constants (Equation 4.7).[24] After dividing C_{DL} by the geometric surface area of the electrode (0.07 cm^2), the values obtained are 16 µF cm^{-2} and 50 µF cm^{-2} which are reasonable values for glassy carbon.[25]

$$C_{DL} = Q^{1/\alpha}\left(\frac{R_S R_{CT}}{R_S + R_{CT}}\right)^{(\alpha-1)/\alpha} \qquad 4.7$$

R_{CT} values were obtained from the fits and used to calculate k^0 for the first and second reduction of **SiW12**. Noting that the exchange current density, j_0, is equal to i_0/A, where A is the surface area of the electrode, and that $i_0 = nFAk_0c$, Equation 4.6 can be rewritten as:[26]

$$R_{CT} = \frac{RT}{nFj_0A} = \frac{RT}{n^2F^2Ak^oc} \qquad 4.8$$

k_0 can be calculated by rearranging Equation 4.8.

The values calculated were of the order of 10^{-2} cm s^{-1}: k^0 = 0.011 cm s^{-1} for the first reduction and k^0 = 0.018 cm s^{-1} for the second reduction. These values are indicative of **SiW12** exhibiting charge transfer kinetics that are facile, faster than the V^{3+}/V^{2+} redox couple for instance. This result was used in support of the application of **SiW12** in the **SiW12-PV14** POM RFB, as it indicated that **SiW12** was a species with facile redox kinetics.[1] The value of k^0 obtained for the second reduction of **SiW12** indicates that electron transfer was faster in this reaction than in the first reduction of **SiW12**. This is an interesting result, which could be a starting point for further research into the electron transfer kinetics of **SiW12**.

4.5 Summary and Conclusions

Chronoamperometry was attempted as a method to elucidate a value of k^0 for **SiW12**. However, it was decided that this technique could not provide an accurate value of k^0 due to the questionable method of extrapolating to $t = 0$ when there is difficulty elucidating if electrical double layer charging has ceased. Further, inherent to this technique is an error in potential from the ohmic drop in each potential step. However, the results are included here for completeness and discussion.

EIS was employed instead and the k^0 values obtained for both the first and second one-electron reduction of **SiW12** were of the order of 10^{-2} cm s^{-1}. This indicates relatively fast electron transfer kinetics when compared to k^0 values reported for the VO_2^+/VO^{2+} and V^{3+}/V^{2+} redox couples of the VRFB.

The experiments in this work were carried out using a glassy carbon electrode. Despite the proposed outer-sphere mechanism of electron transfer, it has been shown that the k^0 values of **SiW12** are dependent on electrode material in aqueous solutions. The first and second electron transfers of **SiW12** were slower on a boron-doped diamond electrode compared to a gold electrode or a glassy carbon electrode.[13] The k^0 values of the first and second electron transfers of **SiW12** at boron-doped diamond electrodes were also found to be have a dependence on the identity of the cation in the supporting electrolyte, increasing in the order

$LiNO_3$ < $NaNO_3$ < KNO_3 ≈ NH_4NO_3.[27] Such influences on the kinetics could be an interesting aspect of **SiW_{12}** to consider during further work.

While the results of EIS provide an indication of a relatively high k^0 value, it would be desirable to corroborate this by using other techniques. While the k^0 values calculated for **SiW_{12}** in this work are the same order of magnitude as a k^0 value obtained for $[PW_{12}O_{40}]^{3-}$,[17] they are lower than the k^0 value of **SiW_{12}** on glassy carbon reported elsewhere, where the reduction processes of **SiW_{12}** were described as too fast to obtain a reliable measurement of k^0 if glassy carbon and gold electrodes are used.[13] Something considered during this work was the use of current step techniques to study the kinetics of **SiW_{12}**. These techniques have the benefit that correction for the ohmic drop is simple, as the current is constant. The simplest current step technique involves using single current steps in which a constant current is applied to an electrode, that is initially at equilibrium, for a certain amount of time.[18] The resulting potential transient rises steeply as charging of the electrical double layer proceeds. Following this, a linear portion with a lower gradient becomes evident which corresponds to current that is practically all due to the faradaic reaction.[18] The extrapolation of this linear region to $t = 0$ gives "a good estimate for the corresponding overpotential".[18]

The maximum value of k^0 that can be determined using a current step technique can be increased by an order of magnitude (from 10^0 to 10^1) if the double current step technique is used.[19] In this technique, a short pulse to charge the electrical double layer precedes the current pulse. The desirable height of this initial pulse is a value that ensures that the potential transient is horizontal at the beginning of the second pulse ($d\eta/dt = 0$), allowing extrapolation to $t = 0$ in order to determine the activation overpotential, with concentration polarisation able to be disregarded.[19] In practice, difficulty observing the conditions for $d\eta/dt = 0$ lowers the upper limit of k^0 values that can be determined,[19] one estimate being ~0.5 cm s^{-1}.[28] The technique also requires relatively complex instrumentation (a double current pulse generator and an oscilloscope[19]), but could be an avenue to explore if the study of the kinetics of **SiW_{12}** was continued.

A further technique that could be investigated is the Koutecký-Levich method which uses a rotating disc electrode (an electrode that can be set to rotate at a certain rate to cause a steady flow of solution to the electrode surface). In voltammograms obtained using a rotating disc electrode, as the speed of rotation is increased, the measured current approaches the kinetic current as the influence of mass transport is lessened.[29] The kinetic current can be determined at each rotation rate and these values plotted against the overpotential to yield a Tafel plot from which k^0 can be determined.

Each kinetics technique may have its limitations but concurrent results with different techniques would be the best way to verify that k^0 values for **$\mathbf{SiW_{12}}$**, and other POMs, are relatively high.

4.6 References

1. J. Friedl, M. V. Holland-Cunz, F. Cording, F. L. Pfanschilling, C. Wills, W. McFarlane, B. Schricker, R. Fleck, H. Wolfschmidt and U. Stimming, *Energy & Environmental Science*, 2018, DOI: 10.1039/C8EE00422F.
2. B. Keita and L. Nadjo, *J Electroanal Chem*, 1987, **217**, 287-304.
3. B. Keïta and L. Nadjo, *Journal of Electroanalytical Chemistry and Interfacial Electrochemistry*, 1985, **191**, 441-448.
4. J. Friedl and U. Stimming, *Electrochim Acta*, 2017, **227**, 235-245.
5. P. Alotto, M. Guarnieri and F. Moro, *Renewable and Sustainable Energy Reviews*, 2014, **29**, 325-335.
6. A. Z. Weber, M. M. Mench, J. P. Meyers, P. N. Ross, J. T. Gostick and Q. H. Liu, *Journal of Applied Electrochemistry*, 2011, **41**, 1137-1164.
7. F. Sepehr and S. J. Paddison, *Chemical Physics Letters*, 2013, **585**, 53-58.
8. B. Li, M. Gu, Z. Nie, Y. Shao, Q. Luo, X. Wei, X. Li, J. Xiao, C. Wang, V. Sprenkle and W. Wang, *Nano Letters*, 2013, **13**, 1330-1335.
9. L. Wei, T. S. Zhao, L. Zeng, X. L. Zhou and Y. K. Zeng, *Applied Energy*, 2016, **180**, 386-391.
10. P. Chen and R. L. McCreery, *Analytical Chemistry*, 1996, **68**, 3958-3965.
11. H. Agarwal, J. Florian, B. R. Goldsmith and N. Singh, *ACS Energy Letters*, 2019, **4**, 2368-2377.
12. I. A. Weinstock, *Chem. Rev.*, 1998, **98**, 113-170.
13. K. Bano, J. Zhang, A. M. Bond, P. R. Unwin and J. V. Macpherson, *The Journal of Physical Chemistry C*, 2015, **119**, 12464-12472.
14. J. Friedl, PhD Thesis, Technical University of Munich, 2015.
15. A. J. Bard and L. R. Faulkner, in *Electrochemical Methods - Fundamentals and Applications*, John Wiley & Sons, New York, 2nd edn., 2001, ch. 10, pp. 368-416.
16. J. Friedl, R. Al-Oweini, M. Herpich, B. Keita, U. Kortz and U. Stimming, *Electrochim Acta*, 2014, **141**, 357-366.
17. T. Feng, H. Wang, Y. Liu, J. Zhang, Y. Xiang and S. Lu, *J Power Sources*, 2019, **436**, 226831.
18. W. Schmickler and E. Santos, in *Interfacial Electrochemistry*, Springer-Verlag, Berlin, 2nd edn., 2010, ch. 19, pp. 235-257.
19. E. Yaeger, Kuta, J., in *Physical Chemistry - An Advanced Treatise*, ed. H. Eyring, Academic Press, New York/London, 1970, ch. 4, pp. 378-383.
20. J. C. Myland and K. B. Oldham, *Analytical Chemistry*, 2000, **72**, 3972-3980.

21. G. Denuault, M. Sosna and K.-J. Williams, in *Handbook of Electrochemistry*, ed. C. G. Zoski, Elsevier, 1st edn., 2007, ch. 11, pp. 431-469.
22. D. Klotz, A. Weber and E. Ivers-Tiffée, *Electrochim Acta*, 2017, **227**, 110-126.
23. C. Gabrielli, *Identification of Electrochemical Processes by Frequency Response Analysis*, 004/83, Solartron Analytical, 1998.
24. B. Hirschorn, M. E. Orazem, B. Tribollet, V. Vivier, I. Frateur and M. Musiani, *Electrochim Acta*, 2010, **55**, 6218-6227.
25. R. L. McCreery, *Chem. Rev.*, 2008, **108**, 2646-2687.
26. M. V. Holland-Cunz, F. Cording, J. Friedl and U. Stimming, *Frontiers in Energy*, 2018, DOI: 10.1007/s11708-018-0552-4.
27. J. Li, A. M. Bond and J. Zhang, *Electrochim Acta*, 2015, **178**, 631-637.
28. D. J. Kooijman and J. H. Sluyters, *Journal of Electroanalytical Chemistry and Interfacial Electrochemistry*, 1967, **13**, 152-156.
29. H. Wang, S. Y. Sayed, E. J. Luber, B. C. Olsen, S. M. Shirurkar, S. Venkatakrishnan, U. M. Tefashe, A. K. Farquhar, E. S. Smotkin, R. L. McCreery and J. M. Buriak, *ACS Nano*, 2020, **14**, 2575-2584.

Chapter 5 - The Application of $[CoW_{12}O_{40}]^{6-}$ in an Asymmetric Polyoxometalate Redox Flow Battery

5.1 Introduction

In Chapter 4, work on determining a value of k^0 for the redox reactions of $[SiW_{12}O_{40}]^{4-}$ (**SiW_{12}**) was outlined. This work focused on the first and second one-electron reduction of **SiW_{12}** and did not involve the third two-electron reduction. It has been reported that carrying out cyclic voltammetry or electrolysis at the potential of the third two-electron wave of **SiW_{12}** causes derivatization of glassy carbon electrodes.[1] Further, it was found that only the first and second one-electron reductions could be used as the anode reactions in an asymmetric POM RFB where **SiW_{12}** was used in the anolyte.[2] This supports that there are undesirable effects associated with the reduction of **SiW_{12}** by more than two electrons.

This chapter describes preparatory work on the concept of an asymmetric POM RFB employing the Keggin structure $[CoW_{12}O_{40}]^{6-}$ (**CoW_{12}**). The aim of this endeavour was to investigate **CoW_{12}** as the anolyte species in an RFB, and an alternative to **SiW_{12}**. It was thought that **CoW_{12}** may have better electrochemical properties for use as an anolyte, including improved stability after reduction by more than two electrons.

As has been noted, there have been different approaches taken in designing an all-POM RFB among the few concepts that have been published. Several symmetric POM RFBs have been presented which used identical POM species in both half-cells.[3-6] Conversely, in the work of Friedl *et al.*, different POM species in the positive and negative half-cell were used to create an asymmetric POM RFB.[2] **SiW_{12}** and the bi-capped Keggin structure $[PV_{14}O_{42}]^{9-}$ (**PV_{14}**) were the anions used in the anolyte and catholyte respectively.[2]

The CV of **PV_{14}** shown previously in Figure 4.1c indicates that this species undergoes multiple electron transfers whereas **SiW_{12}** exhibits a characteristic reduction pattern of two one-electron redox reactions and one two-electron redox reaction (a $1e^-$, $1e^-$, $2e^-$ process). The flow cell that used **PV_{14}** and **SiW_{12}** transferred four electrons between half-cells during charge and discharge.[2] Coulombic efficiencies of 94% were reported over 155 cycles. The capacity fade of the cell, around 0.16% per cycle, was attributed to the ingress of atmospheric oxygen into the system and not to instability of the POM species. ^{51}V NMR spectra of the **PV_{14}** catholyte after cycling and CVs of the cycled **SiW_{12}** anolyte did not indicate decomposition of either molecule. Further, in additional experiments with **PV_{14}**, it was determined that this POM could store up to seven electrons per molecule.[2] As such, **PV_{14}** showed promise for application as a POM RFB electrolyte species. However, the use of the **SiW_{12}** anolyte introduced limitations.

In order to create a cell that transferred four electrons between half-cells during charge and discharge, **SiW_{12}** was used at twice the concentration of **PV_{14}**, i.e., the active species concentration of the anolyte needed to be double that of the catholyte. In spite of the $1e^-$, $1e^-$, $2e^-$ reduction pattern for **SiW_{12}** (illustrated in Figure 4.1a), the access of electrons from the third two-electron reaction was not attempted in the flow cell due to negative effects associated with reducing the POM to this extent, which were previously discussed: derivatization of a range of electrode surfaces and resulting catalysis of the hydrogen evolution reaction has been reported at potential values where the third two-electron reduction of **SiW_{12}** is initiated.[1, 7] Reducing **SiW_{12}** to this extent has also been associated with decomposition of the POM.[2] Therefore, charge/discharge testing involved the reduction and oxidation of each **SiW_{12}** molecule by two electrons in the negative half-cell whereas **PV_{14}** was reduced and oxidised by four electrons in the positive half-cell.[2]

Additionally, **PV_{14}** underwent proton-coupled electron transfer (PCET) when it was oxidised and reduced[2] whereas the two one-electron reductions of **SiW_{12}**, used as the anode reactions, are not proton coupled. This led to a shift in pH of the **PV_{14}** electrolyte when the electrolyte pH was monitored during extended, scaled-up testing of this system, where the pH change of the electrolyte correlated with charge and discharge of the battery.[8] Conversely, the pH of the **SiW_{12}** electrolyte did not alter much during a single charge/discharge cycle, but showed an increase in the average pH as cycling continued, changing from pH 1.5 to 2.0 over 1400 cycles.[8] When operating a flow cell, it would be desirable to have proton release and reuptake occur in both half-cells during charge and discharge. While it was assumed that Li^+ was mostly responsible for charge balance during charge/discharge testing of the **SiW_{12}-PV_{14}** system, protons could also cross the ion exchange membrane and be involved in the charge balance of the half-cells. The occurrence of PCET in both half-cells of a flow cell could prevent a drift in pH of the electrolytes during operation as proton uptake in one electrode would be balanced by proton release at the other electrode. Therefore, there was scope for improvement of the **SiW_{12}-PV_{14}** system in two ways:

- An alternative POM for the anolyte that is stable to reduction by more than two electrons would be desirable as this would allow equal concentrations of anolyte and catholyte to be used.
- An anolyte species that also undergoes PCET as the cell is charged and discharged would be preferable in order to avoid unbalanced proton release and reuptake occurring in one half-cell.

In the search for other anolyte species, the investigation of an additional Keggin structure could be a pertinent next step. Aspects of the aforementioned Keggin structure chosen for investigation, **CoW_{12}**, are discussed in the following sections. This includes the electrochemistry of **CoW_{12}** and the results of preliminary charge/discharge testing of this species when it was coupled with the **PV_{14}** catholyte that was used previously in the **SiW_{12}-PV_{14}** flow cell.

5.2 Experimental

5.2.1 Materials

Sodium tungstate dihydrate (99.0–101.0%), cobalt(II) acetate tetrahydrate (98%), potassium chloride (99%), and glacial acetic acid (99+%) were supplied by Alfa Aesar. Sulphuric acid (95%–98%) was supplied by Sigma Aldrich. Anhydrous lithium chloride (99%), used to prepare supporting electrolytes, was supplied by Alfa Aesar. Hydrazine (35 wt. % in H_2O), used as a reducing agent, was supplied by Sigma Aldrich.

5.2.2 Synthesis of $[CoW_{12}O_{40}]^{6-}$

The potassium salt of $[CoW_{12}O_{40}]^{6-}$ was prepared by following literature procedures.[9-11]

In a representative procedure, sodium tungstate dihydrate (19.8 g, 0.0600 mol) was dissolved in water (40 mL) in a beaker. The pH of the solution was adjusted to 6.5–7.5 by addition of glacial acetic acid (3.0–3.5 mL). A second solution was prepared by dissolving cobalt(II) acetate tetrahydrate (2.50 g, 0.0100 mol) in water (13 mL) to which two drops of acetic acid were added. The solution of sodium tungstate dihydrate was heated to near boiling point before the cobalt(II) acetate tetrahydrate solution was added slowly with stirring. The mixture was boiled for 15 minutes. A hot solution of potassium chloride (13.0 g, 0.174 mol) in water (30 mL) was prepared and added to the mixture. The solution was then cooled to room temperature, during which time a solid that was teal in colour precipitated. The teal precipitate was removed by vacuum filtration using a sintered glass filter and then transferred to a beaker. 2 M H_2SO_4 (40 mL) was added to the precipitate in the beaker and a dark blue solution formed. A white precipitate was also visible in the solution. This insoluble material was removed from the solution by gravity filtration. The volume of the solution was reduced by ~75% through slow evaporation on a hot plate. A dark turquoise precipitate formed when the reduction in the volume of the solution was sufficient. The solution was filtered and the turquoise precipitate was dried in air to yield 7.38 g of crude product. This crude **CoW_{12}** sample still contained traces of the insoluble white precipitate, which became evident when it was dissolved in water.

The crude product was recrystallised by dissolving it in a minimum amount of water that had been heated to boiling point and then cooling the solution in an ice bath. Dark turquoise crystals formed upon cooling which were filtered and dried in air, to produce 2.81 g of $K_6[CoW_{12}O_{40}]\cdot 16H_2O$ (yield: 16%).

UV-visible spectra were obtained using a Shimadzu UV-1800 spectrophotometer and showed a peak characteristic of the $[CoW_{12}O_{40}]^{6-}$ anion in water with λ_{max} = 625 nm.

5.2.3 Electrochemistry

A Biologic SP300 potentiostat was used for cyclic voltammetry and bulk electrolysis. For cyclic voltammetry, the cell used was either a custom-built three-electrode cell with a glassy carbon working electrode (surface area = 0.02 cm^2), gold wire counter electrode and an MSE (1 M H_2SO_4) reference electrode, or a commercial glass cell (BASi) with a glassy carbon working electrode (surface area = 0.02 cm^2, or 0.07 cm^2 in Figure 5.17a), a platinum wire counter electrode and a Ag/AgCl (3 M NaCl) reference electrode. Prior to beginning an experiment, solutions were purged with nitrogen for 10 minutes and the working electrode was polished with alumina polish (0.05 μm).

A commercial bulk electrolysis cell that was described previously (Section 4.2.3) was used for the bulk electrolysis of **SiW_{12}** and **CoW_{12}** solutions. Chronoamperometry was used to reduce a 50 mM solution of **SiW_{12}** and a 20 mM solution of **CoW_{12}** in a supporting electrolyte of 1 M H_2SO_4. **SiW_{12}** was reduced by applying a potential of -0.311 V vs SHE and then -0.441 V vs SHE. **CoW_{12}** was reduced by applying a potential -0.131 V vs SHE and then -0.371 V vs SHE. After a passage of charge equivalent to two electrons per molecule (80.4 mAh for **SiW_{12}** and 21.5 mAh for **CoW_{12}**), the OCP of the solution was monitored for one hour after both reductions and then a CV was obtained. CVs before reduction and one hour after reduction were recorded while the solution was still in the electrolysis cell by switching the working electrode to a glassy carbon disc electrode (surface area = 0.02 cm^2) and using the glassy carbon mesh electrode as the counter electrode. The solutions were continuously stirred and purged with nitrogen during chronoamperometry.

5.2.4 Charge/Discharge Testing

Samples of $Na_{4.75}H_{4.25}[PV_{14}O_{42}]$ were provided by Matthäa V. Holland-Cunz (experiments shown in Figure 5.12 and Figure 5.14) and Jochen Friedl (experiments shown in Figure 5.15 and Figure 5.16). To make the catholyte, a quantity of hydrazine (35 wt. % in H_2O) that was enough to reduce **PV_{14}** by four electrons was added to the **PV_{14}** solution which was then stirred and purged with nitrogen for ~1 hour.

A Biologic BCS-810 battery tester was used for charge/discharge testing. The design and conditions of the operation of the stationary cells and flow cells were as described previously (Section 3.2.4) but with the difference that membranes were boiled in 1 M LiCl instead of 1 M Li_2SO_4 for 30 minutes prior to construction of a cell.

5.3 Fundamentals, Electrochemistry and Proton-Coupled Electron Transfer of $[CoW_{12}O_{40}]^{6-}$

The preparation of **CoW_{12}** was first published in 1956 by Baker and McCutcheon, who reported synthesis procedures for several different salts of this anion, along with the related cobalt(III) compound $[Co^{III}W_{12}O_{40}]^{5-}$.[9] The original formula reported was $[Co^{II}(W_2O_7)_2]^{10-}$, following the historical Miolati-Rosenheim theory which supposed that '12-class' acids were derived from central $[XO_6]^{y-}$ groups with oxygen atoms replaced by W_2O_7 groups.[12] A later article by Baker and Simmons clarified that the structures of both the cobalt(II) and cobalt(III) tungstocobaltate anions were in fact analogous to the previous structures deduced by Keggin, containing 40 oxygen atoms with a central CoO_4 tetrahedral unit.[13]

The electrochemistry of **CoW_{12}** was reported later by Pope and Varga, who described a two-electron wave corresponding to tungsten reduction with a formal potential of -0.035 vs SHE, and a further two-electron tungsten wave at -0.149 V vs SHE (recalculated from the Saturated Calomel Electrode).[14] A CV of **CoW_{12}** is shown in Figure 5.1 in the same supporting electrolyte as that used in this earlier study.

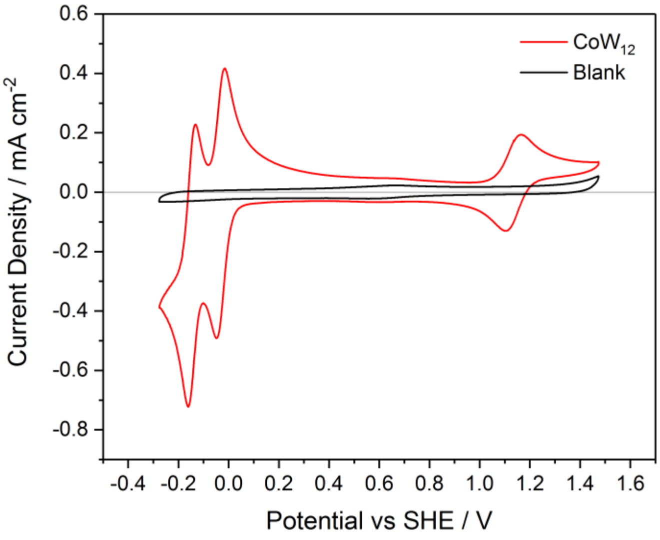

*Figure 5.1 - A CV of **CoW_{12}** (1 mM) in 1 M H_2SO_4. (WE: glassy carbon, CE: gold wire, RE: MSE (1 M H_2SO_4), scan rate: 100 mV/s)*

The CV shows that, along with the pair of two-electron tungsten peaks, an additional single electron transfer occurs at high potential. This is due to the redox reaction of the central Co^{II} heteroatom, cobalt being among the transition metals that can show electrochemical activity when incorporated in a POM. For instance, a cobalt-substituted Wells-Dawson structure with a formula of $[Co(OH_2)P_2Mo_2W_{15}O_{61}]^{8-}$ showed electrochemical activity, albeit irreversible, corresponding to oxidation of the Co^{II} atom, whereas no electrochemical activity could be detected for Ni^{II} and Zn^{II} in analogous Ni^{II}-substituted and Zn^{II}-substituted compounds.[15] More recently, electrochemical studies captured the redox reactions of multiple cobalt centres in the four-cobalt cluster species $[(Co_4(OH)_3PO_4)_4(A\text{-}\alpha\text{-}SiW_9O_{34})_4]^{28-}$.[16] The peaks observed in the Figure 5.1 correspond to the following redox reactions of **CoW12**.[4]

$$[Co^{II}W_{12}O_{40}]^{6-} \leftrightarrow [Co^{III}W_{12}O_{40}]^{5-} + e^- \ (E_{1/2} = 1.13 \text{ V vs. SHE}) \qquad 5.1$$

$$[CoW_{12}O_{40}]^{6-} + 2e^- + 2H^+ \leftrightarrow [H_2CoW_{12}O_{40}]^{6-} \ (E_{1/2} = -0.032 \text{ V vs. SHE}) \qquad 5.2$$

$$[H_2CoW_{12}O_{40}]^{6-} + 2e^- + 2H^+ \leftrightarrow [H_4CoW_{12}O_{40}]^{6-} \ (E_{1/2} = -0.147 \text{ V vs SHE}) \qquad 5.3$$

As shown, each reduction of the tungsten atoms is a two-electron process. With this in mind, **CoW12** could possess the electrochemical properties necessary to allow the operation of a POM RFB that transfers four electrons between half-cells and has equal concentrations of active species in the catholyte and anolyte. Evidence of this is illustrated in Figure 5.2, which shows a CV of the tungsten waves of **CoW12** overlaid with a CV of **SiW12** in identical supporting electrolyte. The two two-electron tungsten redox reactions of **CoW12** are juxtaposed with the two one-electron reductions of **SiW12** which occur at similar potentials ($E_{1/2}$ for the first reduction of **CoW12** is -0.032 V vs SHE compared to 0.030 V vs SHE for $E_{1/2}$ of the first reduction of **SiW12**). This differing electrochemical profile of **CoW12** suggests that it could accept more electrons than **SiW12** and offer a similar theoretical voltage in an RFB when combined with **PV14**. This electrochemistry makes **CoW12** a more desirable candidate for an anolyte if compared to **SiW12**.

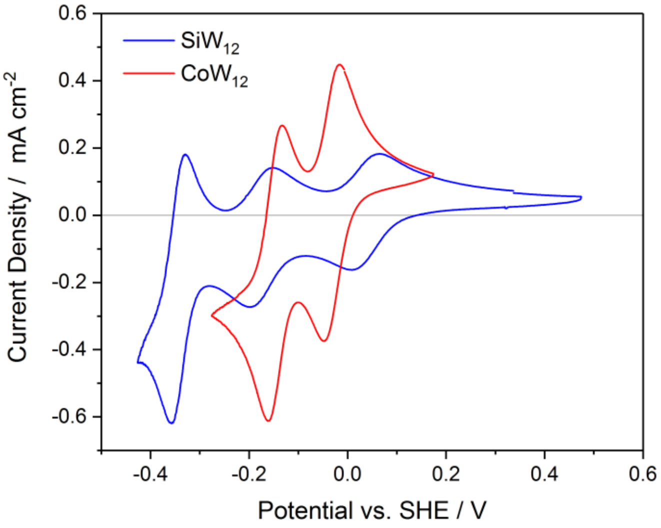

Figure 5.2 - CVs of ***CoW12*** *(1 mM) and* ***SiW12*** *(1 mM) in 1 M H_2SO_4. (WE: glassy carbon, CE: gold wire, RE: MSE (1 M H_2SO_4), scan rate: 100 mV/s)*

Indeed, the stability of **CoW12** to reduction by four electrons in a flow cell has already been evidenced in a symmetric **CoW12** RFB published by Liu *et al*. in which the redox-active cobalt heteroatom of **CoW_{12}** was the high potential reaction in the catholyte and the tungsten redox reactions were used as the low potential reactions in the anolyte.[4] Data from charge/discharge testing indicated that both of the two-electron reactions of **CoW_{12}** were accessed during flow cell testing with a stable capacity observed for 30 cycles. However, it is arguable that **CoW_{12}** is not best suited to application in a symmetric RFB as only one electron is transferred at high potential in the Co^{II}/Co^{III} redox reaction. This necessitated the use of a volume of catholyte that was four times higher than the volume of anolyte in the symmetric **CoW_{12}** flow cell, in order to access both two-electron tungsten redox reactions during charge/discharge testing.[4] The mismatch of a single high potential Co^{II}/Co^{III} redox reaction and a pair of two-electron tungsten redox reactions at more negative potentials supports the testing of **CoW_{12}** solely as an RFB anolyte instead, which can be coupled with a different catholyte species that supplies more electrons at higher potential.

It is illustrated in Equations 5.2 and 5.3 that the tungsten reductions of **CoW_{12}** are both processes in which PCET occurs. Thus, the suggested superior electrochemical properties of **CoW_{12}** are two-fold; a greater number of electrons transferred at a similar potential to **SiW_{12}** and electron transfer reactions that are coupled with protonation and deprotonation of the POM.

The subject of PCET of a range of Keggin structures has been covered by Pope and Varga who investigated the electrochemical properties of several structures (**SiW_{12}**, $[PW_{12}O_{40}]^{3-}$, $[FeW_{12}O_{40}]^{5-}$, **CoW_{12}** and $[H_2W_{12}O_{40}]^{6-}$) and described the pH dependence of the reduction of the anions.[14] No pH dependence of $E_{1/2}$ was observed for the first two one-electron reductions of $[PW_{12}O_{40}]^{3-}$ up to pH 1.3 (signs of partial decomposition of this species became evident at this pH) and up to pH 5.0 for **SiW_{12}**. The third two-electron wave of **SiW_{12}** moved to more negative potentials by around 80 mV pH^{-1}, indicating PCET occurred. While $[FeW_{12}O_{40}]^{5-}$ displayed a 1:1:3 electron reduction pattern, only the potentials of the second and third peak shifted to more negative values with increasing pH (80 mV pH^{-1} and 90 mV pH^{-1} respectively), up to a pH value of 6.95. The electrochemical profiles of **CoW_{12}** and $[H_2W_{12}O_{40}]^{6-}$ were similar to one another. For both compounds, a peak shift for the pair of two-electron waves was observed as the pH increased up to 3.0. Above pH 3.0, the first peak began to split into a pair of one-electron peaks that became independent of pH at pH 4.9 (first peak) and pH 5.4 (second peak). The disappearance of the second two-electron peak occurred at pH 5.5.

A reduction scheme was presented for the range of Keggin anions that were studied which summarises these observations and is reproduced below.[14]

In solutions of $pH \leq 1$:

$$[PW_{12}O_{40}]^{3-} \rightarrow [PW_{12}O_{40}]^{4-} \rightarrow [PW_{12}O_{40}]^{5-} \rightarrow H[PW_{12}O_{40}]^{6-} \qquad 5.4$$

$$[SiW_{12}O_{40}]^{4-} \rightarrow [SiW_{12}O_{40}]^{5-} \rightarrow [SiW_{12}O_{40}]^{6-} \rightarrow H_2[SiW_{12}O_{40}]^{6-} \qquad 5.5$$

$$[FeW_{12}O_{40}]^{5-} \rightarrow [FeW_{12}O_{40}]^{6-} \rightarrow H_4[FeW_{12}O_{40}]^{6-} \qquad 5.6$$

$$[CoW_{12}O_{40}]^{6-} \rightarrow H_2[CoW_{12}O_{40}]^{6-} \rightarrow H_4[CoW_{12}O_{40}]^{6-} \qquad 5.7$$

$$[H_2W_{12}O_{40}]^{6-} \rightarrow [H_4W_{12}O_{40}]^{6-} \rightarrow [H_6W_{12}O_{40}]^{6-} \qquad 5.8$$

In solutions of pH ≥ 5:

$[PW_{12}O_{40}]^{3-}$ is decomposed

$$[SiW_{12}O_{40}]^{4-} \rightarrow [SiW_{12}O_{40}]^{5-} \rightarrow [SiW_{12}O_{40}]^{6-} \rightarrow [SiW_{12}O_{40}]^{8-} \qquad 5.9$$

$$[FeW_{12}O_{40}]^{5-} \rightarrow [FeW_{12}O_{40}]^{6-} \rightarrow [FeW_{12}O_{40}]^{7-} \rightarrow [FeW_{12}O_{40}]^{7-} \qquad 5.10$$

$$[CoW_{12}O_{40}]^{6-} \rightarrow [CoW_{12}O_{40}]^{7-} \rightarrow [CoW_{12}O_{40}]^{8-} \qquad 5.11$$

$$[H_2W_{12}O_{40}]^{6-} \rightarrow [H_2W_{12}O_{40}]^{7-} \rightarrow [H_2W_{12}O_{40}]^{8-} \qquad 5.12$$

The authors noted that “when the reduction product had a charge of -6 or less, there was no pH dependence of reduction potential”.[14] Although without a theoretical basis, this observation explains why the first two reductions of **SiW_{12}** are not proton-coupled (**SiW_{12}** has a charge of -4 in its fully oxidised form) and why **CoW_{12}**, with a charge of -6 when it is fully oxidised, undergoes PCET for both of the tungsten reduction reactions.

A Keggin structure analogous to **CoW_{12}**, in the sense that the fully oxidised anion bears a charge of -6, is $[ZnW_{12}O_{40}]^{6-}$. $[ZnW_{12}O_{40}]^{6-}$ has similar electrochemical properties to **CoW_{12}**: four electrons are transferred in two two-electron redox reactions that occur at similar potentials to the two one-electron redox reactions of **SiW_{12}**.[17] Further, a dependence of the redox potentials of $[ZnW_{12}O_{40}]^{6-}$ on pH was also demonstrated, whereas **SiW_{12}** and $[PW_{12}O_{40}]^{3-}$ did not exhibit any pH dependence for the first and second reductions.[17] This also supports that tungsten-based Keggin anions with a charge of -6 in the fully oxidised state will undergo PCET from the first reduction of their addenda atoms onwards.

When considering a POM to be used in the anolyte of an RFB with a **PV_{14}** catholyte, it could therefore be beneficial to employ a Keggin structure bearing a charge of -6 in its fully oxidised form, such as **CoW_{12}**, as PCET in the negative half-cell is desirable. Further, the optimum pH range for observing the PCET of **CoW_{12}** (up to pH 3.0 [14]) is within the pH range where **PV_{14}** is most stable, which would allow the pH of the supporting electrolyte to be matched for both the anolyte and catholyte. **PV_{14}** exists in equilibrium with free vanadium within a pH range of 1.3 < pH < 4.0 with an optimum pH for its formation of 2.3.[18] Outside of this pH range, free vanadium exists as decavanadates of formula $[HxV_{10}O_{28}]^{6-x}$ at higher pH and as VO_2^+ at lower pH.[18]

To summarise, the PCET of **CoW12** and the potential for the access of a greater number of electrons per molecule than **SiW12** are desirable and potentially beneficial properties for a POM RFB. This supports the investigation of **CoW12** as the anolyte species in a second iteration of an asymmetric POM RFB.

Although the electrochemistry of **CoW12** has been described in literature,[4, 14] CVs of the isolated cobalt and tungsten redox reactions are included here for completeness (Figure 5.3). The oxidation peak currents for the Co^{II}/Co^{III} reaction and the reduction peak currents for the two W^{VI}/W^{V} reactions were plotted against the square root of the scan rate (Figure 5.4). Plots for a reversible voltammogram are linear and the diffusion coefficient can be determined from the slope by using the Randles-Sevcik equation. As linearity was shown by the plots, the diffusion coefficient was estimated for **CoW12** using Equation 3.4. Using the slope of the plot of the anodic current for the Co^{II}/Co^{III} reaction, the diffusion coefficient was calculated to be 4.30×10^{-6} cm^2 s^{-1}. This is of the same order of magnitude as values that were previously reported for **CoW12**.[4]

$$D = \left(\frac{slope}{0.4463nFAC}\right)^2 \frac{RT}{nF} \qquad 3.4$$

For a reversible voltammogram, the peak potential, E_p, should be independent of scan rate and Equation 2.51 and Equation 2.52 apply:

$$\frac{i_{pa}}{i_{pc}} = 1 \qquad 2.51$$

$$\Delta E_p = \frac{2.3\,RT}{nF}(0.059/\mathrm{n\ V\ at\ 25°C}) \qquad 2.52$$

E_p was independent of scan rate for the Co^{II}/Co^{III} peaks and both sets of tungsten peaks. The ratios of the peak anodic current to the peak cathodic current, i_{pa}/i_{pc}, were 1.40 (10 mV/s), 1.23 (25 mV/s), 1.19 (50 mV/s) and 1.22 (100 mV/s) for the Co^{II}/Co^{III} peaks and 1.02 (10 mV/s), 1.12 (25 mV/s), 1.03 (50 mV/s) and 0.96 (100 mV/s) for the first set of tungsten peaks. These values are close to the theoretical value. For the second set of tungsten peaks, i_{pa}/i_{pc} deviated from the theoretical value. The values were 0.31 (10 mV/s), 0.40 (25 mV/s), 0.37 (50 mV/s) and 0.53 (100 mV/s) and it can be seen in Figure 5.3b that the second set of tungsten peaks are not symmetrical about the baseline of the CV. However, the peak separations, ΔE_p, for each set of peaks are close to the theoretical value, which is an indicator that a process is chemically and electrochemically reversible.[19] ΔE_p for the Co^{II}/Co^{III} peaks is 0.058 V which is close to the theoretical value for a one-electron reaction. For the first set of tungsten peaks of **CoW12**, ΔE_p is 0.030 V which is close to the theoretical value for a two-electron reaction. For the second set of tungsten peaks, ΔE_p is 0.026 mV which is also close to the theoretical value for a two-electron reaction.

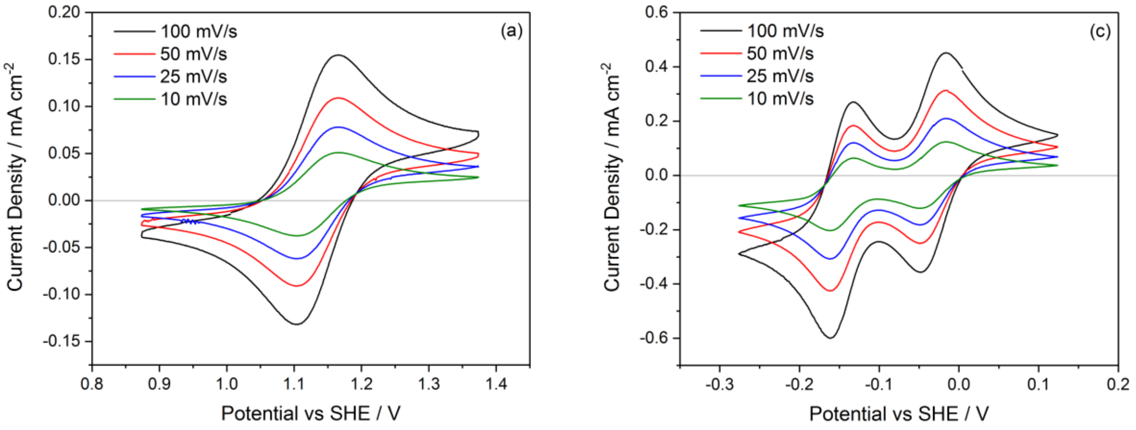

Figure 5.3 - CVs of ***CoW$_{12}$*** *(1 mM) in 1 M H_2SO_4 at varying scan rates. (a) The Co^{II}/Co^{III} peaks. (b) The W^{VI}/W^{V} peaks. (WE: glassy carbon, CE: gold wire, RE: MSE (1 M H_2SO_4), scan rate: 100 mV/s)*

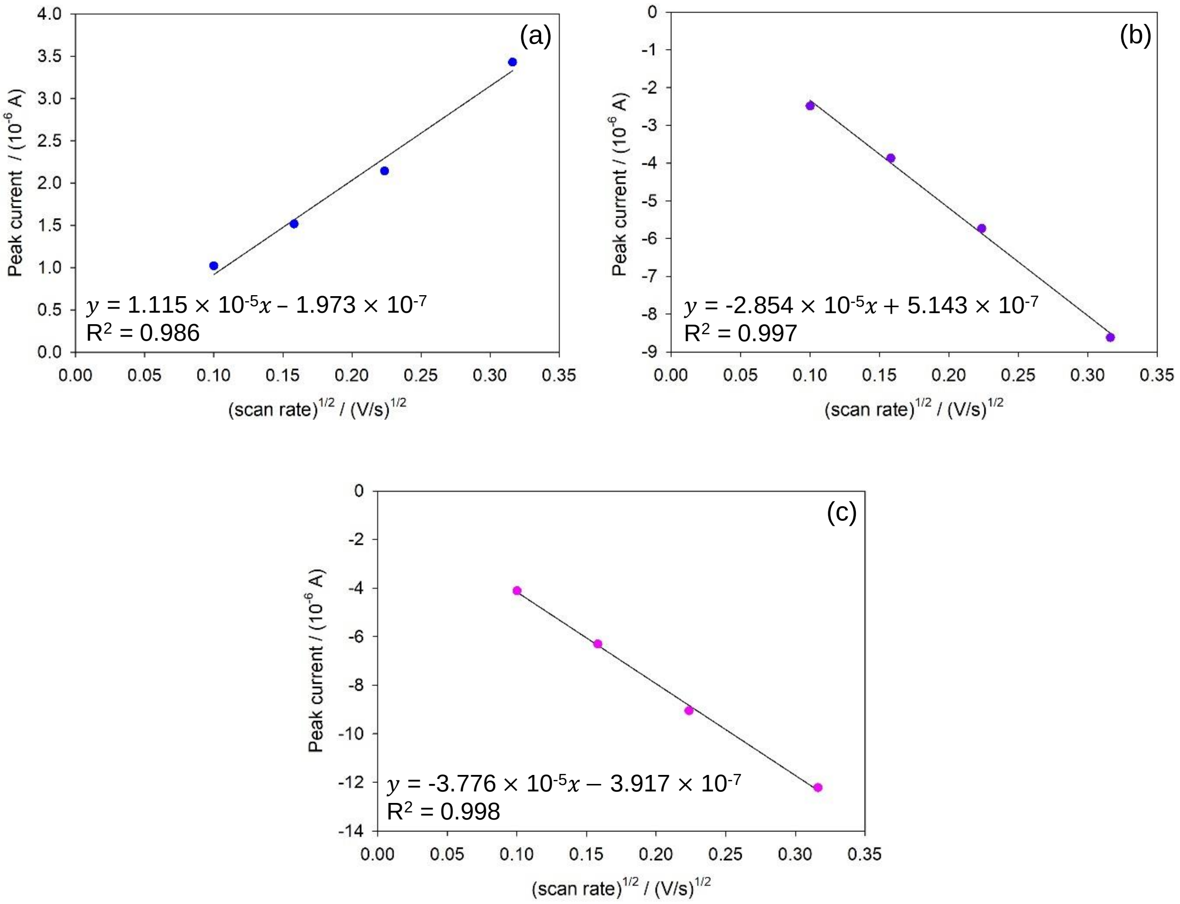

Figure 5.4 - (a) A plot of oxidation peak current vs the square root of the scan rate for the Co^{II}/Co^{III} redox couple of ***CoW$_{12}$****. (b) A plot of reduction peak current vs the square root of the scan rate for the first W^{VI}/W^{V} reduction peak of* ***CoW$_{12}$****. (c) A plot of reduction peak current vs the square root of the scan rate for the second W^{VI}/W^{V} reduction peak of* ***CoW$_{12}$****. (All currents were measured from the baseline of the first cycle of the CVs shown in Figure 5.3.)*

CVs at different pH are shown in Figure 5.5a. A linear relationship is shown between $E_{1/2}$ of the first two-electron reduction of **CoW$_{12}$** and the pH of the supporting electrolyte in Figure 5.5b, which is indicative of proton-coupled reactions. A slope of -0.089 V pH^{-1} was determined using this data. The theoretical value for a two-electron two-proton reaction is -0.118 V pH^{-1}.[20] Pope and Varga reported slopes that were at odds with the theoretical value (values in the range of -0.070 V pH^{-1} to -0.100 V pH^{-1} for the pH-dependent waves of $[FeW_{12}O_{40}]^{5-}$, **CoW$_{12}$** and $[H_2W_{12}O_{40}]^{6-}$).[14] However, this was attributed to the waves becoming less reversible and beginning to split into two one-electron waves as the pH value increased towards pH 5.[14] Additional data points would aid the comparison of the slope obtained in this work with the work of Pope and Varga. In spite of the deviation of the slope from the theoretical value, a proton dependence of the reactions of **CoW$_{12}$** is indicated by the CVs obtained.

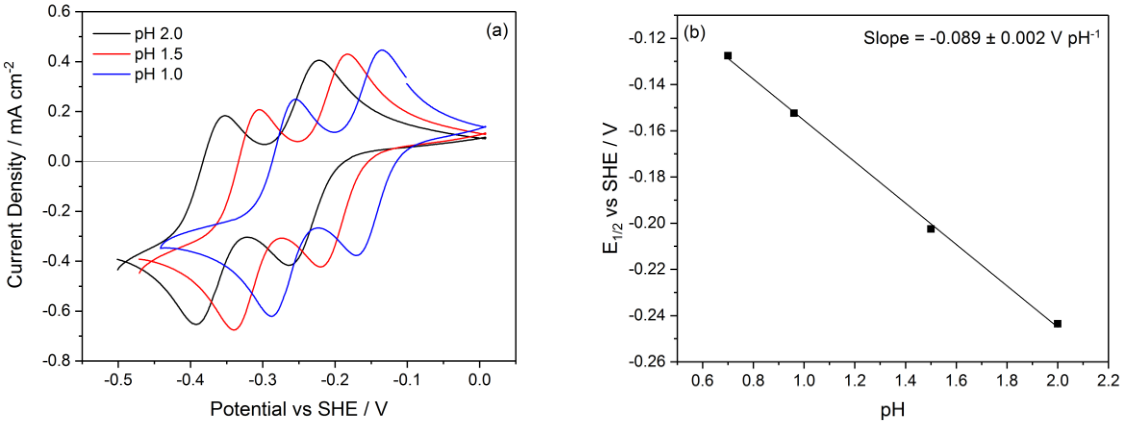

*Figure 5.5 - (a) CVs of **CoW$_{12}$** (1 mM) in 1 M LiCl at different pH values. (b) A plot of $E_{1/2}$ versus the pH of the supporting electrolyte for the first tungsten redox reaction of **CoW$_{12}$**. (WE: glassy carbon, CE: platinum wire, RE: Ag/AgCl (3 M NaCl), scan rate: 100 mV/s)*

5.4 Stability of $[CoW_{12}O_{40}]^{6-}$ during bulk electrolysis

As a first step in the investigation, an attempt was made to verify the stability of **CoW$_{12}$** to reduction by four electrons using bulk electrolysis. The reduction of **SiW$_{12}$** by four electrons was carried out in a separate study and the results are also presented here, and discussed first.

To look for evidence of instability of **SiW$_{12}$** if bulk reduction by more than two electrons was carried out, a 50 mM solution of the POM was subjected to CPE and reduced by two electrons, thereby forming **SiW$_{12}$$^{2-}$**, and then four electrons to form **SiW$_{12}$$^{4-}$** (i.e., $[SiW_{12}O_{40}]^{6-}$ and $[H_2SiW_{12}O_{40}]^{6-}$ respectively). A CV of the solution before reduction is shown in Figure 5.6a. During CPE, the potential was held at -0.311 V vs SHE until a quantity of charge corresponding to two electrons per **SiW$_{12}$** molecule was passed. The OCP was then monitored for one hour (Figure 5.6b) and a CV obtained. CPE was then continued at -0.441 V vs SHE and a further quantity of charge corresponding to two electrons per molecule was passed to the POM solution.

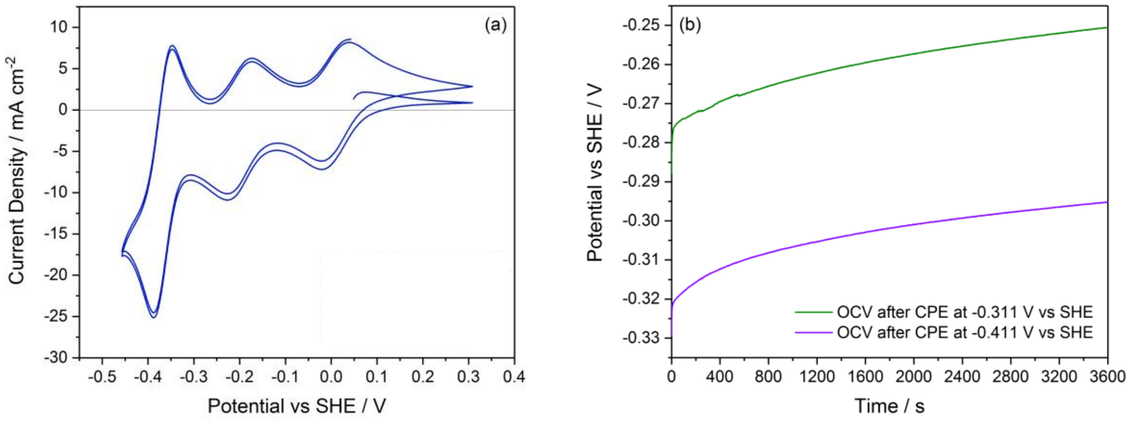

Figure 5.6 - (a) A CV of 50 mM ***SiW$_{12}$*** *in 1 M H_2SO_4 before CPE. (WE: glassy carbon, CE: glassy carbon mesh, RE: Ag/AgCl (3 M NaCl), scan rate: 100 mV/s) (b) The OCP of the solution in the bulk electrolysis cell monitored for one hour after two-electron and four-electron reductions of* ***SiW$_{12}$****.*

During CPE at -0.311 V vs SHE, the current versus capacity curve showed a reduction in current as the amount of charge passed approached the theoretical amount of charge required for the reduction of each **SiW$_{12}$** molecule in the solution by two electrons (~80 mAh) (indicated by the grey vertical line in Figure 5.7a). The current would expectedly decrease due to the smaller amount of oxidised species in solution as reduction progressed, and this indicated that the electrolysis was approaching its end. The CV obtained one hour after CPE ceased showed no new features, indicating intact reduced **SiW$_{12}$$^{2-}$** was in the solution (Figure 5.7b).

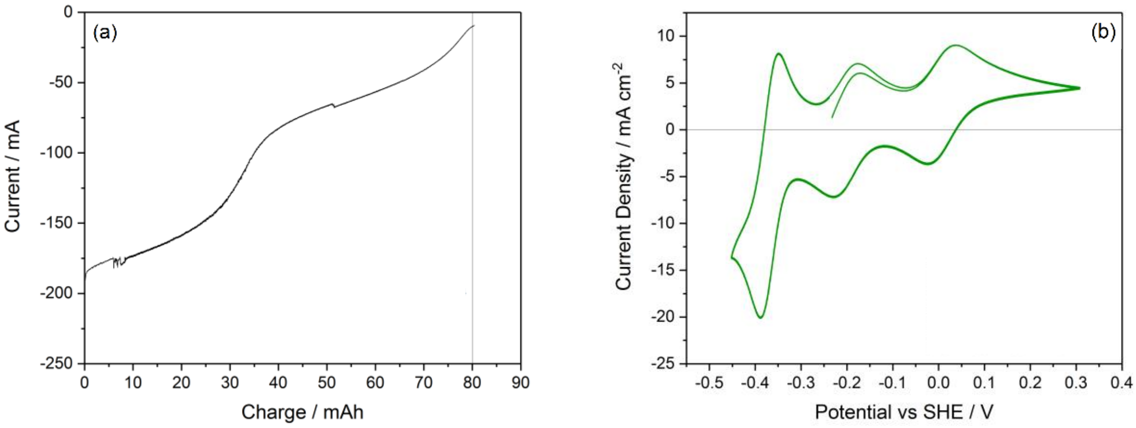

Figure 5.7 - (a) The current vs capacity curve for CPE of ***SiW$_{12}$*** *at -0.311 V vs SHE. (WE: glassy carbon, CE: platinum wire, RE: Ag/AgCl (3 M NaCl)) (b) A CV of* ***SiW$_{12}$*** *obtained in the bulk electrolysis cell after CPE at -0.311 V vs. SHE. (WE: glassy carbon, CE: glassy carbon mesh, RE: Ag/AgCl (3 M NaCl), scan rate: 100 mV/s)*

When reduction of **SiW$_{12}$**$^{2-}$ was resumed (Figure 5.8a) the current versus capacity curve did not show the same reduction of the current as the theoretical amount of charge for a further two-electron reduction is reached (for the formation of **SiW$_{12}$**$^{4-}$). Instead, a steady current was approached and maintained until the reduction was stopped after 80 mAh of charge had been passed, as though the electrons supplied during CPE were being consumed in a further process. This could be the hydrogen evolution reaction, as the occurrence of this was suggested in previous electrolysis experiments of **SiW$_{12}$**.[1]

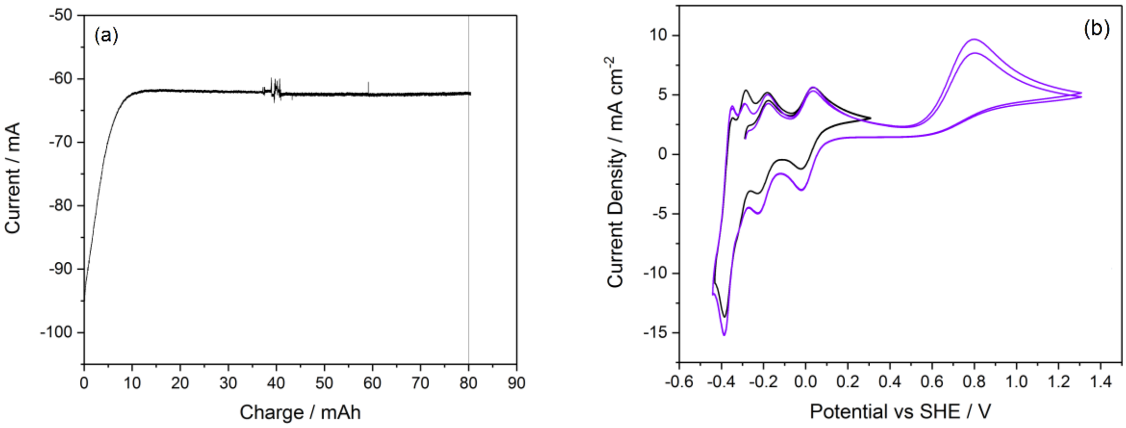

Figure 5.8 - (a) The current vs capacity curve for CPE of ***SiW$_{12}$*** *at -0.441 V vs SHE. (WE: glassy carbon, CE: platinum wire, RE: Ag/AgCl (3 M NaCl)) (b) CVs of* ***SiW$_{12}$*** *obtained in the bulk electrolysis cell after CPE at -0.441 V vs SHE. (Black line: scanned between 0.309 V vs SHE and -0.431 V vs SHE. Purple line: scanned between 1.21 V vs SHE and -0.441 V vs SHE.) (WE: glassy carbon, CE: glassy carbon mesh, RE: Ag/AgCl (3 M NaCl), scan rate: 100 mV/s)*

While a stable OCP was indicated for one hour after CPE (Figure 5.6b), a CV of the reduced solution afterwards showed changes in the peak appearance at low potential (black line in Figure 5.8b). An additional peak was also visible when scanning to higher potentials which looked irreversible and could be associated with decomposition products that were present in the solution (purple line in Figure 5.8b). This result supports the reasoning of Friedl *et al*. for not attempting to reduce **SiW$_{12}$** by more than two electrons during operation of a flow cell.[2] In their studies of **SiW$_{12}$**, Keita and Nadjo specifically noted that "cycling up to the third wave [of **SiW$_{12}$**] or electrolysis on this wave . . . results in derivatization of the [glassy carbon] electrode".[1] Disproportionation or the hydrogen evolution reaction were under investigation as possible causes of the passage of more than the theoretical number of electrons per molecule in electrolysis experiments of **SiW$_{12}$**.[1]

Bulk electrolysis of **CoW$_{12}$** was subsequently carried out to allow a comparison with the results obtained for **SiW$_{12}$**, but the concentration of the solution was 20 mM instead of 50 mM due to a limited amount of **CoW$_{12}$** sample being available. However, the experimental sequence was the same as that of the bulk electrolysis experiment of **SiW$_{12}$**. A CV of the solution before reduction was obtained (Figure 5.9a) and CPE was then carried out in which the required amount of charge corresponding to reduction by two electrons was passed (~21 mAh) in order to generate $[H_2CoW_{12}O_{40}]^{6-}$ (**CoW_{12}^{2-}**) in the first instance and then $[H_4CoW_{12}O_{40}]^{6-}$ (**CoW_{12}^{4-}**). The OCP was then monitored for one hour and a CV of the reduced solution was obtained. The potentials used in CPE were -0.131 V vs SHE and -0.371 V vs SHE to reduce **CoW_{12}** by two electrons and four electrons respectively. A stable OCP was indicated for both the **CoW_{12}^{2-}** and **CoW_{12}^{4-}** solutions (Figure 5.9b).

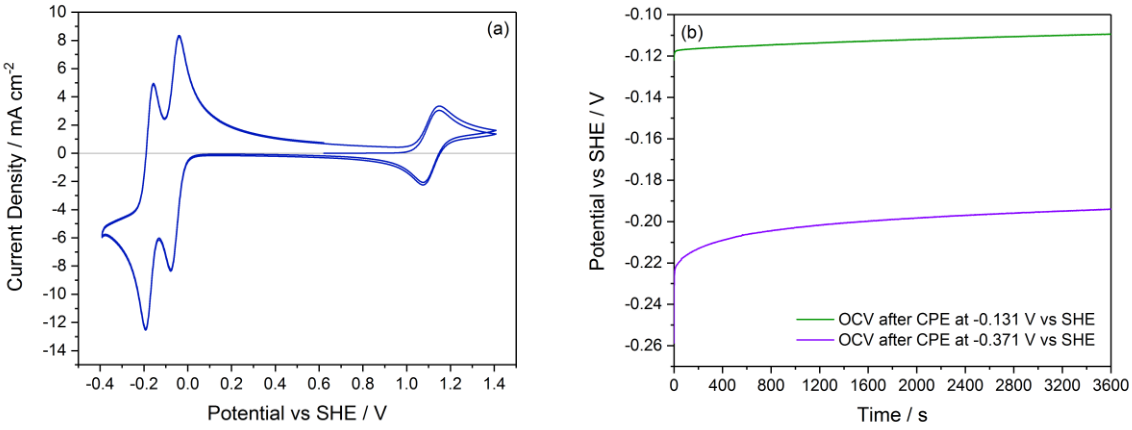

Figure 5.9 - (a) A CV of 20 mM **CoW_{12}** *in 1 M H_2SO_4 before CPE. (WE: glassy carbon, CE: glassy carbon mesh, RE: Ag/AgCl (3 M NaCl), scan rate: 100 mV/s) (b) The OCP of the solution in the bulk electrolysis cell monitored for one hour after two-electron and four-electron reductions of* **CoW_{12}**.

CVs of the reduced species indicated that **CoW_{12}** had remained intact in the solutions after CPE (Figure 5.10b and Figure 5.10d). However, the current versus capacity curve for CPE at -0.371 V vs SHE still showed a large background current after the theoretical amount of charge needed to generate **CoW_{12}^{4-}** was passed (Figure 5.10c, indicated by the grey vertical line), as though electrons were being consumed in a further process. As the second two-electron redox reaction of **CoW_{12}** is closer to the potential of the hydrogen evolution reaction, these two reactions could compete.

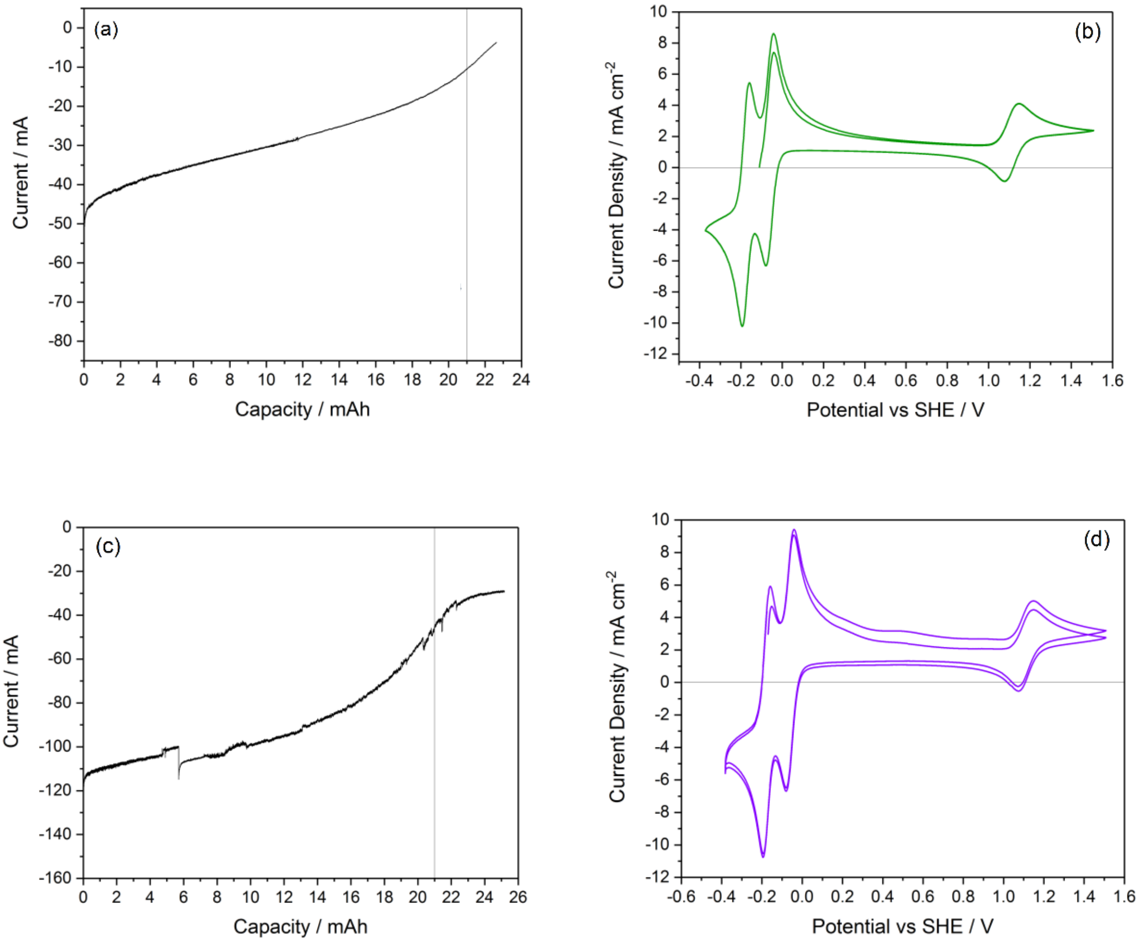

*Figure 5.10 - CPE and CVs of **CoW_{12}** (20 mM) in 1 M H_2SO_4 (a) The current vs capacity curve from CPE of **CoW_{12}** at -0.131 V vs SHE. (WE: glassy carbon, CE: platinum wire, RE: Ag/AgCl (3 M NaCl)) (b) A CV of **CoW_{12}** obtained in the bulk electrolysis cell after CPE at -0.131 V vs SHE. (WE: glassy carbon, CE: glassy carbon mesh, RE: Ag/AgCl (3 M NaCl), scan rate: 100 mV/s) (c) The current vs capacity curve from CPE of **CoW_{12}** at -0.371 V vs SHE. (d) A CV of **CoW_{12}** obtained in the bulk electrolysis cell after CPE at -0.371 V vs SHE.*

When compared to the results for **SiW_{12}**, the CVs of the reduced species support that **CoW_{12}** could exhibit increased stability to reduction by four electrons, given that distinct changes occurred in the CV of **SiW_{12}** following attempted reduction by four electrons. Therefore, the testing of **CoW_{12}** as an anolyte was not deterred by the results of this experiment and the POM was taken forward into charge/discharge testing.

5.5 Asymmetric CoW_{12}-PV_{14} stationary cells

It is known that **PV_{14}** exists in a pH window of $1.3 < pH < 4.0$ and decomposes to decavanadate species at higher pH and VO_2^+ at lower pH.[18] Therefore, the electrochemistry of **CoW_{12}** at higher pH values was investigated by carrying out CVs in the supporting electrolyte used in the **SiW_{12}-PV_{14}** flow cell (Figure 5.11). Interestingly, a third tungsten reduction peak was visible in the supporting electrolyte of 1 M LiCl at pH 1.7 indicating further electrons could be transferred to the anion at this pH. At lower pH values (e.g. in 1 M H_2SO_4), the onset of the hydrogen evolution reaction is shifted to more positive potentials which would shroud the third reduction in more acidic conditions. This explains why this third reaction could not be observed in previous CVs (e.g. Figure 5.3). The CV was cycled 100 times and no changes were visible after cycling which supported the stability of the POM at this pH, even to reduction by more than four electrons.

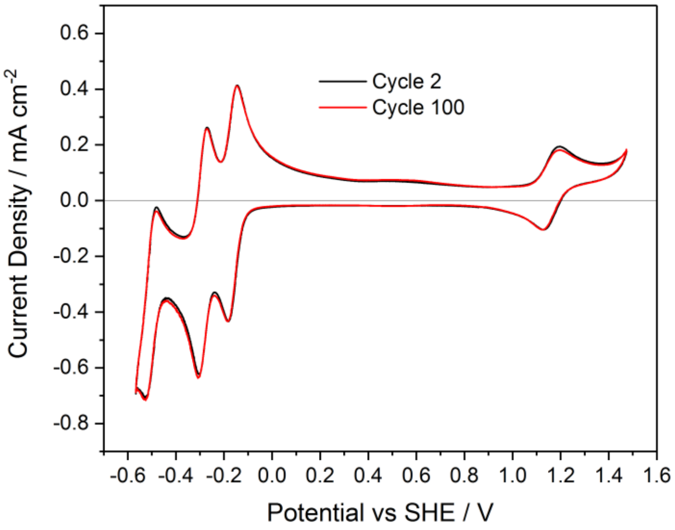

Figure 5.11 - A CV of ***CoW₁₂*** *(1 mM) in 1 M LiCl at pH 1.7. (WE: glassy carbon, CE: gold wire, RE: MSE (1 M H_2SO_4), scan rate: 100 mV/s)*

Based on $E_{1/2}$ for the first set of tungsten peaks of **CoW_{12}** at pH 1.7 (-0.166 V vs SHE) and $E_{1/2}$ estimated for **PV_{14}** (0.60 V vs SHE[2]), the theoretical voltage for a **CoW_{12}-PV_{14}** RFB is 0.77 V. If the second two-electron tungsten reaction of **CoW_{12}** ($E_{1/2}$ = -0.289 V) could be accessed in a **CoW_{12}-PV_{14}** RFB, the maximum theoretical voltage is 0.89 V. The maximum concentration of the potassium salt of **CoW_{12}** that was determined in this work was 0.785 M. However, the maximum solubility of **PV_{14}** (which is prepared as a sodium salt) has been indicated to be 0.2 M.[21] This limits the theoretical energy density of a **CoW_{12}-PV_{14}** RFB. Using a theoretical voltage of 0.77 V, a concentration of 0.2 M, and assuming that both of the two-electron tungsten reactions of **CoW_{12}** can be used in the cell reactions, the theoretical volumetric energy density of a **CoW_{12}-PV_{14}** RFB is 8.3 Wh L^{-1}. If **PV_{14}** could be reduced by more than four electrons, which is possible,[2] then the energy density could be increased.

To obtain an indication of the charge/discharge results possible for a cell using **CoW_{12}** in the anolyte, a stationary cell was set up. The result is shown in Figure 5.12. The concentration of the **PV_{14}** catholyte was doubled to 20 mM for this test to ensure that the **CoW_{12}** anolyte was not a limiting source of electrons. The supporting electrolyte for the POM solutions was 1 M LiCl with a pH of 1.7. Before assembly of the cell, a stoichiometric amount of hydrazine was added to the catholyte to reduce **PV_{14}** by four electrons, so that the cell was in the discharged state when it was assembled. The cell then underwent 50 charge/discharge cycles.

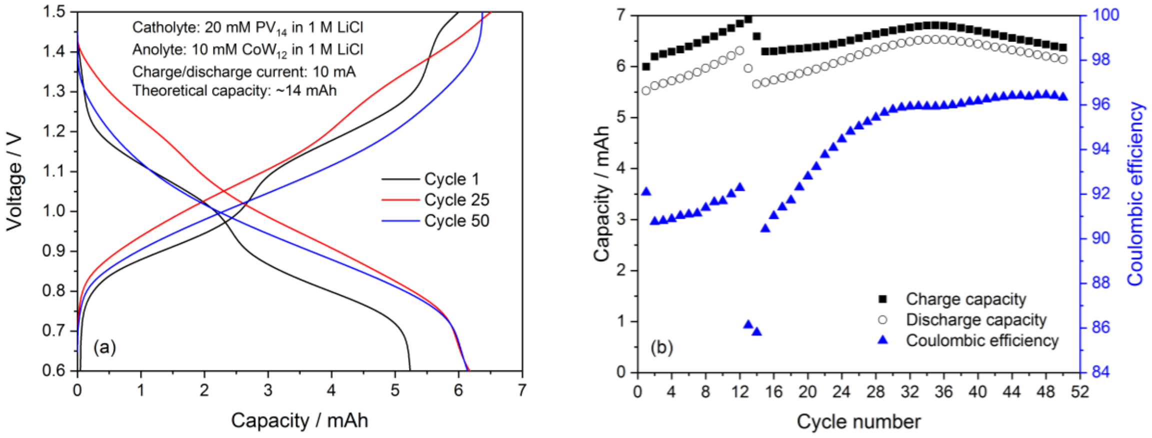

Figure 5.12 - (a) Charge/discharge curves of a ***CoW_{12}-PV_{14}*** *stationary cell. (b) Charge capacity, discharge capacity and coulombic efficiency versus cycle number.*

During cycle 13, the discharge cut-off voltage was changed from 0.0 to 0.6 V as it was deemed unnecessary to discharge the cell to 0 V due to the range of charging and discharging voltages shown in previous charge/discharge cycles. This caused a reduction in the charge and discharge capacity and the coulombic efficiency over the next few cycles (Figure 5.12b). However, as shown in later cycles, the capacity and coulombic efficiency of the cell recovered and substantial capacity fade was not evident over 50 cycles. Further, coulombic efficiencies of 95–96% were observed from cycle 26 to cycle 50. The electrochemical yield of the cell was low (around 6 mAh out of a theoretical value of 14 mAh) but two plateaus can be seen in cycle 1 in Figure 5.12a which suggests that both two-electron reduction reactions of a proportion of the **CoW_{12}** species present in the solution were active.

Coupling of the first tungsten reaction with the reactions of **PV_{14}** would be expected to result in a first plateau at a lower voltage upon charging the cell (theoretical voltage of 0.77 V). The first plateau in Figure 5.12 begins at close to this voltage (~0.75 V) and lasts until ~1.0 V. The discharge plateau that corresponds to this reaction occurs at ~0.70–0.92 V. Coupling of the second tungsten reaction with the reactions of **PV_{14}** would be expected to result in a second plateau of higher voltage than the first plateau when charging the cell (theoretical voltage of 0.89 V). The second plateau visible in Figure 5.12 occurs at a higher voltage than the theoretical voltage (~1.08–1.31 V). The discharge plateau that corresponds to this reaction occurs at ~0.97–1.20 V which is also higher than the theoretical voltage. However, the appearance of the charge/discharge curves, with two plateaus, was similar to the charge/discharge curves in the work by Liu *et al*. for their symmetric **CoW_{12}** flow cell that used both of the two-electron tungsten redox reactions.[4] The voltages of the plateaus are also similar to voltages of the two plateaus observed in charge/discharge testing of the **SiW_{12}-PV_{14}** flow cell where the first charging plateau occurred at ~0.60–0.95V and the second charging plateau occurred at ~1.0–1.3 V.[2] The voltage efficiency calculated for cycle 10 was 83%.

A UV-visible spectrum of the anolyte after cycling (Figure 5.13) showed the characteristic absorption peak described in the literature for **CoW_{12}** with λ_{max} = 625 nm.[11] Therefore, the spectrum does not suggest that **CoW_{12}** was unstable and the low capacity of the cell was not attributed to instability of the POM. It also does not suggest that the disappearance of the two plateaus as cycling continued was related to instability of the POM.

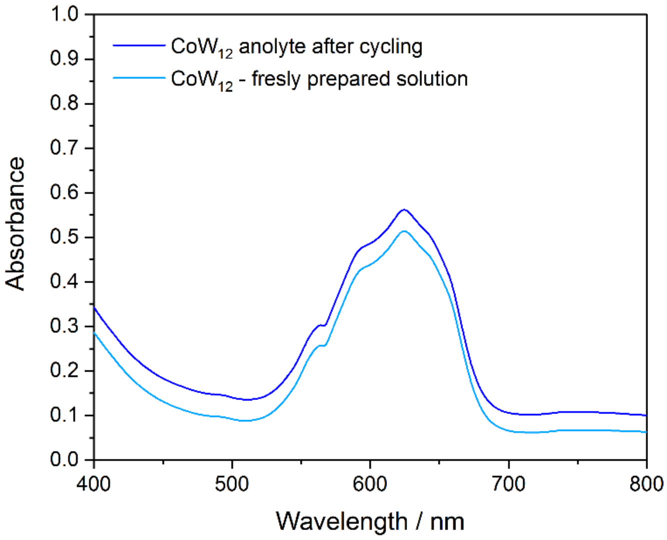

Figure 5.13 - UV-visible spectrum of a 2 mM ***CoW_{12}*** *solution and the* ***CoW_{12}*** *anolyte after cycling, following dilution to 2 mM.*

As the electrochemical yield of the **CoW_{12}-PV_{14}** stationary cell was low, a second cell with an identical electrolyte composition was set up. The results are shown in Figure 5.14. The discharge cut-off voltage was changed during cycle 21 which led to a drop in capacity and coulombic efficiency for that cycle, but the capacity stabilised as cycle 50 was approached. However, this stationary cell showed a low electrochemical yield once again; around 6 mAh out of a theoretical 13 mAh were accessed.

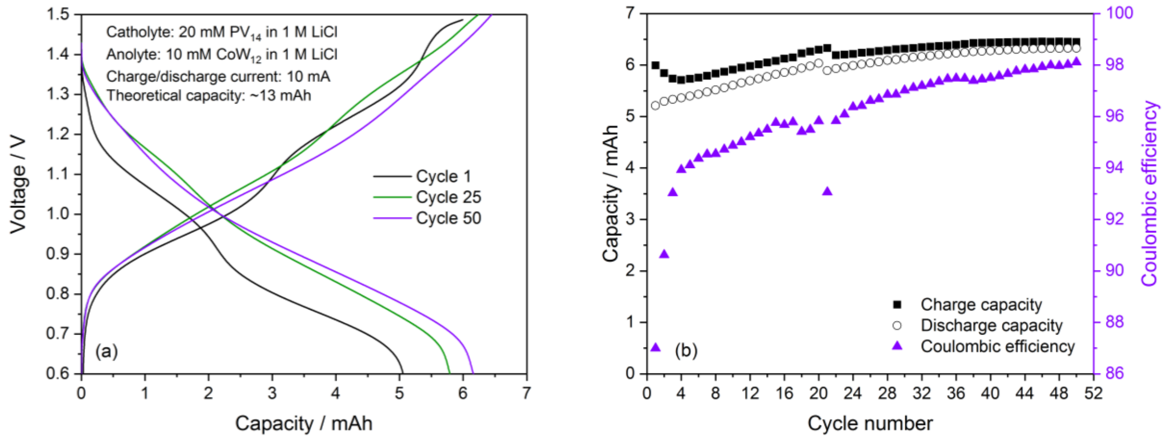

Figure 5.14 - (a) Charge/discharge curves of a further ***CoW_{12}-PV_{14}*** *stationary cell test. (b) Charge capacity, discharge capacity and coulombic efficiency versus cycle number.*

The cause of the low electrochemical yield of both **CoW_{12}-PV_{14}** cells could not be ascertained. Each electrolyte compartment was filled with 12–13 mL of electrolyte, around the limit of the volume of electrolyte that the stationary cell can hold, which suggests that the carbon felt electrodes were sufficiently wetted. However, as both stationary cells did not demonstrate capacity fade over 50 cycles, instability of the **CoW_{12}-PV_{14}** system was not indicated by these tests and it was decided that flow cell testing should proceed.

5.6 Flow cell testing

The work on a **CoW_{12}-PV_{14}** flow cell was continued as part of the research project of an MChem student, Thomas Beresford-Peirse, during the 2017/18 academic year. Selected results from this work are included in this section due to their importance in illustrating that **CoW_{12}** has potential as an anolyte in a POM RFB. The individuals who carried out the experiments shown are highlighted in the figure captions.

To further the charge/discharge testing of the **CoW_{12}-PV_{14}** system, a flow cell was constructed. The anolyte was a 20 mM **CoW_{12}** solution in 1 M LiCl, adjusted to pH 2.0 before cycling of the cell commenced. The catholyte was a 20 mM **PV_{14}** solution also in 1 M LiCl adjusted to pH 3.2, one hour after the stoichiometric addition of hydrazine to reduce **PV_{14}** by four electrons. Unfortunately, leakage of the **CoW_{12}** electrolyte occurred soon after testing began and the flow cell failed. However, the data from the first cycle is shown in Figure 5.15, before electrolyte leakage was substantial, to indicate the appearance of the charge/discharge curves for this system. Three plateaus are visible. The first smaller plateau occurs at ~0.6 V and could not be related to a CV of **CoW_{12}**. The second and third plateau occur at similar charging and discharging voltages to the plateaus observed in the stationary cell tests. The second plateau begins at ~0.67 V upon charge and lasts until ~1.0 V, when the third plateau begins. These two plateaus are assigned to the first and second tungsten reactions of **CoW_{12}** respectively, which are coupled with the reactions of **PV_{14}**. Upon discharge, the third plateau lasts until ~0.90 V before the second plateau begins which lasts until ~0.64 V, close to the voltage it began at when the cell was charged.

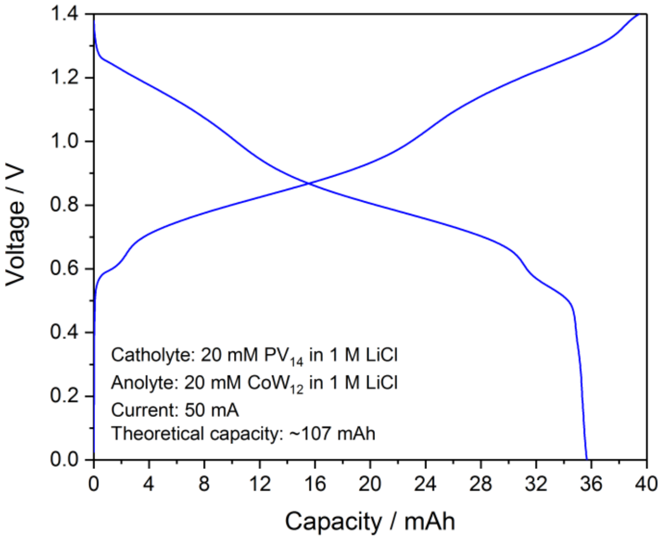

*Figure 5.15 - Cycle 1 of a **CoW_{12}-PV_{14}** flow cell. Anolyte: 50 mL of 20 mM **CoW_{12}** in 1 M LiCl. Catholyte: 50 mL of 20 mM **PV_{14}** in 1 M LiCl. **This experiment was carried out by Faye Cording, Thomas Beresford-Peirse and Jochen Friedl**.*

The experiment was later repeated and the result was more promising (the electrolyte preparation and flow cell construction were carried out by Thomas Beresford-Peirse and Jochen Friedl). The results of this flow cell test are shown in Figure 5.16.

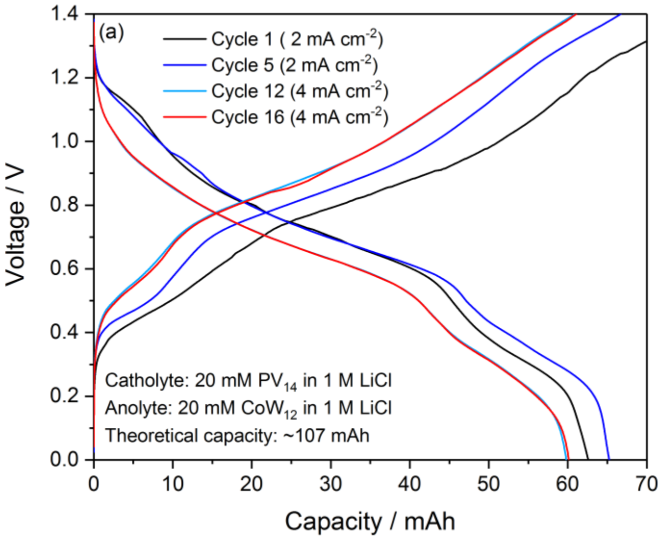

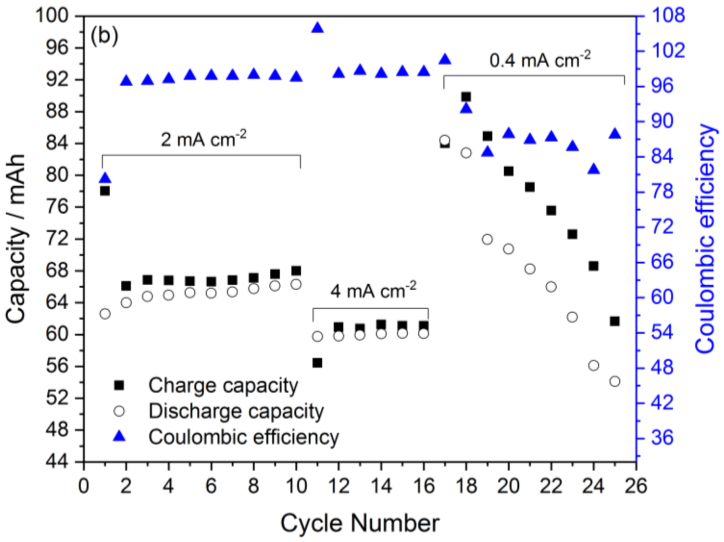

Figure 5.16 - The results of the second ***CoW$_{12}$-PV$_{14}$*** *flow cell test. (Anolyte: 50 mL of 20 mM* ***CoW$_{12}$*** *in 1 M LiCl. Catholyte: 50 mL of 20 mM* ***PV$_{14}$*** *in 1 M LiCl.) (a) Charge/discharge curves. (b) Charge capacity, discharge capacity and coulombic efficiency versus cycle number.* ***This experiment was carried out by Thomas Beresford-Peirse and Jochen Friedl.***

The **CoW$_{12}$-PV$_{14}$** flow cell ran for 25 charge/discharge cycles. Over this time, coulombic efficiencies of >97% were observed from cycle 4 to cycle 17. The theoretical capacity was 107 mAh. Varying the value of the charge and discharge current density between 0.2 mA cm^{-2} and 4 mA cm^{-2} resulted in a variation in the amount of theoretical capacity of the battery that could be accessed. The largest capacity was observed in cycle 17, where the discharge capacity was 79% of the theoretical value.

Capacity fade became evident after cycle 17. During later cycles, a reduction in the electrolyte volume was noticed in the flow cell tanks which correlated with the appearance of water condensation on the inside of the polycarbonate box that contained the flow cell. Evaporation of water from both electrolytes and the consequent reduction in electrolyte volume may explain the onset of this capacity fade. Nonetheless, charge/discharge curves with a stable appearance were observed and capacity fade was not evident from cycle 1 to cycle 16, indicating a **CoW$_{12}$-PV$_{14}$** flow cell with stable capacity was possible.

Analysis of the anolyte and catholyte was later carried out to look for signs of decomposition. The **CoW$_{12}$** anolyte was diluted with 1 M H_2SO_4, which allowed a comparison of the peak positions with previous CVs in this supporting electrolyte. A ^{51}V NMR spectrum was obtained of the **PV$_{14}$** catholyte.

Due to evaporation of the electrolytes during flow cell testing, the concentration of **CoW$_{12}$** could no longer be taken as 20 mM, but carrying out a 1:9 dilution with 1 M H_2SO_4 yielded a CV, shown in Figure 5.17a, with peaks at positions comparable to a CV of a freshly prepared **CoW$_{12}$** solution, which was shown previously in Figure 5.1. This indicated that

CoW$_{12}$ had not decomposed during the charge/discharge testing. There is a larger non-faradaic current shown in Figure 5.17a compared to the CV of **CoW$_{12}$** in Figure 5.1. A different glassy carbon electrode with a larger geometric surface area was used to obtain the CV in Figure 5.17a, which explains why the underlying non-faradaic current is larger.

The ^{51}V NMR spectrum of **PV$_{14}$** showed peaks at -597 ppm, -580 ppm and -529 ppm which correspond to the three different vanadium environments in **PV$_{14}$**,[18] indicating that intact **PV$_{14}$** was present in the sample. The two further peaks at -523 ppm and -505 ppm correspond to decavanadate, $[H_xV_{10}O_{28}]^{(6-x)-}$,[18] perhaps indicating that the pH of the catholyte had shifted away from the optimum pH for formation of **PV$_{14}$**. This would lead to a proportion of the vanadium in the sample being incorporated into decavanadate species.

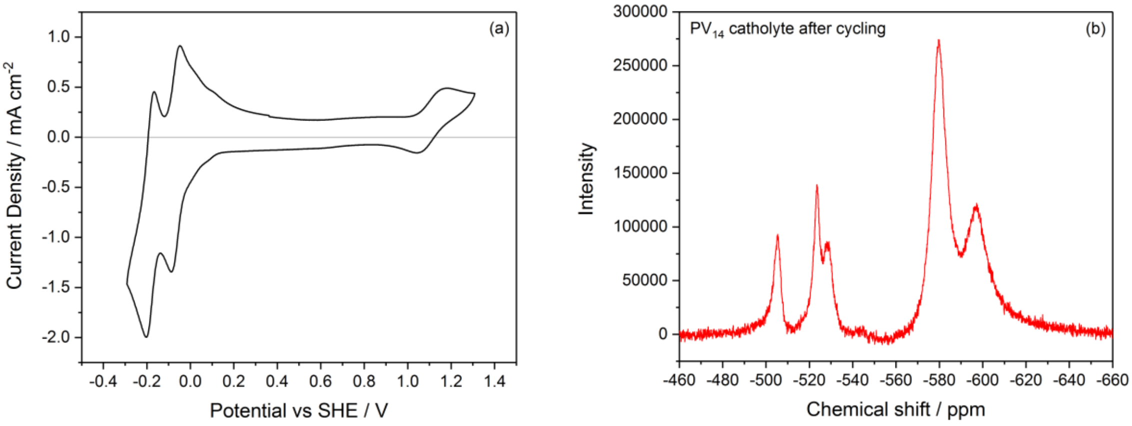

*Figure 5.17 - An analysis of the **CoW$_{12}$** anolyte and **PV$_{14}$** catholyte after cycling in a flow cell. (a) A CV of the anolyte, diluted with 1 M H_2SO_4. (WE: glassy carbon, CE: platinum wire, RE: Ag/AgCl (3 M NaCl), scan rate: 100 mV/s) (b) A ^{51}V NMR spectrum of the catholyte. **The CV and NMR spectrum were obtained by Faye Cording**.*

Nonetheless, the results of the flow cell and the analysis of the electrolytes after testing indicate that a **CoW$_{12}$-PV$_{14}$** flow cell is worthy of further investigation. The steady charge/discharge capacity observed over 16 cycles and the CV of the anolyte after cycling, which contained features that match a CV of an uncycled **CoW$_{12}$** solution, suggest that **CoW$_{12}$** is a stable anolyte species. The presence of a proportion of decavanadate in the **PV$_{14}$** solution is a well-described pH-related effect[18] and could therefore be rectified by better control of the pH of the catholyte if testing were continued.

In terms of further experiments, it would be desirable to demonstrate a **CoW$_{12}$-PV$_{14}$** flow cell with similar concentrations to the values used in the **SiW$_{12}$-PV$_{14}$** system (0.1 M and 0.2 M respectively[2]) and therefore use a 0.1 M **CoW$_{12}$** anolyte. However, POM solubility is related to the counterion and increases in the order $K^+ < Na^+ < Li^+ < H^+$ and, when following the procedure of Baker and McCutheon,[9] **CoW$_{12}$** is synthesised as the potassium salt. Therefore, the solubility could be of concern if increased concentrations are sought and cation exchange treatment could be necessary. Indeed, Liu *et al*. exchanged the K^+ counterion of **CoW12** for H^+ to make the electrolytes for their symmetric **CoW12** flow cell.[4]

To investigate the highest concentration that could be reached for the potassium salt of **CoW12**, a solubility test was carried out. Small portions of deionised water were added to a sample of **CoW12** in a sample vial and the contents of the vial agitated after each addition of water until all of the solid was seen to dissolve. It was found that 1.91 g of **CoW12** could be dissolved in 710 μL of deionised water at room temperature, corresponding to a solubility of 269 g per 100 mL or 0.785 M. Therefore, it is likely that an electrolyte with a concentration of 0.1 M could be obtained for a flow cell using the potassium salt of **CoW12**, without the need for cation exchange treatment. A particularly high solubility of 460 g per 100 mL of solution, or 1.34 M, for **CoW12** was reported by Baker and McCutcheon at 28°C, in comparison to $[Co^{III}W_{12}O_{40}]^{5-}$ which had a solubility of 70 g per 100 mL or 0.204 M.[9] For comparison, the solubility limit of $H_4[SiW_{12}O_{40}]$ is 0.875 M in water at room temperature.[2]

5.7 Synthesis Difficulties

Whereas **SiW12** can be purchased commercially, as 'tungtosilicic acid hydrate', **CoW12** needs to be synthesised on-site. This extends the preparation time for the electrolytes of a **CoW12-PV14** flow cell, particularly if higher electrolyte concentrations are sought or if the system were scaled up and a larger electrolyte volume was necessary. A yield reported in the literature for **CoW12** is relatively low at 21.9%,[22] and an even smaller value was obtained in this work (16%). Conversely, a reported yield for the synthesis of the potassium salt of the α isomer of **SiW12** that is used in the **SiW12-PV14** system is 75%.[23]

The synthesis of **CoW12** is composed of two steps: synthesis of the 12-tungstodicobaltoate anion, $[Co_2(H_2O)W_{11}O_{39}]^{8-}$, and conversion of this to **CoW12**. The addition of 2 M H_2SO_4 to $[Co_2(H_2O)W_{11}O_{39}]^{8-}$ induces the replacement of the additional cobalt atom in the POM framework with a tungsten atom, to form **CoW12**.

In the original synthesis procedures reported for **CoW12**, during preparation of the ammonium salt it was reported that the crude sample of the precursor $[Co_2(H_2O)W_{11}O_{39}]^{8-}$ contained two insoluble substances, "a white ammonium tungstate and a pink cobaltous tungstate".[9] Five recrystallisations were required to yield a product that dissolved without leaving a solid residue.[9] In the synthesis of the potassium salt of **CoW12**, five recrystallisations of the precursor were also required to reach a pure product.[9]

As reported in the description of the synthesis of **CoW12** in this work (Section 5.2.2), the formation of a white insoluble substance was also experienced when preparing the potassium salt of **CoW12**. In this procedure, the recrystallisation of $[Co_2(H_2O)W_{11}O_{39}]^{8-}$ was omitted to try and reduce the time taken to prepare **CoW12**, as recrystallisation of the precursor was time-consuming. Upon adding acid to the crude sample of $[Co_2(H_2O)W_{11}O_{39}]^{8-}$ in order to convert it to **CoW₁₂**, formation of the white precipitate was evident in the solution which was removed by gravity filtration. The crude **CoW_{12}** sample obtained from evaporation of the filtrate still contained traces of the insoluble precipitate and required further recrystallisation. Clearly, a side-reaction occurs during the formation of $[Co^{II}_2(H_2O)W_{11}O_{39}]^{8-}$, which will decrease the final yield of **CoW_{12}**.

5.8 Summary and Conclusions

An investigation of **CoW_{12}** as an anolyte species for a POM RFB is outlined. The electrochemical profile of the POM is presented along with evidence that this species undergoes PCET, a desirable property for a POM that is coupled with a **PV_{14}** catholyte in a flow cell (as **PV_{14}** also undergoes PCET). Bulk electrolysis experiments supported the previous reporting by Friedl *et al*. that **SiW_{12}** could not be reduced by four electrons per molecule,[2] as signs of decomposition were evident after electrolysis ceased. There were no signs of decomposition in a CV of **CoW_{12}** after reduction by four electrons through bulk electrolysis.

Stationary cell tests that used a catholyte of **PV_{14}** and an anolyte of **CoW_{12}** did not exhibit substantial capacity fade, indicating **CoW_{12}** was not unstable during charge/discharge testing. In later flow cell tests, a cell with an electrolyte concentration of 20 mM had a stable capacity over 16 cycles. A solubility test of the potassium salt of **CoW_{12}** indicated that a solubility of 0.785 M was possible in water at room temperature, highlighting that a **CoW_{12}** RFB electrolyte of 0.1 M could be prepared without the need for cation exchange treatment of the potassium salt of the POM. This would match the concentration of the **SiW_{12}** anolyte that was previously used in a **SiW_{12}-PV_{14}** flow cell.

However, promising initial results in flow cell testing are countered by the decreased availability of the POM compared to **SiW_{12}**. Whereas the synthesis of **SiW_{12}** has been commercialised, literature methods must be relied upon to synthesise **CoW_{12}** and the yield obtained in this work was 16%. In spite of this, further work could focus on increasing the **CoW_{12}** electrolyte concentration to 0.1 M, in line with concentrations used in the published **SiW_{12}-PV_{14}** system, to test if this is possible. Monitoring of the pH of the electrolytes to assess how this value changes when PCET occurs in both half-cells of a flow cell could also be carried out.

In the search for an alternative anolyte species to **SiW_{12}**, another avenue that could be explored is the investigation of $[ZnW_{12}O_{40}]^{6-}$ instead of **CoW_{12}**. It has been shown that $[ZnW_{12}O_{40}]^{6-}$ has similar properties to **CoW_{12}**[17] (it can be reduced by four electrons and also undergoes PCET) and it may be that this POM can be prepared in higher yield. For instance, percentage yields calculated using the yield reported for two preparations of $[ZnW_{12}O_{40}]^{6-}$ are 32% for the tetrabutylammonium salt ($H_2[C_4H_9)N]_4[ZnW_{12}O_{40}]$) and 40% for the tetramethylammonium salt ($(Me_4N)_6[ZnW_{12}O_{40}]$).[24, 25] These values are higher than the literature value for **CoW_{12}**, and the yield obtained in this work.

5.9 References

1. B. Keïta and L. Nadjo, *Journal of Electroanalytical Chemistry and Interfacial Electrochemistry*, 1985, **191**, 441-448.
2. J. Friedl, M. V. Holland-Cunz, F. Cording, F. L. Pfanschilling, C. Wills, W. McFarlane, B. Schricker, R. Fleck, H. Wolfschmidt and U. Stimming, *Energy & Environmental Science*, 2018, DOI: 10.1039/C8EE00422F.
3. H. D. Pratt Iii, N. S. Hudak, X. Fang and T. M. Anderson, *J Power Sources*, 2013, **236**, 259-264.
4. Y. Liu, S. Lu, H. Wang, C. Yang, X. Su and Y. Xiang, *Advanced Energy Materials*, 2017, **7**, 1601224.
5. J.-J. J. Chen and M. A. Barteau, *Journal of Energy Storage*, 2017, **13**, 255-261.
6. L. E. Vangelder, A. M. Kosswattaarachchi, P. L. Forrestel, T. R. Cook and E. M. Matson, *Chemical Science*, 2018, **9**, 1692-1699.
7. B. Keita and L. Nadjo, *Materials Chemistry and Physics*, 1989, **22**, 77-103.
8. J. Friedl, F. L. Pfanschilling, M. V. Holland-Cunz, R. Fleck, B. Schricker, H. Wolfschmidt and U. Stimming, *Clean Energy*, 2019, DOI: 10.1093/ce/zkz019.
9. L. C. W. Baker and T. P. McCutcheon, *Journal of the American Chemical Society*, 1956, **78**, 4503-4510.
10. F. Walmsley, *Journal of Chemical Education*, 1992, **69**, 936.
11. A. L. Nolan, R. C. Burns and G. A. Lawrance, *Journal of the Chemical Society, Dalton Transactions*, 1998, DOI: 10.1039/A804598D, 3041-3048.
12. L. Pauling, *Journal of the American Chemical Society*, 1929, **51**, 2868-2880.
13. L. C. W. Baker and V. E. Simmons, *Journal of the American Chemical Society*, 1959, **81**, 4744-4745.
14. M. T. Pope and G. M. Varga, *Inorg. Chem.*, 1966, **5**, 1249-1254.
15. B. Keita, Y. W. Lu, L. Nadjo, R. Contant, M. Abbessi, J. Canny and M. Richet, *J Electroanal Chem*, 1999, **477**, 146-157.
16. M. Ibrahim, A. Haider, Y. Lan, B. S. Bassil, A. M. Carey, R. Liu, G. Zhang, B. Keita, W. Li, G. E. Kostakis, A. K. Powell and U. Kortz, *Inorg. Chem.*, 2014, **53**, 5179-5188.
17. J. Lei, J.-J. Yang, T. Liu, R.-M. Yuan, D.-R. Deng, M.-S. Zheng, J.-J. Chen, L. Cronin and Q.-F. Dong, *Chemistry – A European Journal*, 2019, **25**, 11432-11436.
18. A. Selling, I. Andersson, L. Pettersson, C. M. Schramm, S. L. Downey and J. H. Grate, *Inorg. Chem.*, 1994, **33**, 3141-3150.
19. N. Elgrishi, K. J. Rountree, B. D. McCarthy, E. S. Rountree, T. T. Eisenhart and J. L. Dempsey, *Journal of Chemical Education*, 2018, **95**, 197-206.

20. J. Friedl, R. Al-Oweini, M. Herpich, B. Keita, U. Kortz and U. Stimming, *Electrochim Acta*, 2014, **141**, 357-366.
21. M. V. Holland-Cunz, PhD Thesis, Newcastle University, 2018.
22. E. N. Glass, J. Fielden, Z. Huang, X. Xiang, D. G. Musaev, T. Lian and C. L. Hill, *Inorg. Chem.*, 2016, **55**, 4308-4319.
23. R. G. Finke, C. A. Green and B. Rapko, in *Inorganic Syntheses*, ed. A. P. Ginsberg, John Wiley & Sons, New York, 1990, vol. 27, ch. 3, pp. 128-135.
24. K. Nomiya and M. Miwa, *Polyhedron*, 1983, **2**, 955-958.
25. K. Nakajima, K. Eda and S. Himeno, *Inorg. Chem.*, 2010, **49**, 5212-5215.

Chapter 6 - Discussion and Outlook

6.1 Discussion

In this study, **SiV_3W_9** was investigated as an active species for a symmetric POM RFB and aspects of **SiW_{12}** and **CoW_{12}** were considered in the context of their application as the anolyte species in an asymmetric POM RFB.

POMs have been proposed as being possible RFB active species for reasons such as fast electron transfer, electron transfer that is coupled to proton transfer (PCET), the high solubility of some POMs and multi-electron redox reactions.[1] The fast electron transfer of POMs could enable RFB operation at high current densities, and PCET ensures that the overall charge of a POM does not change upon oxidation or reduction, so could increase the stability of a POM undergoing a redox process. PCET is common in both chemical and biological redox reactions, providing "reaction pathways in which electrons and protons are transferred simultaneously, thus avoiding high energy intermediates."[2] RFB active species that are highly soluble and/or that undergo multiple redox reactions per molecule are desirable because the energy density of an RFB is related to the solubility of the active species and the number of electrons transferred in the cell reaction.

The desirable properties of POMs described above were all exhibited by the POMs in this study. The k^0 values determined for the first and second redox reactions of **SiW_{12}** were relatively large. Investigation of **SiV_3W_9** indicated that both the vanadium and tungsten redox reactions of this species involved proton transfer. **CoW_{12}** also underwent PCET, transferred more electrons than **SiW_{12}** at similar potentials and was a relatively soluble species compared to other POMs. In addition to the demonstration of properties such as fast electron transfer kinetics, PCET and high solubility, it was also shown that the POMs under investigation were stable to charge/discharge testing.

SiV_3W_9 was stable to charge/discharge testing in the supporting electrolyte selected in this study, which differed to what was used in a previous study (a 0.5 M H_2SO_4 supporting electrolyte[3]). After CVs indicated that reduced **SiV_3W_9** was unstable in acidic conditions (1 M H_2SO_4), a supporting electrolyte with a pH of 2 was selected for charge/discharge testing. The electrochemical yield was 67% and capacity fade was observed, the capacity decreasing by 2.7% over 50 cycles. In spite of the capacity fade, the stability of **SiV_3W_9** to the charge/discharge testing was evidenced by the analysis of the electrolytes afterwards which showed that the **SiV_3W_9** solutions after cycling had the same features as freshly prepared solutions. Coulombic efficiencies were >98% in flow cell testing, showing that side reactions were not of great concern. Increasing the electrochemical yield, confirmation of the source of capacity fade and minimisation of capacity fade should be a focus if work is continued.

Difficulties in the synthesis of **α-SiV_3W_9** were experienced, but it was proposed that the β isomer could be substituted for the α isomer as it was shown that the synthesis of **β-SiV_3W_9** resulted in a product of greater purity. A charge/discharge test of **β-SiV_3W_9** in an electrolyte with a pH of 2 had indicated some decomposition of the POM could have occurred during testing, but it was not substantial. As the difficulties in synthesising **SiV_3W_9** were avoided by preparing the β isomer instead, the investigation of **β-SiV_3W_9** could be continued. It was shown in Section 3.5 that the stability of a POM can be related to pH and thus, charge/discharge testing of **β-SiV_3W_9** could be carried out at other pH values to see if any decomposition occurs at higher pH values.

SiW_{12} has been used as an anolyte in an asymmetric POM RFB that underwent scaled-up testing from a cell with a membrane surface area of 25 cm^2 to one with a surface area of 1400 cm^{-2}.[1, 4] As such, this is a promising anolyte species. In this work, the kinetics of the first and second one-electron redox reaction of **SiW_{12}** were shown to be facile. The k^0 value was ~10^{-2} cm s^{-1}, which is three–four orders of magnitude greater than k^0 values reported for the VO_2^+/VO^{2+} and V^{3+}/V^{2+} redox reactions of the VRFB.[5] Studies of the kinetics of the redox reactions of **SiV_3W_9** and **CoW_{12}** were not carried out. However, a preliminary analysis of the kinetics was carried out using the results from cyclic voltammetry by determining the separation between the oxidation and reduction peaks (ΔE_p) of each species and comparing this to the theoretical value for a Nernstian reaction. The value of ΔE_p deviates from its theoretical value of $0.059/n$ V at 25°C when the electron transfer kinetics are sluggish. For instance, the peak separation reported for the VO_2^+/VO^{2+} redox couple was 0.929–1.532 V, depending on the supporting electrolyte.[6] In the case of **SiV_3W_9**, ΔE_p for the first redox reaction of vanadium was 0.055 V, close to the theoretical value for a one-electron reaction, and was 0.031 V for the first redox reaction of tungsten which is close to the theoretical value of ΔE_p for a two-electron reaction. For **CoW_{12}**, ΔE_p was 0.030 V for the first tungsten redox reaction which is also close to the theoretical value for a two-electron reaction. The values of ΔE_p for both **SiV_3W_9** and **CoW_{12}** indicate that the kinetics of electron transfer are faster for the POMs than for a sluggish redox couple like VO_2^+/VO^{2+}. Further work on the study of the kinetics of POM reactions could encompass other POMs, so that k^0 values can be obtained and compared to the k^0 values for **SiW_{12}**. Also, as discussed in Section 4.5, different techniques could be investigated in addition to the use of EIS to determine k^0.

The differing electrochemical properties of **CoW_{12}** compared to **SiW_{12}** were also highlighted in this work: the redox reactions of **CoW_{12}** occur at similar potentials to **SiW_{12}**

but the reactions of **CoW_{12}** are proton coupled and involve four electrons (two two-electron redox reactions) whereas the reactions of **SiW_{12}** that can be used in an RFB involve two electrons (two one-electron redox reactions) and are independent of pH. When **CoW_{12}** was tested as an anolyte and was paired with a **PV_{14}** catholyte, 79% of the theoretical capacity was accessed, suggesting that both of the two-electron redox reactions of **CoW_{12}** were active (the theoretical capacity was calculated by assuming an anolyte reaction that involved four electrons per molecule). Coulombic efficiencies were >97% and the stability of **CoW_{12}** to charge/discharge testing was evidenced by analysis of the anolyte by cyclic voltammetry after cycling. It was discussed in Section 5.6 that the yield of **CoW_{12}** was low (16% in this work), whereas literature on **SiW_{12}** indicates that the yield is higher and **SiW_{12}** can also be purchased commercially. Based on this, a trade-off between the use of **CoW_{12}** or **SiW_{12}** as an anolyte can be summarised:

- **SiW_{12}** can accept fewer electrons per molecule than **CoW_{12}** in an RFB (two electrons per molecule) but it may be easier to access the amounts of this POM that are required to prepare electrolytes for continued flow cell testing.
- While the work on **CoW_{12}** supports that this POM can accept more electrons per molecule than **SiW_{12}**, the low yield of **CoW_{12}** suggests that the difficulty in accessing the amounts of this POM that are required for continued flow cell testing would be greater compared to **SiW_{12}**.

Further work on the **SiW_{12}-PV_{14}** or **CoW_{12}-PV_{14}** RFBs may need to consider this trade-off.

In spite of the synthesis difficulties described, the results of the flow cell testing of **SiV_3W_9** and **CoW_{12}** do not discourage the use of these POMs when investigating POM RFBs further. Testing with electrolytes of higher POM concentrations should be the next step. As noted, better active material utilisation and gaining an understanding of the capacity fade should also be a focus of subsequent **SiV_3W_9** studies. Increasing the concentration of **CoW_{12}** so that it matches the concentration of **SiW_{12}** already used in an asymmetric RFB (0.1 M) would be the focus of additional study of this species. In the kinetics investigation of **SiW_{12}**, a relatively high value of k^0 was obtained and the use of other kinetic techniques to corroborate this result would be useful if continuing this investigation.

6.2 Outlook

POM RFBs were discussed in the Introduction (Section 1.3). The most promising aqueous POM systems to date, based on volumetric energy density and volumetric capacity, have active species concentrations above 0.1 M. The RFB presented by Chen *et al.*, in which a $[P_2W_{18}O_{62}]^{6-}$ anolyte was coupled with a catholyte containing HBr/Br_2, had the largest volumetric capacity reported amongst the POM systems discussed, a value of 230 Ah L^{-1} for a

0.5 M $[P_2W_{18}O_{62}]^{6-}$ electrolyte, corresponding to a volumetric energy density of 225 Wh L^{-1}.[7] Of the RFBs to use POMs in both half-cells, a symmetric RFB based on **CoW_{12}** had a volumetric capacity of 13.5 Ah L^{-1} for 0.8 M **CoW_{12}** electrolytes, which corresponded to a volumetric energy density of 15.4 Wh L^{-1} based on measured cell voltages during charge/discharge testing.[8] However, the volume of catholyte was four times the volume of the anolyte, to balance the number of electrons released in the anodic reaction. This is an aspect of RFB operation that could be improved by designing a symmetric RFB based on a species like **SiV_3W_9** as equal concentrations of POM could be used in the catholyte and anolyte, due to the number of electrons transferred in the anodic and cathodic reactions being balanced. However, a symmetric RFB based on **SiV_3W_9** would need to rival the active species concentrations of the current most promising POM systems to have a future beyond laboratory-scale testing and, thus, further work is required.

The additional work that could follow on from this thesis has been summarised: further charge/discharge testing of **SiV_3W_9** and **CoW_{12}**, including at higher concentrations, and the expansion of the kinetics study to encompass additional techniques and other POMs. Underlining the work carried out using **SiV_3W_9**, **SiW_{12}** and **CoW_{12}** was the question of whether POMs are suitable materials to use in RFBs. While additional experiments are described that could provide further evidence, overall, the results of the work in this thesis support the possibility of using POMs in RFBs. The results of charge/discharge testing of **SiV_3W_9** and **CoW_{12}** support this possibility because both POMs could hold charge in flow cell testing and decomposition after testing was not evident. The results of the kinetics study of **SiW_{12}** also support the use of POMs in RFBs: it was indicated that the kinetics of the redox reactions of **SiW_{12}** are faster than the redox reactions of the mature VRFB (the RFB to which any new chemistry is likely to be compared to for some time yet).

The major difficulty experienced in this work was in the synthesis of the POMs under study. However, the well-described synthesis of specific POM isomers was of benefit to the work on **SiV_3W_9** as the use of an alternative species to **α-SiV_3W_9**, the β isomer of **SiV_3W_9**, could be proposed. Further, the heteroatoms of POMs are highly variable and if a substitute for **CoW_{12}** was desired, other Keggin structures with a different heteroatom exist such as $[ZnW_{12}O_{40}]^{6-}$. This has electrochemical properties that are similar to **CoW_{12}** and it may be possible to prepare this POM in higher yield, as discussed in Section 5.8. The wealth of POM structures that are known could therefore mean that the route to finding an alternative when one species of interest is found to be unsuitable, due to a difficult or low-yielding synthesis for instance, is relatively simple. This is a positive aspect of investigating POMs for RFBs.

To summarise, **SiV_3W_9**, **SiW_{12}** and **CoW_{12}** display the properties that have previously been discussed as being desirable for RFB active species and are thus good candidates for further scientific study. However, the potential volumetric energy densities of the POM RFBs studied in this work may not be competitive with other RFBs. Based on the maximum solubility of **PV_{14}** in water (0.2 M[9]), a theoretical cell voltage of 0.77 V and a cell reaction in which four electrons are transferred, the theoretical volumetric energy density of a **CoW_{12}-PV_{14}** RFB is ~8 Wh L^{-1}. The energy density is limited by the solubility of **PV_{14}** as the maximum solubility of **CoW_{12}** in water was determined to be 0.785 M in Section 5.6. Based on the maximum solubility in water (0.45 M[3]) and a theoretical voltage of 0.895 V, the theoretical volumetric energy density of an **SiV_3W_9** RFB is 16 Wh L^{-1}. Theoretical volumetric energy densities for other proposed RFBs include ~17 Wh L^{-1} for an anthraquinone and ferri-/ferrocyanide RFB chemistry,[10] 20 Wh L^{-1} for an RFB chemistry consisting of a viologen derivative and a ferrocene derivative,[11] and 38 Wh L^{-1} for an RFB chemistry based on methyl viologen and a TEMPO derivative.[12] For the commercialised VRFB, the energy density is 20–33 Wh L^{-1}.[13] Increasing the solubility of POMs by altering the counterion is one measure that could be investigated to increase the volumetric energy densities of a **CoW_{12}-PV_{14}** or **SiV_3W_9** RFB.

The other issues highlighted in this work such as difficulties in synthesis or low yields may be specific to a particular POM and so could be alleviated by searching for other POMs with similar properties. There is also a broader implication of the use of POMs like **SiV_3W_9**, **SiW_{12}** and **CoW_{12}** that will now be discussed,

The cost of POMs has not been discussed in this work but is an important aspect of their use to consider because the desired culmination of a study of a POM for an RFB could be demonstration beyond laboratory-scale cells, or the prospect of commercialisation. There is a discrepancy between the numbers of metal atoms in POMs and the number of electrons involved in their redox activity. Whereas one electron is available per vanadium ion for the active species of the VRFB, some of the metal atoms in POMs can be viewed as being structural components only. **SiW_{12}** is reducible by two electrons in flow cell testing but has 12 tungsten atoms in its structure. **CoW_{12}** could offer four electrons per molecule in flow cell testing, but also contains 12 tungsten atoms. **PV_{14}** was not a focus of this study but can be reduced by up to seven electrons in a flow cell environment,[1] which is an improved metal-atom-to-electron ratio but there is still material in this POM that is not utilised for redox reactions. Cyclic voltammetry indicates that the three vanadium atoms in **SiV_3W_9** are redox-active, which is a better utilisation of the vanadium in the structure, but there are nine tungsten atoms in this structure and four electrons involved in the tungsten-based redox reactions.

While cost may be a minor aspect of the exploration of POM properties in scientific studies, it could be an important factor to consider for a POM RFB that goes beyond laboratory-scale because of the emphasis placed on the cost of large-scale energy storage. In 2010, a cost of \$100 per kWh was suggested by the Advanced Research Projects Agency-Energy (ARPA-E), an agency of the US Department of Energy, for large-scale storage of energy from renewable sources.[14] Meeting this target is one of the focuses of RFB research. A total capital cost of US\$380 kWh^{-1} was calculated for a 1 MW/1.2 MWh VRFB in one study, of which 37% was attributed to the vanadium electrolytes (assuming a cost of US\$21.13 kg^{-1} of vanadium in 2011).[15] The average price of vanadium (as V_2O_5) was US\$26.01 kg^{-1} in 2019.[16] This shows that vanadium remains a costly element to use in RFB electrolytes which is of concern when considering the application of vanadium-based POMs in RFBs, particularly as the metal-atom-to-electron ratio in POMs that contain vanadium is not always 1:1 (i.e. for POMs like **PV_{14}**). Tungsten is a dense element with a relatively high price per unit of weight. In 2019, the average price of tungsten was \$US270 per metric ton unit of WO_3, or US\$27 kg^{-1}.[17] As the price of tungsten is similar to vanadium, the use of tungsten-based POMs is unsuitable if a lowering of the cost of RFB active materials is desired. Molybdenum, another common addenda atom, is less dense than tungsten so would be cheaper but also has a less negative reduction potential.[18] Molybdenum redox reactions could be less suitable for use as anolyte reactions in RFBs as the theoretical voltages would be smaller than if tungsten redox reactions were used.

In a search for cheaper POM components, the range of other metals that can be incorporated into POMs as addenda atoms is limited. In order for a metal to be an addenda atom, the radius of the cation and the character of the bonds it forms with oxygen are important. Some elements are not of the correct ionic radius and/or do not display the correct properties. A metal must have a large enough radius to allow expansion of its coordination number from four to six and should have “the ability to act as a good acceptor of oxygen pπ electrons”.[19] The elements largely studied as addenda atoms in POMs are tungsten, molybdenum and vanadium, with niobium and tantalum POMs also known. Cations smaller than V^{5+} may only display a maximum coordination number of four and cations larger than Nb^{5+} do not exhibit metal-oxygen bonding that is conducive to POM formation, and tend to adopt larger coordination numbers.[19] POMs based on palladium, platinum and gold are known,[20-22] but are not of use to a search for RFB active materials. Elements such as iron and manganese can be incorporated into lacunary POMs and show redox activity,[23] and there are scattered reports of ‘Keggin-like’ structures based on other elements such as iron, manganese and aluminium[24-26] but, in general, the literature published this century and last century about POMs has a focus on the elements of tungsten, molybdenum and vanadium. Importantly, these elements can also show redox activity which is a necessity for application in RFBs.

Considering the price of vanadium and tungsten, the cost of POMs based on these metals does not look to be of help to ensuring that POM RFBs can meet the target set by ARPA-E. If the cost of the active materials of an RFB for large-scale energy storage is not something that can be addressed by POMs, a reduction in cost could come from changes to RFB design and operation that are made possible by using POMs. Switching from ion exchange membranes to less costly size exclusion membranes could be a benefit of the use of POMs in RFBs for instance.[1] Further, the fast redox kinetics mean that the use of POMs could target RFB power density, and it has been shown that increases in power density can have a significant impact on the cost of an RFB system.[27] At a typical power density for an RFB of 100 mW cm^{-2}, a combined cost calculated for three key RFB components was US\$100 kWh^{-1}–US\$200 kWh^{-1} (separator, two electrodes and separator plate, costed based on area in \$ m^{-2}).[27] It was found that the cost of these components decreased as a function of the power density, to ~US\$20 kWh^{-1}–US\$40 kWh^{-1} at 500 mW cm^{-2} and to ~US\$10 kWh^{-1}–US\$20 kWh^{-1} at 1 W cm^{-2}.[27] The lower acidity of the supporting electrolytes used with POMs compared to the supporting electrolyte of the VRFB is also beneficial to promoting the safety of RFBs over other energy storage devices. It is these aspects of the applications of POMs in RFBs that could be an incentive for further research.

6.3 References

1. J. Friedl, M. V. Holland-Cunz, F. Cording, F. L. Pfanschilling, C. Wills, W. McFarlane, B. Schricker, R. Fleck, H. Wolfschmidt and U. Stimming, *Energy & Environmental Science*, 2018, DOI: 10.1039/C8EE00422F.
2. M. H. V. Huynh and T. J. Meyer, *Chem. Rev.*, 2007, **107**, 5004-5064.
3. H. D. Pratt Iii, N. S. Hudak, X. Fang and T. M. Anderson, *J Power Sources*, 2013, **236**, 259-264.
4. J. Friedl, F. L. Pfanschilling, M. V. Holland-Cunz, R. Fleck, B. Schricker, H. Wolfschmidt and U. Stimming, *Clean Energy*, 2019, DOI: 10.1093/ce/zkz019.
5. J. Friedl and U. Stimming, *Electrochim Acta*, 2017, **227**, 235-245.
6. M. V. Holland-Cunz, J. Friedl and U. Stimming, *J Electroanal Chem*, 2018, **819**, 306-311.
7. J.-J. Chen, M. D. Symes and L. Cronin, *Nature Chemistry*, 2018, DOI: 10.1038/s41557-018-0109-5.
8. Y. Liu, S. Lu, H. Wang, C. Yang, X. Su and Y. Xiang, *Advanced Energy Materials*, 2017, **7**, 1601224.
9. M. V. Holland-Cunz, PhD Thesis, Newcastle University, 2018.
10. D. G. Kwabi, K. Lin, Y. Ji, E. F. Kerr, M.-A. Goulet, D. De Porcellinis, D. P. Tabor, D. A. Pollack, A. Aspuru-Guzik, R. G. Gordon and M. J. Aziz, *Joule*, 2018, **2**, 1894-1906.
11. E. S. Beh, D. De Porcellinis, R. L. Gracia, K. T. Xia, R. G. Gordon and M. J. Aziz, *ACS Energy Letters*, 2017, **2**, 639-644.
12. T. Janoschka, N. Martin, M. D. Hager and U. S. Schubert, *Angewandte Chemie International Edition*, 2016, **55**, 14427-14430.
13. M. Skyllas-Kazacos, G. Kazacos, G. Poon and H. Verseema, *Int. J. Energy Res.*, 2010, **34**, 182-189.
14. ARPA-E Program - Grid-Scale Rampable Intermittent Dispatchable Storage, https://arpa-e.energy.gov/?q=arpa-e-programs/grids, (accessed 4 March, 2020).
15. M. Zhang, M. Moore, J. S. Watson, T. A. Zawodzinski and R. M. Counce, *J Electrochem Soc*, 2012, **159**, A1183-A1188.
16. *Vanadium - Mineral Commodity Summary 2020*, U.S. Geological Survey, 2020.
17. *Tungsten - Mineral Commodity Summary 2020*, U.S. Geological Survey, 2020.
18. I. K. Song and M. A. Barteau, *Journal of Molecular Catalysis A: Chemical*, 2004, **212**, 229-236.

19. M. T. Pope, in *Heteropoly and Isopoly Oxometalates*, Springer-Verlag, Berlin, 1983, ch. 8, pp. 128-136.
20. E. V. Chubarova, M. H. Dickman, B. Keita, L. Nadjo, F. Miserque, M. Mifsud, I. W. C. E. Arends and U. Kortz, *Angewandte Chemie International Edition*, 2008, **47**, 9542-9546.
21. M. Pley and M. S. Wickleder, *Angewandte Chemie International Edition*, 2004, **43**, 4168-4170.
22. N. V. Izarova, N. Vankova, T. Heine, R. N. Biboum, B. Keita, L. Nadjo and U. Kortz, *Angewandte Chemie International Edition*, 2010, **49**, 1886-1889.
23. J. Liu, F. Ortega, P. Sethuraman, D. E. Katsoulis, C. E. Costello and M. T. Pope, *Journal of the Chemical Society, Dalton Transactions*, 1992, DOI: 10.1039/DT9920001901, 1901-1906.
24. O. Sadeghi, L. N. Zakharov and M. Nyman, *Science*, 2015, **347**, 1359-1362.
25. G. N. Newton, S. Yamashita, K. Hasumi, J. Matsuno, N. Yoshida, M. Nihei, T. Shiga, M. Nakano, H. Nojiri, W. Wernsdorfer and H. Oshio, *Angewandte Chemie International Edition*, 2011, **50**, 5716-5720.
26. G. Johansson, *Acta Chem. Scand.*, 1960, **14**, 771-773.
27. M. L. Perry, R. M. Darling and R. Zaffou, *ECS Transactions*, 2013, **53**, 7-16.